The Dissertation Committee for John Caleb Barentine
certifies that this is the approved version of the following dissertation:

The Role Of Gas In Galaxy Evolution: Infall, Star Formation, And Internal Structure

Committee:

John Kormendy, Supervisor

Shardha Jogee

Edward L. Robinson

Gregory Shields

Bart P. Wakker

The Role Of Gas In Galaxy Evolution: Infall, Star Formation, And Internal Structure

by

John Caleb Barentine, B.S., M.S., M.A.

DISSERTATION

Presented to the Faculty of the Graduate School of

The University of Texas at Austin

in Partial Fulfillment

of the Requirements

for the Degree of

DOCTOR OF PHILOSOPHY

THE UNIVERSITY OF TEXAS AT AUSTIN

May 2013

This work is dedicated to the memory of my father,

John Bruce Barentine

(11 August 1952 – 17 January 2010)

Acknowledgments

I give thanks to many people whose contributions, support, and commiseration have made this work possible and helped sustain my efforts long after I stopped believing in myself.

In 2001, the journal *Science* published an editorial[1] titled "An Algorithm For Discovery" in which two neuroscientists from UMass tried to somehow parameterize the process of science and distill it into "a kind of flow chart that could be carried on a laminated card." A photocopy of this article hung on my office door for a long time. The authors' conclusions, distilled into a series of bullet points, reads:

1. **Slow down to explore.**
2. **Read, but not too much**
3. **Pursue quality for its own sake.**
4. **Look at the raw data.**
5. **Cultivate smart friends.**

I learned all five of these elements and their importance from different people along the way.

[1] D. Paydarfar and W.J. Schwartz, 2001, *Science*, 292, 5514, 13

To my supervisors in grad school, Drs. John Kormendy, John Lacy, and Bart Wakker. The contents herein bear your indelible marks. I also thank Drs. Shardha Jogee, Rob Robinson, and Greg Shields for their service on my supervising committee. (2, 3, 4)

To my parents, John and Delsia Barentine, for never once questioning my ridiculous decision to go into science as a career choice. They often didn't understand what I did for a living, but they were no less proud as a result. One of the greatest disappointments in life is that my father did not live to see this work completed. I have done my best to honor his memory as I finished up this work in his absence. (1, 2, 3)

To my friends, too numerous to name individually, for their counsel and sympathy (and for not talking me out of grad school). I would be remiss if I didn't thank the staff of Texas Coffee Traders at Robert Lee Moore Hall, who literally fueled this work with caffeine for several years (in particular, Candice Dublin, Patrick Edwards, and Joseph Duke). (5)

To my class, Amanda Bayless, Guillermo Blanc, Sean Couch, Bi-Qing For, Candace Gray, Amanda Heiderman, Randi Ludwig, Jeremy Murphy, Sehyun Hwang, Hyo-Jeong Kim, Masatoshi Shoji, and Tim Weinzirl, I owe a debt for years of reassurance, camaraderie, and commiseration as needed. No one could ask for a better cohort with which to endure this experience. We turned mostly okay, didn't we? (3, 4, 5)

To former mentors in science, Drs. Roger Culver, Stuart Field,

Ian Gatley, Karen Harvey, Charlie Lindsey, Stuart Jeffries, K. Mike Merrill, and Caty Pilachowski, from whom I learned the nuts and bolts fundamentals of how science is done, for teaching me the craft of science. (1, 2, 3, and especially 4)

To my principal counselor throughout nearly the entire grad school experience, Dr. James Gay, who proved to me that attitude really *is* everything (3, 5).

In 1936, in *Physics and Reality*, Einstein wrote, "The whole of science is nothing more than a refinement of everyday thinking.' Practicing this art does not require elaborate instrumentation, generous funding, or prolonged sabbaticals. What it does require is a commitment to exercising one's creative spirit – for curiosity's sake." However, Einstein also famously quipped, "Science is a wonderful thing if one does not have to earn one's living at it."

John Barentine
Austin
April 2013

The Role Of Gas In Galaxy Evolution: Infall, Star Formation, And Internal Structure

Publication No. _____

John Caleb Barentine, Ph.D.
The University of Texas at Austin, 2013

Supervisor: John Kormendy

The story of a typical spiral galaxy like the Milky Way is a tale of the transformation of metal-poor hydrogen gas to heavier elements through nuclear burning in stars. This gas is thought to arrive in early times during the assembly phase of a galaxy and at late times through a combination of hot and cold "flows" representing external evolutionary processes that continue to the present. Through a somewhat still unclear mechanism, the atomic hydrogen is converted to molecules that collect into clouds, cool, condense, and form stars. At the end of these stars' lives, much of their constituent gas is returned to the galaxy to participate in subsequent generations of star formation. In earlier times in the history of the universe, frequent and large galaxy mergers brought additional gas to further fuel this process. However, major merger activity began an ongoing decline several Gyr ago and star

formation is now diminishing; the universe is in transitioning to an era in which the structural evolution of disk galaxies is dominated by slow, internal ("secular") processes. In this evolutionary regime, stars and the gas from which they are formed participate in resonant gravitational interactions within disks to build ephemeral structures such as bars, rings, and small scale-height central bulges. This regime is expected to last far into the future in a galaxy like the Milky Way, punctuated by the periodic accretion of dwarf satellite galaxies but lacking in the "major" mergers that kinematically scramble disks into ellipticals. This thesis examines details of the story of gas from infall to structure-building in three major parts.

The High- and Intermediate-Velocity Clouds (HVCs/IVCs) are clouds of H I gas at velocities incompatible with simple models of differential Galactic rotation. Proposed ideas explaining their observed properties and origins include (1) the infall of low-metallicity material from the Halo, possibly as cold flows along filaments of a putative "Cosmic Web"; (2) gas removed from dwarf satellite galaxies orbiting the Milky Way via some combination of ram pressure stripping and tidal disruption; and (3) the supply and return feeds of a "Galactic Fountain" cycling gas between the Disk and Halo. Numerical values of their observed properties depend strongly on the Clouds' distances. In Chapter 2, we summarize results of an ongoing effort to obtain meaningful distances to a selection of HVCs and IVCs using the absorption-line bracketing method. We find the Clouds are not at cosmological distances, and with the exception of the Magellanic Stream, they are generally situated within a few kiloparsecs

of the Disk. The strongest discriminator of the above origin scenarios are the heavy element abundances of the Clouds, but to date few reliable Cloud metallicities have been published. We used archival UV spectroscopy, supplemented by new observations with the Cosmic Origins Spectrograph aboard the *Hubble Space Telescope*and H I 21 cm emission spectroscopy from a variety of sources to compute elemental abundances relative to hydrogen for 39 HVC/IVC components along 15 lines of sight. Many of these are previously unpublished. We find support for all three origin scenarios enumerated above while more than doubling the number of robust measurements of HVCs/IVCs in existence. The results of this work are detailed in Chapter 3.

In Chapter 4 we present the results of a spectroscopic study of the high-mass protostellar object NGC 7538 IRS 9 made with the Texas Echelon Cross Echelle Spectrograph (TEXES), a sensitive, high spectral resolution, mid-infrared grating spectrometer and compare our observations to published data on the nearby object NGC 7538 IRS 1. Forty-six individual lines in vibrational modes of the molecules C_2H_2, CH_4, HCN, NH_3 and CO were detected, including two isotopologues (^{13}CO, $^{12}C^{18}O$) and one combination mode ($\nu_4+\nu_5$ C_2H_2). Fitting synthetic spectra to the data yielded the Doppler shift, excitation temperature, Doppler b parameter, column density and covering factor for each molecule observed; we also computed column density upper limits for lines and species not detected, such as HNCO and OCS. We find differences among spectra of the two objects likely attributable to their differing radiation and thermal environments. Temperatures and column densities for the

two objects are generally consistent, while the larger line widths toward IRS 9 result in less saturated lines than those toward IRS 1. Finally, we compute an upper limit on the size of the continuum-emitting region ($\sim$2000 AU) and use this constraint and our spectroscopy results to construct a schematic model of IRS 9.

In Chapters 5 and 6, we describe studies of the bright, nearby, edge-on spiral galaxies NGC 4565 and NGC 5746, both previously classified as type Sb spirals with measured bulge-to-total luminosity ratios $B/T \simeq 0.4$. These ratios indicate merger-built, "classical" bulges but in reality represent the photometric signatures of bars seen end-on. We performed 1-D photometric decompositions of archival *Hubble Space Telescope*, *Spitzer Space Telescope*, and Sloan Digital Sky Survey images spanning a range of wavelengths from the optical to near-infrared that penetrate the thick midplane dust in each galaxy. In both, we find high surface brightness, central stellar components that are clearly distinct from the boxy bar and from the disk; we interpret these structures as small scale height "pseudobulges" built from disk material via internal, resonant gravitational interactions among disk material − not classical bulges. The brightness profiles of the innermost component of each galaxy is well fitted by a Sérsic function with major/minor axis Sérsic indices of $n = 1.55 \pm 0.07$ and 1.33 ± 0.12 for NGC 4565 and $n = 0.99 \pm 0.08$ and 1.17 ± 0.24 for NGC 5746. The true "bulge-to-total" ratios of these galaxies are considerably smaller than once believed: $0.061^{+0.009}_{-0.008}$ and 0.136 ± 0.019, respectively. Therefore, more galaxies than we thought contain little or no

evidence of a merger-built classical bulge. We argue further that a classical bulge cannot hide behind the dust lane of either galaxy and that other structures built exclusively through secular evolution processes such as inner rings, both revealed through the infrared imagery, argue strongly against any merger violence in the recent past history of these objects. From a formation point of view, NGC 4565 and NGC 5746 are giant, pure-disk galaxies, and we do not understand how such galaxies form in a ΛCDM universe. This presents a challenge to our picture of galaxy formation by hierarchical clustering because it is difficult to grow galaxies as large as these without making big, classical bulges.

We summarize the work presented in this thesis in Chapter 7 and conclude with speculations about the future direction of research in this field.

Table of Contents

List of Tables

List of Figures

Chapter 1

Introduction

The universe originated approximately 13.7 billion years ago in an energetic event – the Big Bang. Density fluctuations in the expanding fireball were magnified, becoming the basis for the foamy large-scale structure (LSS) of the cosmos seen at later times. Matter concentrated along the surfaces of "bubbles" in the LSS form the filaments of a "cosmic web"; galaxies are thought to have formed through the hierarchical clustering and merging of dark matter haloes on these surfaces, into whose gravitational potential wells baryons fell, cooled, and formed stars. Some fraction of gas did not participate in this process and likely remains in the web to this day. As galaxies grew through mergers and accretion of dwarf satellites, some of their gas content was removed through ram-pressure stripping while early generations of stars phase mixed and became the old, low-metallicity halo populations we see today. While the most massive mergers appear to effectively shut off the process of star formation, possibly by feedback from supermassive black holes, galaxies subjected to less merger violence found a new fuel source through smaller mergers and satellite accretion. Vigorous star formation proceeded, but the metallicity of the interstellar medium (ISM) in galaxies like the Milky Way did not increase steadily with time as expected if each galaxy were treated as a "closed box".

As the intensity of merger activity began to wane over cosmic time, influences driving the physical and chemical evolution of galaxies have shifted in nature from external to largely internal, manifested in transient structures such as bars and rings. Throughout cosmic history, gas played an important role in the narrative of the universe from the formation of hydrogen in the Big Bang to its incorporation into stars and galaxies. The relation between the parts of this thesis may seem tenuous at first, but further examination shows they are tied together by the story of gas in different astrophysical settings. Along the way, it has afforded me the chance to receive research training in several diverse areas of astronomy.

Since their discovery in the 1960s, the H I high- and intermediate-velocity clouds (HVCs/IVCs) have posed a challenging problem for models of both galaxy formation and their chemical evolution. Briefly, these are cloud of neutral hydrogen generally seen at high Galactic latitude whose observed motion is not predicted by models of the differential rotation of the Milky Way. Analogous clouds are seen around external galaxies, so we think they play a role in the circumgalactic ecosystem of many galaxies. Until recently, the principal unknown properties of the HVCs and IVCs were their distances and metallicities; discriminating among the proposed scenarios explaining the origin of the Clouds hinges on a reliable determination of both.

My involvement in this area of research began in 2003 while I was on the staff at Apache Point Observatory. Working with Dr. Bart Wakker and collaborators, I helped collect, reduce, and analyze medium-resolution

APO spectra of stars used as probes for placing distance brackets on various individual Clouds and Cloud complexes. The result of this effort has allowed us, for the first time, to make a definitive statement concerning the location of the Clouds in the vicinity of the Galaxy, which is that they are almost certainly not found at cosmological distances, but instead within a range of about 1-15 kpc above the plane of the disk. We therefore have established the "classical" HVCs/IVCs as a local galactic phenomenon with implications for the external evolution of the Milky Way. I summarized our efforts to date in a poster given at the 2007 symposium "New Horizons In Astronomy", honoring Professor Frank Bash, at UT. The conference proceedings paper is reproduced here as Chapter 2 to represent my work on the distances project.

Cloud metallicities are important predictions of the models developed to explain both where HVCs and IVCs originated and their role in the chemical evolution of the Galaxy. To date, few measurements of the metal abundances in the Clouds have been published, broadly suggesting a division according to velocity: HVCs appear to have subsolar metallicites, near $Z = 0.1\ Z_{\odot}$, while IVCs tend to have solar or slightly supersolar abundances. But abundance determinations published to date vary widely according to data source and quality, and analysis methods. We aimed to develop a uniform approach to obtaining gas-phase abundances for a selection of sightlines toward background objects probing Clouds with few or no previously published metallicity determinations, along with a few well-studied sightlines used as a check on the reliability of our measurements. We aimed to make this a valuable literature

reference for future researchers. This work forms the basis for Chapter 3 where we present new measurements of abundances along ten sightlines, of which half are previously unpublished.

The dominant ideas about the nature of the HVC assert that they represent the infall of "pristine" material from outside the Milky Way's sphere of influence or condensations of low-metallicity gas from the Halo that "rain" down onto the disk. In both cases, their role in the Galactic environment seems to involve contributing to the ongoing process of star formation, and they serve a regulatory function that has kept the average metallicity of long-lived dwarf stars in the Disk roughly constant over the Galaxy's history. The higher metallicity IVCs, on the other hand, appears to trace the cycling of gas between the Disk and Halo in a process governed by the deaths of massive stars in supernovae. These events inject large amounts of both mechanical energy and metal-enriched gas into the lower reaches of the Halo; when it returns to the Disk, it participates in the next round of massive star formation. For my master's work at UT, I collaborated with Dr. John Lacy on an effort to study the molecular chemistry of massive protostars in the starforming region NGC 7538 with his very high-resolution, mid-infrared spectrograph TEXES. This work is included here as Chapter 4.

Gas and stars newly-formed from it eventually phase-mix with the existing contents of the Galaxy and participate in its internal evolution. For a time in my graduate career, I worked with Dr. John Kormendy, who has researched and written extensively on the "secular" galaxy evolution, in which

internal processes determine the macro-structure of disk galaxies like the Milky Way. Quiescent, long time scale galaxy evolution is contrasted with the rapid changes associated with the violence of galaxy mergers; since the major merger rate began an ongoing decline at $z \sim 1$, secular evolution is emerging as the dominant mechanism by which galaxies evolve in (relative) isolation. But this picture is unexpectedly complicated: despite the observed merger frequency in earlier times, nearly 2/3 of the most massive field galaxies in the nearby universe show no sign of having experienced a "major" merger at least since the time the major merger rate began to decline. We found indications among edge- on spiral galaxies – those in which vertical structure is most clearly articulated absent the projection effects of high inclination to the line of sight – that secularly-built structures like bars were frequently misinterpreted by earlier investigations as the large scale height bulges made in mergers. Dr. Kormendy and I developed an approach to show that despite previous misclassification of bars as bulges, two nearby, massive, field edge-on galaxies in fact show evidence of recent merger activity. The method was first applied to NGC 4565, reproduced here as Chapter 5, and further developed in Chapter 6 as a follow-up paper on NGC 5746. We find both are reliably characterized as giant, pure-disk galaxies whose nature is difficult to explain given the current paradigm of galaxy formation by hierarchical clustering.

Finally, in Chapter 7, I summarize the results of my graduate work and speculate on the future of this story, in which gas finds its way into galaxies, cycles through repeated instances of star formation, and eventually

participates in the reorganization of galactic structure through largely internal processes. The goal is a future, integrated view of galaxy formation, on which I provide some concluding remarks.

Chapter 2

Distances To The High Velocity Clouds

J. Barentine, B. Wakker, D. York, J. Howk, R. Wilhelm, H. van Woerden, R. Peletier, T. Beers, P. Richter, Ž. Ivezić, and U. Schwarz, in *New Horizons in Astronomy: Frank N. Bash Symposium*, 2007 ASP Conference Series Vol. 393, p. 179

Wakker coordinated the distance project. York was the PI for the APO spectroscopic observations. Wilhelm furnished model atmosphere grids for classifying probe stars observed at APO. Richter provided institutional access to apply for VLT time as PI. Ivezić provided specific expertise in identifying probe star candidates in SDSS data. All other authors are collaborators who provided advice at various stages of the project. I obtained and reduced almost all of the APO data, collected the Keck data and carried out some of the KPNO photometric observations, and wrote the text of this paper.

Abstract

A full understanding of the High Velocity Clouds (HVCs) is still lacking more than four decades after their discovery. Determining the clouds' locations in relation to the Galaxy is an important constraint on hierarchical assembly

models of galaxies in a Λ-CDM universe. However, quantifying physical cloud properties such as mass and size have been difficult because of their unknown distances. We report the first definitive distance determinations for three HVCs (Complex C, 6.4-11.3 kpc; the Cohen Stream, 5.0-11.7 kpc; Complex GCP, 9.8-15.1 kpc) and two intermediate-velocity clouds (IVCs: IV-South, 1.0-2.7 kpc; cloud g1, 1.8-3.8 kpc) using the absorption line bracketing method. From the distances to the larger cloud complexes we calculate H I masses ranging from $1.5{\times}10^6$ $M_\odot$ to $8{\times}10^6$ $M_\odot$. In the case of Complex C this implies a mass inflow rate of $\sim$0.1 $M_\odot$ yr^{-1}. The measured distances place the HVCs in the hot Galactic Corona and the IVCs in the lowest reaches of the Halo. With this information we may now positively identify at least two roles played by HVCs in the internal and external dynamics of the Milky Way: (1) the infall of low-metallicity gas and (2) the supply and return streams of the Galactic Fountain.

2.1 Introduction

Of the outstanding problems in the formation and evolution of galaxies, an important example is the nature of the Galactic high velocity clouds (HVCs). These are clouds of H I gas at observed velocities not predicted by simple galactic differential rotation models; see the review by Wakker & van Woerden (1997a). Interpretations of the HVCs include infalling, low-metallicity gas from the intergalactic medium; material left over from the original assembly of the Milky Way; cycling of gas between the Disk and Halo

in a Galactic Fountain; and tidally-stripped debris from passing dwarf galaxies.

Testing these hypotheses requires knowing the basic parameters of the clouds, such as their masses and sizes. However, empirical measurements of these quantities have been frustrated for decades by a more fundamental unknown: their distances. HVC distances allow us to (1) quantify the inflow rate of low-metallicity gas into the Galaxy, possibly solving the G-dwarf problem (Pagel 1989) and explaining why the ISM was not completely turned into stars long ago; (2) place meaningful constraints on the strength of the metagalactic ionizing radiation field; (3) probe the shape of the dark matter potential of the Milky Way; and (4) understand observed clouds of H I with anomalous velocities around external galaxies in the context of galaxy formation and evolution

2.2 Experimental Method

We use the absorption line bracketing method to constrain HVC/IVC distances. This involves searching for interstellar (IS) absorption at cloud velocities toward probe stars in the direction of cloud complexes. Upper distance limits are set by detection of IS lines. Lower limits are established by "significant" non-detections in which the ratio of the expected equivalent width (EW) of an IS line to the observed EW upper limit is at least ten (Wakker 2001a). Expected EWs come from the empirical relation between N(H I) and N(Ca II) of Wakker & Mathis (2000).

Our probe star selection criteria require candidates to be (1) observable

at large distances; (2) relatively metal-poor, to avoid contamination of the IS metal line regions of the spectrum with stellar photospheric lines; and (3) hot enough to ensure sufficient flux in the near-UV near the Ca II H&K lines. The blue horizontal branch (BHB) stars meet these requirements but until recently have been difficult to identify in large quantities. We select probe candidates from the HK survey, SDSS and 2MASS. Candidates are correlated with H I maps of the HVCs, noting N(H I) toward each star. Photometry and medium-resolution spectroscopy are conducted to derive T_{eff}, log g, [Fe/H] and M_V (Wilhelm et al. 1999). A final check compares the medium-resolution spectroscopy against the H I spectra to ensure the stellar lines do not obscure the IS lines. This sample is then observed at high spectral resolution to detect the IS lines.

2.3 Observations

Probe stars are correlated with the 21 cm maps of Hulsbosch & Wakker (1988) and Morras et al. (2000). These provide a list of HVCs on a $1^\circ \times 1^\circ$ grid at 16 km s^{-1} resolution. The H I spectrum is checked using the Leiden-Argentina-Bonn (LAB) survey (Kalberla et al. 2005a), which covers the sky on a $0.5^\circ \times 0.5^\circ$ grid with 1 km s^{-1} resolution. For SDSS stars we used SDSS photometry and spectroscopy when available. Photometry of other candidates was performed at the ESO/Danish 1.5-m, WIYN 0.9-m, CTIO 0.9-m, Yale 1.0-m and MDM 2.4-m. We obtained spectroscopy with the ARC 3.5-m at Apache Point for HK and 2MASS stars and some SDSS stars. We observed

some relatively nearby HK stars toward complex C at high-resolution in 1997 with the 4.2-m William Herschel Telescope at a resolution of 6 km s^{-1}.

High-resolution spectroscopy of 25 probe stars in the direction of HVC complexes GCP and IVCs IV-South and cloud g1 was obtained with the VLT 8.4m telescope and UV-Visual Echelle Spectrograph in 37 hours between April-September 2006. Observations of three stars toward complex C at a resolution of 8.8 km s^{-1} were obtained in April 2007 with the 10-m Keck I telescope. The VLT observations were highly successful while the night of Keck time was plagued with poor seeing and foggy conditions. However, we obtained spectra of three probe stars toward complex C sufficient to determine a meaningful distance bracket.

2.4 Results

Distances for the clouds we measured are given in Table 2.1. We specify heliocentric distances to the clouds, and where available, the z distance above (positive) or below (negative) the plane of the MW. Using the H I masses derived from 21 cm maps, we calculated the mass inflow rates associated with complex C and the Cohen Stream. We conclude by summarizing the implications of our distance measurements for each cloud or complex.

complex C: Located high above the Disk of the MW, this subsolar-metallicity complex represents infalling gas that has not been previously cycled through the Galaxy. The mass infall rate associated with complex C is 0.1-0.25 $M_\odot$ yr^{-1}, a substantial fraction of the estimated $\sim$1 $M_\odot$ yr^{-1} (depending on some

Table 2.1 Distance brackets and derived physical parameters of HVCs and IVCs observed.

HVC/IVC	Distance (kpc)	z (kpc)	H I Mass ($M_\odot$)	$\dot{M}$ ($M_\odot$ yr^{-1})
complex C	3.7-11.2	3-9	0.7-6$\times10^6$	0.1-2.5
Cohen Stream (CS)	9.3-11.4	(-6.4)-(-8.4)	2.5-3.9$\times10^5$	4×10^{-3}
g1	1.8-3.8	(-0.8)-(-1.7)	$< 1\times10^4$	–
complex GCP	9.8-15.1	(-2.5)-(-3.9)	1×10^6	–
IV-South	1.0-4.5	–	1×10^5	–

assumptions) required to solve the G-dwarf problem.

Cohen Stream: This cloud complex is falling into the MW from high above the Disk, but at present its metallicity is not constrained.

cloud g1: The location of this cloud suggests that it is in an outflow of the Galactic Fountain. Cloud g1 may be condensing out of this flow.

complex GCP: A cloud complex of still unknown origin, and with still unknown metallicity. Its location and motion suggests a close association with the Disk, but modeling is required.

IV-South: This IVC represents the return flow of the Galactic Fountain and is identified specifically with the Perseus Arm of the MW.

Chapter 3

Elemental Abundances In The High- and Intermediate-Velocity Clouds

3.1 Introduction

The prevailing ΛCDM cosmological paradigm has had great success explaining the observed large-scale structure of the Universe, but it may not be the whole story on the level of individual galaxies. Some disk-dominated galaxies appear to never have suffered a major merger; how such galaxies are built is not addressed in the ΛCDM picture (see Chapters 5 and 6). While recent efforts such as the Sloan Digital Sky Survey (SDSS) have revealed a number of previously unknown, very low surface brightness dwarf galaxies in the Milky Way's vicinity, even a steady stream of accreted dwarfs may not adequately explain the phenomenon.

The assembly of the Galaxy technically continues up to the present. We would like to know the gas accretion rate as it relates to models that attempt to reconcile the rate of star formation in the Milky Way to other galaxies. The infall rate of high-velocity H I gas from the Halo to the Disk may serve as a direct measure of the rate at which the Milky Way is growing. The average metallicity of the interstellar medium (ISM), measured by proxy

in the metallicities of dwarf stars in the Galactic disk, is observed to have been roughly constant over much of the lifetime of the Milky Way; if the rate of implied mass infall required is added up over even a Gyr, the HVCs would during that period have added 10^9 $M_\odot$ of mass to the Galaxy. This speaks fundamentally to the process by which the Galaxy formed – and whether that formation continues to the present day. Accounting for the existence and and explaining the properties of the high- and intermediate-velocity clouds (HVCs/IVCs) are important in order to understand the history of the Galactic ecosystem as well as its current configuration and future evolution.

Our work on the HVC distances (summarized here in Chapter 2) suggests that some low-metallicity clouds are truly infalling and are delivering "fresh" material to the disk, therefore altering the chemical evolution of the ISM. Chemical models therefore must take into account this process and need reliable estimates of the mass inflow rate. It is also unclear whether HVCs have a significant dark matter component, in which case they might also deliver it to the disk along with baryons.

Finally, there is the issue of the HVCs as a fundamental class of objects worthy of study. Given that they are observed around other galaxies they are clearly a common if not ubiquitous phenomenon that we should understand around our own Galaxy if we are to understand their role in others.

3.1.1 History and Definitions

Observations extending back to the 1940s showed interstellar absorption due to material 500-1500 pc from the plane of the Milky Way (Münch & Zirin 1961), interpreted by Spitzer (1956) as clouds in equilibrium with a hypothetical Galactic Corona with a vertical extent ~ 8 kpc, temperature $\sim 10^6$ K, and hydrogen density $n_H \simeq 5 \times 10^{-4}$ cm^{-3}. Jan Oort reasoned that such a Corona might also consist of neutral hydrogen (H I) at high velocity which would condense out of the hot phase and "rain" onto the Disk, replacing gas that appeared to expand outward from the region of the Galactic Center. A search for high-velocity emission in the 21 cm spin-flip transition of H I was undertaken at the Dwingeloo Radio Observatory in the Netherlands in 1958, culminating in the discovery of the predicted gas as reported by Muller et al. (1963). Attempts to create comprehensive catalogs of HVCs and IVCs were made by Wakker in his PhD thesis (1990), and later in Wakker & van Woerden (1991) and Wakker (2001a).

The high-velocity clouds (HVCs) (and their related counterparts, the Intermediate Velocity Clouds, or IVCs) are broadly defined as clouds of neutral hydrogen whose velocities are incompatible with a simple model of differential galactic rotation (see comprehensive reviews by Wakker & van Woerden 1997b and Putman et al. 2012b). While these clouds are in part defined by the degree to which their observed velocities are therefore "anomalous" with respect to differential rotation models, there is no universally agreed-upon definition of what constitutes an "anomalous velocity". Wakker (1991) set an arbitrary

cutoff for the deviation velocity (v_{dev} = observed velocity - velocity predicted by differential rotation) of the Clouds at $|v_{dev}| = 50$ km s^{-1}, largely to avoid including gas at low galactic latitudes with high but otherwise normal velocities. A further definition distinguishes "high-velocity" gas ($|v_{dev}| > 100$ km s^{-1}) from "intermediate-velocity" gas ($100 \geq |v_{dev}| \geq 50$ km s^{-1}) thought to have a different origin. Most authors adopt velocity limits similar to these.

3.1.2 Properties of Anomalous-Velocity Gas

We now have a relatively clear, broad picture of the physical situation and nature of the HVCs, thanks to modern 21 cm H I surveys. HVCs consist of a combination of individual, isolated clouds down to the few-arcminute angular resolution limit of those surveys (Braun & Burton 1999) up to large contiguous associations of clouds known as "complexes", which may span ~ 1000 deg^2 across the sky (e.g., Wakker 2001a, Putman et al. 2002, Stanimirović et al. 2008, Hsu et al. 2011). The grouping of clouds into complexes assumes their physical proximity based on spatial and kinematic reasoning. Complexes have a morphology consisting of dense "cores" for which N(H I) may be up to 10^{20} cm^{-2} embedded in envelopes of column density down to the detection limit of $\sim 10^{17}$ cm^{-2}, corresponding to that of the faintest isolated clouds (e.g., Wakker et al. 2002, Lockman et al. 2002, Braun & Thilker 2004). The structure of many complexes and even individual clouds may have a fractal nature (Vogelaar & Wakker 1994). HVC complexes (excluding the Magellanic Stream; see Section 3.5.4) have masses of $10^5 - 10^6$ $M_\odot$ and are up to $\sim$15

kpc in physical extent; the mass of all known clouds is about $7 \times 10^7\ M_\odot$ after accounting for H I, H^+, and He (Wakker 2012, Putman et al. 2012b). The warm phase of the HVCs alone contributes $\sim 3.5 \times 10^7\ M_\odot$ to the mass of the Halo. Estimates for the volume density of the HVCs range from $0.05 - 0.15$ cm^{-3}, consistent with expectations from simulations of Halo clouds (Wakker 2001a, Hsu et al. 2011).

There is to date no definitive, direct detection of dust in HVCs on the basis of far-IR emission, but suggestions of dust emission have been seen in Complexes C (Miville-Deschênes et al. 2005, Planck Collaboration et al. 2011) and M (Peek et al. 2009). The absence of significant dust content is implied by the low depletion of refractory elements in many HVCs, although it is difficult to render judgment on this point based on the largely unknown ionization conditions of the gas and intrinsic abundance pattern of refractories in the clouds. It is widely thought that dust grains are the dominant sites of the formation of H_2 molecules in the universe (Shull & Beckwith 1982); the apparent absence of significant dust content in HVCs should result in little or no H_2 in HVCs. The evidence is mixed; Sembach et al. (2001a) saw H_2 in the Leading Arm of the Magellanic Stream at column densities of $N(H_2) = 10^{16} - 10^{17}$ cm^{-2}, and Richter et al. (2001c) saw similar columns toward the main body of the Stream itself. H_2 was also seen in the Magellanic Bridge, a gas structure connecting the Large and Small Magellanic Clouds, by Lehner (2002). It is unclear, though, whether this molecular component formed on dust *in situ* before being stripped from the Magellanic Clouds or in the Stream proper afterward.

No significant quantity of H_2 has been reported along sightlines toward other major cloud complexes, such as Complex C (Murphy et al. 2000, Richter et al. 2001b, 2003, Collins et al. 2003). While other H_2 formation mechanisms are known in the gas phase (e.g., Black 1978), these must not operate efficiently enough to allow diffuse H_2 to exist in HVCs even at high H I column densities. Alternately, any H_2 produced via whatever formation route might not survive once exposed to ionization conditions in the Halo. There is very limited evidence for the presence of other molecules in HVCs, such as the detection of CO in the Magellanic Bridge by Muller et al. (2003). By and large, HVCs have a distinctly atomic nature. On the other hand, IVCs generally have near-solar metallicities, significant depletion of refractories indicative of dust, and clear detections of H_2 (Richter et al. 2003).

Distance estimates for the HVCs, discussed in Chapter 2, generally place them within the Halo, of which they are clearly the coldest and most dense component. Further evidence for their proximity in the Disk is found in their detailed 21 cm H I structure and detection of Hα emission from the clouds, suggesting they are at least partially ionized by an external radiation field (Sternberg et al. 2002, Maloney & Putman 2003, Weiner 2003, Brüns & Mebold 2004, Madsen et al. 2006, Haffner & Madsen 2011). IVCs are found in the presumed Disk-Halo interface region. Searches to date have not yielded any evidence of recent or otherwise ongoing star formation in HVCs or IVCs (Ivezic & Christodoulou 1997, Simon et al. 2006), but other observations imply that the presence of clouds is at least correlated with, if not causative of, star

formation (Schulman et al. 1994, 1996, 1997a).

3.1.3 Evolution and Fate of HVCs/IVCs

Absorption line ratios obtained from UV spectroscopy require both photoionization and collisional ionization to properly model (e.g., Fox et al. 2006, 2010, Shull et al. 2011). 21 cm observations of individual clouds reveal typical linewidths of 20−30 km s^{-1}, or velocity dispersions of $\sigma = 8.5-13$ km s^{-1} (Putman et al. 2002, de Heij et al. 2002, Kalberla & Haud 2006), indicating the HVCs exist in a warm neutral medium at a temperature of $\sim$ 9000 K (Hsu et al. 2011). Many individual clouds show a characteristic "head-tail" shape consisting of a dense, cold core and a warmer envelope streamingaway from the head like the tail of a comet (Brüns et al. 2000, Brüns & Mebold 2004, Westmeier et al. 2005, Ben Bekhti et al. 2006, Putman et al. 2011); citetMeyerdierks91 first interpreted this shape as the result of an interaction between an HVC gas either in the Halo or at the Disk-Halo interface in which the tail defines the HVC's direction of motion. Widths of absorption lines in the UV often vary among ions within individual HVCs (e.g., Collins et al. 2004, Fox et al. 2005, 2006 supporting the idea of a multiphase structure. Absorption lines with smaller width seem to correspond to narrow 21 cm line profiles indicating cold gas at $\lesssim$500 K (Kalberla & Haud 2006). These warm and cold phases are consistent with a model in which the HVCs are in pressure equilibrium with hot, diffuse Halo gas (Wolfire et al. 1995), but this equilibrium is unlikely to persist beyond a few hundred million years absent

some kind of strong support mechanism. Means proposed for achieving long-term stability include confinement by a significant dark matter component (Braun & Burton 2000, Nichols & Bland-Hawthorn 2009) and/or magnetic fields (McClure-Griffiths et al. 2010), and dynamic shielding of cores by the envelopes of HVC complexes (Putman et al. 2012b). HVCs are ultimately destroyed via the Kelvin-Helmholtz instability resulting from ram-pressure interactions with the ambient Halo medium as gas is ablated around the edges of clouds, forming the observed tails (Vietri et al. 1997, Putman et al. 2012b). Given their masses and positions relative to the Galactic disk plane, it is unlikely that individual clouds survive a plunge through the Disk.

However the gas gets to the Disk, it probably helps trigger star formation (Comerón & Torra 1995, Hetem 1995). Simulations show that an H I cloud impinging on the Galactic disk generates shocks in the ISM; energy dissipated during the infall of these clouds may contribute to the heating of the extended hot Halo medium and helping maintain the multiphase structure of the ISM (Murray & Lin 2004). The propagation of shocks through the ISM results in the turbulence that precedes the collapse of molecular clouds to form stars. The end products of massive star formation – the destruction of those stars in Type II supernovae – inject considerable amounts of mechanical energy and metal-enriched gas into the lower reaches of the Halo. This is the basis for ideas concerning the origin of the IVCs (see Section 3.1.5, below).

3.1.4 The HVC Phenomenon in External Galaxies

Anomalous-velocity H I is certainly not unique to the Milky Way. Similar clouds have been observed around other nearby galaxies such as M31 (Thilker et al. 2004, Westmeier et al. 2005, 2007), M83 and M51 (Miller & Bregman 2005), NGC 5668 (Schulman et al. 1996), and NGC 891 (Oosterloo et al. 2007). On the other hand, some studies have turned up instances in which there is no significant H I in the halos of external galaxies to the detection limits of the searches (UGC 12732; Schulman et al. 1997a), while others show H I at implied total masses below expectations based on the Milky Way (NGC 1300; Schulman et al. 1997b). Observations of extragalactic HVCs show their properties are broadly consistent with those of the Milky Way HVC population. Masses of individual H I clouds seen around external galaxies range down to 10^5 $M_\odot$ (Thilker et al. 2004), but this lower limit is likely imposed by the resolution limitations of current observations. The total mass of H I in the M31 halo is comparable to the mass of all known Milky Way HVCs excepting the Magellanic Stream (Putman et al. 2012b). The M31 clouds are generally found within $\sim$10 kpc of the disk, and none are seen at distances > 80 kpc (Westmeier et al. 2007, Pisano et al. 2007). Halo H I features may occur with a frequency approaching 50% among field galaxies (Haynes et al. 1998, Sancisi et al. 2008).

3.1.5 Origin Scenarios

A number of models have been proposed to account for both the existence and observed properties of HVCs and IVCs. Putman et al. (2012b) enumerated a list of eight specific properties of the clouds and viable model must explain and/or predict:

1. Large spatial-scale flows of multiphase gas are common in the halos of many galaxies, including the Milky Way.

2. Halo gas increases in density with decreasing height above disks.

3. Gas at or near the interface between the disk and the halo shows clear gradients in temperature and rotational velocity, becoming increasingly hot and decreasing in rotation as the disk is approached.

4. Halo gas has non-primordial metal abundance, and gas at the base of the halo or in the disk-halo interface region is more enriched than gas at larger disk heights.

5. Galaxies with higher rates of star formation show more extensive halo gas than those with lower rates.

6. Spiral galaxy halos show diffuse gas at large radii (> 100 kpc).

7. The mass of warm and cold halo gas in the Milky Way is $< 10^9\ M_\odot$ while the hot halo gas mass may be in excess of $10^{10}\ M_\odot$Both are consistent with estimates for other low-redshift spiral galaxies of similar total mass.

8. Halo gas appears to be gravitationally bound to the dark matter halos of spiral galaxies.

Five main theories to account for the existence of HVCs/IVCs have been suggested:

- **Infalling low-metallicity gas**. In this scenario, the Clouds represent nearly 'pristine' hydrogen from the intergalactic medium (IGM), possibly delivered via the filaments of the Cosmic Web and/or cold flows (Kereš & Hernquist 2009). At the current rate of star formation, the total mass of the ISM would be converted into stars within about 1 Gyr unless low-metallicity gas is being supplied at a roughly constant rate. To avoid this fate, an infall rate of pristine material into the ISM of about 1 $M_{\odot}$ yr^{-1}, averaged over the lifetime of the Galaxy, is required (Wakker et al. 2008). Fresh gas is also needed to solve the so-called "G Dwarf Problem" in which the narrow observed distribution of metallicities of long-lived dwarf stars implies that the overall metallicity of the Galaxy has remained essentially constant over its history (van den Bergh 1962, Larson 1972, Tosi 1988, Matteucci & François 1989, Pagel 1997, Wakker et al. 1999a, Gibson 2002) . This continual infall is also crucial in developing detailed models of Galactic chemical evolution and the emergence of radial abundance gradients (Matteucci & Francois 1989, Chiappini et al. 1997, 2001).

- **Fragmentation in a hot Galactic corona or wind**. Maller & Bullock (2004) examined the possibility first proposed by Oort (1970) that gas in the vicinity of the Milky Way falls slowly into the potential well of the Galaxy, heating to the virial temperature ($T_{vir} \sim 10^6$ K), then cools and accretes onto the Disk. This picture correctly reproduces the inferred accretion rate and bulk Cloud properties, but it overpredicts the number of Clouds in the Halo relative to observations by an order of magnitude. Alternately, the Clouds could form as condensations in an outward-flowing Galactic wind (e.g., Fujita 2001). Density fluctuations in the wind may lead to thermal instabilities that radiatively cool and condense before falling back toward the Disk.

- **Material left over from the assembly of the Milky Way**. The Clouds could be material that failed to become dwarf galaxies for lack of sufficient dark matter in their cores. Oort (1966) was the first to propose an extragalactic origin for the HVCs, believing them primordial clouds undergoing active accretion by the Milky Way. Orbiting at large distances (hundreds of kiloparsecs), they might occasionally be perturbed into decaying orbits with velocities that would project as negative along the line of sight (Wakker & van Woerden 1997b). However, this model predicts large cloud sizes (of order many kiloparsecs), unrealistically low H I volume densities, and metallicities well below solar, none of which is observed. Also, ideas attempting to reconcile HVCs with otherwise normal galactic structure (e.g., part of some large outer ring, a polar

ring, or an extreme warp) imply geometry, morphology, and velocities that do not fit well with observations (Hulsbosch & Oort 1973).

Blitz et al. (1999) later revived Oort's idea, proposing that the HVCs are large (diameter $D \sim 25$ kpc) clouds of $\sim 3 \times 10^8\ M_\odot$ at distances greater than a few kpc falling into the Local Group. This would imply they are participants in the hierarchical structure formation picture that is a consequence of ΛCDM cosmological models. The best current distance estimates place HVCs in the Halo or near the Disk-Halo interface. The distances alone seem to rule out the idea that most small HVCs are dark matter halos distributed through the Local Group. However, our knowledge of HVC distances is ultimately limited by the sensitivity of modern observations, which does not necessarily preclude the possibility that they exist, undetected, at cosmological distances (Braun & Burton 1999).

- **Evidence of a "Galactic Fountain"**. First proposed by Shapiro & Field (1976), this model accounts for a hot ($T \sim 10^6$ K), diffuse component of the interstellar medium (ISM) via a convective-radiative mechanism cycling gas between the Disk and Halo. The driving force behind the mechanism is supernovae whose ejecta are pressure-confined azimuthally within the Disk; the only direction for pressure relief is perpendicular to the Disk in a 'champagne cork' manner. The Fountain model predicts that the gas rises and cools, condensing and then ballistically raining back down on the Disk. Wakker (1990) found that the

Galactic Fountain represents a mass flow rate of about 5 $M_\odot$ yr^{-1}, implying that the entire ISM circulates through the Halo each Gyr. Some IVCs (and, to a lesser extent, HVCs) may represent the supply and return flows of the Fountain. Each subsequent circuit made by gas in the Fountain results in further metal enrichment, likely explaining why some IVC metallicities appear to be supersolar. Understanding this process is important if we wish to also under the global chemical evolution of the Milky Way and other galaxies.

- **Tidally stripped gas from dwarf satellite galaxies**. Of the proposed explanations, this one is backed by the most direct evidence. Passing dwarfs that approach the Milky Way too closely are known to be subject to distortion, and in some cases, outright disruption, forming long tails of gas and stars around the Galaxy (e.g., the Sagittarius Tidal Stream; Ibata et al. 2001, and the SDSS "Field Of Streams"; Belokurov et al. 2006). The best known dwarf satellites are the Magellanic Clouds; while sufficiently far for the moment to prevent disruption, the Milky Way's gravity is tidally stripping H I from these objects, forming a neutral hydrogen 'wake' behind them in their orbits. The gas is observed as the Magellanic Stream, and manifests as a sharp redshift/blueshift as we look in alternate directions along their orbits. Since some of the gas exceeds the threshold for being considered "anomalous velocity," we count the clouds in the Stream as HVCs/IVCs. Many of the H I structures seen in the halos of external galaxies appear related to the accretion

of tidally-disrupted dwarf satellites or otherwise to interaction with a companion galaxy (Putman et al. 2012b).

3.1.6 Abundance Measurements of HVCs and IVCs

Metallicity is a key property of anomalous-velocity gas predicted by various models of their origins and evolution. Infalling gas associated with late-time accretion, possibly through cold flows, is expected to have very low metallicity ($Z \lesssim 0.01\ Z_{\odot}$). Gas originating in or near the Halo should be of roughly comparable metallicity to the stellar population there ($Z \lesssim 0.03\ Z_{\odot}$; Shull et al. 2009). Material participating in the Galactic Fountain has likely been cycled in and out of the Disk at least once; each additional pass results in further pollution by metals, so Fountain gas should have metallicities comparable to young Disk stars ($Z \sim 1\ Z_{\odot}$). Some sightlines may sample gas originating in more than one of these scenarios, so a relatively wide distribution of measured metallicities is expected. In some cases, additional information such as independent distance estimates may help resolve uncertainties about the origins of particular clouds when taken in concert with metallicity measurements. Gas-phase metallicities also trace the star formation history of gas in the Halo more directly than the dust, helps separate Galactic disk gas from halo gas (Putman et al. 2012b), and are the most direct way of discriminating between Galactic and extragalactic origins of HVCs (Blitz et al. 1999).

Currently there are published metallicities for only a handful of HVCs and IVCs. The five published HVCs include Complex C (0.1-0.3$Z_{\odot}$; Fox et al.

2004, Collins et al. 2007, Shull et al. 2011), a compact high velocity cloud (CHVC) (<0.5$Z_\odot$; Sembach et al. 2002), and the Magellanic Stream (0.25$Z_\odot$) and one small HVC (1$Z_\odot$; Wakker 2001b). Wakker has unpublished metallicities for three HVCs, which are ∼0.7-1$Z_\odot$ $\sim 0.5\ Z_\odot$ and $\sim 0.2\ Z_\odot$. Although most are low relative to solar, there values span a significant range. We would like to increase the number of measurements performed in a consistent manner, for the distribution of HVC metallicities sheds light on the history of the gas. Metallicities of the clouds associated with the Galactic Fountain are a kind of snapshot in time of the enrichment of the ISM, while for infalling clouds, the metallicity yields a direct measurement of chemical conditions in the Halo. In some instances where clouds are thought to be falling into the Milky Way for the first time, metallicity measurements are useful for comparison with measurements of the IGM along sightlines toward quasars. The method uses lines of low ions of various metals in spectra toward the clouds to measure equivalent widths and column densities; lines in different ionization states of the same element can be combined to get N(ions)/N(H I). An important complicating issue is the relatively low resolution of H I observations, which tends to wash out structure on small scales. Only high resolution data and an understanding of small-scale structure fluctuations in the clouds can overcome this limitation and is beyond the scope of this work. Future efforts should address those concerns.

Throughout this work we use the conventions [X/Y] = log(N_X/N_Y) - log$(N_X/N_Y)_\odot$, (X/Y) = $N_X/\ N_Y$, A_X = (X/ H), and $A_{X\odot}$ = (X/H)$_\odot$.

3.2 Method

We aimed to determine the metallicity and elemental abundance of a sample of HVCs and IVCs, using a consistent approach. To this end, we obtained archive spacecraft data from several missions consisting of UV spectroscopy of a sample of background continuum sources in directions of known HVCs and IVCs, supplemented by new data obtained specifically for this project. From the calibrated spectra, we measured equivalent widths of various low- and high-ion atomic lines which were converted to column densities using two independent, complementary approaches detailed below. Abundances of those ions with respect to H I was determined by comparison with H I column densities obtained from a variety of archival sources of 21 cm spectroscopy. We computed ionization corrections to these abundances through photoionization modeling, and compare the results against the pattern expected due to depletion of refractory elements in various stages of the ISM and the Galactic halo (Section 3.3.8). While we considered proper line profile fitting as an alternative to our approach, the UV data are typically noisy and therefore not well suited to that method. In order to assess the reliability of our measurement scheme, we included in our dataset several well-studied sightlines with ready comparison abundances from the literature; throughout our discussion of results on specific sightlines in Section 3.4, we refer to published comparison values when available. We also collect them in tabular form in the summaries of various individual clouds and cloud complexes in Section 3.5.

Our approach is summarized below; we elaborate on these points as

necessary in the following subsections.

1. Calibrated FITS files in the MAST archive[1] were retrieved for all *HST* and *FUSE* data used.

2. In each data file, continuua for each line were fitted and normalized individually and interactively, using low-order polynomial fits.

3. We make judgments concerning the suitability of individual ionic lines for determining abundances to eliminate lines rendered unusable for a variety of reasons. The judgments are made by manual, human inspection of each reduced UV spectrum. In cases of non-detections, we allow for upper limits to be calculated.

4. Equivalent widths for all detected lines are measured and column densities determined via the curve-of-growth (COG) method. To break column density degeneracies in the COGs, an estimate of the intrinsic linewidth is made from ions with multiple detected lines; in cases where we cannot directly estimate the intrinsic linewidth, we assume a linewidth based on observed values in "typical" HVCs. Once the intrinsic linewidths are known, an average value can be applied to ions with only single measurable lines. Oscillator strengths for observed transitions are taken from Morton (2003)

[1] `http://archive.stsci.edu/`

5. The absorption profile of each line is converted into an optical depth profile and scaled to a column density profile using the "apparent optical depth" (AOD) method of Savage & Sembach (1991). Integrating the profile yields an independent measurement of the column density, provided the lines are unsaturated, which is typically the case. These column density estimates serve as a check on those obtained from the COGs and serves to estimate measurement uncertainties.

6. H I column densities for referring metal-line abundances to hydrogen are obtained by fitting 21 cm spectra, or by direct integration of those spectra when fitting is not possible. Upper limits on N(H I) are calculated from the noise statistics in the 21 cm spectra, while lower limits can be found by fitting the H I Lyman series line profiles in the UV data. Solar elemental abundances are drawn from Asplund et al. (2005).

3.3 Observations and Reductions

Ultraviolet spectroscopy was performed with four space-based observing facilities. Data were drawn from the public archives of the *Far Ultraviolet Spectroscopic Explorer* (*FUSE*; Sahnow et al. 2000) spectrograph, the Space Telescope Imaging Spectrograph (STIS; Kimble et al. 1998) and Goddard High Resolution Spectrograph (GHRS; Brandt et al. 1994) aboard the *Hubble Space Telescope* (*HST*). Observations of ESO265-G23 were obtained in 2010 November with the Cosmic Origins Spectrograph (COS; Green et al. 2003) under *HST* Proposal 12275. Basic information about each facility is collected in

Table 3.1. Some additional data was obtained with the Goddard High Resolution Spectrograph (GHRS; Brandt et al. 1994), also aboard HST. We sampled abundances along forty sightlines toward background objects, summarized in Table 3.2; circumstances of the observations are given in Table 3.3.

3.3.1 UV Data Sources

3.3.1.1 *FUSE*

The Far Ultraviolet Spectrometer (FUVS; Sahnow et al. 2000) aboard *FUSE* was designed to produce high-resolution ($R \geq 20{,}000$) spectra across the $905 - 1187$ Å bandpass with a large (20-70 cm^2) effective area to a sensitivity of $\sim 10^{-14}$ erg cm^{-2} s^{-1} Å^{-1}, or $V \sim 16$. It consisted of four separate telescopes and spectrographs labeled LiF1, LiF2, SiC1, and SiC2, each of which was divided into two overlapping "segments," A and B. The sensitivity of the segments varied considerably, such that we preferentially relied on some (e.g., LiF1A/LiF2B) as data sources much more than others. However, in a handful of cases we rely on noisier segments that provide otherwise unique data at particular wavelengths.

A detailed discussion of the reduction of *FUSE* data is given in Wakker et al. (2003) and Wakker (2006), which we briefly summarize here. The raw spectra were calibrated using either version 2.1 or 2.4 of CalFUSE[2], the *FUSE* calibration pipeline (Dixon et al. 2007). The pipeline performs basic image

[2] `http://fuse.pha.jhu.edu/analysis/pipeline.html`

Table 3.1. Summary of UV Data Sources

Facility	Instrument	Channel or Grating	Resolving Power[a]	Wavelength Coverage (Å)	Dispersion (mÅ pix^{-1})	Velocity Resolution (km s^{-1})
FUSE	FUVS	LiF	9000 – 23000	979 – 1188	1.12[b]	20
	FUVS	SiC	11000 – 23000	905 – 1104	1.03[b]	20
HST	STIS	E140M	45800	1144 – 1730	12.5 – 18.9[c]	6.5
	STIS	G140M	11400 – 17400	1140 – 1741	–	50
	GHRS	G140M	18500 – 32000	1100 – 1900	52 – 56	20
	GHRS	G160M	17500 – 27500	1150 – 2300	66 – 72	10.9 – 17.1
	COS	G130M	16000 – 21000	$\sim$ 1150 – 1450	9.97	14.3 – 18.7
	COS	G160M	16000 – 21000	$\sim$ 1405 – 1775	12.23	14.3 – 18.7

Note. — Data obtained from each facility/instrument's instrument handbook. Instrumental resolutions are cited per 2-pixel, Nyquist- sampled resolution element.

[a]Resolving power depends on the choice of aperture or slit.

[b]Specified in Å mm^{-1}.

[c]Dispersion varies with wavelength as $\lambda/91.7$ mÅ pix^{-1} where λ is given in Å.

reduction, corrects for scattered light, distortion due to astigmatism, image jitter, bad pixels, and "bursts" (short-duration, significant increases in detector count rate as the spacecraft flew through the South Atlantic Anomaly), and performs a flux calibration. Wavelengths were calibrated using a dispersion solution obtained from multiple observations of interstellar lines among well-studied, bright targets (Sahnow et al. 2000), but the calibration was sensitive to small misalignments in target positioning at the 10-20 km s^{-1} level which vary temporally from one observation of a given target to the next. These residual shifts were corrected in each individual detector segment by using Milky Way interstellar lines as wavelength references and tied to LSR velocities derived from STIS E140M data (if available) or the LSR velocity of the strongest component in the corresponding 21 cm H I spectrum. In cases with complementary STIS E140M data, the resulting wavelength calibration is accurate to $\sim$1 km s^{-1}(REF). Shifts for sightlines with the highest S/N (> 10 near 1031 Å) were published by Wakker (2006). Once reliable wavelength shifts are obtained, a final *FUSE* spectrum for each object is composed by adding the LiF1A and LiF2B data. These spectra are aligned on a common LSR velocity scale before being combined.

3.3.1.2 STIS

STIS (Kimble et al. 1998) is a long-slit grating spectrograph aboard *HST* optimized for operation in the visible and the near- and far-UV. STIS is complementary to, but not superseded by, the Cosmic Origins Spectro-

graph (COS; Section 3.3.1.4). It has three large-format (1K×1K) detectors: a charge-coupled device (CCD) sensitive from $\sim$ 2000 Å to 1 μm and two photon-counting Multi-Anode Microchannel Arrays (MAMAs) with UV coverage down to 1150Å. A set of low-, medium-, and high-resolution gratings is available, resulting in fifteen configurations of spectral resolutions (up to $R \sim 200000$) and wavelength window coverage. High spatial resolution echelle spectroscopy in the ultraviolet is also possible.

Raw STIS data are processed through the CALSTIS pipeline (Hodge et al. 1998). Basic 2-D image calibrations (e.g., overscan and bias subtraction) are performed, along with cosmic ray rejection, dark subtraction, and flat fielding. Wavelength calibration files are processed to obtain dispersion solutions and zeropoint shifts in the spectral and spatial directions. From these, spectroscopic wavelength and flux calibration are performed. Wakker & Savage (2009) note that the MAST reduction of STIS data is of sufficiently high quality except as concerns observations made with the G140M grating at a central wavelength of 1222 Å, in which a redward 12 km s^{-1} ($\sim$ 1 pixel) shift in the dispersion solution is necessary. Archived E140M data are served by MAST as individual orders extracted separately from the 42-order echellogram. The orders were combined into a single 1-D spectrum by interpolating the rms-weighted photon counts and errors onto a common grid, adding the counts, and converting back to flux.

3.3.1.3 GHRS

GHRS (Brandt et al. 1994) was one of the four original axial instruments aboard *HST* when it was launched in 1990; it was removed from *HST* during Servicing Mission 2 in 1997. It was a long-slit, grating spectrograph designed for high resolution UV spectroscopy from $1150 - 3200$ Å. Spectra were imaged onto photon-counting Digicon detectors off a set of first-order gratings and an echelle grating that enabled medium to high spectral resolutions ($R = 2000 - 80000$). The photocathode detectors involved subtleties in terms of light sensitivity and a mismatch between the solid angle seen by each photodiode and the *HST* point-spread function (PSF), requiring careful handling of the data acquisition and reduction. Nevertheless, spectrophotometry of UV standard stars showed absolute fluxes to be accurate to 10% and stable to $\leq 1\%$ over long periods of time.

GHRS data were calibrated using the Routine Science Data Processing system (RSDP; Parsons et al. 1993). The calibration process assigned flux and wavelength values to each data point by converting input data numbers to count rates, correcting for the background, and correcting for non-uniformity in photodiode response and for dead photodiodes. This yielded calibrated spectra, wavelength solutions, and error estimates.

3.3.1.4 COS

COS (Green et al. 2003) is the newest space-based UV spectrograph, installed aboard *HST* in 2009. It is a circular-aperture, grating spectro-

graph consisting of two independent observing channels containing a cross delay line (XDL), far-UV detector ("FUV") sensitive from $900-2150$ Å and a MAMA near-UV detector ("NUV") sensitive to $1650-3200$ Å. Each channel is equipped with low-resolution ($R \sim 3000$) and medium-resolution ($R \sim 20000$) gratings. On-orbit analysis of COS lineshape functions found distinct, broad non-Gaussian wings that increase the equivalent widths of absorption features in COS spectra by effectively lowering the spectral resolution relative to pre-flight lab measurements (Ghavamian et al. 2009). Further, light scattered into the wings of the lineshape function affects the depths of saturated or nearly-saturated absorption lines (Kriss 2011).

Raw COS data are processed through the Space Telescope Science Institute (STScI) OPUS pipeline (Rose et al. 1995) in which individual exposures are unpacked and combined into files containing uncalibrated data. The raw files are processed through the COS calibration pipeline CALCOS (Kaiser et al. 2008) which performs basic image and spectroscopic reduction including (1) correction for instrumental effects such as noise, thermal drifts, geometric distortion, and pixel-to-pixel sensitivity variations, (2) determination and application of a global dispersion solution, and (3) extraction of wavelength- and flux-calibrated 1-D spectra.

3.3.2 Continuum Fitting

For each sightline in our dataset, we fit a continuum model to the spectra on a line-by-line basis by fitting a low-order (up to 4th) polynomial through

line-free regions in the manner of Sembach & Savage (1992). In relatively uncomplicated parts of a given spectrum, we fit the continuum over a velocity range of up to 10000 km s^{-1}, but in special cases we fit the continuum in several discreet, often overlapping pieces. For example, some sightlines have very strong intrinsic H I absorption, of which the damping wings of the Lyman series lines may span several thousand km s^{-1}; in such cases where regions of interest fell well away from the line core on the wings, we allowed the local continuum fit to follow the wing profile over relatively short velocity intervals. Similarly, instances of severe contamination by telluric geocoronal emission (Section 3.3.5.4) were dealt with by fitting continuua in the night-only spectra and applying the fit to the total spectrum.

The polynomial fit describing the overall shape of the continuum was supplemented models accounting for absorption features of H I and H_2. We see H I absorption in our spectra from three origins: the Milky Way, HVCs/IVCs, and intrinsic absorption in the background continuum source. We use 21 cm detections corresponding to each H I source to estimate its velocity centroid, N(H I), and FWHM; these are used as inputs to an elementary 1-D radiative transfer model predicting the H I absorption spectrum that is added to our continuum model. In many instances, HVCs and IVCs are not detected in 21 cm emission; we therefore use the velocities and FWHMs of observed ionic lines and empirically estimate N(H I) by trying various values and comparing the resulting continuum model against the data, iterating until a good fit is obtained. The H_2 absorption spectrum is computed according to the method

detailed by Wakker (2006) with parameters previously determined for each sightline, and is crucial in the line judgment process (Section 3.3.5) to sense and reject contamination of HVC/IVC absorption lines by H_2.

3.3.3 Target Selection

Each sightline is oriented in the direction of a bright background object, usually a QSO or Seyfert galaxy, which themselves have low intrinsic abundances or are of sufficiently high recessional velocity that their intrinsic ionic lines are Doppler shifted well away from intermediate- and high-velocity gas in the foreground. In practice this is not always possible, and careful account must be made of this contamination in assessing the quality of HVC/IVC line detections. We correlated the position of bright background sources with H I 21 cm surveys, looking for instances in which a particular line of sight intercepted gas at column densities sufficiently large to match the detection thresholds of the highest angular resolution 21 cm data. The best interferometric maps currently available have resolutions of order several arcminutes, while it is believed that many HVCs and IVCs have structure on smaller angular scales. As a result of beam smearing, the highest-resolution 21 cm observations are likely insensitive to small, dense clumps of anomalous-velocity gas. While we attempted to supplement column density estimates from 21 cm surveys with targeted observations at higher angular resolution, in some cases we are only left with the lower-resolution survey data themselves from which to obtain N(H I).

Establishing an N(H I) cutoff comparable to the sensitivity of the observations, near 10^{17} cm^{-2}, increases the likelihood of seeing UV line absorption among the selected sightlines. It is also useful in the sense that such components are more likely to be *detections* in 21 cm emission, leading to more robust estimates of N(H I) for the purpose of computing abundances with respect to H I. However, our N (H I) cutoff means ionic line absorption toward some clouds – particularly angularly small and/or highly ionized ones – will go undetected in the absence of a thorough search of the UV spectra of many thousands of bright background objects. Mounting such a search is impractical given the difficulty inherent in obtaining good quality, high-resolution FUV spectra. As a result, and in consideration of the need to increase the number of known HVC/IVC metallicities, we focused our efforts on unpublished clouds, even along sightlines previously investigated by other authors. As a means of establishing the reliability of our abundance determination for unpublished clouds, we included observations of a few well-studied sightlines (e.g., Markarian 279) to compare our results against those in the literature. Basic information about the sightlines we chose for this study are summarized in Table 3.2, and particulars concerning the data sources, exposure times, S/N estimates, and program IDs in Table 3.3.

Table 3.2. Basic Sight Line Information

Object Designation	$\alpha_{2000.0}$ (h m s)	$\delta_{2000.0}$ (° ′ ″)	l (°)	b (°)	Type	z	B	$E(B-V)$
3C249.1	11 04 13.8	+76 58 58	130.394	+38.550	Sey1	0.313	–	0.035
3C273.0	12 29 06.7	+02 03 08.6	289.95	+64.36	QSO	0.158	13.07	0.021
ESO265−G23	11 20 48.03	−43 15 50.66	285.911	+16.5919	Sey1	0.056799	15.26	0.095
Mrk 106	09 19 55.34	+55 21 37.09	161.139	+42.879	Sey1	0.12295	16	0.027
Mrk 153	10 49 04.57	+52 19 57.60	156.726	+56.007	G	0.008206	14.6	0.013
Mrk 205	12 21 43.97	+75 18 37.99	125.447	+41.6723	Sey1	0.07084	15.64	0.040
Mrk 279	13 53 03.3	+69 18 29.00	115.040	+46.86	Sey1	0.031	14.5	0.016
Mrk 509	20 44 09.8	−10 43 24.40	35.97	−29.86	Sey1	0.034	13	0.057
Mrk 817	14 36 22.10	+58 47 38.90	100.3	+53.48	Sey1	0.031	14.3	0.007
Mrk 876	16 13 57.20	+65 43 10.70	98.27	+40.38	Sey1	0.12	16.03	0.027
NGC 1705	04 54 13.50	−53 21 39.80	261.08	−38.74	SBG	0.0021	12.82	0.008
NGC 5253	13 39 55.99	−31 38 24.11	314.860	+30.106	H2G	0.001349	11.17	0.056
PG1011−040	10 14 20.68	−04 18 40.48	246.501	+40.749	Sey1	0.058	15.49	0.037
PG1259+593	13 01 12.90	+59 02 06.7	120.56	+58.05	Sey1	0.472	15.6	0.008
PG1626+554	16 27 56.10	+55 22 31.60	84.515	+42.1886	Sey1	0.132	–	0.006

Note. — Data obtained from the SIMBAD database (`http://simbad.u-strasbg.fr/simbad/`) except for $E(B-V)$, which was obtained from the NASA/IPAC Galactic Reddening and Extinction Calculator (`http://irsa.ipac.caltech.edu/applications/DUST/`) and is based on the extinction maps of Schlegel et al. (1998). Object types are as follows: "bCG" = blue compact galaxy; BLL = BL Lacertae object; '; H2G = H_2 galaxy; "G" = galaxy; "QSO" = quasar; rG = radio galaxy; "SBG" = starburst galaxy; "Sey1" = Seyfert Type 1.

Table 3.3. Circumstances of UV Observations

Designation	Facility	Channel/ Grating	Exptime (ks)	S/N 977Å	S/N 1031Å	S/N 1238 Å	Program ID(s)
3C249.1	*FUSE*	–	246.5	3	15	8	P1071601, P1071602, P1071603, S6010901, D1170101, D1170102, D1170103, U1027501, U1027502
	STIS	E140M	68.6	3	15	8	O6E124-30
3C273.0	*FUSE*	–	43.2	19	31	27	P101350
	STIS	E140M		19	31	27	O5D301
ESO265−G23	COS	G130M	1.983	–	–	–	LBH413OCQ
Mrk 106	*FUSE*	–	121.9	2	13	–	3C1490501
	GHRS	G270M	–	–	–	–	Z2N90105T
Mrk 153	*FUSE*	–	105.6	–	–	–	A0940101, A0940102
Mrk 205	*FUSE*	–	223.8	6	17	8	Q1060203, S6010801, D0540101, D0540102, D0540103, U1031102
	STIS	E140M	62.1	6	17	8	O62Q03-05
Mrk 279	*FUSE*	–	181.8	21	45	32	P1080303, P1080304, D1540101
	STIS	E140M	13.2	21	45	32	O6JM01
	STIS	E140M	41.4	–	–	–	O8K101-05
Mrk 509	*FUSE*	–	114.3	7	30	14	X0170101, X0170102, P1080601
Mrk 817	*FUSE*	–	161.5	20	44	43	P1080403, P1080404
	GHRS	G160M	26.8	20	44	43	Z3E70108T, Z3E70106T, Z3E70104T
	STIS	G230MB	–	–	–	–	O6CT36010
Mrk 876	*FUSE*	–	127.4	11	34	11	P1073101, D0280203
	STIS	E140M	29.2	11	34	11	O8NN01-02
NGC 1705	–	–	24.0	–	–	–	A0460102, A0460103
NGC 5236	–	–	26.5	–	–	–	A0460505

3.3.4 Determining Velocity Integration Limits

To measure the equivalent width of absorption lines from which to compute column densities, we let the apparent UV absorption guide the choice of integration velocities, using the continuum fits (Section 3.3.2) as a reference. This process is aided by the strength and line widths of corresponding H I 21 cm emission that inform the initial guesses. In cases of strong particularly H I columns ($\gtrsim 10^{19}$ cm^{-2}), the range of velocities present in H I emission generally match the absorption limits of the metal ions we considered. However, as noted previously, in some cases H I emission is weak or absent. When UV absorption is also weak or absent, we assume velocity intervals depending on whether a given component is at high or intermediate velocities, using widths of 40 km s^{-1} and 20 km s^{-1} respectively. In a few special cases, the apparent width of a component in the UV spectra is dependent on the ion and ionization stage, indicating that material sampled by the sightline has a multiphase nature. Such situations manifest themselves in two characteristic widths among lines of the same component. We treated these situations as if they were two otherwise unrelated components sharing the same velocity centroid, but with different widths.

We measure the equivalent width of a line by straight integration over the defined velocity limits of the component; in this process, we also obtain the LSR velocity centroid and linewidth by fitting a single Gaussian component to the observed line profile. We also make an estimate of the measurement uncertainty consisting of a statistical part and a systematic part; this method is

Table 3.3 (cont'd)

Designation	Facility	Channel/ Grating	Exptime (ks)	S/N 977Å	S/N 1031Å	S/N 1238 Å	Program ID(s)
PG1011−040	*FUSE*	–	85.3	17	7	–	B0790101
	COS	–	–	–			
PG1259+593	*FUSE*	–	553.8	14	37	8	P1080101, P1080102, P1080103, P1080104, P1080105, P1080106, P1080107, P1080108, P1080109 U1031801
	STIS	E140M	95.8	14	37	8	O63G05-11
PG1626+554	*FUSE*	–	90.9	0	14	–	C0370101
	FOS	G130H, G190H, G270H					Y38O1602T, Y38O1605T, Y38O1604T

Note. — Largely adapted from Table 1 of Wakker & Savage (2009).

discussed in detail by Wakker et al. (2003). The statistical error consists of the random noise in the data associated with the choice of continuum placement, and the systematic error combines the uncertainties inherent in the selection of the velocity integration limits with the known, fixed-pattern noise in each data source. In the former case, we take this to be the change in the measured equivalent width resulting from allowing the velocity limits to vary by ± 5 km s^{-1}, while the latter case is instrument specific (e.g., 6 mÅ for FUSE, 1.2 mÅ for STIS G140M, and 0.3 mÅ for STIS E140M). If a line is a clear non-detection, we determine a 3σ upper limit for its equivalent width as three times the quadrature sum of the statistical and systematic errors obtained in this fashion. Other authors take different approaches to computing equivalent width upper limits, and it is worth noting the differences in order to properly compare our limits against those reported previously in the literature.

3.3.5 Quality Control

Relatively few lines occur cleanly separated from other nearby lines and are unaffected by any number of potential contaminants. Each velocity component of each ionic line was examined manually along the sightlines to discriminate useful lines from those that could only provide upper or lower limits, or were judged non-useful on the basis of a number of criteria. We developed a list of qualifiers that were used to label each case and provided input to our analysis program to assign proper caveats to individual column density measurements. The subsections that follow describe each qualifier,

the reasons motivating its use, and how it was applied in describing the lines. We also note the symbol used to designate each type of quality judgment and collect those symbols in the key shown in Table 3.4.

3.3.5.1 Blends

Blended lines were treated as detections, subject to deblending using one or more Gaussian components. We reserved this judgment for cases where the line cores of adjacent components were unambiguously resolved in the spectra. The judgment symbol for blends is **B**.

3.3.5.2 Contamination by Adjacent Velocity Components

The ionic lines in the UV we used are sufficiently dense in wavelength space that often a given line is partially or totally contaminated by a line from the same or a different species at a different velocity. The degree of contamination determines the usefulness of a line; some cases may provide useful limits, while others involve lines of interest that are rendered effectively useless. Lines with multiplet structure, such as the UV triplets of N I, frequently contaminate both N Iat other velocities as well as lines of other ionic species. This can also lead to cases of mistaken identity, which made manual validation of essentially all lines inevitable.

3.3.5.3 Contamination by Telluric Geocoronal Emission

The spacecraft used to obtained our spectra are situated in low Earth orbit, below the much of the direct geomagnetic environment of the planet. While this protects the spacecraft from most damaging radiation events, it presents a source of UV flux contamination in the spectra that is dependent on the orbital phase of the spacecraft at the time of observation. The same elements whose interstellar spectra we observed are trapped in the Earth's geomagnetic environment and fluorescently excited by absorption of solar UV radiation; their re- emission of the solar UV at zero velocity frequently overwhelms even the underlying Galactic absorption by several orders of magnitude. The wings of these "geocoronal" lines can extend beyond ±100 km s^{-1} about zero velocity, obliterating IVC lines in many cases. These lines are usually flagged as useless as a result. However, in many cases, we have corresponding data obtained during orbital night, when telluric emission is minimized. In such circumstances, we used the lower S/N ratio, night-only spectra to measure column densities. The judgment symbol for all types of contamination is **X**.

3.3.5.4 Contamination by Galactic H_2

Molecular hydrogen (H_2) has a rich FUV spectrum. Its lines are associated with transitions from the ground electronic state, $X\ ^1\Sigma_g^+$ to excited electronic states, $B\ ^1\Sigma_u^+$ (Lyman bands) and $C\ ^1\Pi_u$ (Werner bands). The transitions originate in the ground ($v = 0$) vibrational state, each of which

has an associated rotational state (J) ladder, and ortho- and para-H_2 states exist depending on the parity of J. Our dataset includes transitions starting from $J = 0$ to $J = 5$ that often pollute spectral regions where our interstellar lines of interest lie. However, these lines are often intrinsically weak, and if properly modeled, their contribution can be removed. We used the H_2 model described in detail by Wakker (2006) and the decontamination procedure of Wakker et al. (2003) to remove the contribution of weak H_2 lines in cases where the absorption depth was $\leq 25\%$ of the continuum and the apparent absorption closely followed the model. If the apparent absorption was fully fit by the model and the expected depth of the ionic line based on other lines was particularly weak, we designated the resulting decontaminated equivalent width as an upper limit. For stronger H_2 absorption, we did not attempt decontamination and considered such lines useless. In cases where the data was fully fit by the H_2 model and we expected to see no underlying ionic line absorption, we used the decontaminated flux to establish an upper detection limit. The judgment symbol for lines subject to H_2 decontamination is **D**.

3.3.5.5 Saturation

Saturated components result from one of two situations. First, a line due to an HVC or IVC can be intrinsically saturated by virtue of the strength of its column. Alternately, an HVC/IVC line can be termed "saturated" if there is essentially zero flux over the inferred velocity integration limits for a given component. This may happen in the case of an intrinsically *unsaturated* line

that is of sufficiently low velocity that it is superimposed on the damping wing of a saturated Galactic ionic line. While not intrinsically saturated, we treat such lines as useless because of our inability to separate out components in cases of complete saturation. The judgment symbol for saturated components is _ (**underscore**).

3.3.5.6 Upper Limits

"Clean" non-detections of components (i.e., those not rendered useless by any type of contamination) were flagged for the computation of 3σ upper noise limits on their equivalent widths. As described previously, we defined an upper limit as three times the quadrature sum of the statistical and systematic equivalent width errors. The judgment symbol for blends is $<$ (**less than**).

3.3.5.7 Lower Limits

In some instances, very strong (but unsaturated) lines showed absorption wings that exceeded the defined velocity integration limits for a given component. In such circumstances, provided the line was not otherwise contaminated, we denoted their equivalent width measurements and resulting column densities as lower limits. The judgment symbol for lower limits is $>$ (**greater than**).

3.3.5.8 "Uncertain" Detections

We reserved this judgment for difficult cases in which we were reasonably confident real absorption existed, but the shape of the line profile did not match our expectations. Such circumstances might involve, for example, the expected detection of a particular line on the basis of the positive detection of the next-intrinsically-strong line of that ion but one whose line profile did not resemble those of other detected lines. We marked these differently from more secure, "clean" detections in order to more clearly discern their influence on the COGs. The judgment symbol for "uncertain" detections is **U**.

3.3.5.9 Detector Flaws, Nonlinearities, and Data Dropouts

A variety of inconsistencies exist in the data we used, which are of generally otherwise very high quality. Intrinsic problems affect only a few percent of the spectra in our dataset, and range in their consequences from insignificant to absolute in cases of hardware failure resulting in dropouts. The judgment symbol for flawed or absent data is **.** (**period**).

3.3.5.10 Low S/N

Some of the UV spectra in our dataset are of particularly low S/N, either whole or in part. In many instances, this resulted in lines whose measured equivalent widths were either exceptionally uncertain or impossible to measure. We judged these of insufficient quality to include in our curves of growth and were rejected. The judgment symbol for "low S/N" is # (**octothorpe**).

Table 3.4. Summary of Quality Control Flags Used in Spectra Plots

Flag	Symbol	Judgment
"use"	+	Clean detection; use
"blend"	**B**	Blended lines; use after deblending
"decont"	**D**	H_2 contamination; use after running decontamination routine
"upper"	<	Clean upper limit
"lower"	>	Clean lower limit
"uncertain"	**U**	Tentative detection; use but check COG
"mix"	**M**	Too heavily blended or adversely impacted by adjacent lines; do not use
"saturated"	(underscore)	Line saturated; do not use
"contam"	**X**	Contaminated; do not use
"lowsn"	#	Low S/N data; do not use
"noflux" / "nodata"	(dot)	Data do not exist or the flux is zero; do not use

3.3.6 Obtaining N(H I) from 21 cm Spectra

Elemental abundances derived from UV absorption spectra were converted to metallicities with respect to hydrogen. Ideally we would obtain N(H I) from Lyman series lines in our UV spectra, but in nearly all cases these lines are either saturated or unacceptably blended with H I absorption in the Galaxy. A common means of obtaining N(H I) under these circumstances is to measure H I column densities from 21 cm emission spectra, although in many cases emission features are also difficult to disentangle from Milky Way emission at low velocities. The picture is further complicated by unresolved velocity structure in 21 cm spectra obtained from single-dish data. Spatial variation in H I column densities below the resolution of the best single-dish

21 cm surveys can be significant compared to the subarcsecond effective beam sizes of our UV spectra sources (Wakker & Schwarz 1991). Absent interferometric data, in obtaining N(H I) we used the highest-resolution single-dish 21 cm spectrum available to us. The 21 cm data sources used to obtain N(H I) in this study are summarized in Table 3.5.

Highly ionized or very low density clouds often yield no 21 cm detection; Lyman series lines may not be saturated under those circumstances but their velocity structure remains difficult to work with. For components seen in metal line absorption in the UV but not detected in 21 cm spectra, we calculate 5σ upper limits to 21 cm non-detections according to:

$$N(\text{H I}) \leq 5 \left[1.8 \times 10^{18} (\text{rms}) \Delta v \sqrt{N}\right] \text{cm}^{-2} \tag{3.1}$$

where 1.8×10^{18} conversion factor in units of cm^{-2} K^{-1} km s^{-1}, "rms" is the rms noise in units of K in the 21 cm spectrum over a velocity interval corresponding to observed UV absorption, Δv is the channel spacing of the 21 cm observations in units of km s^{-1}, and N is the number of pixels in the velocity window of the UV spectrum. The linewidth is taken to be 40 km s^{-1}, or twice the FWHM of a typical line. N is therefore the assumed linewidth divided by Δv.

Table 3.5. Summary of 21 cm Data Sources

Facility	Survey	Aperture (m)	Angular Resolution (′)	Velocity Resolution (km s^{-1})	Sensitivity (mK)
Effelsberg	–	100	9	0.65	50
NRAO 140-foot	–	43	21	–	–
NRAO GBT	–	100	9	2.1	20
Villa Elisa	LAB[a]	30	30.0	1.27	70
Dwingeloo	LAB[a]	25	35.7	1.25	90

Note. — Instrumental resolutions are cited per 2-pixel, Nyquist-sampled resolution element.

[a]Kalberla et al. (2005b)

3.3.7 Abundance Determination

Column densities are derived using the traditional curve of growth (COG) approach that relates the observed absorption line equivalent width, W_λ, and the quantity $Nf\lambda$, which is the product of the column density, N, the transition oscillator strength, f, and the wavelength. This method benefits from the fact that W_λ measures the fraction of the total energy removed by the absorption line and is thus unaffected by $\phi(\Delta\lambda)$. The run of optical depth with velocity is given by

$$\tau_\nu = -\ln[I_n(\nu)]. \tag{3.2}$$

The range of possible column densities in a COG is determined in part by the intrinsic linewidth, which can be constrained by fitting a model to a COG in which multiple detections of a particular ion exist. Often, more than one ion provides this information and the results can contradict each other. Therefore, we devised a method by which we assign weights to the linewidths indicated by each multiply-detected ion and then compute a weighted average that is then applied to the COGs of all ions for a given component in a given sightline. The method involves the following four rules:

1. The FWHMs of ions with three or more detected lines receive the highest weight, 1. The FWHMs of ions with two detected lines are assigned a weight of 0.25.

2. The FWHMs of ions in which a well-circumscribed region exists in the log N vs. FWHM χ^2-plot receive the highest weight.

3. The FWHMs of ions consisting of all limits that show a branch over a large range of column densities in the log N vs. FWHM χ^2- plot receive higher weight than FWHMs of similar ions whose range of possible values give little or no leverage on the FWHM, which receive weights of zero.

4. In instances where ions meeting conditions 2 and 3 exist, ions giving no leverage on the FWHM are not be included at all unless no better alternative exists. Their weights depend on individual circumstances.

As a check on the columns obtained through the COG method, we independently calculate column densities using the Apparent Optical Depth (AOD) method of Savage & Sembach (1991). AOD can be used if there are two or more absorption lines of a given species which differ in the value of the product $f\lambda$. Absorption line measurements are converted into apparent optical depths, $\tau_a(v) = \ln\,[I_0(v)/I_{obs}(v)]$ and then into apparent column densities per unit velocity interval, $N_a(v)$, via Equation 3.12. Total column densities are found by integrating $N_a(v)$:

$$N_a = \int N_a(v)dv. \tag{3.3}$$

In regions of the spectrum where unresolved, saturated structure is not significant, the $N_a(v)$ integral yields valid column densities, including the effects of instrumental profile smearing, over the velocity range of the integration. Elemental radiative transfer theory gives the intensity profile as a function of wavelength for an interstellar absorption line of optical depth $\tau(\lambda)$:

$$I(\lambda) = I_0(\lambda)\,\exp\,[-\tau(\lambda)] \tag{3.4}$$

in which $I_0(\lambda)$ is the intensity of light before the absorption and $I(\lambda)$ is the intensity incident on the observer. The incident intensity is modified by the intrinsic lineshape function of the measuring instrument, $\phi(\Delta\lambda)$:

$$I_{obs}(\lambda) = \{I_0(\lambda)\ \exp\ [-\tau(\lambda)]\} \otimes \phi(\Delta\lambda) \tag{3.5}$$

Typically, changes in the intensity of the illumination source with wavelength are very small over the width of the lineshape function, so the previous expression can be simplified to

$$I_{obs}(\lambda) = I_0(\lambda)\{\exp\ [-\tau(\lambda)] \otimes \phi(\Delta\lambda)\} \tag{3.6}$$

Using these equations, two types of optical depth can be defined: "true" and "apparent". Their definitions depend on which of the intensities is used, that before or after modification by the lineshape function. The "true" optical depth is defined by the unmodified intensity,

$$\tau(\lambda) = \ln\left[\frac{I_0(\lambda)}{I(\lambda)}\right], \tag{3.7}$$

while the "apparent" optical depth is as observed after instrumental modification:

$$\tau_a(\lambda) = \ln\left[\frac{I_0(\lambda)}{I_{obs}(\lambda)}\right]. \tag{3.8}$$

The intrinsic blurring due to the convolution of the spectrum with the instrumental lineshape function is given according to Equation 3.6, so the expression for the apparent optical depth can be rewritten as

$$\tau_a(\lambda) = \ln[\{\exp\ [-\tau(\lambda)] \otimes \phi(\Delta\lambda)\}^{-1}] \tag{3.9}$$

For weak lines ($\tau(\lambda) \ll 1$), the apparent optical depth reduces to a simple convolution of the true optical depth with the instrumental lineshape function itself:

$$\tau_a(\lambda) = \tau(\lambda) \otimes \phi(\Delta\lambda). \tag{3.10}$$

In the limit in which the instrumental resolution is very high compared to the typical linewidth, the S/N is high, and the continuum is well- defined, $\tau_a(\lambda)$ becomes a good representation of $\tau(\lambda)$. Once $\tau_a(\lambda)$ is known, it can be used to derive the corresponding column density, N, via the relation

$$\tau(\lambda) = \frac{\pi e^2}{m_e c^2} f \lambda^2 N(\lambda), \tag{3.11}$$

where m_e and e are the electron mass and charge, respectively, and c is the speed of light. The total column density is found by integrating $N(\lambda)$ over all wavelengths: $N = \int N(\lambda) d\lambda$. These quantities can be rewritten in terms of velocities such that the optical depth per unit velocity is

$$\tau(v) = 2.654 \times 10^{-15} f \lambda N(v), \tag{3.12}$$

where λ is in Å and $N(v)$ is in atoms cm^{-2} (km s^{-1})$^{-1}$ and the corresponding total column density

$$N_a(v) = \int N(\lambda) d\lambda = \frac{m_e c^2}{\pi e^2 f \lambda} \int \tau(v) d(v) = \frac{m_e c^2}{\pi e^2 f \lambda} \int \ln \left[\frac{I_0(v)}{I(v)} \right] dv \tag{3.13}$$

.

This approach has many advantages. It is particularly sensitive to unresolved lines and is useful for measuring equivalent widths down to ∼0.25

of the instrumental lineshape FWHM. Large discrepancies between derived columns from lines of the same species may indicate unresolved, saturated cloud structures. On the other hand, it has significant shortcomings. It does not work well on saturated lines, and cannot be used on individual lines unless the intrinsic line widths are known a priori.

3.3.8 Depletion of Refractory Elements

The abundances of many metals are observed to be less than the expected cosmic abundances due to varying degrees of incorporation into interstellar dust grains in a process called depletion (Savage & Sembach 1996). The presence of dust in some HVCs and IVCs is inferred from the observation of H_2 (Section 3.1.2) and possibly by direct thermal imaging (Section **??**). The amount of dust depletion therefore correlates with the metallicity of a given cloud, but is also determined in part by the condensation temperature of the element relative to the ambient temperature of the medium in which a grain is immersed. At high temperatures such as those encountered in the Halo, refractory elements (e.g., Fe and Si) are found entirely in the gas phase, while in dense, cold disk gas they are almost entirely sequestered in grains. The amount by which a particular element is depleted can be estimated by taking abundance ratios with respect to undepleted species. By comparing the pattern of abundances to those derived theoretically, we can estimate the physical conditions of the gas and infer the phase of the medium in which clouds are situated.

Of the ions we observed, intrinsic (undepleted) abundances were measured using lines of N I, O I, S II, P II, and Ar I; these elements are expected to exist almost entirely in the gas phase (Jenkins 1987, Wakker 2001a, Savage & Sembach 1996). Given the expected abundances of these elements, we typically cite the intrinsic metallicity of components in our sample sightlines in terms of [O I/H I] when available. O I is the best metallicity indicator among the undepleted ions we observe because it has an ionization potential similar to that of H Iand its ionization fraction is strongly coupled to that of H I through a charge-exchange reaction at typical interstellar cloud densities:

$$\mathrm{O}^+(^4S_{3/2}) + \mathrm{H}^0 \rightarrow \mathrm{O}^0(^3P_2) + \mathrm{H}^+ + 0.02 \text{ eV} \tag{3.14}$$

(Field & Steigman 1971, Sofia & Jenkins 1998, Wakker 2001a, Sembach et al. 2004). S II is the next most reliable metallicity indicator among undepleted species, followed by P II, both of which suffer from ionization effects (Jenkins 1987, Savage & Sembach 1996). Ar I has a larger photoionization cross section than and is not coupled to H I, so it is strongly affected by ionization (Wakker 2001a). N I, for reasons described below in Section 3.3.10, is least reliable metallicity indicator among these elements. C II and Si II have intrinsically strong lines, reaching optical depths of $\tau \sim 3$ at relatively low $N(\mathrm{H\ I}) \sim\ 1 \times 10^{18}$ cm^{-2} for clouds with solar abundances and standard depletion patterns (Wakker 2001a). They are therefore among the easiest to detect at low column densities. Of the ions we typically detect in HVCs and IVCs, Fe II is most well-suited to measuring the degree of refractory depletion since it has a wealth of strong lines over a range of oscillator strengths in the UV. Of the ions we

see in the clouds, Fe appears to be most tightly bound to grains in the form of a durable iron core (Savage & Sembach 1996).

3.3.9 Photoionization Correction

Estimating of the expected amount of refractory depletion requires prior knowledge the density, temperature, and intrinsic metallicity of a cloud; often we do not know these a priori and are left to quantify the amount of depletion empirically through abundance measurements. A problem we can address, however, is external photoionization of the clouds that requires a correction to column densities and therefore abundances. The degree of ionization of a cloud of gas depends on its density, as lower-density gas is less protected by self-shielding and susceptible to ionizing radiation. An estimate of the ionization fraction of the gas (and therefore, the degree to which any particular species is diminished or "absent" due to being in a higher ionization state) can be made from the degree of H I ionization measured via Hα emission or absorption by, e.g., C IV, Si IV, and O VI. To correct for this in cases where strong ionization is indicated, we use the method of Fox et al. (2010) in which models are made with CLOUDY (Ferland et al. 1998) to search a parameter space consisting of N(H I), the ionization parameter U, and metallicity. Such modeling is only strictly necessary in cases where measurements of a given sightline yield no O or S abundances, and is unnecessary for large N(H I).

3.3.10 Apparent Underabundance of N I

N appears at first to be a good indicator of overall metallicity since it is not known to deplete onto dust, has an ionization potential similar to H I and its ionization tends to couple to that of H (Wakker 2001a). However, it is often found to be underabundant relative to, e.g., O I in measurements of HVCs; this tells us something about the kinds of stars, as sources of metals, that have contributed to the composition of the HVCs (Tripp et al. 2003). This apparent abundance discrepancy is explained by a delay in the production of N in nucleosynthesis in stars of intermediate mass (3-8 $M_{\odot}$; Lu et al. 1998a).

The "primary" production of N is thought to occur during the asymptotic giant branch phase of intermediate-mass stars in which thermal pulses dredge up C-rich material from the He-burning shell into the H-burning shell (Renzini & Voli 1981). The N produced in the H-burning shell is later dispersed into the ISM via stellar winds. It is labeled "primary" because its production does not require pre-existing C in the material from which the star was originally formed as seed nuclei for N synthesis. In contrast, "secondary" N is made in the CNO cycle during the Main Sequence phase of stars of any mass if the zero-age metallicity is sufficiently large. Closed-box Galactic chemical evolution models predict N/O should be independent of the overall metallicity for "primary" N production, while N/O $\sim$ O/H for "secondary" production (Pagel & Patchett 1975, Edmunds 1990). In starforming environments with typical initial mass functions, one then expects a time delay between the release of "primary" N from intermediate-mass stars and O from shorter-lived, massive

stars. The delay can be as long as 5×10^8 years and is expected to result in a large scatter in N/O at low O/H (Garnett 1990, Pilyugin 1993, Marconi et al. 1994). The N/O scatter should be more pronounced at low metallicity as the effects of the time delay become relatively more important. N/O is often < 0.5 in HVCs, implying that intermediate-mass stars have had little if anything to do with the heavy element enrichment of HVCs. Rather, the enrichment source appears to be Type II supernovae drawn from a relatively metal-poor parent population.

3.3.11 Factors Influencing Accuracy Of Derived Column Densities

Absent considerations complicating the analysis, it would seem simple enough in principle to find the metal abundance in HVCs/IVCs by taking the ratio of metal column densities to the N(H). There are several reasons why this is not true in practice.

First, the hydrogen content of HVCs and IVCs is not solely in the form of H I. Ionized hydrogen (H^+) could dominate the total hydrogen content of some clouds. For a simple plane-parallel cloud of constant volume density n and thickness t, illuminated on both sides by ionizing photons, a critical total hydrogen column density exists below which the recombination rate is insufficient to balance ionization rate. Quoting Maloney (1993), It has a value of

$$N_c = 7.7 \times 10^{18} \left(\frac{\phi_i}{10^4 \text{ photons cm}^{-2} \text{ s}^{-1}} \right) \left(\frac{n}{10^{-2} \text{ cm}^3} \right) \text{ cm}^{-2} \qquad (3.15)$$

in which ϕ_i is the incident ionizing photon flux. Gas of density $N < N_c$ will be mostly ionized, assuming the typical observed value in HVCs of $n \sim 0.1$ cm^{-3}. Above N_c, the gas will transition from mostly ionized to mostly neutral and at sufficiently high columns ($\sim 3 \times 10^{19}$ cm^{-2}) representatives of the cold interiors of HVC cores. The ionized fraction of a cloud may be estimated from the presence of highly ionized ionic species such as Si IV, C IV, and O VI, or by the direct detection of Hα emission. The contribution of ionization to the total elemental abundance uncertainty depends on the measured ionization fraction. Closely related to this is the degree to which ionization of metals contributes to their apparent underabundance, for an element could be undercounted in column density estimates by virtue of being in a different ionization state. We have attempted to account for this by making photoionization models as described previously in Section 3.3.9; here, too, the effect of metal ionization on the total error budget depend on the degree of ionization present.

Second, variations in H I column density on angular scales much smaller than the typically arcminute-sized beams of 21 cm observations compromise accurate hydrogen column density measurements, which affects the reliability of derived metal abundances. This is because the method typically used to get the metal column densities is the "pencil beam" approach, in which ionic absorption is measured toward bright background sources such as AGN and Seyfert galaxies. Uncertainties in derived H I column densities are proportional to the beam size; as an example, the beam size of the LAB survey (Kalberla et al. 2005b) is $36'$, for which Wakker (2001a) and Wakker et al. (2011) find

an uncertainty in N(H I) measurements of of about 25%. They compare this to a 10′ beam, similar to data from the Effelsberg telescope (9′), which yields an N(H I) uncertainty of 10%. The use of interferometers can reduce the effective beam size, but many sources are too faint to be observed with such facilities at present. The lower detectible limit of angular variations in N(H I) is not known, so some degree of uncertainty remains as currently insurmountable from an instrumental standpoint. In certain cases, we know our sightlines probe the edges of Clouds where sharp spatial gradients in N(H I) exist, further raising uncertainties. We comment on these individual cases as warranted in Section 3.4.

Third, accurate placement of the continuum in UV spectra is essential to get the correct equivalent widths. Often this is not a complicated matter, given that the shape of the continuua is known for background sources like QSOs and AGN, but the continuum if often found modified for a number of reasons. On the data handling side, these include fixed-pattern noise and bad flat fielding that tend to cause undulations or "ripples" in the continuua of reduced and extracted spectra that are difficult to remove with low-order polynomial fits. Other effects are intrinsic to the spectra; for example, very strong absorption in the Lyman series H I lines originating in the background source can lead to wings many thousands of km s^{-1} wide that impact regions in which we expect to see interstellar absorption. In some cases, the impact on those neighboring regions is so severe as to render equivalent widths essentially unmeasurable, but these are exceptional instances. Rather, we are

concerned with the systematic error associated with setting the zero level of the continuum in the simple cases. The error contribution by uncertainties in finding and fitting the continuum were derived in detail by Sembach & Savage (1992), who quote an error of 2% due to this source.

Finally, the accuracy of our line quality judgments ultimately controls the reliability of our derived abundances. This is why we relied principally on the curve-of-growth method for obtaining column densities, as it involves the fewest number of assumptions about the lines and is least sensitive to the influence of individual lines on N. Bad line judgments manifest clearly in the COGs as outlier points that cannot immediately be reconciled with those of other lines with more secure judgments. Comparison with column densities computed via the $N_a(v)$ integral (Section 3.3.7) also serves to alert us to reconsider line judgments. While the effect of a bad judgment is not completely mitigated through the use of COGs, we are often led by them toward better judgments that bring the equivalent widths into agreement with expectations. The goal in iterating decisions about line judgments is to effectively eliminate this as a significant source of systematic error in the resulting abundances.

3.4 Notes on Individual Sightlines

3.4.1 3C273.0

This sightline, toward the QSO 3C 273, samples a remarkably rich assortment of clouds in the intergalactic medium (IGM). An early, comprehensive study was done by Savage et al. (1993) using pre-COSTAR observations with

GHRS, but the spectral lineshape function of the data is sufficiently large ($\sim$ 20 km s^{-1}, with broad wings) such that they could not resolve any absorption at small $v_{\rm LSR}$. Since they integrated over the zero-velocity Galactic absorption, no information is available among their results about intermediate-velocity gas. Sembach et al. (2001b) identified eight distinct absorbers in the redshift range $z = 0.00338-0.14660$ in their study of *FUSE* and archival GHRS data. Of these, H I is seen in absorption at two redshifts associated with the Virgo Cluster, $z = 0.00335$ ($v_{\rm LSR} = +1005$ km s^{-1}) and $z = 0.00532$ ($v_{\rm LSR} = +1595$ km s^{-1}); Wakker et al. (2003) identifies three galaxies in Virgo (NGC 4420, UGC 7612, UGC 7512) with impact parameters < 300 kpc that may be responsible for the observed absorption. However, the internal velocity dispersion of cluster members in Virgo is too high to positively identify the galaxies responsible for the absorption at these velocities. Sembach et al. saw two absorption components attributable to gas near the Milky Way at centroid velocities of ~ -15 and $+23$ km s^{-1}, finding structure within each component in high-resolution GHRS data. More recently, Shull et al. (2009) examined STIS E140M data of this sightline for evidence of Si II and Si III absorption, noting a strong component centered at $v_{\rm LSR} = +40$ km s^{-1}. Other, highly ionized gas is seen at additional velocities, which we document below. A representative sample of ions detected in our UV spectra is shown in Figures 3.1-3.2.

Absorption in several ions is seen in the UV data in the range $+10$ km s$^{-1} \leq v_{\rm LSR} \leq +45$ km s^{-1}, but is not attributable to any known cloud or cloud complex. Blades & Morton (1983) reported absorption in the optical due to

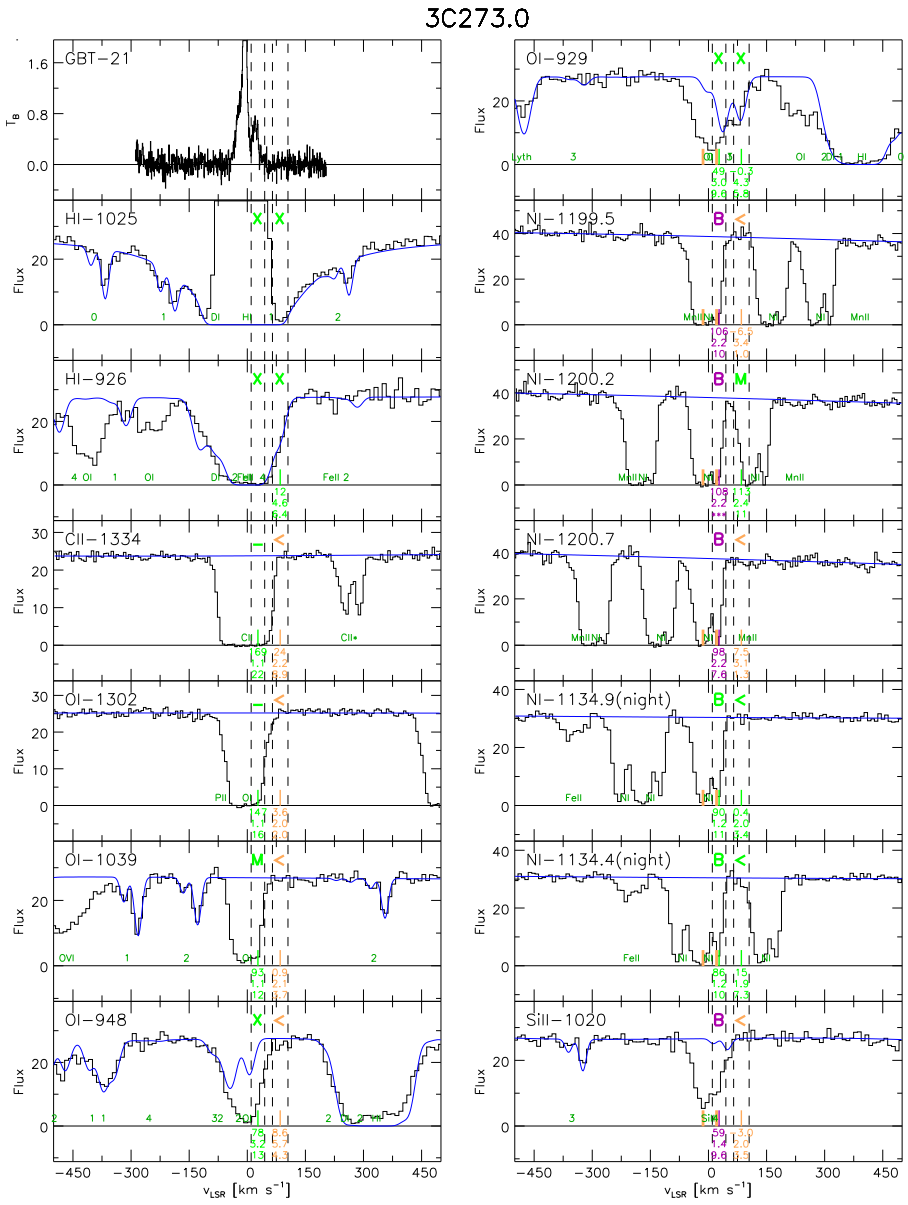

Figure 3.1 Cutouts of the GBT 21 cm spectrum and selected UV spectra toward 3C273.0 highlighting ions and lines most relevant to the determination of the metallicity and depletion of each component. Continuum fits are indicated by blue lines, and alphanumeric symbols above the spectra indicate line quality judgments as described in Section 3.3.5. Ion names, ionization stages, and rest wavelengths in Å are shown at top-left in each panel, and each spectrum is plotted on an LSR velocity scale.

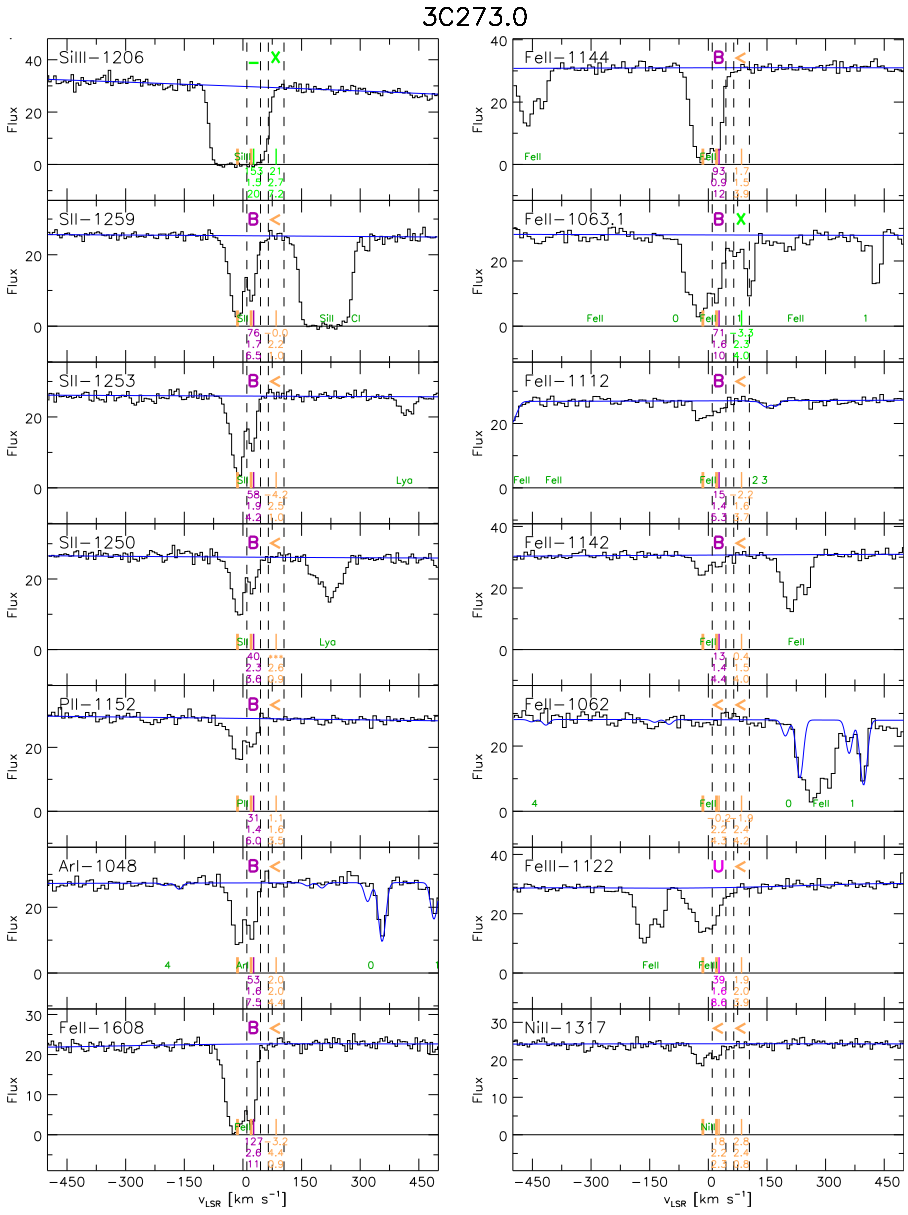

Figure 3.2 Cutouts of selected UV spectra toward 3C273.0 (continued).

Ca II and Na I at $v_{\rm LSR} = +25$ km s^{-1}; Meyer & Roth (1991) also saw lines of interstellar Ca II at +23 km s^{-1}. The presence of dust in this cloud is indicated by the detection of lines of H_2 by Sembach et al. (2001b) at +16 km s^{-1}, which does not trace the main 21 cm emission column density concentration. The shapes of the lines of the absorption lines in the data they analyzed are largely consistent except for those of Ar I, which show a two-component structure; interestingly, the velocity centroid of the positive-velocity component of the Ar I lines matches that of the H_2 lines. They note that the velocity range spanned by lines of high ions such as S III and Fe III is similar to the range seen among the low ions (except Ar I), suggesting an absorbing medium which is of low column density and high turbulence.

This cloud is detected in H I 21 cm emission. We fit a single Gaussian component to the GBT spectrum centered at +25 km s^{-1} with FWHM = 21 km s^{-1} and N(H I) = $(1.94 \pm 0.22) \times 10^{19}$ cm^{-2}, or log N(H I) = 19.29 ± 0.05. We determined an intrinsic linewidth of $13.0^{+7.3}_{-4.4}$ km s^{-1} (Doppler $b = 7.8^{+4.4}_{-2.6}$ km s^{-1}) from multiple detected lines of Fe II and S II. The resulting elemental abundances with respect to H I are shown in Figure 3.3. The large uncertainties on some of the abundance measurements are an effect of very strong lines seen at a comparatively small velocity separation from the zero-velocity Galactic absorption; in fact, the stronger lines of most ions are either severely blended with the Galactic absorption or saturated, rendering them useless in computing column densities. Among detected, undepleted species, we find [S II/H I] = $+0.42 \pm 0.20$ and [N I/H I] = -0.38 ± 1.54. The pattern of measured

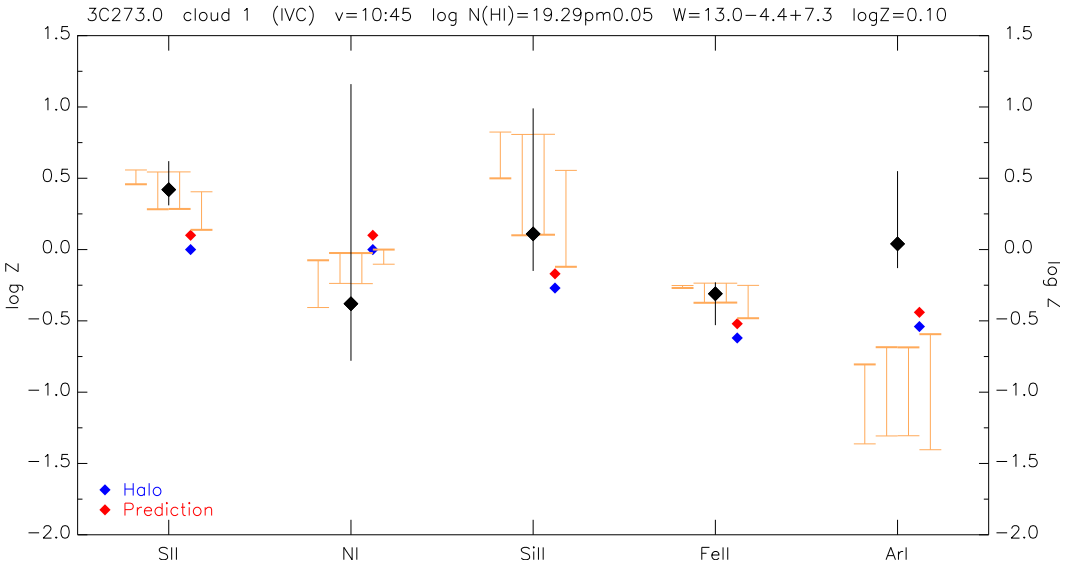

Figure 3.3 Abundance plot for an IVC toward 3C273.0 at +10 km s^{-1} $\leq v_{\rm LSR}$ $\leq$ +45 km s^{-1}. The range of possible ionization corrections is shown for 1, 5, and 10 kpc (log ϕ = 6.66, 5.77, and 5.78) at densities between log n = −3 and −1, and for the extragalactic background, log ϕ = 4.53 (orange bars, left to right). A Halo depletion pattern is indicated with blue points for each ion, and predicted abundances with red points given our inferred metallicity, log Z = +0.10.

abundances, when compared to predictions from our ionization models, is consistent with the range of metallicities log $Z \sim +0.1^{+0.3}_{-0.2}$ ($1.3^{+1.2}_{-0.5}$ $Z_{\odot}$). A disk-like, near-solar metallicity metallicity is consistent with a cloud enriched in metals via participation in the Galactic Fountain.

The abundance of Ar I does not follow the pattern established by the other detected ions, as shown in Figure 3.3. While blended with Galactic absorption at zero velocity, both Ar I lines (λ1048 and 1066) are clear detections with equivalent widths of 53$\pm$1.6$\pm$7.5 mÅ and 36$\pm$2.0$\pm$5.9 mÅ, respectively.

From these we compute log N(Ar I) = $13.74^{+0.50}_{-0.17}$ and [Ar I/H I] = 0.04 ± 0.51; ionization modeling implies a corresponding metallicity of log $Z > 0.7$ (> 5 $Z_{\odot}$). We do not think the apparently excessive Ar I log column density is the result of a measurement error, as Sembach et al. (2001b) reported a very similar value ($\sim$ 13.65). As noted previously, Sembach et al. reported the structure of the Ar I lines is unlike those of the other "dominant" ions in this component (e.g., Si II, P II, S II, and Fe II); they explain that the observed asymmetry in the two Ar I components may be the result of differences in the ionization of the two components if they are in fact physically distinct clouds. Given that Ar I is considerably more susceptible to photoionization than other neutral ions (Sofia & Jenkins 1998), this may explain why its line profile shape is different than those of the singly ionized ions. It may also explain why the Ar I abundance does not match the pattern of theother ions in Figure 3.3.

We see evidence for three other absorption components in the UV data whose velocity range are consistent with the deviation velocities expected for HVC/IVC gas, but for which we did not carry out formal abundance analyses. Both of these components are highly ionized, and neither is detected in the ions we use for making abundance determinations. O VI absorption is seen in the range +65 km s^{-1} $\leq v_{\rm LSR} \leq$ +100 km s^{-1}; we find that an H I component centered at $v_{\rm LSR}$ = +85 km s^{-1} with FWHM = 15 km s^{-1} and N(H I) = $(3.5 \pm 0.5) \times 10^{15}$ cm^{-2}, or log N(H I) = $15.54^{+0.06}_{-0.07}$, is required to adequately fit the observed Lyman series H I line profiles. Given a value for N(H I), we can compare the upper limits for the non-detection of many ions against our

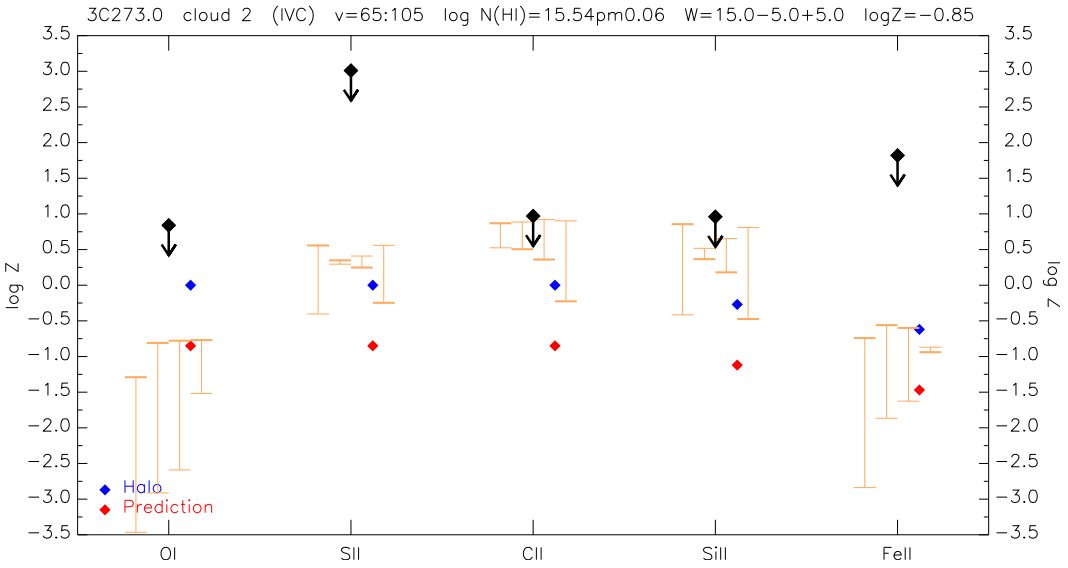

Figure 3.4 Abundance plot for an IVC toward 3C273.0 at +65 km s^{-1} $\leq v_{\rm LSR}$ $\leq$ +100 km s^{-1}. The range of possible ionization corrections is shown for 1, 10, and 50 kpc (log ϕ = 6.66, 5.78, and 5.76) at densities between log $n = -3$ and -1, and for the extragalactic background, log ϕ = 4.53 (orange bars, left to right). A Halo depletion pattern is indicated with blue points for each ion, and predicted abundances with red points given our inferred upper metallicity limit, log $Z > -0.85$.

ionization models; from this, we find a lower limit for the metallicity of this component of log $Z > -0.85$ (> 0.14 $Z_{\odot}$). This is the minimum metallicity specifically compatible with our upper limits of [C II/H I] $< +0.97$ and [Si II/H I] $< +0.96$, given that the distance to this cloud is unknown. Abundance limits and the range predicted by ionization models for this component are shown in Figure 3.4. Absorption by O VI is also seen in the range +185 km s^{-1} $\leq v_{\rm LSR} \leq$ +225 km s^{-1}, but is not seen in H I to a limit of N(H I) = 10^{13} cm^{-2}. We are therefore unable to compute a lower limit for the metallicity of this component.

Finally, we note weak absorption in several ionic lines (e.g., O I λ1302, Si II λ1526, 1193, 1190, and 1304) in the interval +45 km s^{-1} $\leq v_{\rm LSR} \leq$ +65 km s^{-1}. It is not seen in other ions such as S II or Fe II, but it appears saturated in C II λ1036 and 1334, Si II λ1260, and Si III λ1206. However, there is no corresponding feature in the 21 cm spectrum, and we can only establish a lower limit of N(H I) $> 5 \times 10^{15}$ cm^{-2}, or log N(H I) > 15.70, from the H I Lyman series lines. Since this value of N(H I) is very low, in an abundance analysis it would lead to particularly large ionization corrections. Therefore, while a component at $v_{\rm LSR} \sim$ +55 km s^{-1} is needed in order to understand the observed ionic absorption, but we did not attempt to derive a metallicity for this component.

In summary, the 3C273.0 sightline shows evidence of UV absorption due to intermediate- and high-velocity gas in several components, some of which are evidently too strongly ionized to be amenable to abundance determinations through absorption line measurements. An IVC at $v_{\rm LSR} =$ +28 km s^{-1} has a slightly supersolar metallicity ($\sim 1.3\ Z_{\odot}$) and is probably a Galactic Fountain cloud. Additional intermediate-velocity gas is seen in O VI and H I at $v_{\rm LSR} =$ +85 km s^{-1}, for which we establish a lower metallicity limit of $Z > 0.14\ Z_{\odot}$. This is consistent with an HVC-like value and indicates this cloud probably has an origin in the lower Halo. We detect O VI absorption at +205 km s^{-1} without complementary H I; we are unable to establish a meaningful metallicity limit for this cloud. Finally, the ionic lines indicate the need for a component at $\sim$+55 km s^{-1} with very low N(H I), for which we did not perform an

abundance analysis.

3.4.2 3C249.1

This sightline lies a few degrees off the southern edge of Complex C and shows weak H I absorption around -130 km s^{-1}, similar to Complex C velocities in other nearby sightlines. Sembach et al. (2003) noted that this sightline is somewhat further off Complex C than Mrk 205, but is within a few degrees of the edge of H I 21 cm emission we have referred to here as the "C-South" extension of Complex C. They note that no O VI absorption is present to a limit of N(O VI) $<$ 13.83. Fox et al. (2004) confirmed the non-detection of O VI but did not cite a limit; they also assert that there is also no high-velocity H I seen. The non-detection of O VI was again confirmed in Fox et al. (2006), but the authors did not cite a detection limit for negative LSR velocities. We also see absorption attributable to the IV Arch at moderate negative velocities. A representative sample of ions detected in our UV spectra is shown in Figures 3.5-3.7.

Absorption seen in the velocity range -140 km $s^{-1} \leq v_{\rm LSR} \leq -100$ km s^{-1} probably traces Complex C gas on the basis of its proximity to other Complex C sightlines and the range of observed velocities. The determination of N(H I) is important in placing constraints on the possible metallicity of this component. It is not detected in the GBT 21 cm spectrum, from which we obtain a 5σ upper limit of N(H I) $< 7.3 \times 10^{17}$ cm^{-2}, or log N(H I) $<$ 17.86, assuming an intrinsic linewidth of 20 km s^{-1}. We would ordinarily

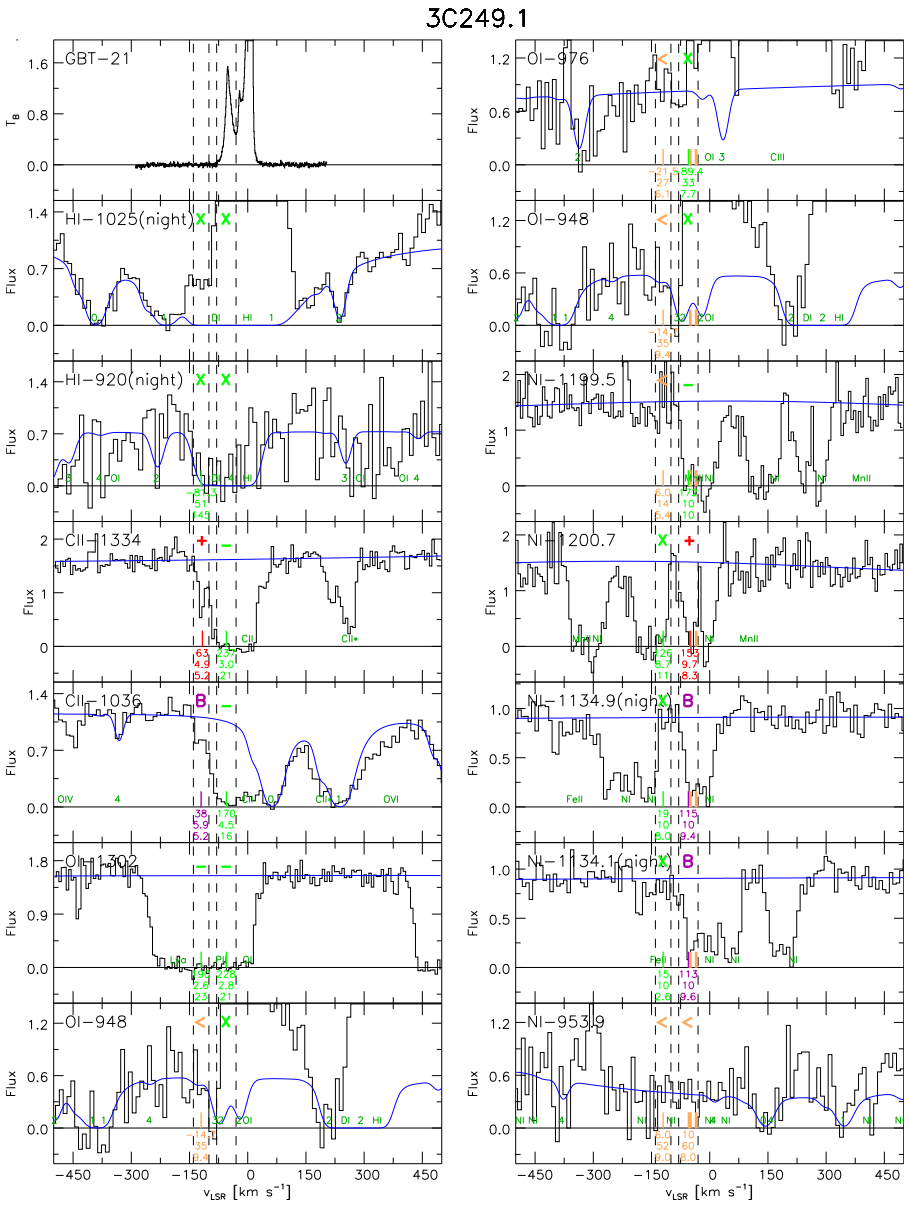

Figure 3.5 Cutouts of the GBT 21 cm spectrum and selected UV spectra toward 3C249.1 highlighting ions and lines most relevant to the determination of the metallicity and depletion of each component. Continuum fits are indicated by blue lines, and alphanumeric symbols above the spectra indicate line quality judgments as described in Section 3.3.5. Ion names, ionization stages, and rest wavelengths in Å are shown at top-left in each panel, and each spectrum is plotted on an LSR velocity scale.

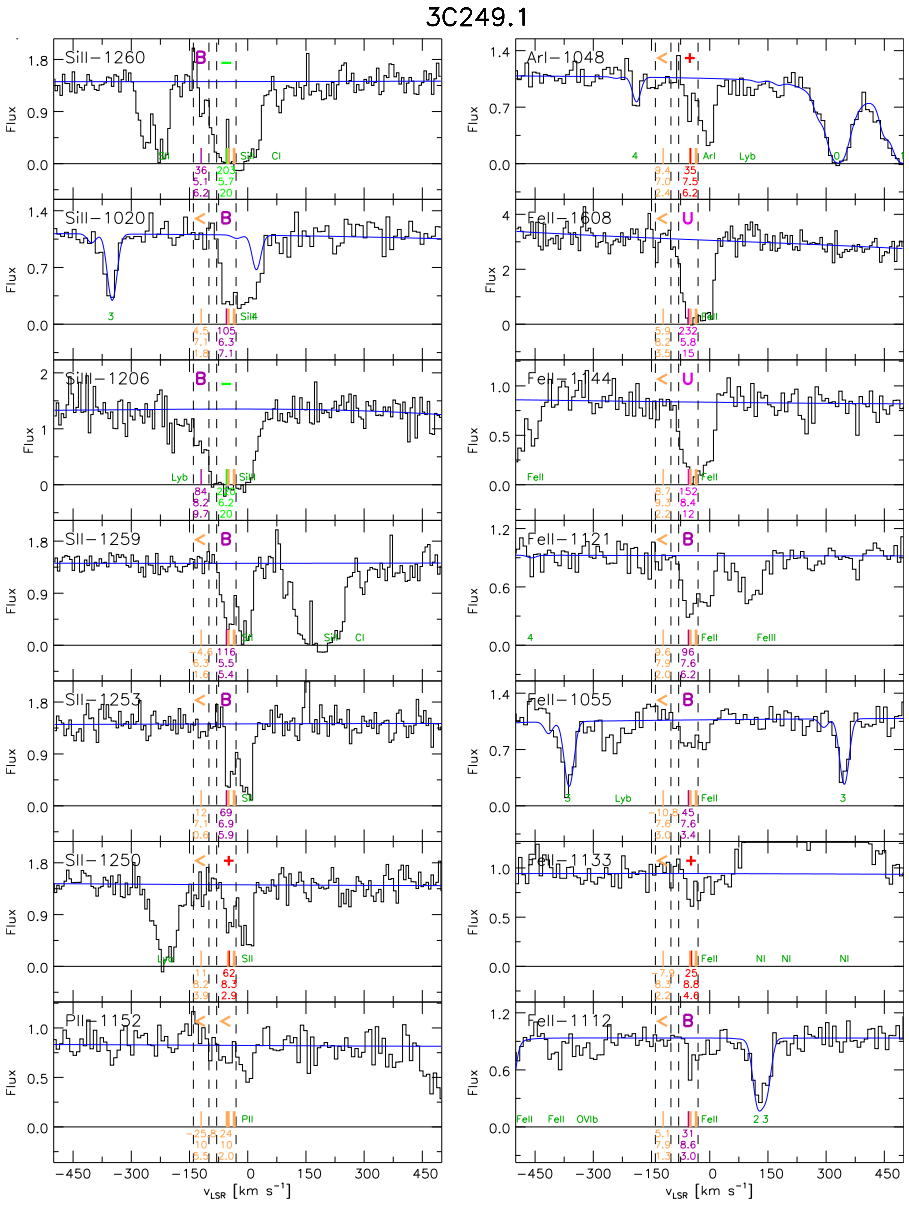

Figure 3.6 Cutouts of selected UV spectra toward 3C249.1 (continued).

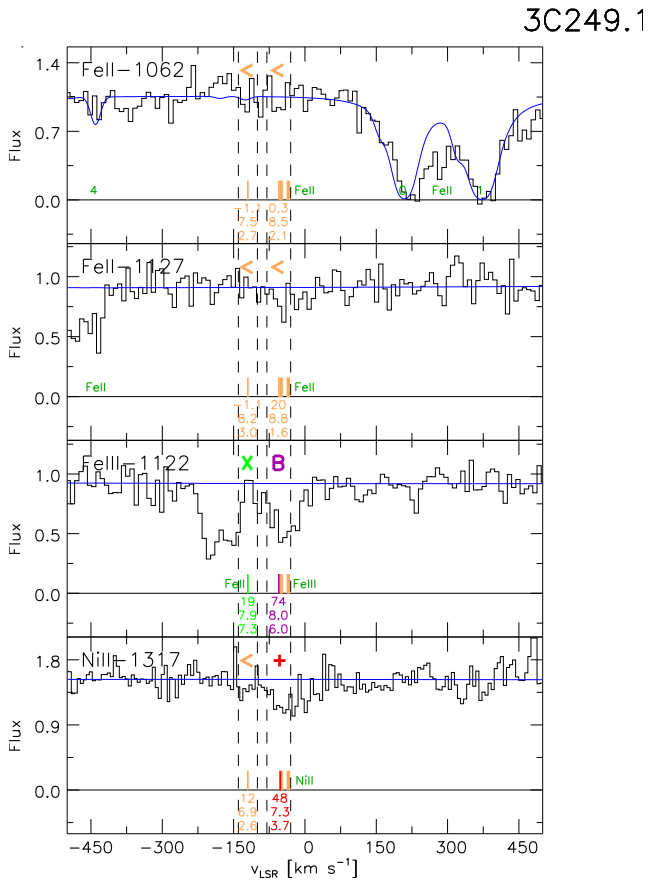

Figure 3.7 Cutouts of selected UV spectra toward 3C249.1 (continued).

find a corresponding lower limit by fitting the Lyman series H I lines in our UV spectra, but the data are particularly noisy and we cannot derive a meaningful lower limit in this manner. We can draw some conclusions about the likely range of N(H I) values by considering the abundances implied by our models of abundances after correcting for ionization and an assumed metallicity. If the material seen in this velocity range is correctly identified with Complex C, we would expect log $Z \sim -0.8$. For this range, H I column densities around

$10^{17} - 10^{18}$ cm^{-2} predict abundances that are too low relative to range allowed by the ionization models. The best fit we can make to the Lyman series lines includes possible values of N(H I) $\simeq (5 \pm 4)$ $\times 10^{16}$ cm^{-2}, or log N(H I) $\simeq 16.70^{+0.26}_{-0.70}$. Abundances are shown for this value in Figure 3.8. From the

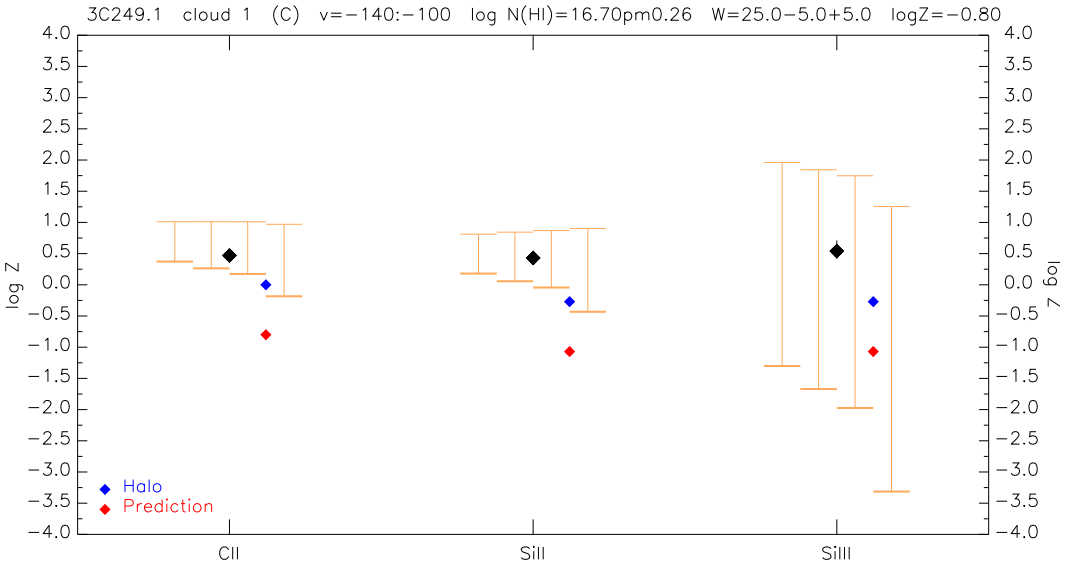

Figure 3.8 Abundance plot for Complex C toward 3C249.1 at -140 km s^{-1} $\leq v_{\rm LSR} \leq -100$ km s^{-1}. The range of possible ionization corrections is shown for 5, 10, and 15 kpc (log ϕ = 5.51, 5.34, and 5.20) at densities between log $n = -3$ and -1, and for the extragalactic background, log ϕ = 4.53 (orange bars, left to right). A Halo depletion pattern is indicated with blue points for each ion, and predicted abundances with red points indicating the expected Complex C metallicity, log $Z = -0.8$.

figure we see that this component has a Complex C-like metallicity for N(H I) no more than a few $\times 10^{16}$ cm^{-2} after accounting for ionization corrections. We feel that it is unlikely N(H I) is much higher than we infer for two reasons: (1) a much higher value would have been detected in the GBT 21 cm data, and (2) a larger N(H I) leads to a predicted metallicity which is unrealistically low

for Complex C ($\log Z < -1$). However, we stress that the available data do not absolutely rule out a higher H I column density than we infer. Rather than arguing for a particular metallicity for this gas, we conclude that the measured column densities of C II, Si II, and Si III are consistent with Complex C-like gas after correction for the effects of ionization. This allows us to make a case for the angular extent to which Complex C is observed.

We detect absorption from a number of ions in the range -80 km s^{-1} $\leq v_{\rm LSR} \leq -30$ km s^{-1}; given the direction of this sightline and the velocities of the absorption, it is associated with the IV Arch. The only reference to this component we find in the literature is Shull et al. (2009), who measured lower limits for N(Si II) and N(Si III) in the identical velocity range. They also report $\log N({\rm H\ I}) = 19.72^{+0.07}_{-0.08}$ from Leiden-Dwingeloo Survey (LDS; Hartmann & Burton 1997) data. A strong emission feature appears in the GBT 21 cm spectrum centered near $v_{\rm LSR} \sim -50$ km s^{-1}; fitting this feature required two Gaussian components. One component was centered at $v_{\rm LSR} = -51$ km s^{-1} with FWHM = 8 km s^{-1} and N (H I) = (1.05 ± 0.04) $\times 10^{19}$ cm^{-2}, and the other was centered at $v_{\rm LSR} = -46$ km s^{-1} with FWHM = 26 km s^{-1} and N(H I) = (4.75 ± 0.11) $\times 10^{19}$ cm^{-2}. The sum of these components gives a total N(H I) = (5.80 ± 0.15) $\times 10^{19}$ cm^{-2}, or $\log N({\rm H\ I}) = 19.76 \pm 0.01$. The resulting abundances are shown in Figure 3.9. We could not measure any O I lines of this component due to a combination of saturation of the stronger lines and contamination by geocoronal emission, but among undepleted ions we obtained good measurements of S II, finding [S II/H I] = $+0.05 \pm 0.13$

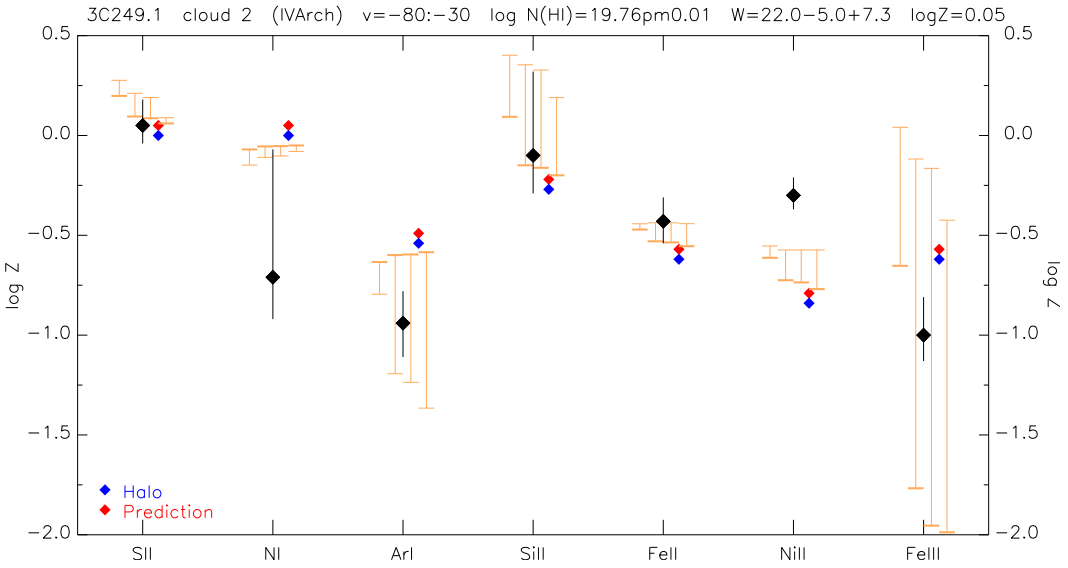

Figure 3.9 Abundance plot for the IV Arch toward 3C249.1 at -80 km s^{-1} $\leq v_{\rm LSR} \leq -30$ km s^{-1}. The range of possible ionization corrections is shown for 1, 5, and 10 kpc (log ϕ = 6.51, 5.51, and 5.34) at densities between log $n = -3$ and -1, and for the extragalactic background, log ϕ = 4.53 (orange bars, left to right). A Halo depletion pattern is indicated with blue points for each ion, and predicted abundances with red points given our measured [S II/H I] = +0.05.

($1.12^{+0.39}_{-0.29}$ $Z_{\odot}$). This is well in line with expectations of a near-solar metallicity cloud at a low z-height above the disk participating in the Galactic Fountain.

In summary, we see absorption from two distinct sources along the line of sight toward 3C249.1. Lines attributed to Complex C appear near $v_{\rm LSR}$ = -120 km s^{-1}, but we are unable to determine a reliable value for N(H I) in this component. Assuming a metallicity of log $Z = -0.8$, consistent with other Complex C measurements, we find log N(H I) $\sim$ 16.70. Absent a better measurement of the H I column density, we cannot independently estimate

the metallicity of this cloud. Absorption due to the IV Arch is seen at $v_{\rm LSR}$ = −55 km s^{-1}, for which we compute a metallicity of log Z = +0.05 (∼1.1 $Z_{\odot}$), in line with our expectation for a low z-height IVC cloud in the Galactic Fountain.

3.4.3 ESO265−G23

This sightline is one of several for which COS data are available, but the background source is relatively faint and the spectra are of low S/N. Because of this, and a lack of high-resolution 21 cm data, there are few published references to anomalous-velocity gas in this direction and in particular, none regarding low-ion abundances. A representative sample of ions detected in our UV spectra is shown in Figures 3.10-3.11.

Absorption at $v_{\rm LSR} \sim +120$ km s^{-1} is identified with the cloud WW226 in Complex WD, part of the "Wannier Clouds" (Wannier et al. 1972, Wakker & van Woerden 1991, van Woerden & Wakker 2004; see Section 3.5.3.1). van Woerden and Wakker quote N(H I) = 5.1×10^{19} cm^{-2}, or log N(H I) = 19.71, and a metallicity of 0.05 $Z_{\odot} \leq Z \leq$ 0.35 $Z_{\odot}$ for WD, while Wakker (2004) reports $Z \sim 0.1$ $Z_{\odot}$ among preliminary results from *FUSE*. We fit a single Gaussian centered at $v_{\rm LSR}$ = +118 km s^{-1} to the LAB 21 cm spectrum with FWHM = 26 km s^{-1}, finding N(H I) = $(4.61 \pm 0.1) \times 10^{19}$ cm^{-2}, or log N(H I) = 19.66 ± 0.01. This component is unambiguously detected several low ions at +90 km s^{-1} $\leq v_{\rm LSR} \leq$ +152 km s^{-1}, including N I λ1134.1, O I λ1039, and two lines of Fe II (λ1144, 1096). It is very strong or saturated in the

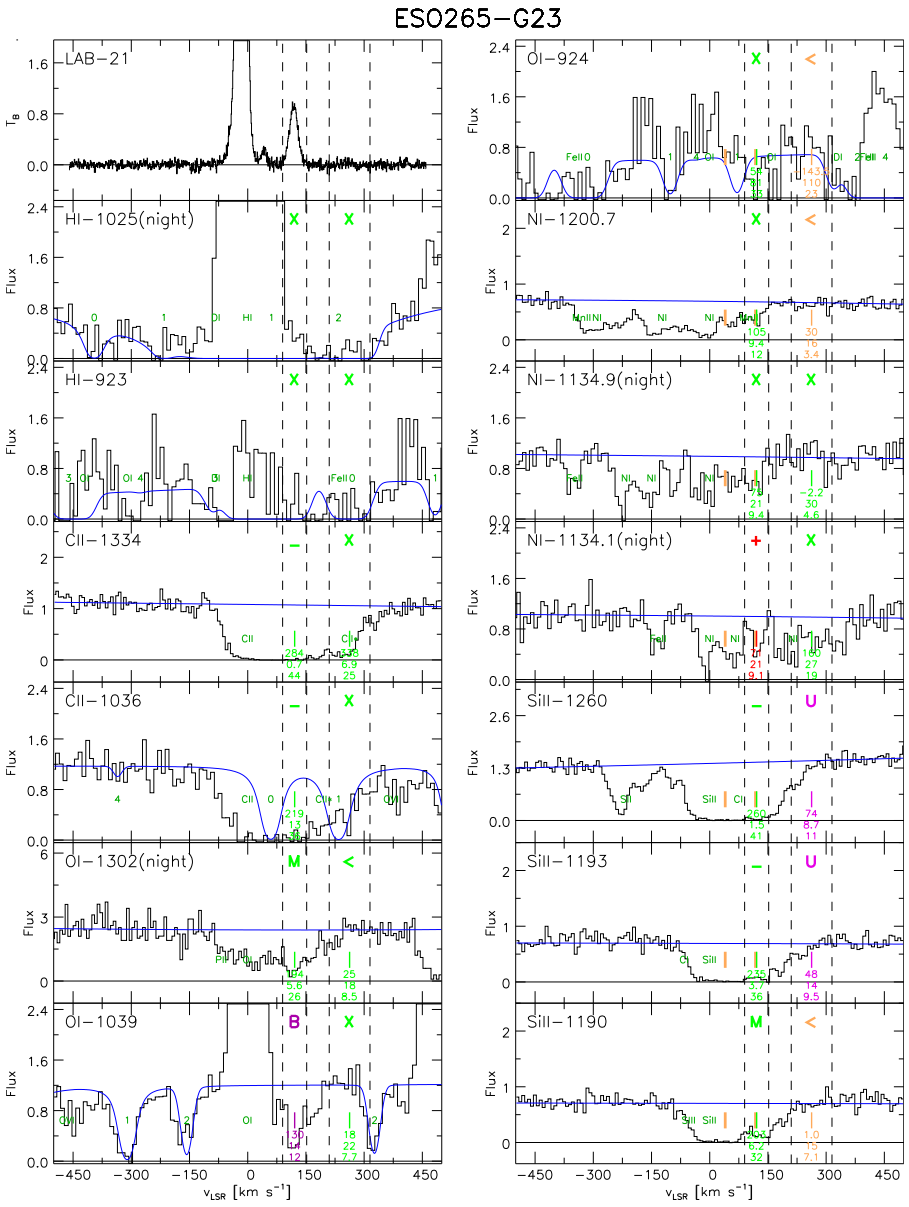

Figure 3.10 Cutouts of the LAB 21 cm spectrum and selected UV spectra toward ESO265−G23 highlighting ions and lines most relevant to the determination of the metallicity and depletion of each component. Continuum fits are indicated by blue lines, and alphanumeric symbols above the spectra indicate line quality judgments as described in Section 3.3.5. Ion names, ionization stages, and rest wavelengths in Å are shown at top-left in each panel, and each spectrum is plotted on an LSR velocity scale.

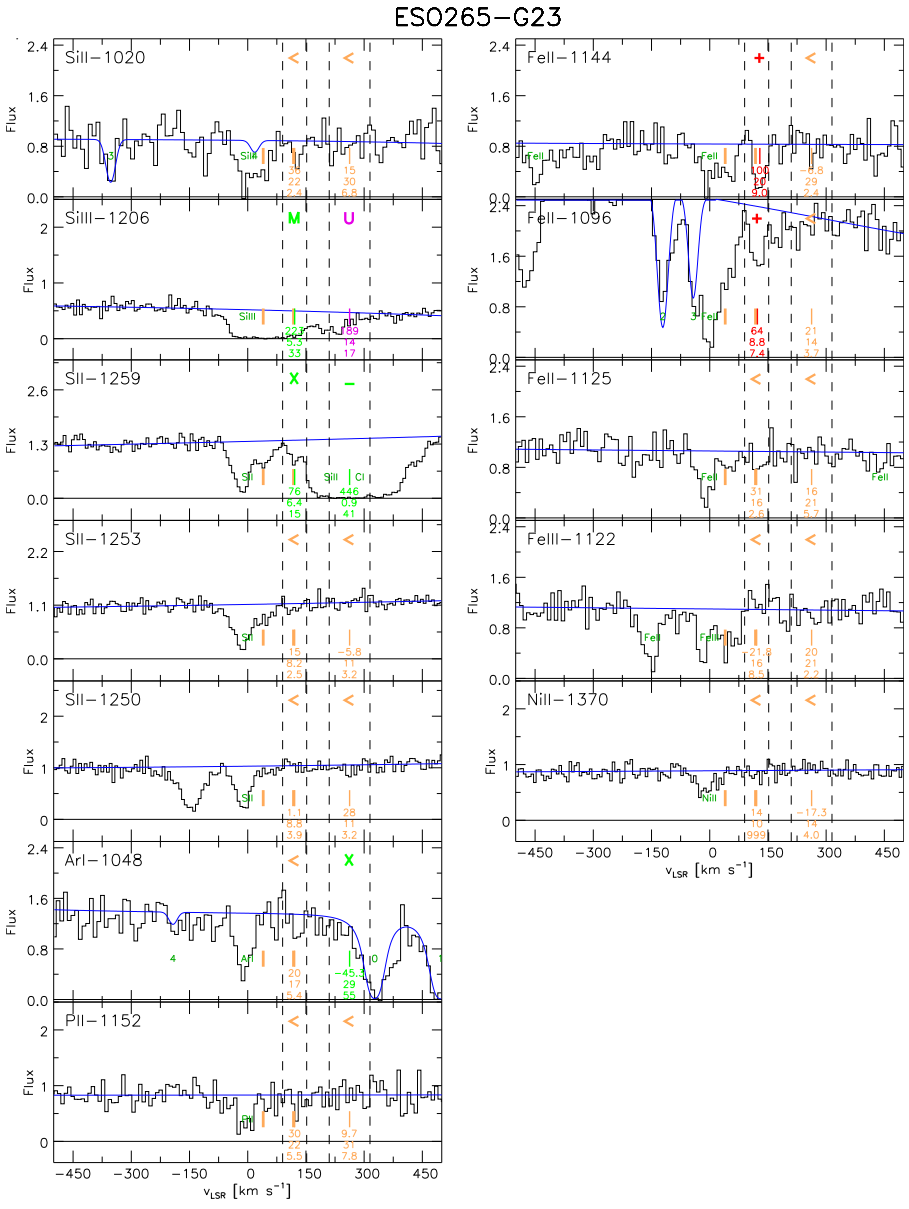

Figure 3.11 Cutouts of selected UV spectra toward ESO265-G23 (continued).

strongest lines of Si II (λ1260, 1193, 1190) and in Si III λ1206, but it does not appear in Si IV λ1393 or 1402. It is also saturated in C II λ1334 and 1036. It is likely present in C III λ977 but the data are of particularly low S/N and thus we could not reliably measure the equivalent width of the line. We have no data for C IV. An abundance plot of the detected ions in this component is shown in Figure 3.12. On the basis of the detection of O I λ1039 alone,

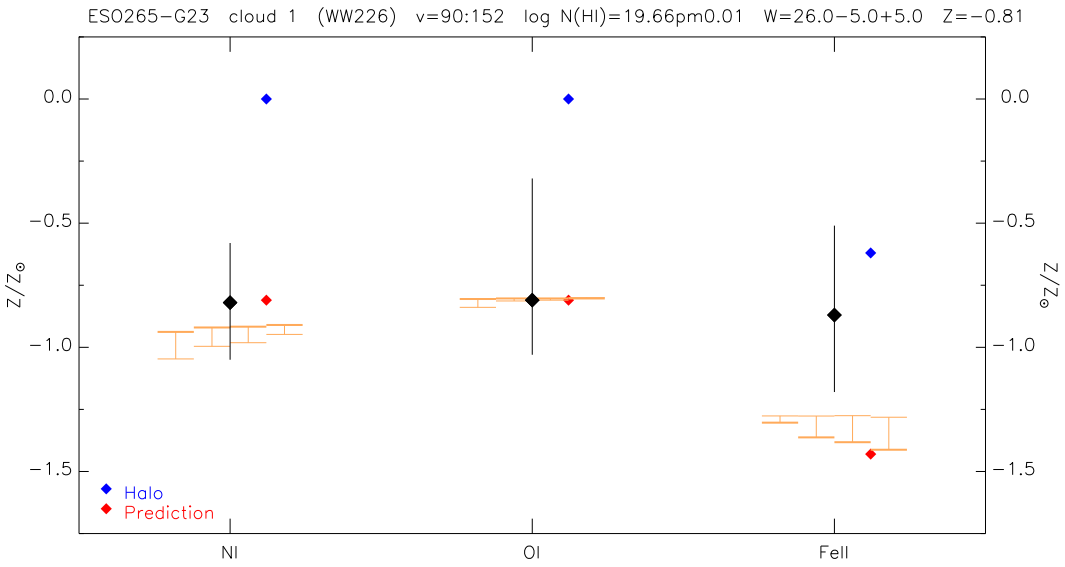

Figure 3.12 Abundance plot for WW226 toward ESO265−G23 at +90 km s^{-1} $\leq v_{\rm LSR} \leq$ +152 km s^{-1}. The range of possible ionization corrections is shown for 1, 5, and 10 kpc at densities between log $n = -3$ and -1, and for the extragalactic background (orange bars, left to right). A Halo depletion pattern is indicated with blue points for each ion, and predicted abundances with red points given our measured metallicity [O I/H I] = −0.81.

we find [O I/H I] = -0.81 ± 0.49 ($0.15^{+0.32}_{-0.10}$ $Z_{\odot}$), which is roughly consistent with the metallicities reported by van Woerden & Wakker (2004) and Wakker (2004). We are unable to get better leverage on this value from other O I

lines. The λ1302 line is nearly saturated and λ988 is contaminated by the W 1−0 $P(2)$ line of H_2. Of note is the N I abundance indicated by the detection of λ1134.1, [N I/H I] $= -0.82 \pm 0.24$. If the detection is reliable, it implies that N I is overabundant relative to expectations, given the almost identical O I metallicity. The departure from expectations does not appear to be an ionization effect. Lu et al. (1998b) suggested that HVCs in the same general direction of the sky as the Magellanic Stream, including Complex WD, may be the result of the same process or processes that produced the Stream itself. While the metallicity of the WW226 component is somewhat higher than the "typical" MS value of $\sim 0.1\ Z_\odot$, it is not fundamentally inconsistent with the metallicity of MS gas. The position of WW226 on the sky would therefore associate it with the "Leading Arm" of the MS (e.g., Brüns et al. 2005).

At larger positive velocities, ionized gas associated with the Magellanic Stream is seen at $v_{\rm LSR} \sim +260$ km s^{-1} including strong O VI absorption with a width of ~ 100 km s^{-1} (Sembach et al. 2003, Fox et al. 2006). There is no corresponding feature in the 21 cm data at these velocities. We computed a 5σ upper limit of N(H I) $< 3.07 \times 10^{18}$ cm^{-2}, or log N(H I) < 18.49, from the LAB spectrum, assuming a linewidth of 40 km s^{-1}, comparable to the O VI width found by Sembach et al. (2003). The S/N of the data is sufficiently low that it is impractical to obtain a lower limit for N(H I) by fitting the Lyman H I line profiles, so we cannot adequately bracket a range of possible metallicities for this component. As in other sightlines sampling the MS, it is detected only in Si II (λ1260, 1193) and Si III (λ1206) in the velocity range $+210$ km s$^{-1} \leq v_{\rm LSR}$

$\leq +315$ km s^{-1}. The Si III absorption is of higher equivalent width than in the case of the Si II lines; in fact, by the next intrinsically strongest line, λ1190, it is no longer confidently detected. The profiles are strongly asymmetric, with the absorption strongest at $v_{\rm LSR} = +235$ km s^{-1}; the basis for the upper positive velocity limit of the integration window is the strength of the Si III feature. In the weaker Si II line, the flux returns to the continuum level with increasing wavelength before the +315 km s^{-1} limit is reached, such that the edge of the window appears to be tracing the wing of a broad line. O I λ1302 shows a profile resembling those of confidently detected lines, but falls short of our detection threshold and thus is judged useful only as an upper limit. From this limit, we find [O I/H I] < -1.36, or $Z \sim 0.4\ Z_{\odot}$. If the true [O I/H I] is closer to other MS measurements at ~ -1.0, the implied value of log N(H I) is closer to ~ 18.15. The result also depends on the actual intrinsic linewidth. Given that this component is a 21 cm non-detection and the Lyman H I lines offered no meaningful constraints, in computing abundances we assumed a typical linewidth for HVCs of 15 ± 5 km s^{-1}, but the unusual profile of the detected lines and the much larger width of the O VI lines suggest that the true linewidth could be much higher than we assume. It also suggests that the equivalent width in our defined velocity integration window undercounts the true absorption. The Si II and Si III abundances plotted in Figure 3.13 are shown assuming $Z = -1$; From this we can at least conclude that the metallicity of the MS toward ESO265−G23 is consistent with measurements along other sightlines of about one-tenth solar, but it could be somewhat below

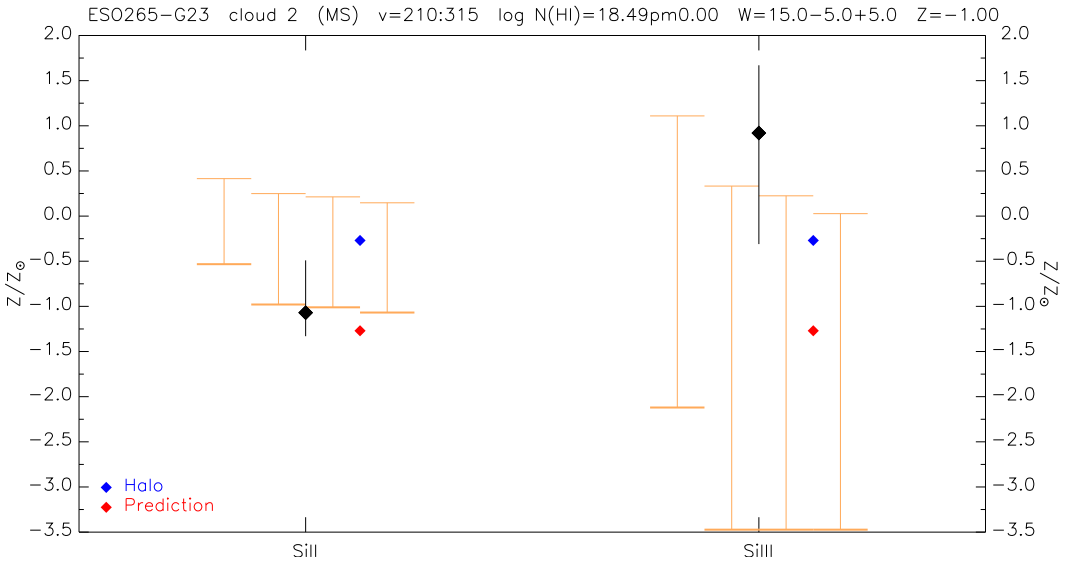

Figure 3.13 Abundance plot for the Magellanic Stream toward ESO265−G23 at +210 km s^{-1} $\leq v_{\rm LSR} \leq$ +315 km s^{-1}. The range of possible ionization corrections is shown for 5, 20, and 50 kpc at densities between log $n = -3$ and -1, and for the extragalactic background (orange bars, left to right). A Halo depletion pattern is indicated with blue points for each ion, and predicted abundances with red points given an assumed typical MS metallicity of $Z = -1$.

this value as well.

Structure in the interval between the two components discussed here (i.e., +152 km s^{-1} $\leq v_{\rm LSR} \leq$ +210 km s^{-1}) is evident in many of the same ions described above, e.g., O I (λ1302, 1039), C II (λ1334), Si II (λ1260, 1193, 1190), Si III (λ1206) as can be seen in Figures 3.10-3.11. However, the profile shape among lines of the same ion is inconsistent. Given that there is no 21 cm emission in this window and the attendant difficulty in constraining N(H I), we elected not to attempt to derive abundances for any possible absorption

component at these velocities. If Complex WD is indeed physically associated with the MS, then a continuum of related absorption may well exist in the range +90 km s^{-1} $\lesssim$ $v_{\rm LSR}$ $\lesssim$ +300 km s^{-1}, all of roughly tenth-solar metallicity.

To summarize, in the direction toward ESO265−G23, we see at least two distinct absorption components in the UV associated with the cloud WW226 in Complex WD ($v_{\rm LSR} \sim 120$ km s^{-1}) and highly ionized gas in the Magellanic Stream ($v_{\rm LSR} \sim 260$ km s^{-1}). The detection of a single O I line (λ1039) in WW226 leads to an estimate of $Z \sim 0.15\ Z_{\odot}$ for this cloud. We cannot confidently quote a metallicity for the MS component, but find a lower limit of $Z \sim 0.04\ Z_{\odot}$; a value closer to 0.1 $Z_{\odot}$ found by other authors in MS sightlines is not inconsistent with our dataset, but we cannot firmly establish an upper limit for Z. Additional absorption evident between these two components may constitute evidence of additional MS material, but we do not have enough information to render a definitive judgment on this question.

3.4.4 Markarian 106

This sightline is the only one in our sample that probes Complex A, but the *FUSE* data have relatively low S/N at 3.6 per resolution element, even after combining both LiF segments. Measurements of these spectra are further complicated by particularly strong geocoronal emission, even in the night-only data. Previous studies of this sightline have largely focused on Galactic O VI absorption (Sembach et al. 2003, Fox et al. 2006)and therefore did not

specifically address abundances in either high- or intermediate-velocity gas. Wakker et al. (2003) noted an a feature in the *FUSE* data near O VI λ1031 (+580 km s^{-1} on its velocity scale) they attribute to intergalactic Lyman β H I absorption associated with the Leo Galaxy Grouping at $v = +1390 \pm 390$ km s^{-1}, but it does not impact any of our measurements of high-velocity gas in this sightline. They also saw O VI absorption in the range -150 km s^{-1} $\leq v_{\rm LSR} \leq -100$ km s^{-1}, but note the feature has only a 3σ significance and concluded it does not overlap with the H I velocities associated with Complex A. A representative sample of ions detected in our UV spectra toward Mrk 106 is shown in Figures 3.14-3.15.

Schwarz et al. (1995) made optical observations of Mrk 106, detecting Ca II absorption from Complex A at $v_{\rm LSR} = -157$ km s^{-1}. Measurements of O VI absorption in this sightline include the work of Sembach et al. (2003), who found log N(O VI) $\simeq$ 13.81 in the velocity range -150 km s^{-1} $\leq v_{\rm LSR} \leq -100$ km s^{-1}, and Fox et al. (2006), who registered a 3σ non-detection in the range -200 km s^{-1} $\leq v_{\rm LSR} \leq -100$ km s^{-1}. However, to date, little work appears in the literature attempting to estimate the metallicity of Complex A. Kunth et al. (1994) observed the IZw 18 sightline with GHRS before the COSTAR optics upgrade, finding a subsolar value for [O I/H I], but with substantial measurement uncertainties (see Section 3.5.1 for a more complete discussion of this work). More recently, Barger et al. (2012) made optical observations with the Wisconsin Hα Mapper (WHAM), including measurements of the Mrk 106 sightline in lines of [S II] and [N II]; they find subsolar composition across

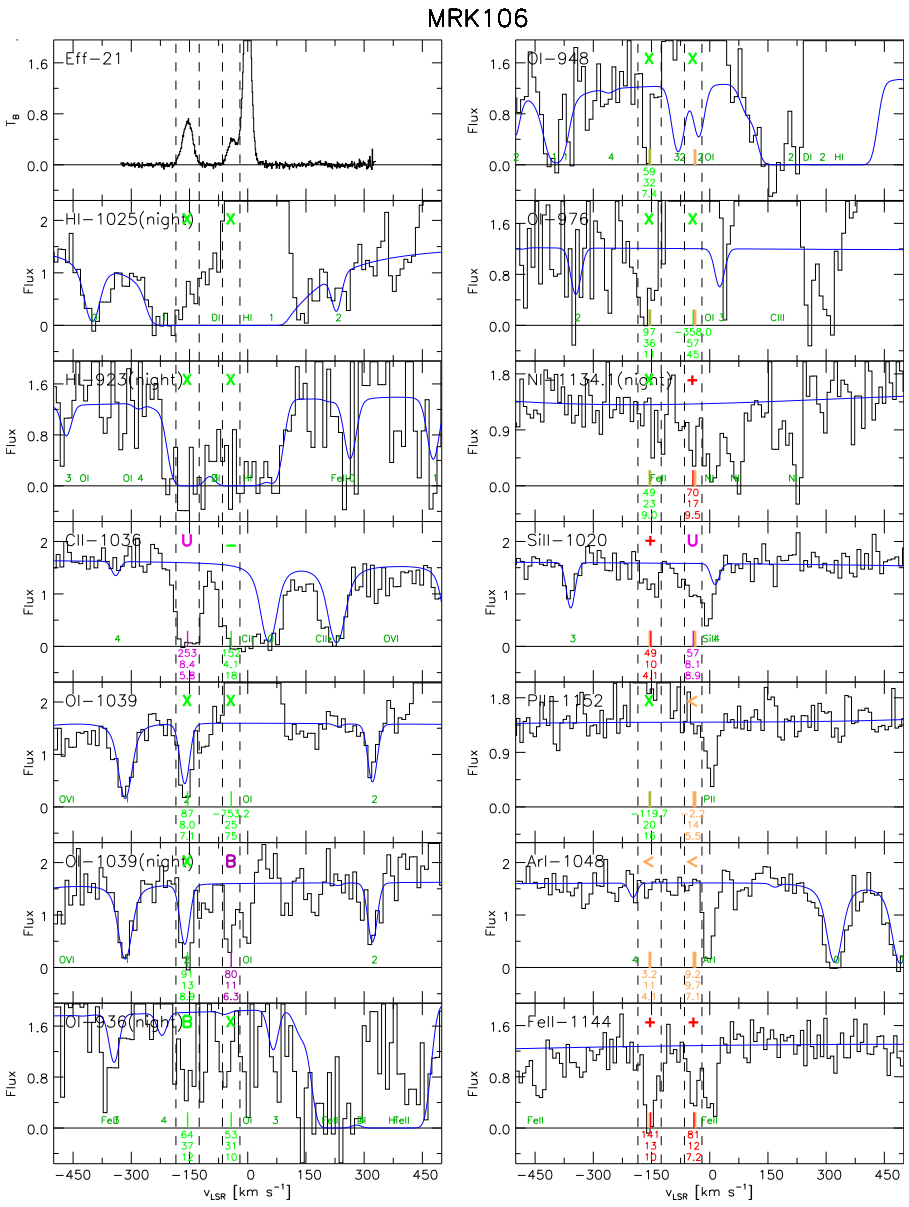

Figure 3.14 Cutouts of the Effelsberg 21 cm spectrum and selected UV spectra toward Mrk 106 highlighting ions and lines most relevant to the determination of the metallicity and depletion of each component. Continuum fits are indicated by blue lines, and alphanumeric symbols above the spectra indicate line quality judgments as described in Section 3.3.5. Ion names, ionization stages, and rest wavelengths in Å are shown at top-left in each panel, and each spectrum is plotted on an LSR velocity scale.

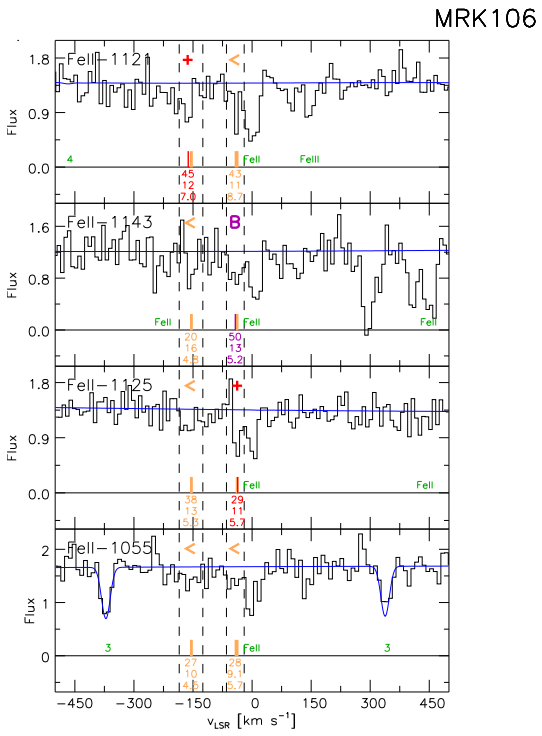

Figure 3.15 Cutouts of selected UV spectra toward Mrk 106 (continued).

a large range of possible electron temperatures and ionization fraction, but caution that their detections do not constrain the abundances in a significant way. Wakker et al. (2001) make a point about the influence of small-scale structure on H I 21 cm observations of this sightline, finding that the measured N(H I) value of the low-velocity component at +7 km s^{-1} is 60% less at low angular resolution. They found a value of N(H I) = (3.8 ± 0.3) $\times 10^{19}$ cm^{-2}, or log N(H I) = $19.58^{+0.03}_{-0.04}$, from a combination of Effelsberg and WSRT data, giving an effective resolution of 1′.

We see absorption attributable to the AVI core of Complex A in several

ions in the velocity range -185 km s$^{-1} \leq v_{\rm LSR} \leq -125$ km s^{-1}, but the wings of C II λ1036 are clearly not well-bound in this interval as seen in Figure 3.14. For this line only, we defined a wider velocity integration window of -205 km s$^{-1} \leq v_{\rm LSR} \leq -105$ km s^{-1} and calculated its column density separately using these limits. Complex A is a strong feature in the Effelsberg 21 cm spectrum to which we fit a single Gaussian component centered at $v_{\rm LSR} = -154$ km s^{-1} with FWHM = 30 km s^{-1} and N(H I) = $(3.98 \pm 0.06) \times 10^{19}$ cm^{-2}, or log N(H I) = 19.60 ± 0.01. However, given that (1) the Wakker et al. (2001) figure for N(H I) was derived from data with a much smaller effective beam size than the Effelsberg spectrum alone and (2) small- scale H I structure in Complex A is a known issue, we adopted their value for our abundance calculations despite its larger uncertainty than that of the Effelsberg-only measurement. Since we do not detect multiple lines of any ion with which to constrain the value of the intrinsic linewidth from the COGs, we adopted for the linewidth the 21 cm FWHM, 30 ± 5 km s^{-1}, or Doppler $b = 18 \pm 3$ km s^{-1}. The resulting abundances with respect to H I are shown in Figure 3.16.

Two lines of O I attributable to Complex A are detected in the spectra: λ1039, which is contaminated by the $5-0$ $R(2)$ line of H_2 at rest wavelength 1038.689 Å, and λ936, which is noisy but uncontaminated. We attempted to decontaminate the λ1039 but found the results unsatisfactory; we discarded it completely in favor of λ936. From this line we measure log N(O I) = $15.63^{+0.24}_{-0.28}$ and compute [O I/H I] = -0.64 ± 0.28 ($0.23^{+0.21}_{-0.11}$ $Z_\odot$). As is evident in Figure 3.16, a metallicity of ~ 0.2 $Z_\odot$ is compatible with the measured abundance

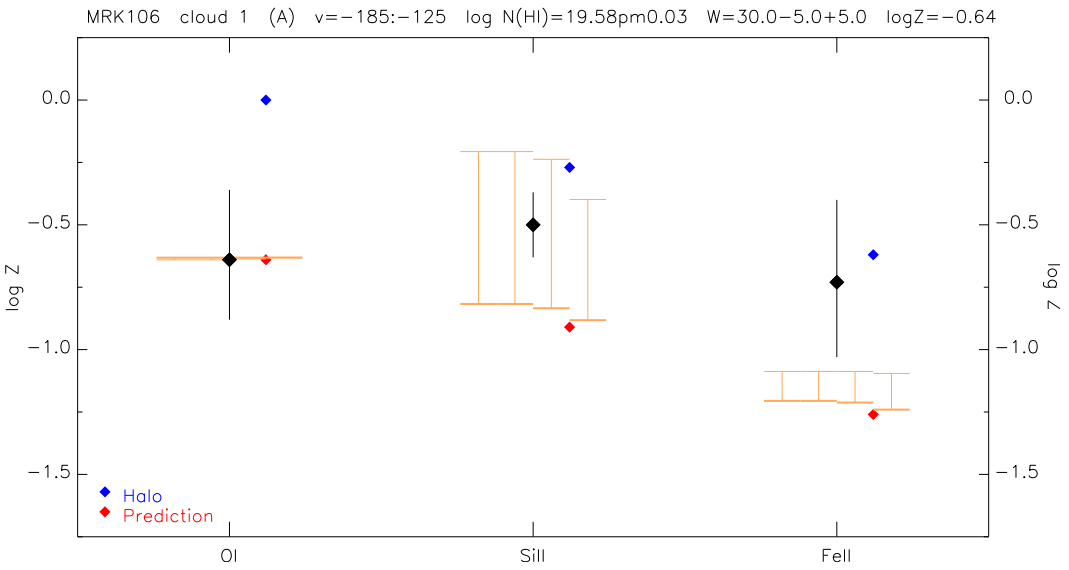

Figure 3.16 Abundance plot for Complex A toward Mrk 106 at -95 km s^{-1} $\leq v_{\rm LSR} \leq -75$ km s^{-1}. The range of possible ionization corrections is shown as the orange bars for, left to right, 5, 10, and 15 kpc (log $\phi = 6.51$, 5.51, and 5.51), and the extragalactic background (log $\phi = 4.53$) at densities between log $n = -3$ and -1. A Halo depletion pattern is indicated with blue points for each ion, and predicted abundances with red points given our measured value of [O I/H I] $= -0.64$.

of Si II given the constraints of our ionization models. Broadly speaking, this metallicity agrees with the "subsolar" figures reported by Kunth et al. (1994) and Barger et al. (2012), so we can effectively rule out a metallicity at or greater than solar and, therefore, a Disk origin for Complex A. Its metallicity and z-height above the Disk are consistent with an origin in the Halo. The rather high Fe II abundance can be explained by a low dust content, leaving much of the Fe II undepleted in the gas phase.

Absorption in the velocity range -65 km s^{-1} $\leq v_{\rm LSR} \leq -20$ km s^{-1}

is attributable to the the Low-Latitude Intermediate Velocity (LLIV) Arch (Wesselius & Fejes 1973, Kuntz & Danly 1996). It is one of several sightlines that lie off the main structure of the LLIV Arch, designated the "LLIV Arch Extension" (LLIVe) by Wakker (2001a); the gas sampled by these sightlines has very nearly the same velocities as the LLIV Arch and is probably spatially close to it. The LLIVe component toward Mrk 106 is clearly detected in the Effelsberg 21 cm spectrum, to which we fit a single Gaussian centered at $v_{\rm LSR}$ = -38 km s^{-1} with FWHM = 29 km s^{-1} and N(H I) = (2.24 ± 0.07) $\times 10^{19}$ cm^{-2}, or log N(H I) = 19.35 ± 0.01. The only ion with a sufficient number of lines detected in the spectra from which to infer the intrinsic linewidth from the COGs is Fe II, which indicates a value around 11 km s^{-1} (Doppler b = 6.6 km s^{-1}); however, an absence of detections among the weakest Fe II lines results in a very large systematic uncertainty. To better constrain the value of the linewidth and its uncertainty we assumed a solar metallicity for this cloud based on characteristics reviewed by Wakker (2001a) and adjusted their values until the abundances of all detected species were brought within the predictions of our ionization models, to within errors. We settled on a value of 12^{+10}_{-3} km s^{-1} ($b = 7.2^{+6.0}_{-1.8}$ km s^{-1}). The resulting abundance pattern for solar metallicity is shown in Figure 3.17. It is clear from the figure that the metallicity of this cloud cannot be significantly subsolar, but it is difficult to argue for any particular metallicity other than "solar", consistent with an origin in the Galactic Fountain. A more reliable estimate of the metallicity of LLIVe along this sightline would certainly benefit from additional UV spectroscopy

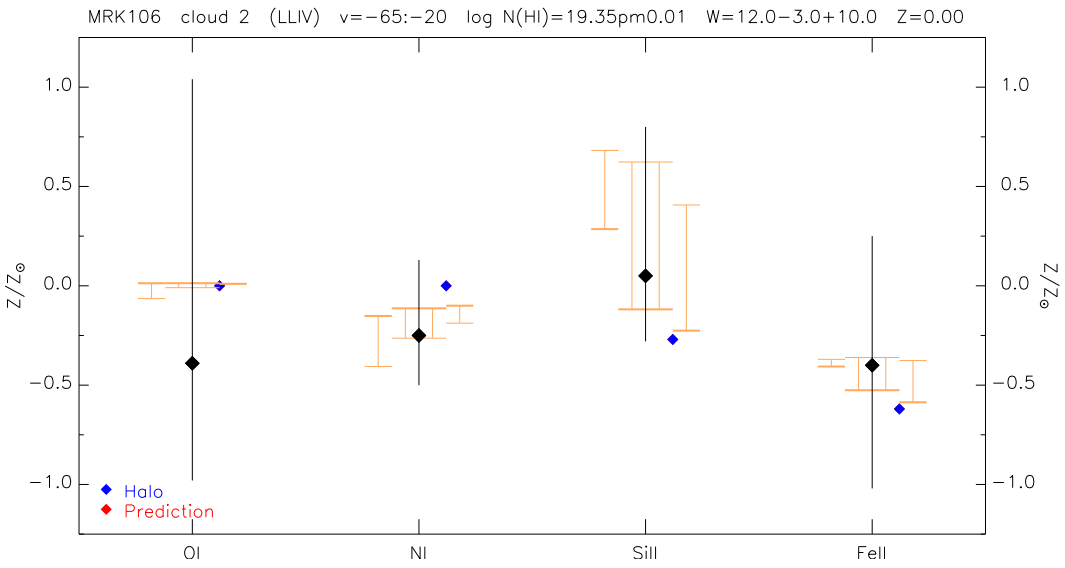

Figure 3.17 Abundance plot for the LLIV Arch extension toward Mrk 106 at -95 km s^{-1} $\leq v_{\rm LSR} \leq -75$ km s^{-1}. The range of possible ionization corrections is shown for 1, 2, and 5 kpc at densities between log $n = -3$ and -1, and for the extragalactic background (orange bars, left to right). The predicted Halo depletion pattern (log $Z = 0$) is indicated with blue points for each ion.

covering a larger range of wavelengths at higher S/N than available to us in the present dataset.

Finally, we see suggestions of absorption due to a previously undescribed, highly-ionized IVC at +30 km s^{-1} $\leq v_{\rm LSR} \leq$ +90 km s^{-1} in C III λ977, O VI λ1031, and H I λ923. An H I component centered at +70 km s^{-1} with FWHM = 20 km s^{-1} and N(H I) = 1×10^{17} cm^{-2}, or log N(H I) = 17.00, is required to adequately fit the red wing of the λ923 line (shown in Figure 3.14). This is not evident in other lines of H I, which as a rule are either too noisy or adversely impacted by residual geocoronal emission in the night-only spectra to fit. There is no 21 cm emission at these velocities in the

Effelsberg spectrum to a 5σ detection limit of N(H I) $= 1.38 \times 10^{18}$ cm^{-2}, or log N(H I) = 18.14, assuming a linewidth of 20 km s^{-1}. The limits imply N(H I) $= (7.4 \pm 6.4) \times 10^{17}$ cm^{-2}, or log N(H I) $= 17.87^{+0.27}_{-0.87}$, although we think the true value lies in the lower half of this range. We measure N(C III) $> 2.48 \times 10^{13}$, or log N(C III) > 13.39 in this velocity interval; however, we do not detect a sufficient number of ions from which to obtain a reliable metallicity estimate for this cloud.

To summarize, in the direction of Mrk 106 we see absorption from the AVI core of Complex A at $v_{\rm LSR} = -155$ km s^{-1}, for which we find a metallicity of $\sim 0.2\ Z_{\odot}$, and the LLIV Arch Extension at $v_{\rm LSR} = -42.5$, which has roughly solar metallicity. An unusually high Fe II abundance in the Complex A component may indicate a relative lack of dust and, therefore, particularly low depletion of refractory elements onto dust. Since few lines of undepleted species in either component are present in the available data, these metallicity estimates depend to various extents on ionization modeling and we caution that both are subject to rather large uncertainties. Lastly, while we see H I, C III, and O VI absorption from an apparent IVC at ~ 70 km s^{-1}, we are unable to estimate its metallicity.

3.4.5 Markarian 153

The sightline toward Markarian 153 is one of few falling near Complex M, which to date has little prior published abundance information. Gas at somewhat lower negative velocities is associated with material in the IV Arch,

while a cloud near +70 km s^{-1} known as IVC157+56+70 (Wakker 2006) offers an opportunity to improve on a single published metallicity measurement. Analysis of this sightline is complicated by limits in the wavelength coverage of the available data and exceptionally strong intrinsic H I absorption within Mrk 153 itself at +2565 km s^{-1}; in fact, the absorption from all sources is sufficiently strong that below Lyθ (λ923), the continuum level is essentially zero due to heavy saturation. Furthermore, contamination by H_2 both in the zero-velocity Galactic component as well as intrinsic absorption in IVC157+56+70 disqualifies many lines of available ions from our analysis. A representative sample of ions detected in our UV spectra toward Mrk 153 is shown in Figures 3.18-3.19.

Absorption seen in our dataset at -60 km s^{-1} $\leq v_{\rm LSR} \leq -25$ km s^{-1} appears to be associated with IV Arch gas, albeit not with any particular cloud core. We find no previous estimates of the metallicity of the IV Arch in the direction of Mrk 153 in the literature. This component is a strong 21 cm detection in the Effelsberg spectrum, exceeding the brightness temperature of the zero-velocity Galactic emission in this direction. We fit a single Gaussian to this component centered at $v_{\rm LSR} = -43$ km s^{-1} with FWHM = 25 km s^{-1} and N(H I) = $(3.63 \pm 0.14) \times 10^{19}$ cm^{-2}, or log N(H I) = 19.56 ± 0.02. We did not measure a sufficient number of lines of any given ion in this component to constrain the intrinsic linewidth from the COGs, so we adopted the H I FWHM. The resulting abundances are shown in Figure 3.20. In the absence of any O I or S II detections, we are left to estimate the metallicity of this cloud

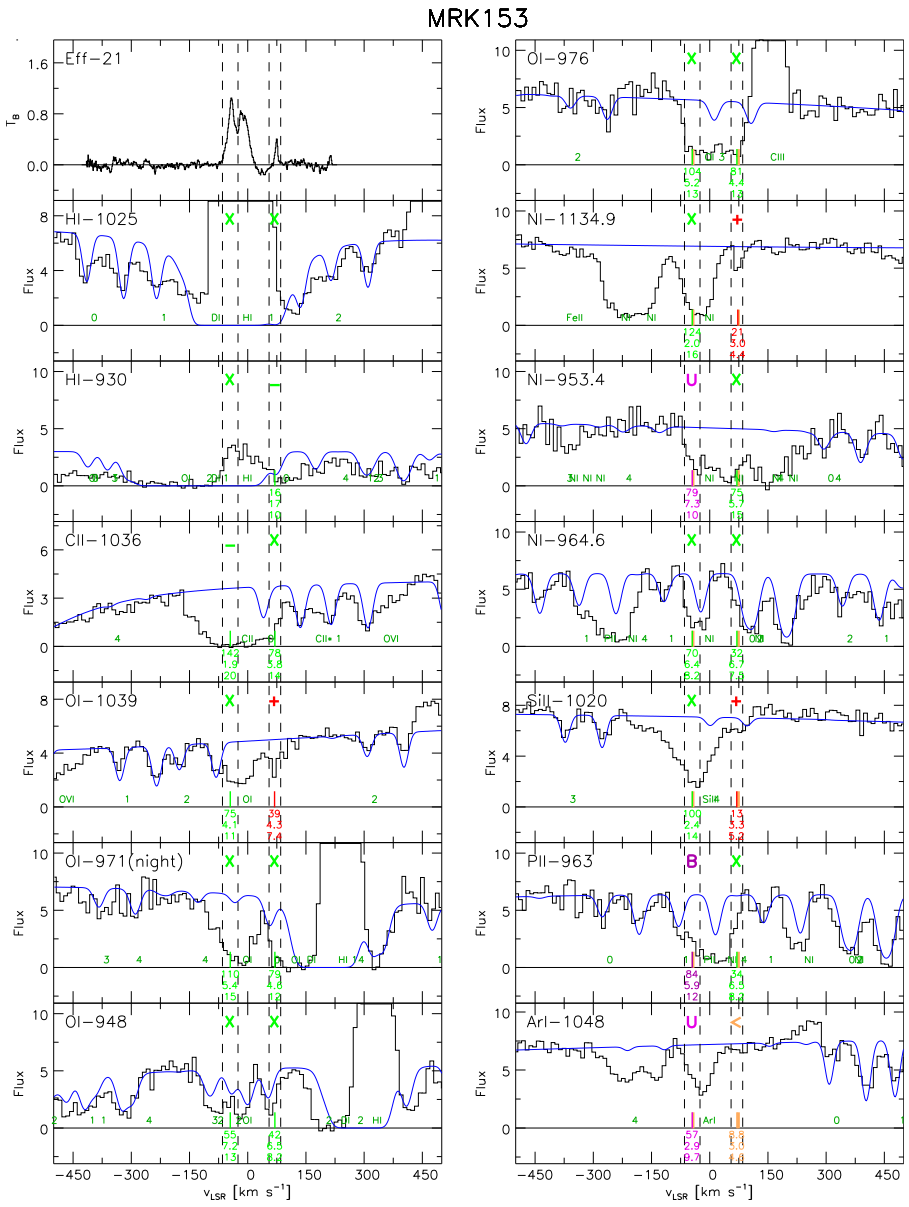

Figure 3.18 Cutouts of the Effelsberg 21 cm spectrum and selected UV spectra toward Mrk 153 highlighting ions and lines most relevant to the determination of the metallicity and depletion of each component. Continuum fits are indicated by blue lines, and alphanumeric symbols above the spectra indicate line quality judgments as described in Section 3.3.5. Ion names, ionization stages, and rest wavelengths in Å are shown at top-left in each panel, and each spectrum is plotted on an LSR velocity scale.

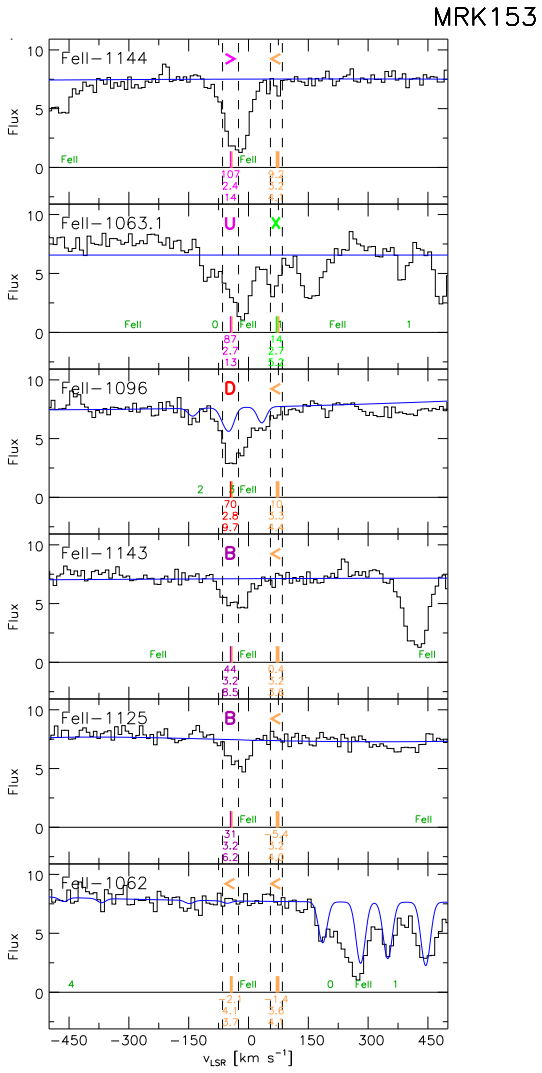

Figure 3.19 Cutouts of selected UV spectra toward Mrk 153 (continued).

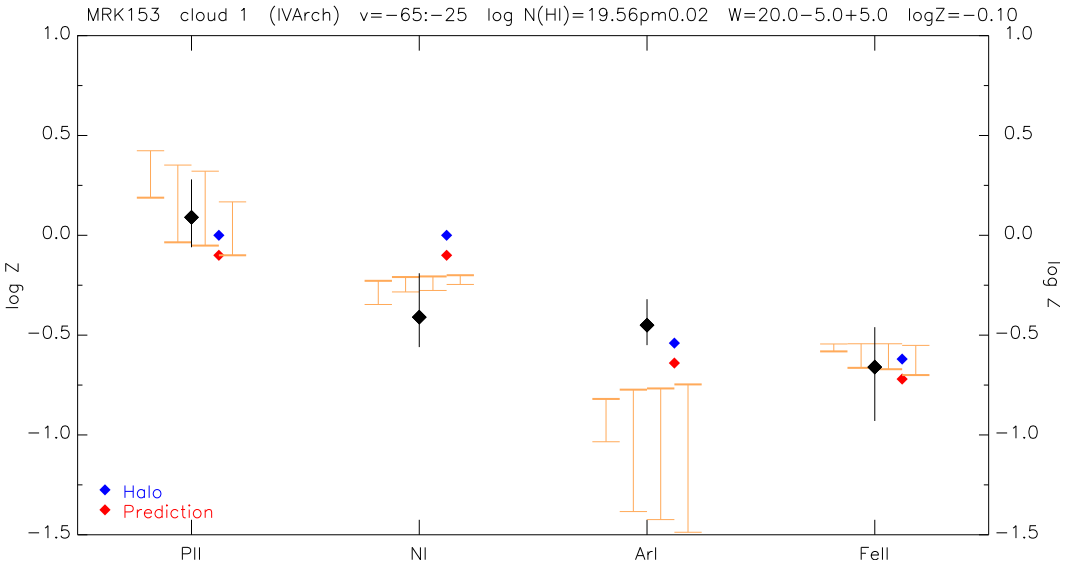

Figure 3.20 Abundance plot for the IV Arch toward Mrk 153 at -65 km s^{-1} $\leq v_{\rm LSR} \leq -25$ km s^{-1}. The range of possible ionization corrections is shown for 1, 2, and 5 kpc (log ϕ = 6.51, 5.51, and 5.34) at densities between log n = -3 and -1, and for the extragalactic background at log ϕ = 4.53 (orange bars, left to right). A Halo depletion pattern is indicated with blue points for each ion, and predicted abundances with red points given our metallicity of log $Z = -0.1$ inferred from ionization modeling.

from ionization models. We find that abundances of the detected species best fit the range of values predicted by the models at this N(H I) and the assumed distance to the IV Arch ($\sim$ 1 kpc) for a cloud metallicity of about log $Z = -0.1$ (0.8 $Z_{\odot}$). This near-solar value is compatible with our other measurements for the IV Arch (see Section 3.6.1), and from it we conclude a Galactic origin for the IV Arch gas.

Absorption seen near +70 km s^{-1} is related to an unusual object, IVC157+56+70, first described in *FUSE* data by Wakker (2006). He noted

that this feature is not detected in 21 cm emission in the 36′ beam of the LDS, but is seen weakly in the 9′ Effelsberg beam with N (H I) = 6.4 × 10^{18}, or log N(H I) = 18.81, at FWHM = 8.2 km s^{-1}. It has strong associated H_2 absorption, with log $N(H_2)$ = 16.14 at a comparable FWHM = 8.5 km s^{-1}; this H_2 component is stronger than the Galactic component (log $N(H_2)$ = 15.51). Wakker suggests that beam dilution may explain why the feature does not appear in the LDS 21 cm data, speculating that IVC157+56+70 may be either a "small cloud or even a circumstellar shell". This idea is supported by the observation that there is no other H I at similar velocities detected in any other direction in the vicinity of Mrk 153 on the sky, although IVC157+56+70 may be an outlier among compact H I clouds detected near +80 km $s^{-1} \leq v_{\rm LSR}$ ≤ +100 km s^{-1} at $\ell > 170°$, $b < 60°$ in the HVC catalog of Wakker & van Woerden (1991). Given the rather large column of H_2 indicated in the UV data to this object's velocity, Wakker argues that formation-dissociation equilibrium of H I/H_2 implies a cloud angular size < 3.′3 and a true N(H I) > 4.8 × 10^{19} cm^{-2}, or log N(H I) > 19.68. On the basis of detections of O I λ1039, N I λ1134.9, and Si II λ1020 and the constraints implied by his assumed N(H I) limit, Wakker concludes IVC157+56+70 probably has slightly subsolar metallicity and is > 1′ in angular size.

We see absorption due to this cloud at +55 km $s^{-1} \leq v_{\rm LSR} \leq$ +85 km s^{-1} in the same three lines as previously reported by Wakker. We independently estimate the H I column density by fitting a single Gaussian component to the Effelsberg spectrum centered at +74 km s^{-1} with FWHM = 7.5 km s^{-1}

and $N(\mathrm{H\ I}) = (5.8 \pm 0.7) \times 10^{18}$ cm^{-2}, or log $N(\mathrm{H\ I}) = 18.76^{+0.06}_{-0.05}$. There is no 21 cm data available to us at present obtained at a higher angular resolution; given the likely angular size of IVC157+56+70, we are unable to substantially improve on Wakker's 2006 estimate of $N(\mathrm{H\ I})$ and discuss below the ways in which his inferred constraints on the cloud's angular size affect the interpretation of our measured abundances. We do not detect a sufficient number of lines of any ionic species to provide a constraint on the intrinsic linewidth from the COGs. The measured FWHMs of individual detected ionic lines are ~ 15 km s^{-1}, about the same as the Nyquist-sampled resolution limit of *FUSE* (~ 20 km s^{-1}); therefore, these lines are unresolved and span only a single resolution element each as can be seen in Figure 3.18. The FWHM of the detected 21 cm emission associated with this cloud is about half this value. Wakker (2006) determined the width of the H_2 lines as 8.5 ± 1.5 km s^{-1}. Taking all this information together, we settled on a linewidth of 8.5 ± 0.5 km s^{-1} (Doppler $b = 5.1 \pm 0.3$), opting for a lower uncertainty than Wakker's H_2 measurement because (1) the linewidth is similar to that of H I, and (2) allowing a width as low as 7 km s^{-1} results in unreasonably large errors on the measured column densities. The resulting abundances are shown in Figure 3.21.

From the singular detection of O I λ1039, we find $[\mathrm{O\ I/H\ I}] = -0.48 \pm 0.30$ ($0.33^{+0.33}_{-0.17}\ Z_\odot$), but have some reservations concerning the reliability of this measurement. The line, shown in Figure 3.18, is detected with a significance of 4.7σ, but much of the signal consists of a downward spike in a single resolution element centered at $v_{\mathrm{LSR}} = +68$ km s^{-1}. This is surely indicative of an un-

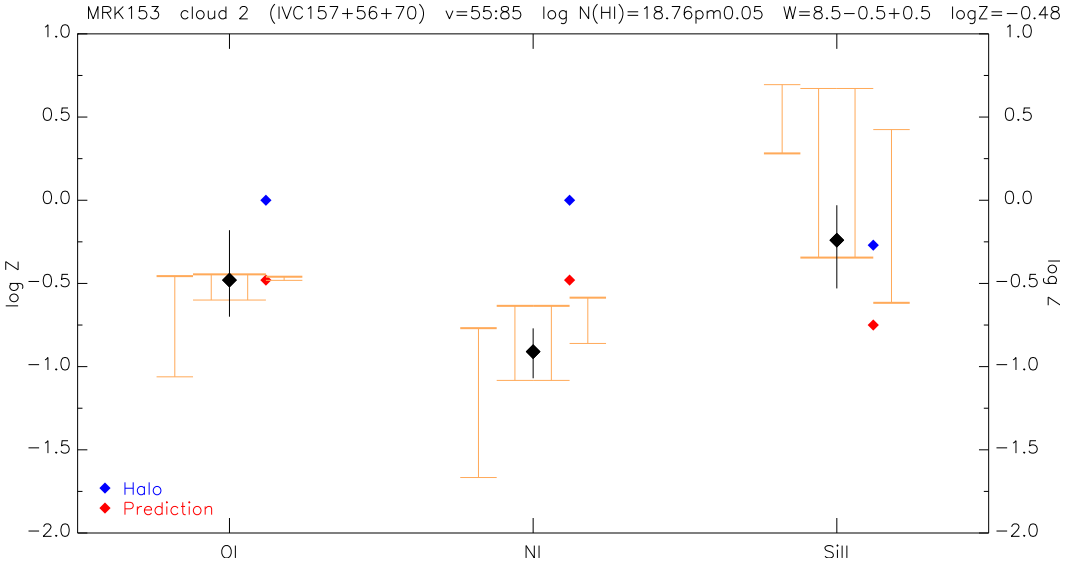

Figure 3.21 Abundance plot for IVC157+56+70 toward Mrk 153 at +55 km s^{-1} $\leq v_{\rm LSR} \leq$ +85 km s^{-1}. The range of possible ionization corrections is shown for 1, 10, and 20 kpc (log ϕ = 6.51, 5.51, and 5.51) at densities between log n = −3 and −1, and for the extragalactic background at log ϕ = 4.53 (orange bars, left to right). A Halo depletion pattern is indicated with blue points for each ion, and predicted abundances with red points given our measured metallicity [O I/H I] = −0.48.

resolved line given our adopted intrinsic linewidth. The measured equivalent width, 28.1 ± 3.4 ± 5.3 mÅ, is determined in part by the continuum placement, which in turn is influenced by the broad wings of the extremely strong intrinsic Lyβ line centered near λ1033.7. The apparent spike is probably an unresolved line, so the measured equivalent width of the line is likely an underestimate. Significant H_2 contamination affects the wavelengths of most other available O I lines in our spectra. λ1039 is the third intrinsically-strongest O I line in the range of available wavelengths; the next strongest, λ988.7, is adversely affected by geocoronal emission and mild contamination by the 1 − 0 $P(2)$

Werner band transition of H_2 at 989.086 Å. It appears improbably weak if we include it in the O I COG, even after H_2 decontamination. No data exist for the strongest O I line, λ1302. While we claim λ1039 as a confident detection, we concede the evidence that the line is spectrally unresolved is convincing enough that we should treat the measured equivalent width – and thus the resulting metallicity – as a lower limit. This conclusion is supported by the N I abundance inferred from the λ1134.9 line equivalent width, which is somewhat higher relative to O I than we see in sightlines through other IVCs. We find the typical [N I/O I] for IVCs in our sample is around -0.3; if this is true of IVC157+56+70, the O I abundance would be closer to -0.61 (0.25 $Z_\odot$). At this lower metallicity, our ionization models for the Si II abundance appear to rule out a z-height of < 1 kpc. The Mrk 153 sightline is at a particularly high Galactic latitude ($b = 56°$), so its distance $D \sim z$. Assuming the revised metallicity suggested by the typical [N I/O I] we see for other IVCs and the constraints on the angular size of the H I-emitting region of IVC157+56+70 given in Wakker (2006), its implied diameter is only $\sim$1 pc, placing it among the smallest IVCs. On the other hand, perhaps [N I/O I] for this cloud is the actual measured value of -0.43 and N I is in fact more underabundant relative to O I than otherwise assumed. An optimistic estimate of its metallicity is still considerably lower than that of other IVCs thought to participate in the Galactic Fountain, so some other process must account for such small, relatively metal-poor clouds.

Finally, as noted before, the Mrk 153 sightline passes near Complex M.

We searched near the expected $v_{\rm LSR} \sim -85$ km s^{-1}, finding some indication of absorption in O I λ and Fe II λ1144, but we felt these features were not sufficiently convincing to warrant an abundance analysis. There appears to be no matching 21 cm emission feature in the Effelsberg spectrum from which to directly obtain an estimate of N(H I); assuming a 20 km s^{-1}-wide line, we find a 5σupper limit of N(H I) $< 9.5 \times 10^{17}$, or log N(H I) < 17.98. However, we note a feature centered at $v_{\rm LSR} = -85$ km s^{-1} with FWHM = 25 km s^{-1} and N(H I) = $(2 \pm 0.5) \times 10^{18}$ cm^{-2}, or log N(H I) = $18.30^{+0.10}_{-0.12}$, is required to adequately fit the Lyman series H I line profiles. While the H I feature may be attributable to absorption by Complex M, we find inadequate absorption in other ionic lines from which to make a robust metallicity estimate.

In summary, we see absorption in the Mrk 153 sightline from IV Arch gas at $v_{\rm LSR} = -45$ km s^{-1} with $Z \sim 0.8\ Z_{\odot}$, consistent with a Disk origin for this cloud. We also measure abundances for the compact cloud IVC157+56+70 at $v_{\rm LSR} = +70$ km s^{-1}, for which we find $Z \sim 0.25\ Z_{\odot}$. Our result, combined with the Wakker (2006) limit on the angular size of this cloud, suggests that it is among the smallest known IVCs with a diameter $\sim$ 1 pc. Given its low metallicity, we do not believe this cloud originates in the Fountain, but rather by way of some other, unidentified process. Finally, while we note possible absorption due to Complex M at $v_{\rm LSR} \sim -85$ km s^{-1}, we are unable to measure abundances and therefore do not quote a metallicity for this gas.

3.4.6 Markarian 205

A small but detectable column of H I exists in this direction associated with the low-latitude side of Complex C, to which we refer hereafter as "C-South". At more negative velocities, this sightline passes through the compact HVC WW84, also known as CHVC 125+41-207. At the least negative velocities, the observed absorption is attributed to the LLIV Arch. The line of sight toward Mrk 205 also passes near (impact parameter 4.3 kpc) the galaxy NGC 4319, from which we see H I Lyman series absorption at $\simeq +1300$ km s^{-1} as well as H_2 absorption (Wakker 2006). The *FUSE* spectrum of Mrk 205 was taken in 2003 for the purpose of studying the absorption associated with NGC 4319; it also contained information about the metallicity of WW84, but these data were not yet analyzed. The spectrum has a high background and thus the flux calibration is somewhat less reliable than that of other spectra considered in this study, but the central part of saturated lines are near zero flux as expected. A representative sample of ions detected in our UV spectra is shown in Figures 3.22-3.23.

WW84 is a typical example of the compact HVC (CHVC) class of objects. 21 cm H I emission maps (Braun & Burton 2000, Brüns et al. 2001) show a characteristic "head-tail" morphology that gives this object a "cometary" appearance. Burton et al. (2004) argue that the cold core/warm halo structure of this cloud, the (well-constrained) low kinetic temperature of its shielded interior, and its small angular size imply it is at extragalactic distances. They estimate its distance at $210 \leq D \leq 1100$ kpc. Brüns et al. (2001) estimated a

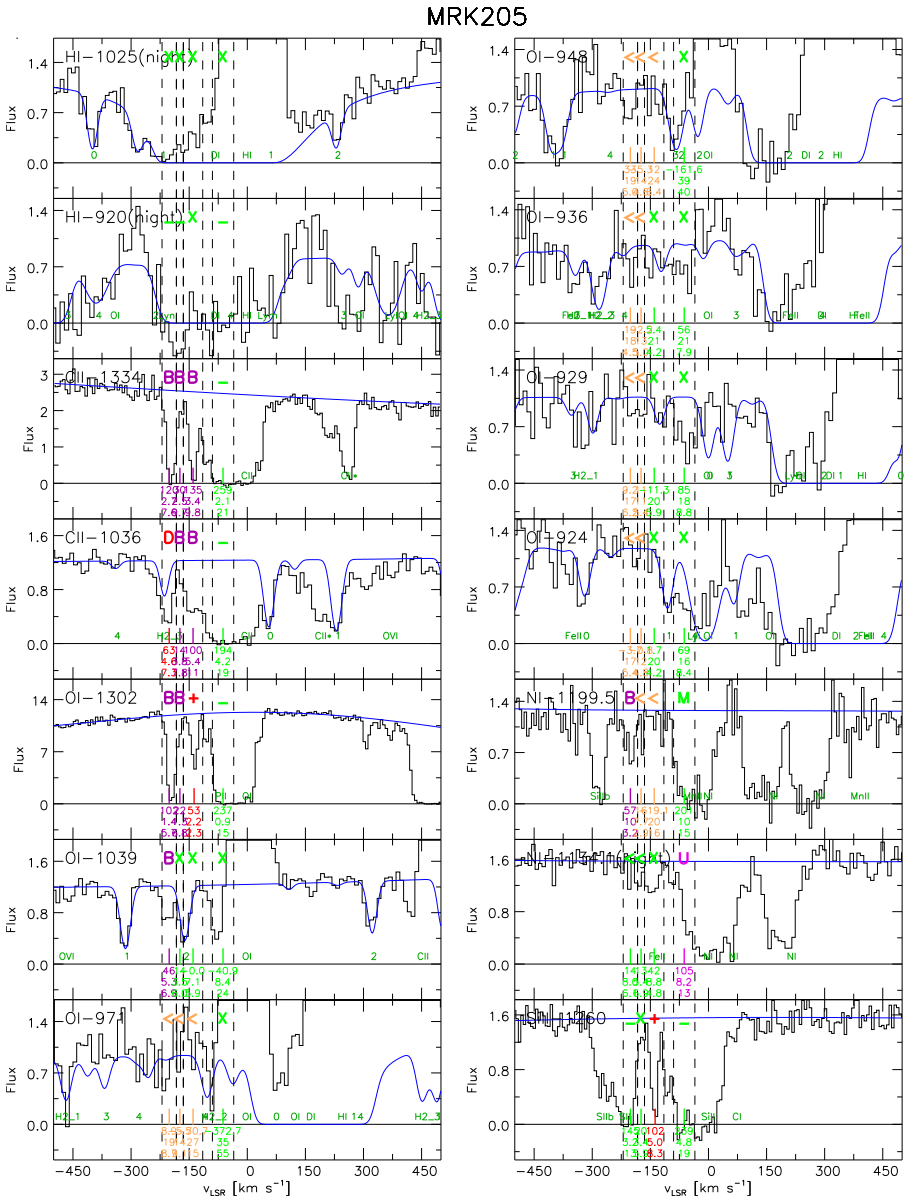

Figure 3.22 Cutouts of the GBT 21 cm spectrum and selected UV spectra toward Markarian 205 highlighting ions and lines most relevant to the determination of the metallicity and depletion of each component.

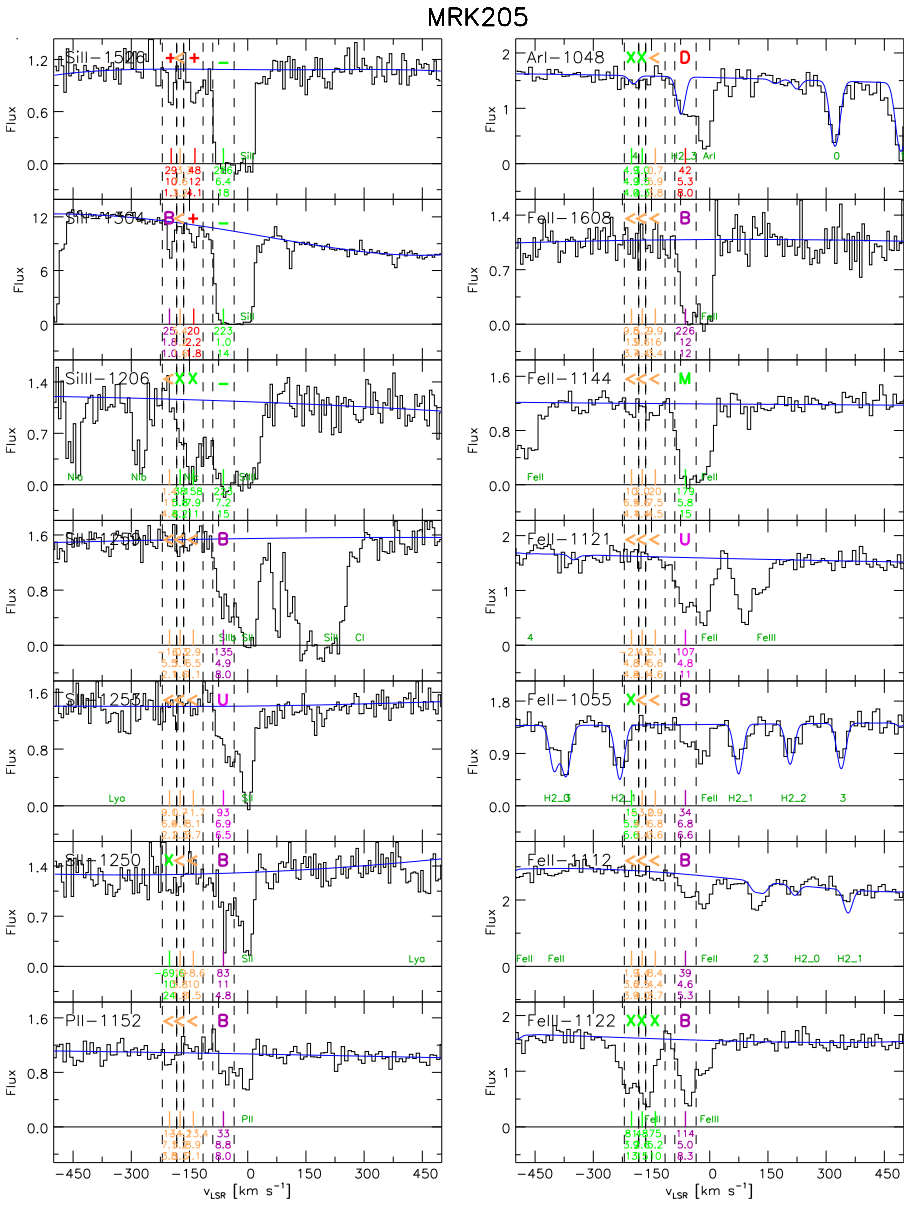

Figure 3.23 Cutouts of selected UV spectra toward Mrk 205 (continued).

slightly lower distance of ~ 130 kpc, placing it perhaps in the outer reaches of the Halo; they interpret the head-tail structure as indicative of an interaction between the HVC and lower-velocity Halo gas. Most authors who studied this sightline previously defined a single WW84 component spanning -225 km s^{-1} $\lesssim v_{\rm LSR} \lesssim -170$ km s^{-1}. Brüns et al. (2001) decomposed the WW84 component in their Effelsberg spectra into two pieces consisting of a narrow, tall peak at $v_{\rm LSR} \sim -209$ km s^{-1} and a shorter, wide peak at $v_{\rm LSR} \sim -206$ km s^{-1} at Doppler temperatures of $T_D = 540$ K and 7000 K, respectively. They argue that they are in the process of separating from each other physically, and the warmer gas represents the more turbulent margins of the cloud where material is being stripped away via a ram-pressure interaction. Gas in the direction of Mrk 205 samples an intermediate position between the cold, high-column-density core and the warmer, more tenuous outer layers. We also split the WW84 absorption toward Mrk 205 into two parts based on the shape of the UV line profiles. The components were labeled WW84a (-220 km s^{-1} $\leq v_{\rm LSR} \leq -183$ km s^{-1}) and WW84b (-183 km s^{-1} $\leq v_{\rm LSR} \leq -165$ km s^{-1}). The division is most readily visible in the plots of O I λ1302, C II λ1334, and Si III λ1260 in Figures 3.22 and 3.23.

Comparison of our abundances with those of other authors is complicated by the fact that they typically integrate over both these components and report results for WW84 taken as a whole. For example, Bowen & Blades (1993) made a detailed study of the Mrk 205 sightline with the pre-COSTAR GHRS aboard *HST* measuring N(Mg II) $= 7 \times 10^{-12}$ cm^{-2}, or log N(Mg II)

= 12.85. They give [Mg II/H I] = -2.0 ± 0.1, assuming the Morton (1991) value for $[\mathrm{Mg/H}]_\odot$ = -4.41. They did not specify the velocity range over which they measured N(Mg II), so we assume they included absorption from both of our WW84 components. On the other hand, Shull et al. (2009) measured absorption by several ionization stages of Si along this sightline in the range -225 km s^{-1} $\leq v_{\rm LSR} \leq -175$ km s^{-1}, corresponding closely to our WW84a, finding [Si/H] = -2.50 and -1.91 for ionization parameters log $U = -3.15$ and -3.05, respectively. Citing the Mg II detection in WW84 toward Mrk 205 in Bowen et al. (1991b,a) and using an estimate of N(H I) = $(8 \pm 5) \times 10^{18}$ cm^{-2}, or log N(H I) = $18.90^{+0.21}_{-0.43}$, Wakker (2001a) reports [Mg II/H I] = $-1.70^{+0.23}_{-0.52}$ (0.020 ± 0.014 $Z_\odot$). However, the N(H I) measurement was presumed unreliable due to small-scale structure not resolved in the Effelsberg beam. Using our total N(H I) for both WW84 components, described below, we obtain [Mg II/H I] = < -2.04 (< 0.009 $Z_\odot$) from the Bowen et al. measurement of N(Mg II). While we note this result in order to highlight the Mg II detection, the abundance does not reflect a reliable metallicity because the degree to which this ion is susceptible to depletion is not well known.

WW84a is very centrally condensed; the $9'$ Effelsberg beam centered on Mrk 205 picks up some bright emission from the cloud center (Wakker 2001a). We fit two Gaussian components to the GBT spectrum to adequately reproduce the observed profile asymmetry with a wider red wing than blue wing. The Gaussians were centered at -203 and -200 km s^{-1} with FWHMs of 6 and 20 km s^{-1}, respectively, and a total N(H I) = $(1.62 \pm 0.10) \times 10^{19}$ cm^{-2}

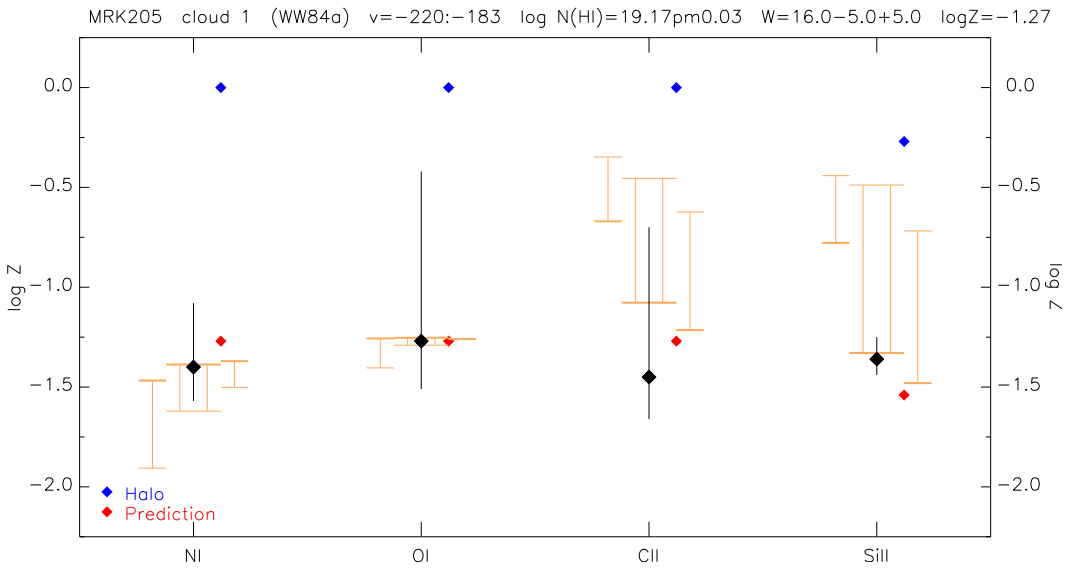

Figure 3.24 Abundance plot for WW84a toward Mrk 205 at -220 km s^{-1} $\leq v_{\rm LSR} \leq -183$ km s^{-1}. The range of possible ionization corrections is shown for 1, 10, and 50 kpc (log $\phi = 6.66$, 5.51, and 5.51) at densities between log $n = -3$ and -1, and for the extragalactic background at log $\phi = 4.53$ (orange bars, left to right). A Halo depletion pattern is indicated with blue points for each ion, and predicted abundances with red points given our measured metallicity [O I/H I] $= -1.27$.

or log N(H I) $= 19.17^{+0.03}_{-0.04}$. We did not detect enough lines of any particular ion in either WW84 component with which to constrain the intrinsic linewidth in the COGs, so we adopted the H I values of +16 km s^{-1} and +15 km s^{-1} for W84a and WW84b, respectively. An abundance plot of the detected ions in WW84a is shown in Figure 3.24. Excluding N I, the only undepleted ion we detect is O I, for which we obtain [O I/H I] $= -1.27 \pm 0.85$ ($0.05^{+0.33}_{-0.05}$ $Z_{\odot}$).

WW84b appears as a red "shoulder" on the line profiles of WW84a. We fit a single Gaussian to the 21 cm spectrum with N(H I) $= (1.0 \pm 0.7)$ $\times 10^{18}$

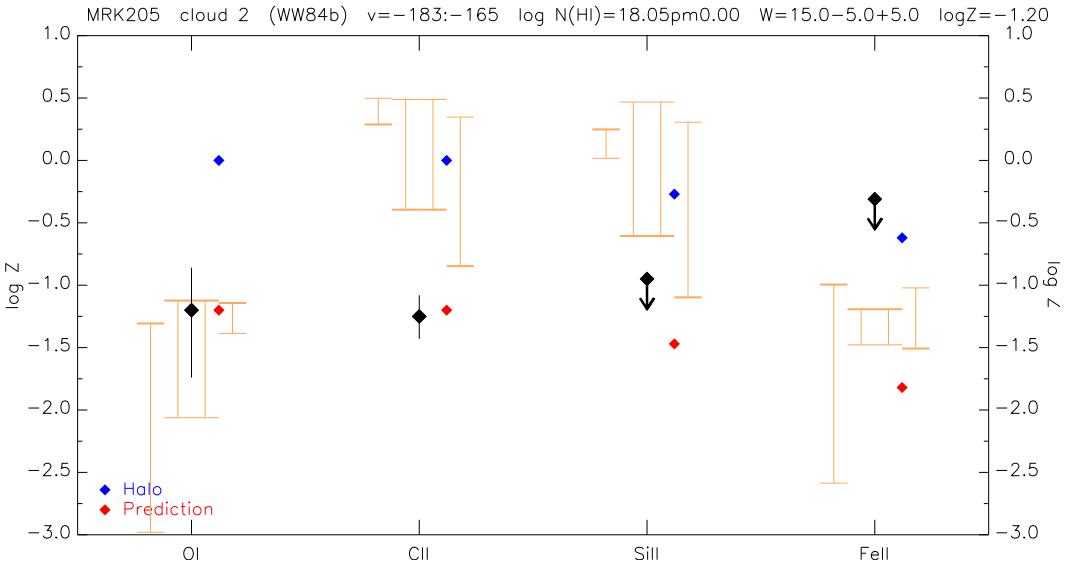

Figure 3.25 Abundance plot for WW84a toward Mrk 205 at -160 km s^{-1} $\leq$ $v_{\rm LSR}$ ≤ -105 km s^{-1}. The plot parameters are the same as in Figure 3.24 but for our metallicity [O I/H I] $= -1.20$.

cm^{-2}, or log N(H I) $= 18.00^{+0.23}_{-0.52}$. Excluding N I, the only undepleted ion we detect is O I, for which we measure [O I/H I] $= -1.20 \pm 0.34$ ($0.06^{+0.08}_{-0.03}$ $Z_{\odot}$). The abundance plot is shown in Figure 3.25. The metallicities we derive for the two WW84 components are broadly consistent with earlier measurements and somewhat below expected values for low-metallicity HVC gas (~ 0.1 $Z_{\odot}$). Together, they represent the lowest metallicities ever measured for an HVC. All indications – morphology/ structure, ionization, and metallicity – point toward WW84 being a distant ($D > 50$ kpc), low-metallicity cloud. Adopting the Brüns et al. (2001) formula for the H I mass of WW84, M(H I) $= 2.4\times10^{6}$ $(D/200$ kpc$)^2$ $M_{\odot}$, we find a lower mass limit of 1.5×10^{5} $M_{\odot}$ for this cloud.

We detect absorption at velocities consistent with Complex C in the

interval -165 km s^{-1} $\leq v_{\rm LSR} \leq -115$ km s^{-1} on the low-latitude side of Complex C. Bowen & Blades (1993) detected this component in Mg II and derived [Mg II/H I] $= +0.4 \pm 0.5$. Most authors have since adopted the value Wakker et al. (2003) claimed for N(H I) $= (1.3 \pm 0.3)$ $\times 10^{18}$ cm^{-2}, or log N(H I) $= 18.11^{+0.09}_{-0.11}$. Lehner et al. (2004) measured [S II/H I] < -0.51 at $v_{\rm LSR}$ $= -120$ km s^{-1}, but apparently misattribute the component in their text as "WW84" when in fact it must be Complex C according to the given velocity. Collins et al. (2007) report measurements of several ions in this component, and assume the Wakker et al. (2003) value of N(H I) to arrive at [O I/H I] $= -0.78^{+0.12}_{-0.13}$ ($0.17^{+0.05}_{-0.04}$ $Z_{\odot}$). We do not confidently discern a component in the 21 cm spectrum corresponding to the lines in our UV spectra and derive only a 5σ upper limit of N(H I) $< 6.8 \times 10^{17}$ cm^{-2}, or log N (H I) < 17.83. Fitting the observed absorption in the Lyman series H I lines suggests a lower limit of N(H I) $> 3 \times 10^{17}$ cm^{-2}, or log N(H I) > 17.48. The upper limit for N(H I) sets a limit for the undepleted metallicity of [O I/H I] > -0.5, well above the expectation for Complex C of log $Z \sim -0.8$ (0.16 $Z_{\odot}$). Furthermore, the derived column densities imply a supersolar log (Si II/O I) ratio of -0.76, higher than we would expect after ionization corrections. These circumstances argue in favor of a higher value of N(H I), which would have the effect of lowering the ionization corrections for, e.g., Si II and Al II. We adopted a value of N(H I) $= (1.0 \pm 0.7)$ $\times 10^{18}$ cm^{-2}, or log N(H I) $= 18.00^{+0.23}_{-0.52}$, with the caveats that (1) it is more in line with both our expectations and previous measurements, and (2) the data do not allow us to

make a more robust estimate. The implied value of [O I/H I], -0.67 ± 0.27 ($0.21^{+0.21}_{-0.09}$ $Z_{\odot}$), is still higher than our expectations for Complex C but it is the best estimate we can make given the uncertain nature of the H I column density. The resulting abundance pattern is shown in Figure 3.26.

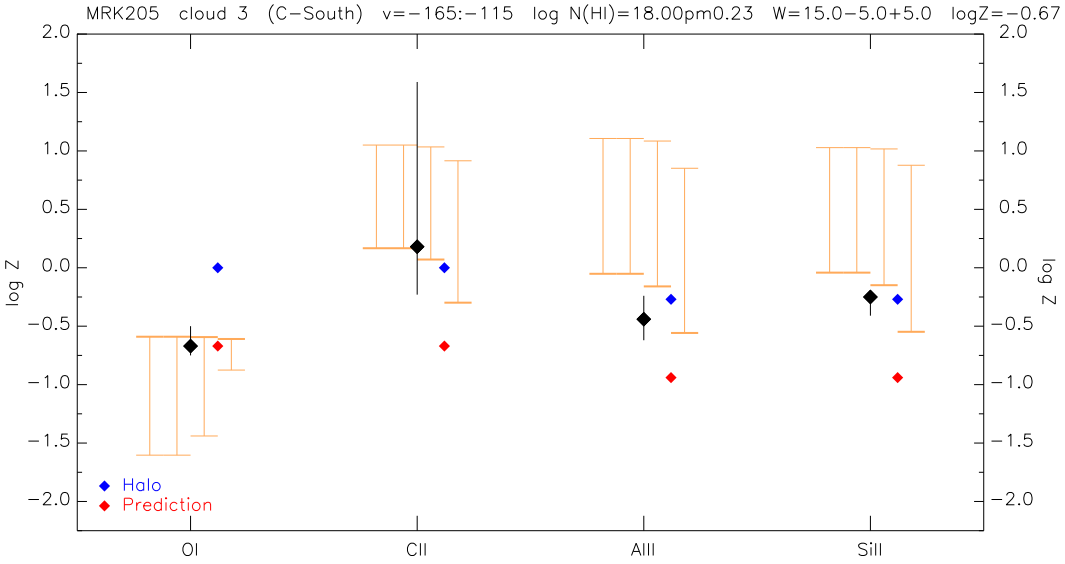

Figure 3.26 Abundance plot for C-South toward Mrk 205 at -160 km s^{-1} $\leq$ $v_{\rm LSR} \leq -105$ km s^{-1}. The range of possible ionization corrections is shown for 5, 10, and 20 kpc (log ϕ = 5.51, 5.51, and 5.34) at densities between log n = -3 and -1, and for the extragalactic background at log ϕ = 4.53 (orange bars, left to right). A Halo depletion pattern is indicated with blue points for each ion, and predicted abundances with red points given our measured metallicity [O I/H I] = -0.67.

Finally in this sightline we see absorption due to the LLIV Arch at -90 km s^{-1} $\leq$ $v_{\rm LSR}$ $\leq$ -35 km s^{-1}. Lehner et al. (2004) measured C II* and S II absorption in this component at a centroid velocity of $v_{\rm LSR} = -48$ km s^{-1}, finding [S II/H I] = $+0.39^{+0.27}_{-0.19}$ ($2.45^{+2.12}_{-0.87}$ $Z_{\odot}$). We fit a single Gaussian to the

21 cm spectrum with N(H I) = $(3.77 \pm 0.01) \times 10^{19}$ cm^{-2}, or log N(H I) = 19.58 ± 0.01. O I was too strongly blended with the Galactic absorption to cleanly measure in any of our detected lines, so we estimated the metallicity from [S II/H I] = $+0.41 \pm 0.33$ ($2.57^{+2.93}_{-1.37}$ $Z_\odot$). We also see C II* absorption with log N(C II*) = $13.79^{+0.10}_{-0.15}$, which may be compared with the Lehner et al. value of $13.80^{+0.19}_{-0.12}$. Abundances are shown in Figure 3.27 assuming our S II metallicity for the cloud. It compares well with the Lehner et al. result, but the supersolar metallicity is surprising even for the metal enhancement we expect for material participating in the Galactic Fountain. We conclude that the clump of LLIV material sampled by the Mrk 205 sightline must be sufficiently condensed such that the GBT beam underestimates N(H I). In the LAB map, there is no clear indication that this cloud is in a direction with sufficient small-scale structure to account for a factor of two difference in N(H I), but we cannot rule out this possibility in accounting for the measured abundances. While a supersolar metallicity still seems likely, the true value is probably somewhat less than what we report here. In any case, it is certainly compatible with the conclusion that this is a Fountain cloud, enriched in metals from relatively recent star formation.

In summary, along the line of sight toward Mrk 205 we see ~ 0.05 $Z_\odot$ gas associated with the compact HVC known as WW84, placing its metallicity a factor of 1.1-2.5 below that of average interstellar gas, as well as below values typically found in low-metallicity HVCs. Its metallicity is the lowest ever measured in an HVC. A distance constraint of $D > 50$ kpc is obtained

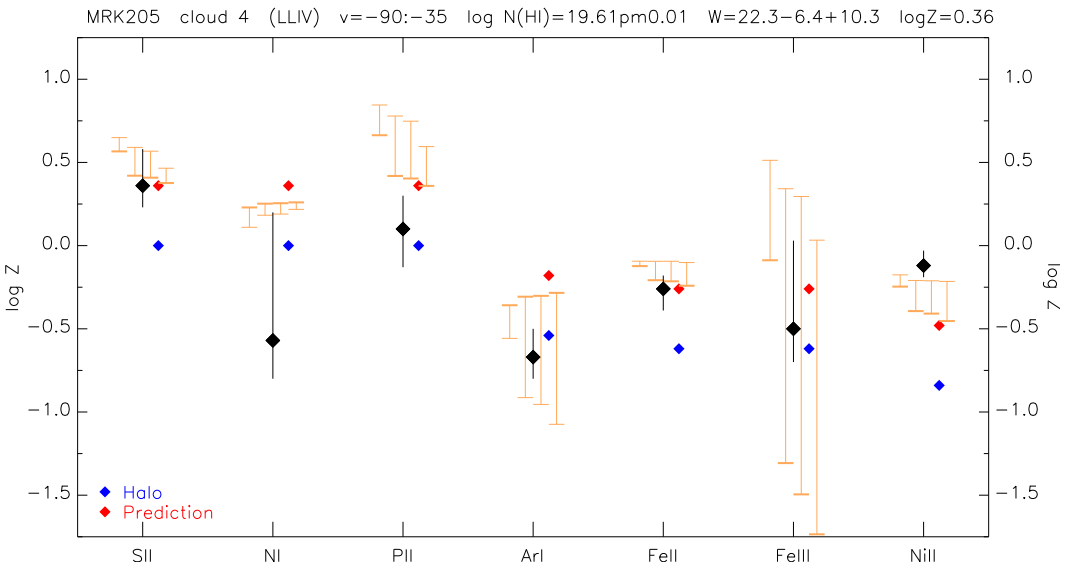

Figure 3.27 Abundance plot for the LLIV Arch toward Mrk 205 at −160 km s^{-1} $\leq v_{\rm LSR} \leq$ −105 km s^{-1}. The range of possible ionization corrections is shown for 1,2, and 5 kpc (log $\phi = 6.66$, 5.51, and 5.34) at densities between log $n = -3$ and −1 and for the extragalactic background at log $\phi = 4.53$ (orange bars, left to right). A Halo depletion pattern is indicated with blue points for each ion, and predicted abundances with red points given our metallicity [S II/H I] = +0.36.

by ionization modeling; from this distance and the H I map of Brüns et al. (2001), we compute a lower cloud mass limit of $M \geq 1.5 \times 10^5\ M_\odot$. The low-latitude side of Complex C ("C-South") is sampled near −140 km s^{-1}, giving $Z \sim 0.2\ Z_\odot$, somewhat higher than observed along other Complex C sightlines but dependent on the exact value of N(H I) used to compute the metallicity. At the lowest negative velocities, we detect absorption due to the LLIV Arch at $Z \sim 2.3\ Z_\odot$, but caution that this result is sensitive to possible unresolved structure in the 21 cm data used to derive N(H I).

3.4.7 Markarian 279

The data for this sightline are among those with the highest S/N ratio in our sample. Collins et al. (2007) note that the UV continuum flux in the quasar varies over time, decreasing by a factor of five over 1999-2002. The Effelsberg 21 cm spectrum in this direction is very complicated, having two high-velocity and two intermediate-velocity and at least five low-velocity components; there is an additional high- velocity component (labeled "C1", below) seen in absorption in the UV that does not have a corresponding 21 cm emission feature. Unresolved structure in the 21 cm spectrum at small angular scales drives the uncertainty in our measurements, and systematic errors on the resulting abundances are therefore higher than those of other sightlines with less complicated 21 cm structure. We describe below how we handled deriving N(H I) values in difficult cases. A representative sample of ions detected in our UV spectra is shown in Figures 3.28-3.30.

The two highest negative velocity components (-210 km s^{-1} $\leq v_{\rm LSR}$ ≤ -165 km s^{-1}, "C1"; -165 km s^{-1} $\leq v_{\rm LSR} \leq -120$ km s^{-1}, "C2") are identified with Complex C cloud CIII and C-South, respectively. There is a large variation in the widths of velocity windows other authors have used to measure absorption in these components. Collins et al. (2007) chose a wide window (-220 km s^{-1} $\lesssim v_{\rm LSR} \lesssim -115$ km s^{-1}) encompassing both C1 and C2, noting that their data suggest the velocity width of high ion absorption is larger than that of the low ions, but we do not see this effect. Others extend the positive-velocity limit of their C2 windows to -90 km s^{-1} in an effort to

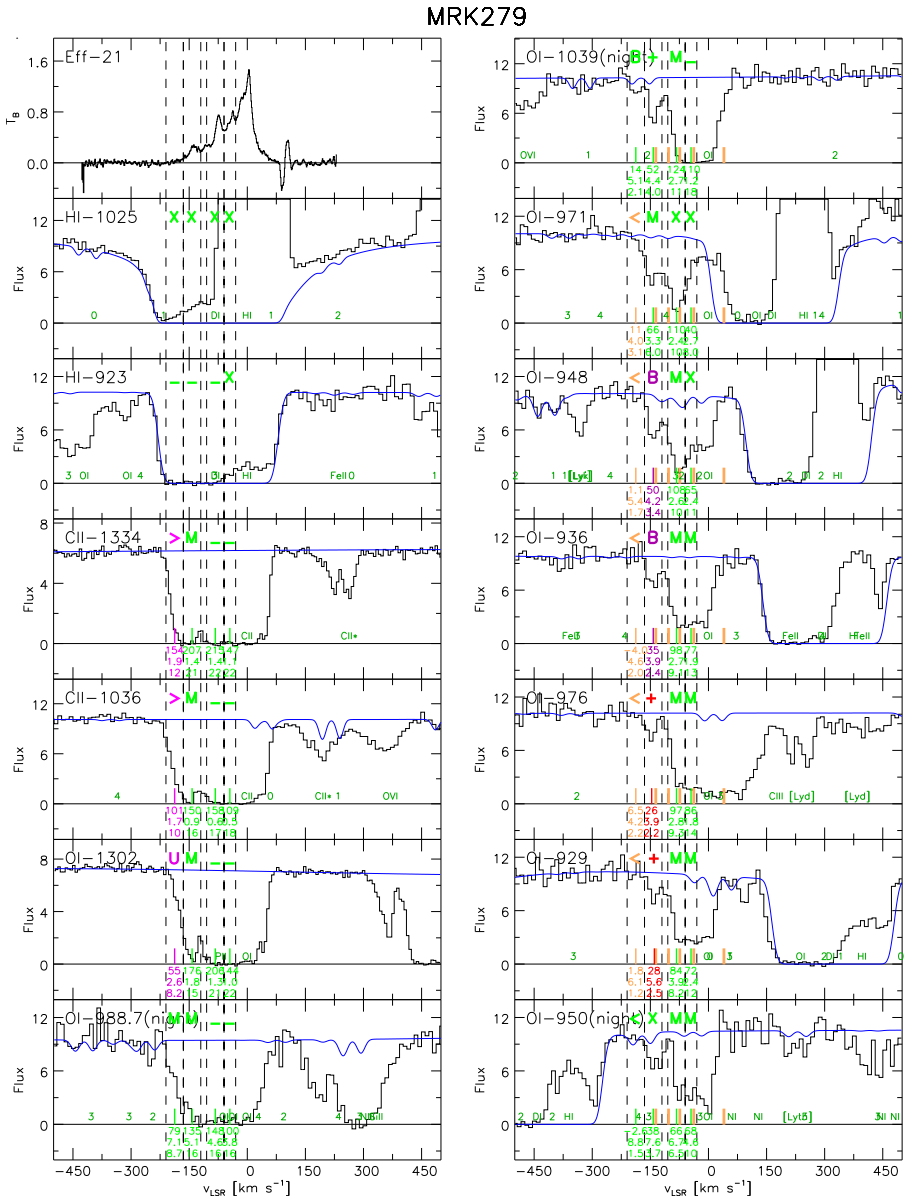

Figure 3.28 Cutouts of the Effelsberg 21 cm spectrum and selected UV spectra toward Mrk 279 highlighting ions and lines most relevant to the determination of the metallicity and depletion of each component.

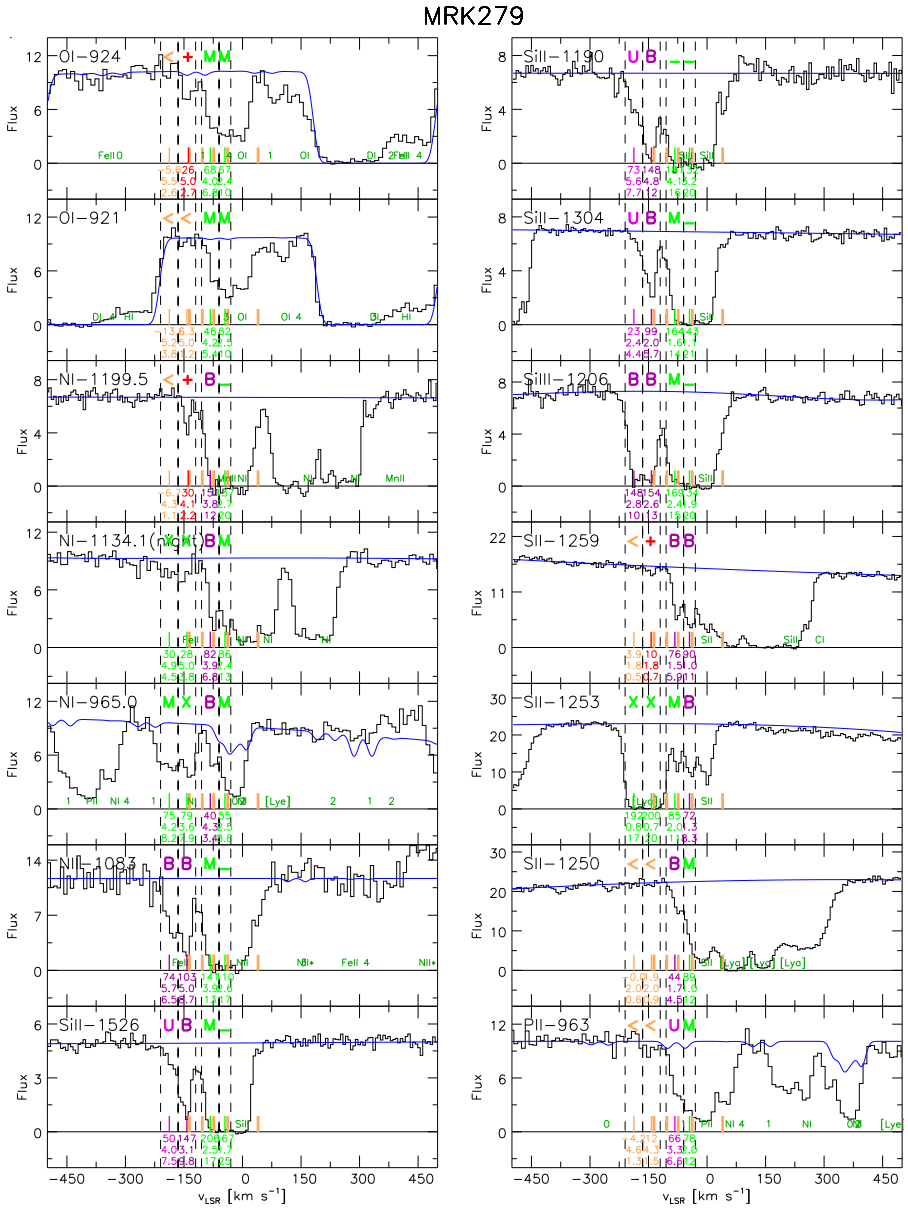

Figure 3.29 Cutouts of selected UV spectra toward Mrk 279 (continued).

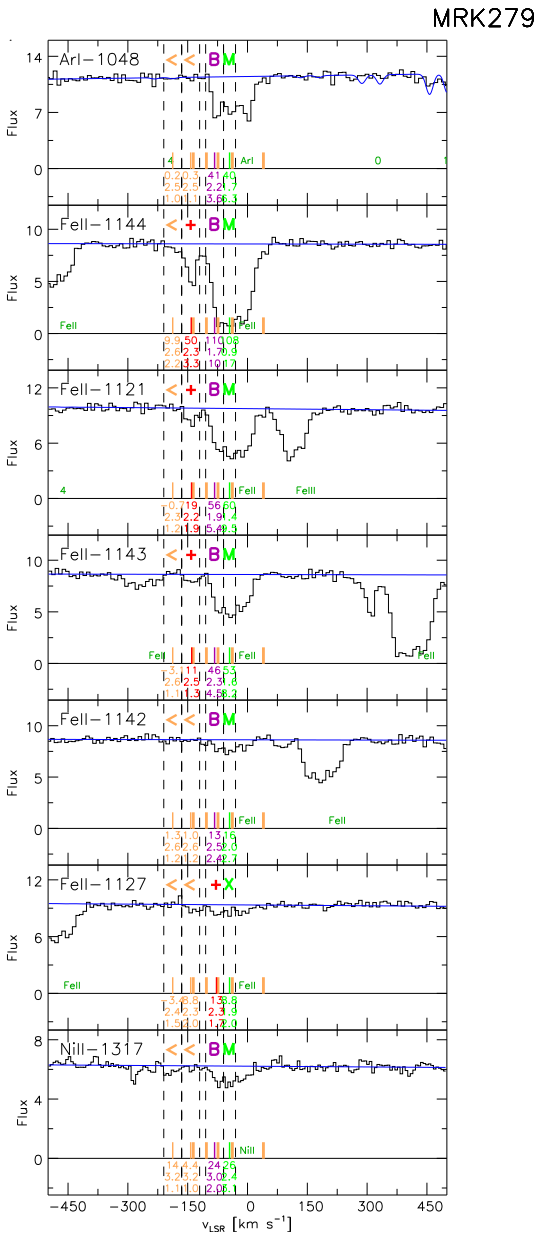

Figure 3.30 Cutouts of selected UV spectra toward Mrk 279 (continued).

preserve as much Complex C absorption in this sightline as possible (Gibson et al. 2001, Collins et al. 2003), although as we discuss below, this velocity limit probably includes intermediate-velocity gas in the Upper IV Arch. We treat absorption in this gas distinctly from the Complex C components, while acknowledging there is some contamination of the measured abundances by Complex C gas as a result.

C1 is not a formal detection in 21 cm emission, in the sense that non-zero flux falls within its velocity window but the low amplitude and strongly asymmetric nature of the flux profile indicate that it is probably contamination from the wing of C2. From the noise in the 21 cm spectrum, we find a 5σ upper limit of $N(\mathrm{H\ I}) \leq 4 \times 10^{18}$ cm^{-2}, or log $N(\mathrm{H\ I}) \leq 18.60$. An additional constraint is provided by the blue wing of the H I absorption in the Lyman series. We estimated the centroid (-180 km s^{-1}) and FWHM (35 km s^{-1}) of this component from metal-line absorption in the UV spectra and used them to fit a model of H I absorption to the wing, adjusting $N(\mathrm{H\ I})$ as a free parameter. This approach sets a lower limit of $N(\mathrm{H\ I}) \geq 8 \times 10^{17}$ cm^{-2}, or log $N(\mathrm{H\ I}) \geq 17.90$. The mean and uncertainty are therefore $N(\mathrm{H\ I}) = 2^{+2}_{-1} \times 10^{18}$ cm^{-2}, or log $N(\mathrm{H\ I})$ 18.30 ± 0.30. The mean implies that the Lyman series absorption is compatible with this cloud having a metallicity log $Z = -0.8$ ($0.16\ Z_{\odot}$), comparable to the expected metallicity of Complex C, but it is neither consistent with log $Z < -1.3$ ($0.05\ Z_{\odot}$) if $N(\mathrm{H\ I}) = 4 \times 10^{18}$ cm^{-2} nor log $Z > -0.4$ ($0.40\ Z_{\odot}$) if $N(\mathrm{H\ I}) = 8 \times 10^{17}$ cm^{-2}. While $N(\mathrm{H\ I})$ and the FWHM are degenerate in the determination of both limits, we are nevertheless

confident that N(H I) lies within the interval they define. On the other hand, C2 is detected in the 21 cm spectra, to which we fit a single Gaussian at -136 km s^{-1} with N(H I) $= (1.9^{+0.23}_{-0.21}) \times 10^{19}$ cm^{-2}, or log N(H I) $= 19.3 \pm 0.1$.

Our column densities for most detected ions are within the errors of those published previously. Discrepancies between our values and those of other authors generally follow the pattern that our column densities are lower than published values and the differences are attributable to mismatched velocity limits. An exception is S II in C2, whose basis is a 5σ detection of the λ1259 line in the *FUSE* spectrum. From this detection we measure log N(Si II) $= 13.68^{+0.10}_{-0.08}$. Gibson et al. (2001) claimed a 4σ detection of the λ1250 line in *HST* GHRS G160M data toward Mrk 279, giving log N(Si II) $= 14.40 \pm 0.41$ over the velocity interval -180 km s^{-1} $\leq v_{\rm LSR} \leq -90$ km s^{-1}. They noted that the resulting implied metallicity, [S II/H I] $= -0.36 \pm 0.18$, was a factor of $\sim$5 higher than the value for Complex C toward Mrk 290 reported by Wakker et al. (1999a,b), but they could not rule out the possibility that the feature in their spectrum was intrinsic Lyα absorption. The λ1250 line is not a significant detection in our spectrum given the continuum placement, and therefore we find only an upper limit to its equivalent width, W(S II λ1250) $< 1.9 \pm 2.0 \pm 0.9$ mÅ. Collins et al. (2003) reported measurements of the 1250 Å line in two velocity intervals corresponding to Complex C in the direction of Mrk 279; the narrower of their intervals (-180 km s$^{-1} \leq v_{\rm LSR} \leq -120$ km s^{-1}) is most closely matched to the velocities of our component C2. They consider the λ1250 line a significant detection and quote log N(Si II) $= 14.21^{+0.15}_{-0.21}$. They

had available only lower resolution *HST* GHRS data for their analysis of S II lines, and the intrinsically stronger λ1259 line was not included in their data. The same authors revisited this sightline using *FUSE* and *HST* STIS E140M data in Collins et al. (2007), in which they detected the λ1259 line and found $\log N(\mathrm{Si\ II}) = 13.69^{+0.11}_{-0.15}$ in the velocity interval -200 km s^{-1} $\leq v_{\mathrm{LSR}} \leq -120$ km s^{-1}, effectively the same interval as the combined velocities of our C1 and C2. We compute an upper limit of $\log N$ (Si II) < 13.86 over the combined interval, which compares favorably with their result.

O I is the only undepleted ion seen in C1; we find a metallicity for this component of [O I/H I] $= -0.99 \pm 0.25$ ($0.10^{+0.08}_{-0.04}$ $Z_{\odot}$). We set FWHM $= 14.9^{+7.6}_{-4.9}$ km s^{-1} for C2 based on multiple detections of Si II and find [O I/H I] $= -0.78 \pm 0.27$ ($0.17^{+0.17}_{-0.07}$ $Z_{\odot}$) and [S II/H I] $= -0.72 \pm 0.09$ ($0.19^{+0.03}_{-0.04}$ $Z_{\odot}$), for a mean and 1σ scatter of $\log Z = -0.74 \pm 0.04$ (0.18 ± 0.02 $Z_{\odot}$). Good agreement between the two individual abundances suggests that no ionization correction is necessary for C2. These metallicities are consistent with literature values of about 1/10 to 1/3 solar for Complex C (Tripp et al. 2003, Sembach et al. 2004, Fox et al. 2004). Abundance plots for these two components are shown in Figures 3.31 and 3.32, respectively.

We see absorption in some lines of several low ions (N I, O I, and Si II) between -120 km s^{-1} $\leq v_{\mathrm{LSR}} \leq -105$ km s^{-1} that corresponds with two blended 21 cm peaks at ~ -108 and -99 km s^{-1}. To estimate the H I column density of this component, we fit a single Gaussian to the 21 cm spectrum over these peaks with $N(\mathrm{H\ I}) = (9.7 \pm 1.6) \pm 10^{18}$ cm^{-2}, or $\log N(\mathrm{H\ I}) =$

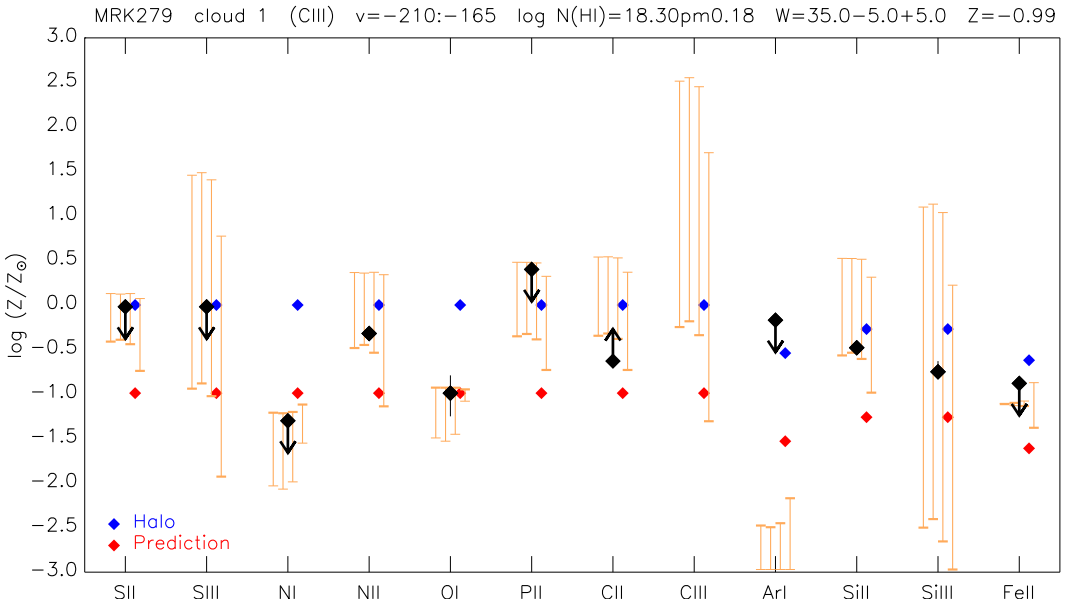

Figure 3.31 Abundance plot for "C1" (Complex C cloud CIII) at -210 km s^{-1} $\leq v_{\rm LSR} \leq -165$ km s^{-1}. The range of possible ionization corrections is shown for 3, 5, and 10 kpc (log $\phi = 5.51$, 5.55, and 5.44) at densities between log $n = -3$ and -1, and for the extragalactic background at log $\phi = 4.53$ (orange bars, left to right). A Halo depletion pattern is indicated with blue points for each ion, and predicted abundances with red points given our measured metallicity [O I/H I] $= -0.99$.

$18.99^{+0.07}_{-0.08}$. While the absorption is undoubtedly real, all of the UV lines are badly blended with the adjacent absorption in C2. These features are likely the result of velocity overlap of Complex C and Upper IV Arch gas in the IV9 cloud (Wakker 2001a), and cannot be unambiguously separated in our analysis, so we made no attempt to measure them. The overlap of components continues below -100 km s^{-1}, where we see distinct absorption in the range -105 km s^{-1} $\leq v_{\rm LSR} \leq -60$ km s^{-1}. It is unclear how much of the signal in this interval is attributable to intermediate-velocity gas, but the overlap necessarily biases

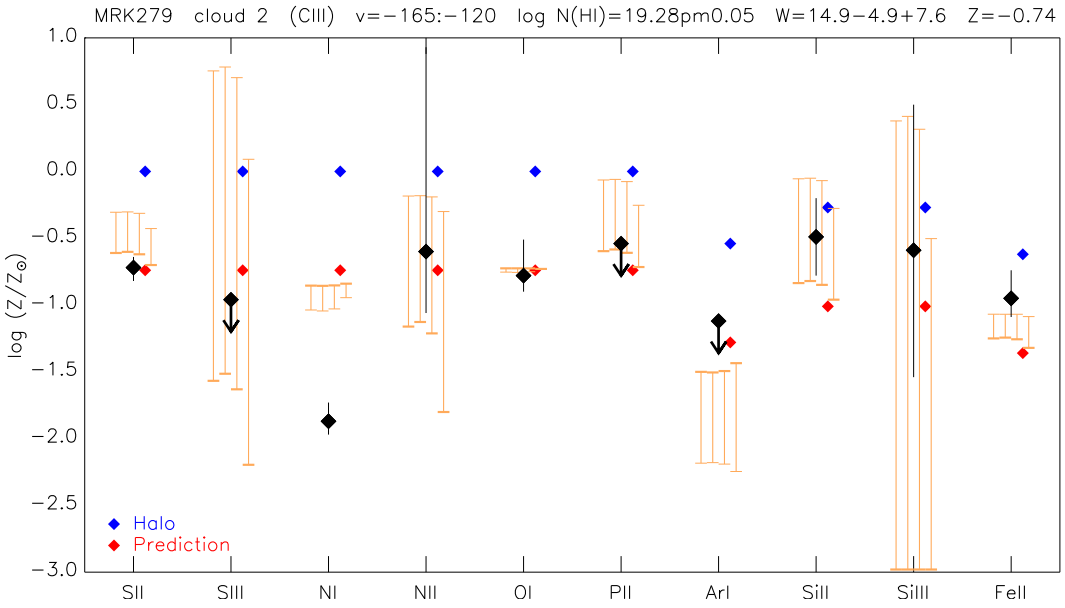

Figure 3.32 Abundance plot for "C2" (C-South) at -165 km s^{-1} $\leq v_{\rm LSR} \leq -120$ km s^{-1}. The plot parameters are the same as in Figure 3.31 but for our mean metallicity $Z = -0.74$.

measurements toward the solar metallicity expected for IVCs. We therefore do not include this component in our Complex C analysis. Collins et al. (2003) quote a metallicity of $Z \sim 0.17\ Z_{\odot}$ from the O I abundance in their -120 km s^{-1} $\leq v_{\rm LSR} \leq -90$ km s^{-1} Complex C velocity interval thought to be "contaminated" by IV9. O I was badly blended or saturated in our spectra and therefore we do not have a measurement against which to directly compare the Collins et al. result. Their measurement interval contains larger negative velocities than ours, so their O I abundance was likely diluted more by low-metallicity gas in Complex C. Given N(H I) and the interstellar radiation field, we expect that [Ar I/H I] should be about -0.6 dex below [Ar/H]; we measure

-0.55 ± 0.25 ($0.28^{+0.55}_{-0.02}$ $Z_\odot$). Also, slightly supersolar abundances [S II/H I] = $+0.22 \pm 0.29$ ($1.66^{+1.43}_{-0.85}$ $Z_\odot$) and [P II/H I] = $+0.10 \pm 0.13$ ($1.26^{+0.65}_{-0.21}$ $Z_\odot$) are compatible with [Fe II/H I] = -0.44 ± 0.09 ($0.36^{+0.14}_{-0.03}$ $Z_\odot$), which is enhanced over the standard halo value by 0.1 dex.

In the 21 cm spectrum velocity region corresponding to the -105 km s^{-1} $\leq v_{\rm LSR} \leq -60$ km s^{-1} component, we fit a single Gaussian to the peak at -74 km s^{-1} due to IV9 with N(H I) = $(3.26 \pm 0.18) \times 10^{19}$ cm^{-2}, or log $N = 19.51 \pm 0.02$. Detections of multiple lines of Fe II and N I constrain the FWHM at $14.4^{+6.7}_{-5.4}$ km s^{-1}. From [S II/H I] = $+0.22 \pm 0.29$ ($1.66^{+1.43}_{-0.85}$ $Z_\odot$) and [P II/H I] = $+0.10 \pm 0.13$ ($1.26^{+0.65}_{-0.21}$ $Z_\odot$) we find a mean log metallicity and 1σ scatter of $+0.15 \pm 0.08$ ($1.41^{+0.30}_{-0.25}$ $Z_\odot$). Two column densities measured for this component are particularly inconsistent with literature values. Lehner et al. (2004) give log N(P II) < 12.62 but specify only the LSR centroid of their velocity window (-102 km s^{-1}), not the width of the window. We detect strong P II λ963 and λ961 and measure log N(P II) = $13.02^{+0.13}_{-0.18}$; however, this component is strongly blended with the intermediate-velocity component at -45 km s^{-1}, possibly accounting for the difference. Our P II abundance is consistent with the S II abundance within errors, so the results for P II are probably reliable. Abundances for this component, shown in Figure 3.33, generally follow a Halo depletion pattern except for Ni II, which is about 0.3 dex higher than the halo depletion prediction. Given the apparent velocity overlap of different sources of absorption within this component, it is difficult to draw firm conclusions about the origins of the gas; however, assuming most

of our detected ions are identified with IV9, our results are broadly consistent with a Galactic Disk origin for this gas.

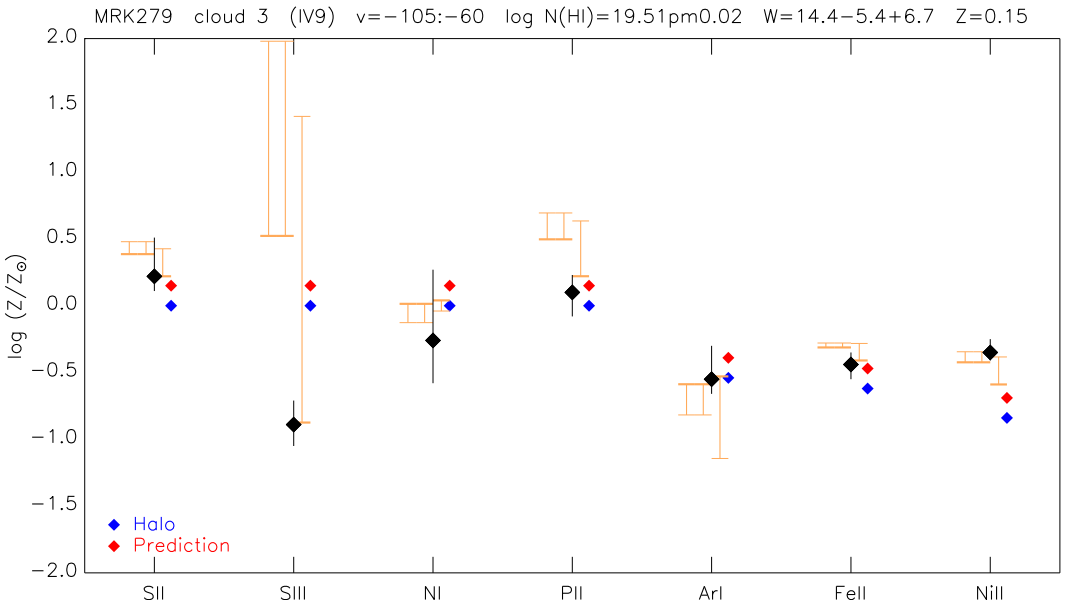

Figure 3.33 Abundance plot for the IV9 cloud at -105 km s^{-1} $\leq v_{\rm LSR} \leq -60$ km s^{-1}. The range of possible ionization corrections is shown for 0, 1, and 2 kpc ($\log \phi = 6.66$, 6.66, and 5.51) at densities between $\log n = -3$ and -1 (orange bars, left to right). A Halo depletion pattern and predicted abundances with red points given our mean metallicity $Z = +0.15$ are shown.

Finally, we identify absorption in the interval -60 km s^{-1} $\leq v_{\rm LSR} \leq -30$ km s^{-1} with the LLIV Arch. Wakker et al. (2012) measured column densities for high ions in the velocity range -65 km s^{-1} $\leq v_{\rm LSR} \leq -20$ km s^{-1}, including S III λ1012 and Fe III λ1122, but we found these lines too severely impacted by Galactic absorption to measure properly. Otherwise, we can only compare our measured abundances against LLIV Arch gas in other sightlines. Richter et al. (2001a) report abundances [O I/H I] $= +0.01 \pm 0.23$ ($1.02^{+0.71}_{-0.42}$

$Z_\odot$) and [P II/H I] = $+0.10 \pm 0.12$ ($1.26^{+0.40}_{-0.30}$ $Z_\odot$) in LLIV Arch gas at -55 km s^{-1} toward PG0804+761, arguing for a near-solar abundance profile for this cloud. de Boer et al. (1993) measured abundances of several low ions in the sightline toward SN 1993J, which passed through LLIV Arch gas at a velocity of -45 km s^{-1}. Among undepleted species, they found log N(S II) = 16.0 from the λ1259 line and log N(Zn II) = 12.7 from the λ2025.48 line, but at the resolution of their rebinned and smoothed *IUE* spectra (20-30 km s^{-1}), our -80 and -45 km s^{-1} components are badly blended and their measurements likely include contributions from both.

There is a single distinct emission peak in the 21 cm spectrum at -37 km s^{-1} in this velocity window. However, there is considerable flux between this peak and the one at -74 km s^{-1}, most notably around -50 km s^{-1}, again likely due to unresolved velocity substructure. We did not try to fit this emission for several reasons: (1) the profile is too blended to allow reasonable identification and fitting of individual Gaussians; (2) adding a component around -50 km s^{-1} would reduce the amplitude of the Gaussian fit to the -74 km s^{-1} component, affecting abundances; and (3) it is possible that the actual profiles, unaffected by instrumental smearing, are non-Gaussian. We therefore fit only a single Gaussian to the -37 km s^{-1} peak with N(H I) = $(4.90 \pm 0.55) \times 10^{19}$ cm^{-2}, or log N(H I) = 19.69 ± 0.05, but we caution that this value may not be as reliable as others in this sightline. It is an estimate based on a single-component fit, guided by the absorption lines, in which emphasis was placed on preserving flux in the wings at the expense of fitting the peak

particularly well. None of the ions observed in the UV constrain the FWHM, so we used 32 ± 5 km s^{-1} based our fit to the 21 cm spectrum. The only undepleted ion confidently detected is S II for which we find [S II/H I] $= -0.07 \pm 0.08$ ($0.85^{+0.13}_{-0.18}$ $Z_{\odot}$), similar to the O I and P II abundances found by Richter et al. (2001a). While we have no direct information from our measurements about ionization conditions in the LLIV Arch along the sightline toward Mrk 279, the strength of the high ion lines argues in favor of its low estimated distance above the plane ($\sim$ 1 kpc; Richter et al. 2001a). We therefore agree with the Richter et al. interpretation that the LLIV Arch gas originated in the Galactic Disk and is part of the Galactic Fountain.

To summarize, along the sightline toward Markarian 279 we detect two Complex C components: cloud CIII, for which we find a metallicity of [O I/H I] ~ -1 (~ 0.10 $Z_{\odot}$), and C-South, which gives a mean metallicity log $Z \sim -0.75$ (~ 0.18 $Z_{\odot}$) from measurements of O I and S II. We conclude that the previous C-South metallicity reported by Gibson et al. (2001), log $Z \sim -0.4$, is erroneous and based on a weak feature in the GHRS spectrum that does not appear in our STIS data. The intermediate-velocity cloud IV9 may have a slightly supersolar metallicity, although that depends on the actual value of N(H I), which remains somewhat uncertain. Finally, only S II gives a metallicity for the LLIV component and is near solar, as expected.

3.4.8 Markarian 509

Mrk 509 is one of the brightest AGN in the UV, and the *FUSE* data are among the highest S/N of all sightlines we analyzed at 26 per resolution element. The STIS data are lower, ranging from ∼22 per resolution element around the N I lines near 1134 Å down to ∼7 below 1000 Å. The background source flux is known to vary over time by at least a factor of 2 (Wakker 2001a). While there are no known large HVC complexes directly coincident with the line of sight toward Mrk 509, it contains gas characterized by Sembach et al. (1999) as a "highly-ionized HVC" because it is seen in absorption in high ions such as C IV, Si IV and N V (Sembach et al. 1999), and O VI (Sembach et al. 2000), without corresponding 21 cm emission. They suggest these HVCs are located either in the distant Galactic halo or beyond in the Local Group and that the highly ionized species observed trace the outer, low-density regions of the clouds while the angular sizes of their cold, dense cores are too small to detect in H I 21 cm emission. Alternately, they may represent the ionized, low-density extensions of otherwise ordinary HVCs located nearer to the Galaxy in which the ionization is primarily the result of photoionization by the extragalactic background (Ferrara & Field 1994). Sembach et al. also note that the Mrk 509 sightline falls within ∼ 5° of the Galactic Center Negative (GCN) complex of HVCs (Mirabel & Morras 1984, Wakker & van Woerden 1991). Some of the GCN clouds in the Mirabel and Morras catalog near the Mrk 509 sightline have velocities near those of H I and UV absorption toward Mrk 509. The low H I column density HVCs seen in this direction may be associated

with low-density gas associated with the GCN clouds (Sembach et al. 1999, Collins et al. 2004, Winkel et al. 2011), but this idea has not been conclusively demonstrated. A representative sample of ions detected in our UV spectra is shown in Figures 3.34-3.36.

Absorption due to high-velocity gas in the direction of Mrk 509 was first reported by Sembach et al. (1995) based on observations with the Goddard High Resolution Spectrograph (GHRS) aboard *HST*; their observations revealed similar, highly-ionized gas toward PKS 2155-304 ($\ell = 17\overset{\circ}{.}7$, $b = -52\overset{\circ}{.}2$) also thought to be associated with the GCN complex. They distinguish these "C IV HVCs" from "classical H I HVCs", likening the gas to the high-ionization metal line systems associated with quasar sightlines given that they show (1) strong C IV absorption, and (2) essentially no detectable low-ion (e.g., C II and Si II) absorption or 21 cm emission to very low levels. They saw two velocity components along this sightline: a "stronger" component at -340 km s^{-1} $\leq v_{\rm LSR} \leq -250$ km s^{-1} and a "weaker" component at -250 km s^{-1} $\leq v_{\rm LSR} \leq -170$ km s^{-1} . Their observations of the C IV and Si IV doublets in which the weaker lines of each doublet are more clearly peaked than the stronger lines is interpreted as the presence of unresolved saturation; they therefore cite only lower limits for N(C IV). Given the possible association with gas in the GCN complex, Sembach et al. favor an origin of the high-ion absorption in the high-velocity gas in this sightline as due to photoionization in warm ($T \sim 10^4$ K) gas. They conclude that the clouds giving rise to this absorption are large ($D \sim 1 - 10$ kpc), highly diffuse, and almost completely ionized, quoting an H

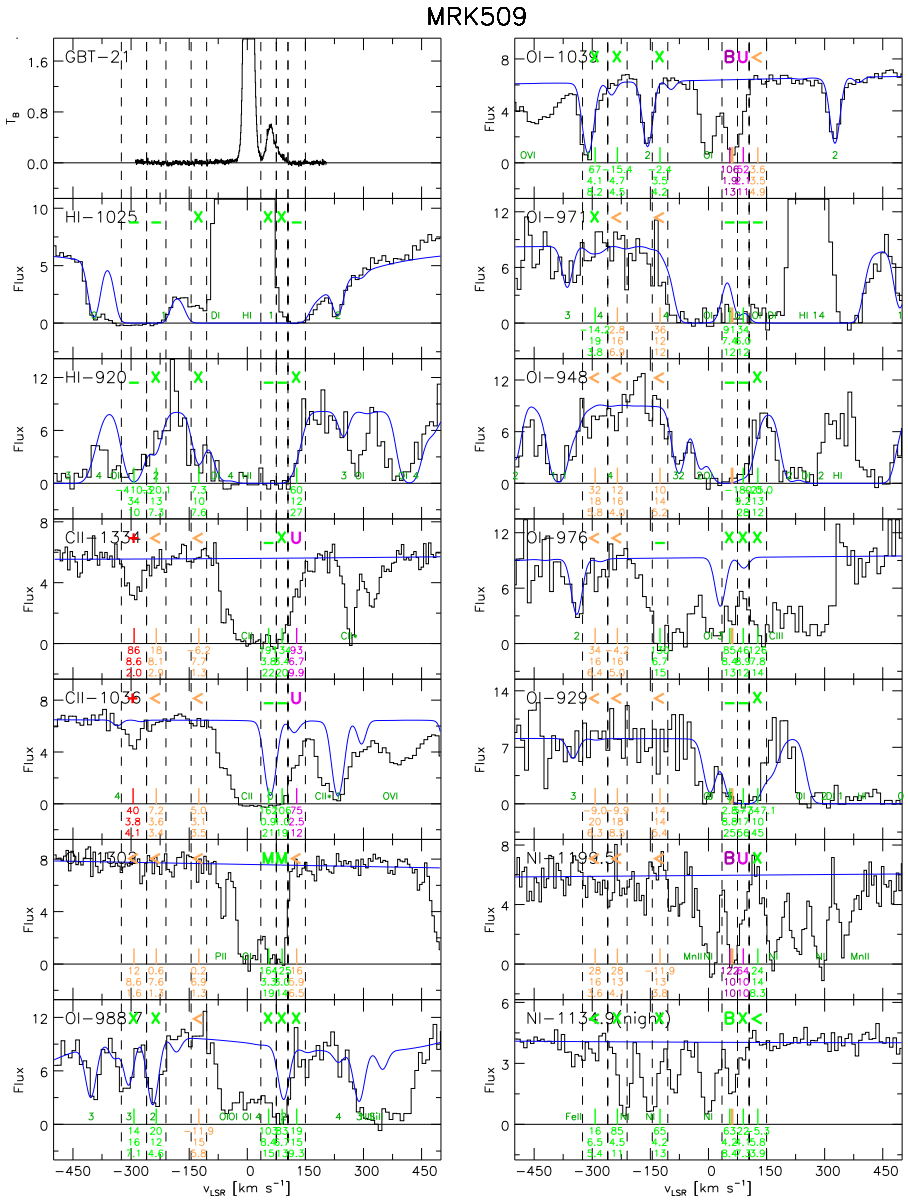

Figure 3.34 Cutouts of the Effelsberg 21 cm spectrum and selected UV spectra toward Mrk 509 highlighting ions and lines most relevant to the determination of the metallicity and depletion of each component.

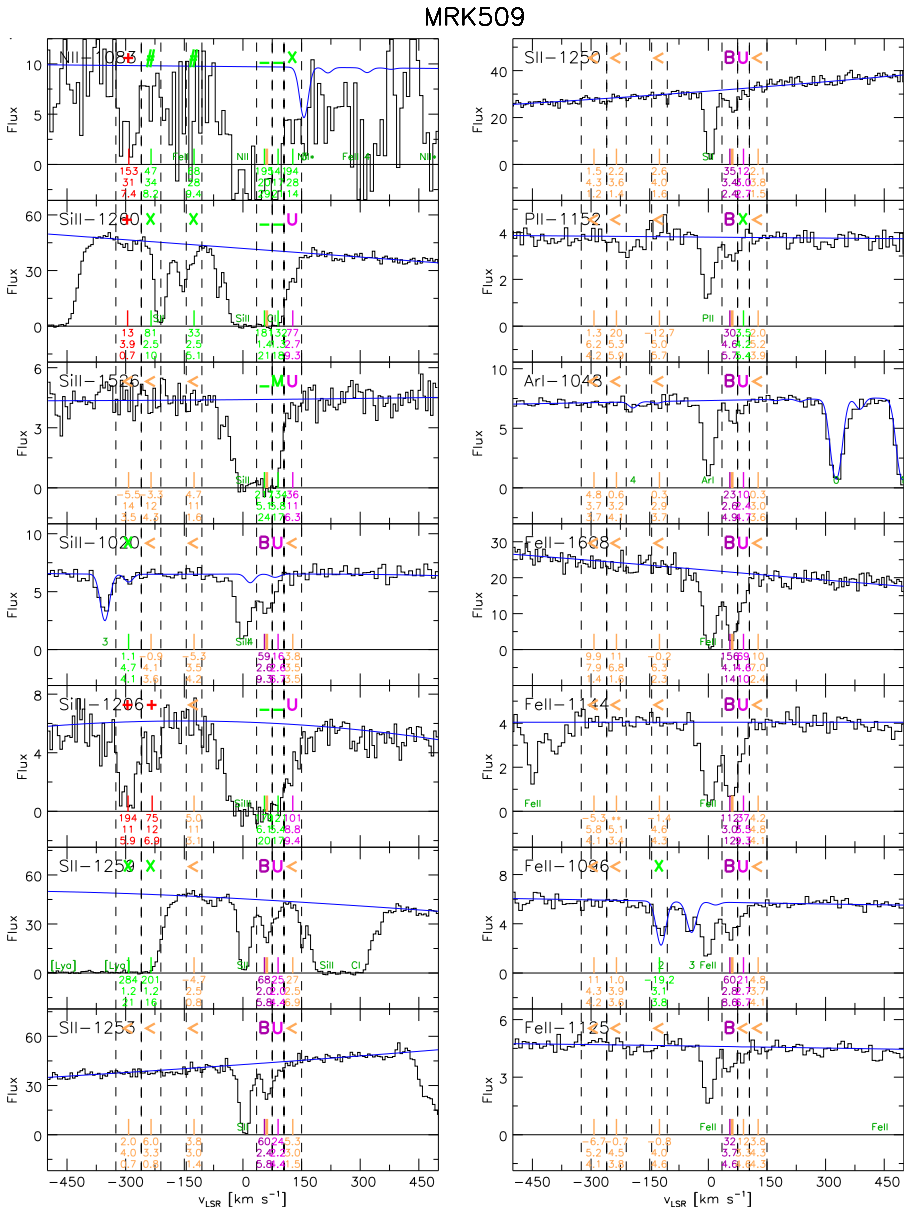

Figure 3.35 Cutouts of selected UV spectra toward Mrk 509 (continued).

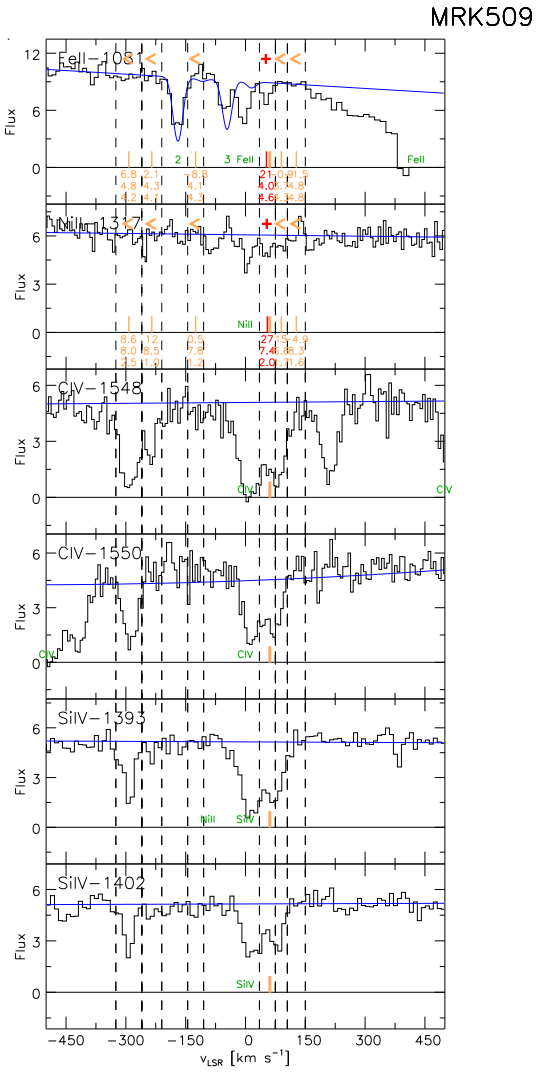

Figure 3.36 Cutouts of selected UV spectra toward Mrk 509 (continued).

I 21 cm emission upper limit toward Mrk 509 at 4σ of 4.9×10^{17} cm^{-2}, or log N(H I) < 17.69, obtained with the NRAO 140-foot (43 m) telescope. The same group obtained additional, intermediate-resolution GHRS spectra specifically to study the ionization conditions in the high-velocity gas in greater detail, reporting updated column density limits in Sembach et al. (1999). Collins et al. (2004) also note the "stronger" and "weaker" components of Sembach et al. in STIS and *FUSE* data at -335 km s^{-1} $\leq v_{\rm LSR} \leq -260$ km s^{-1} and -260 km s^{-1} $\leq v_{\rm LSR} \leq -200$ km s^{-1}, respectively. The "stronger" component was seen only above the 3σ level in C IVλ1548.20 and Si III λ1206. They also obtain a profile for O VI λ1031.93 but note its contamination by Galactic H_2 removes any information about small-scale structure in the line, and confirm the conclusion by Sembach et al. that unresolved saturation affects the C IV and Si IV line profiles. The authors draw a comparison between these highly-ionized HVCs and the gas in Complex C, suggesting that similar high-ion ratios in both sources argue for a common mechanism in both cases to produce the observed C IV and O VI absorption. They did not improve on the 21 cm H I measurement of Sembach et al. (1995). Most recently, Fox et al. (2006) looked for absorption by O VI and C III in *FUSE* data toward Mrk 509, finding log N(C III) > 14.39 in the velocity range -350 km s^{-1} $\leq v_{\rm LSR} \leq -200$ km s^{-1}. Finally, Shull et al. (2009) used STIS and *FUSE* spectra to measure columns for multiple ionizations stages of Si among the highly-ionized components in this sightline. For the "strong" component (-343 km s^{-1} $\leq v_{\rm LSR} \leq -261$ km s^{-1}) they found a limit of log N(Si II) < 12.58 and detected the higher Si ions

with log N(Si III) = 13.30 ± 0.12 and log N(Si IV) = 13.27 ± 0.03. For the "weak" component (-261 km s^{-1} $\leq v_{\rm LSR} \leq -218$ km s^{-1}) they measured log N(Si II) < 12.58, log N(Si III) = $12.47^{+0.08}_{-0.07}$, and log N (Si IV) = $12.34^{+0.10}_{-0.01}$.

We unambiguously detect the Collins et al. "strong" component at -325 km s^{-1} $\leq v_{\rm LSR} \leq -260$ km s^{-1} in C II λ1334 and 1036, N II λ1083, Si III λ1206, and two lines each of C IV and Si IV. Si II λ1260 is weakly detected at a significance of 3.3σ, while C III λ977 is present but nearly saturated and thus rendered useless for the purpose of deriving N(C III). While this component is not a detection in 21 cm emission, we fit the Lyman series H I lines with a single component at $v_{\rm LSR} = -300$ km s^{-1} with FWHM = 30 km s^{-1} and N(H I) = (1.5 ± 0.7) $\times 10^{17}$ cm^{-2}, or log N(H I) = $17.18^{+0.17}_{-0.27}$. We did not detect sufficient lines of any ion from which to derive the intrinsic linewidth for the curves of growth, so we set the linewidth equal to the FWHM of the H I fit. We do not see lines of any undepleted ions in the spectra, but the detection limits provide some useful information. We find log N(O I) < 13.61, which given our upper limit for N(H I) corresponds to [O I/H I] < -0.26. The only point of comparison for this limit is found in Collins et al. (2004) who report log N(O I) < 13.62; taking our N(H I), their limit implies [O I/H I] < -0.25. It is also worth mentioning that we find unusually strong N II at N(N II) =

We detect Si III λ1206 absorption in our data at -260 km s^{-1} $\leq v_{\rm LSR}$ ≤ -210 km s^{-1}, corresponding to the "weak" component, at a significance of 5.4σ. No other species are detected at a significance of $\geq 2.5\sigma$. We find log N(Si III) = $12.59^{+0.42}_{-0.21}$, which compares favorably with the results of other au-

thors when variations in the velocity integration limits are taken into account. The H I absorption corresponding to this component is fitted by a single component at $v_{\rm LSR} = -230$ km s^{-1} with FWHM = 30 km s^{-1} and N(H I) = (3$\pm$1) $\times 10^{15}$ cm^{-2}, or log N(H I) = $15.48^{+0.12}_{-0.18}$. A lack of detected, undepleted species combined with our uncertain limit on N(H I) makes it difficult to argue for a particular metallicity for this component. If a reliable measurement of its distance were available, we could estimate a metallicity based on the allowed range of [Si III/H I] values from photoionization models.

Fox et al. (2006) claimed an upper limit of log N(C III) > 13.84, based on the λ977 line, and a corresponding log N(H I) > 16.0 from the λ926 line, at -200 km s^{-1} $\leq v_{\rm LSR} \leq -100$ km s^{-1} in their *FUSE* spectra. Contamination in this interval in the C III λ977 spectrum includes absorption due to zero-velocity Galactic O I λ976 and the 11-0 R(3) line of H_2 at 976.551Å; Fox et al. describe a modeling procedure for mitigating contamination due to H_2, but the remainder of the claimed limit is likely due to the O I contamination. We looked for evidence of absorption around these limits in our data found none, either in the low ions or in C IV, where we would expect to see strong absorption as in the case of the two highly-ionized clouds previously discussed. We therefore did not attempt to derive any abundances in this velocity range.

Gas at positive velocities in this sightline is associated with the cloud g2 in Complex gp, a set of IVCs in the region $\ell = 30^\circ - 70^\circ$, $b = -45^\circ$ to 20° (Wakker 2001a). In 21 cm maps, this cloud has a somewhat "cometary" head-tail morphology that may indicate interaction with the Halo. Little prior

work has been done to obtain abundances for this cloud. Shull et al. (2009) published the only available results as part of a search for ionized Si in HVCs and IVCs, finding log N(Si II) = $14.74^{+0.07}_{-0.08}$ and log N(Si III) > 13.76 in the interval +35 km s^{-1} $\leq v_{\rm LSR} \leq$ +90 km s^{-1}. They pair the Si results with a measurement of log N(H I) = $19.55^{+0.16}_{-0.25}$ from the Leiden/Dwingeloo Survey, but they do not comment further on this IVC.

We see two blended absorption units in the intervals +35 km s^{-1} $\leq v_{\rm LSR} \leq$ +75 km s^{-1} and +75 km s^{-1} $\leq v_{\rm LSR} \leq$ +105 km s^{-1}, to which we refer hereafter as "g2a" and "g2b". Moderate blending of these two components is clear in Figures 3.34-3.36, in which the core of g2b is not distinct and the absorption in it appears as a "shoulder" on the more clearly-defined red wing of g2a. We fit a single Gaussian to g2a in the GBT spectrum with a velocity centroid at +60 km s^{-1} with FWHM = 23 km s^{-1} and N(H I) = (2.60$\pm$0.05) $\times$ 10^{19} cm^{-2}, or log N(H I) = 19.41$\pm$0.01. Multiple detections of N I and S II give an intrinsic linewidth of $15.0^{+8.7}_{-6.1}$ km s^{-1}. Abundances for detected ions in this component are shown in Figure 3.37. While O I is the undepleted ion we prefer to cite as the best metallicity indicator, N(O I) is highly uncertain on the basis of a single detected line, λ1039. It is the only measurable O I line available, but it is strongly blended with both g2b and neighboring zero-velocity Galactic O I absorption and is nearly saturated. This one line completely determines the O I abundance but leads to a large uncertainty: [O I/H I] = -0.27 ± 3.00. We are then left to our photoionization modeling to try to infer the "true" metallicity of this component. There is also underlying assumption that g2a

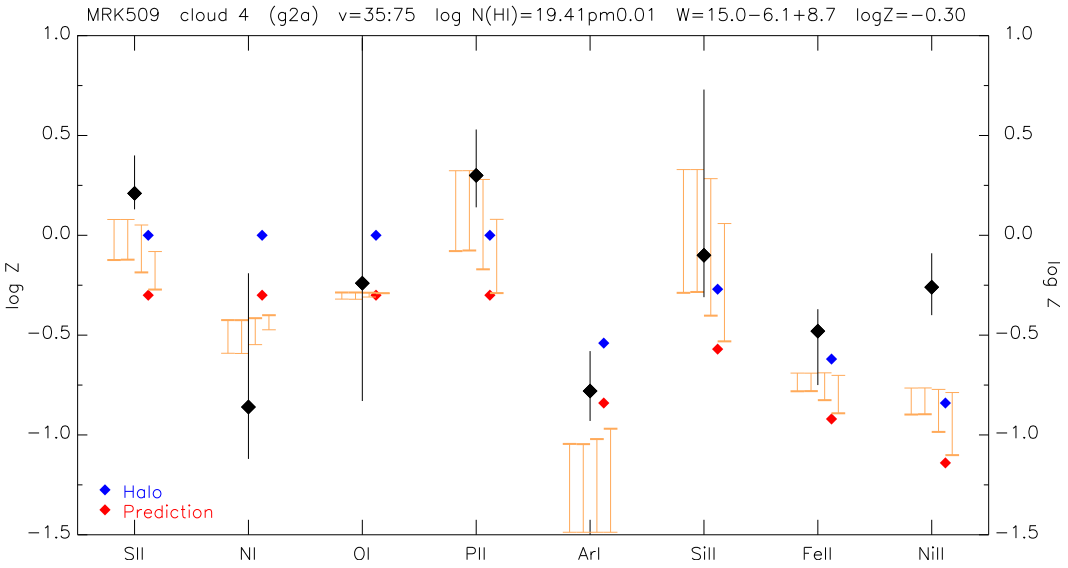

Figure 3.37 Abundance plot for ions the "g2a" component of cloud g2 toward Mrk 509 at $+35$ km s$^{-1} \leq v_{\rm LSR} \leq +75$ km s^{-1}. The range of possible ionization corrections is shown as the orange bars for, left to right, 5, 10, and 20 kpc (log $\phi = 5.98$, 5.99, and 5.62) at densities between log $n = -3$ and -1, and for the extragalactic background (log $\phi = 4.53$). A Halo depletion pattern is indicated with blue points for each ion, and predicted abundances with red points assuming cloud metallicity of log Z = -0.3.

and g2b have the same intrinsic metallicity, as we would expect this of two components of the same cloud. After comparing the abundance patterns of both components, we decided on a systemic metallicity of log $Z \sim -0.3$ (~ 0.5 $Z_{\odot}$) for the cloud, and have plotted the abundances with respect to this figure.

We found the H I column density for g2b by fitting the GBT data with a Gaussian component at $v_{\rm LSR} = +87$ km s^{-1} with FWHM = 21 km s^{-1} and N(H I) = (4.3±2.0) × 10^{18} cm^{-2}, or log N(H I) = $18.63^{+0.17}_{-0.27}$. We do not detect multiple lines of any ions with which to constrain the linewidth, so we adopted

the FWHM of our fit to the H I lines. The resulting abundances are shown in Figure 3.38. N(O I) is again controlled uniquely by the λ1039 line, although it is less problematic than the same line in g2a. The resulting abundance is [O I/H I] $= -0.47 \pm 0.27$ ($0.34^{+0.29}_{-0.16}$ $Z_{\odot}$). We might alternately consider [S II/H I] $= +0.41 \pm 0.18$, but this apparently supersolar value is clearly affected by ionization. Once we correct for ionization, we find a metallicity of about one-half solar, which brings g2a and g2b in agreement with each other. Again,

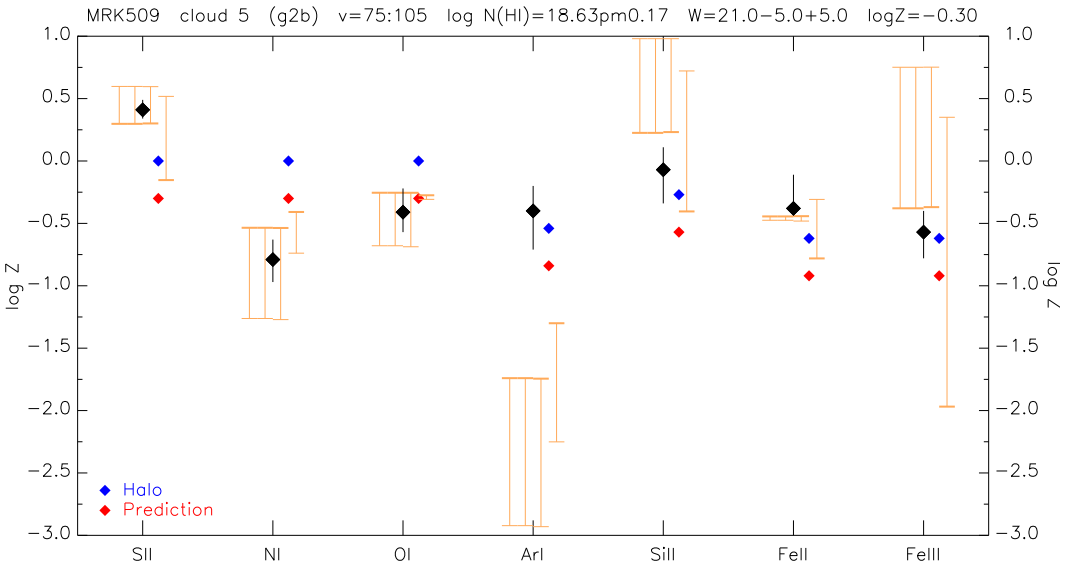

Figure 3.38 Abundance plot for ions the "g2b" component of cloud g2 toward Mrk 509 at +75 km s^{-1} $\leq v_{\rm LSR} \leq$ +105 km s^{-1}. The parameters are the same as in Figure 3.37.

a proper distance estimate would improve the reliability of this result.

Finally, we identified an additional velocity component at +105 km s^{-1} $\leq v_{\rm LSR} \leq$ +150 km s^{-1} but ultimately decided we could not measure abundances for it. Other authors have commented on this feature. Fox et al.

(2006) saw C III absorption at $+100$ km s$^{-1} \leq v_{\rm LSR} \leq +175$ km s^{-1} and report log N(C III) $= 13.72 \pm 0.06$ and an upper limit of log N(H I) > 16.1. Shull et al. (2009) saw Si II and Si III absorption at $+100$ km s$^{-1} \leq v_{\rm LSR} \leq +147$ km s^{-1} finding log N(Si II) $= 12.74^{+0.12}_{-0.15}$, log N(Si III) $= 12.70^{+0.09}_{-0.12}$, and an upper limit log N(H I) ≤ 19.66. Collins et al. (2009) also report Si III absorption in the same velocity interval as Shull et al., corresponding to log N(Si III) $= 12.74^{+0.08}_{-0.11}$. We only clearly detect this gas in Si II λ1260, Si III λ1206, C II λ1036, C III λ977, blended heavily with the adjacent g2 components. While highly uncertain, we measure for these lines log N(Si II) $= 12.83^{+0.14}_{-0.09}$, log N(Si III) $= 12.88^{+0.19}_{-0.12}$, log N(C II) $= 13.88^{+0.15}_{-0.09}$ and log N(C III) $= 13.61^{+0.47}_{-0.20}$, respectively. It is not detected in 21 cm emission in the GBT spectrum to a 5σ upper limit of 7.9×10^{17} cm^{-2}, or log N(H I) ≤ 17.90, assuming a FWHM of 20 km s^{-1}. An H I column of at least 1×10^{16} cm^{-2}, or log N(H I) $= 16.00$, is necessary to fit the red wing of the Lyman series H I lines adequately. Once again, we cannot make a meaningful estimate of the metallicity of this cloud absent a distance with which to constrain photoionization models. Absorption is also seen around $v_{\rm LSR} = +235$ km s^{-1} only in the Lyman H Ilines and certain high ions such as O VI. It is not detected in any of the ions useful for abundance determinations and the limits are not especially interesting, so we have omitted this velocity interval from our results.

To summarize, in the Mrk 509 sightline, we see three absorption components at high negative velocities (centroid $v_{\rm LSR} = -293$, -235, and -125km s^{-1}) that may be associated with the Galactic Center Negative complex of

HVCs. The available data can only provide an upper limit for the metallicity of the -293 km s^{-1} component ($Z \lesssim 0.55\ Z_{\odot}$). Absorption due to the cloud g2 in Complex gp appears in two blended components we call "g2a" and "g2b" at centroid velocities $v_{\rm LSR} = +55$ and $+90$ km s^{-1}, respectively. The abundance patterns of the g2 components are like those of typical Halo IVCs at a metallicity of $\sim 0.5\ Z_{\odot}$. Lastly, while we detect additional absorption in some ions at $v_{\rm LSR} \sim +128$ km s^{-1} and $v_{\rm LSR} \sim +235$ km s^{-1}, we do not have enough information about either to compute meaningful abundances. For many of the Mrk 509 components, otherwise unavailable metallicities could be inferred from photoionization models if distances to the clouds were known.

3.4.9 Markarian 817

This sightline is among those of the highest S/N ratio in our sample element at 29 per resolution element, and is one of nine in which Complex C is seen in O VI absorption. The UV flux of the intrinsic continuum source varies by about a factor of two over a period of decades (Winter et al. 2011). A representative sample of ions detected in our UV spectra is shown in Figures 3.39-3.40.

We see absorption in this direction due to Complex C in two distinct velocity intervals: -180 km s^{-1} $\leq v_{\rm LSR} \leq -135$ km s^{-1} and -135 km s^{-1} $\leq v_{\rm LSR} \leq -70$ km s^{-1}. Previous measurements of this sightline in the literature have combined both into a single unit: Gibson et al. (2001) and Collins et al. (2003) defined the interval as -140 km s^{-1} $\leq v_{\rm LSR} \leq -80$ km s^{-1}. Fox et al.

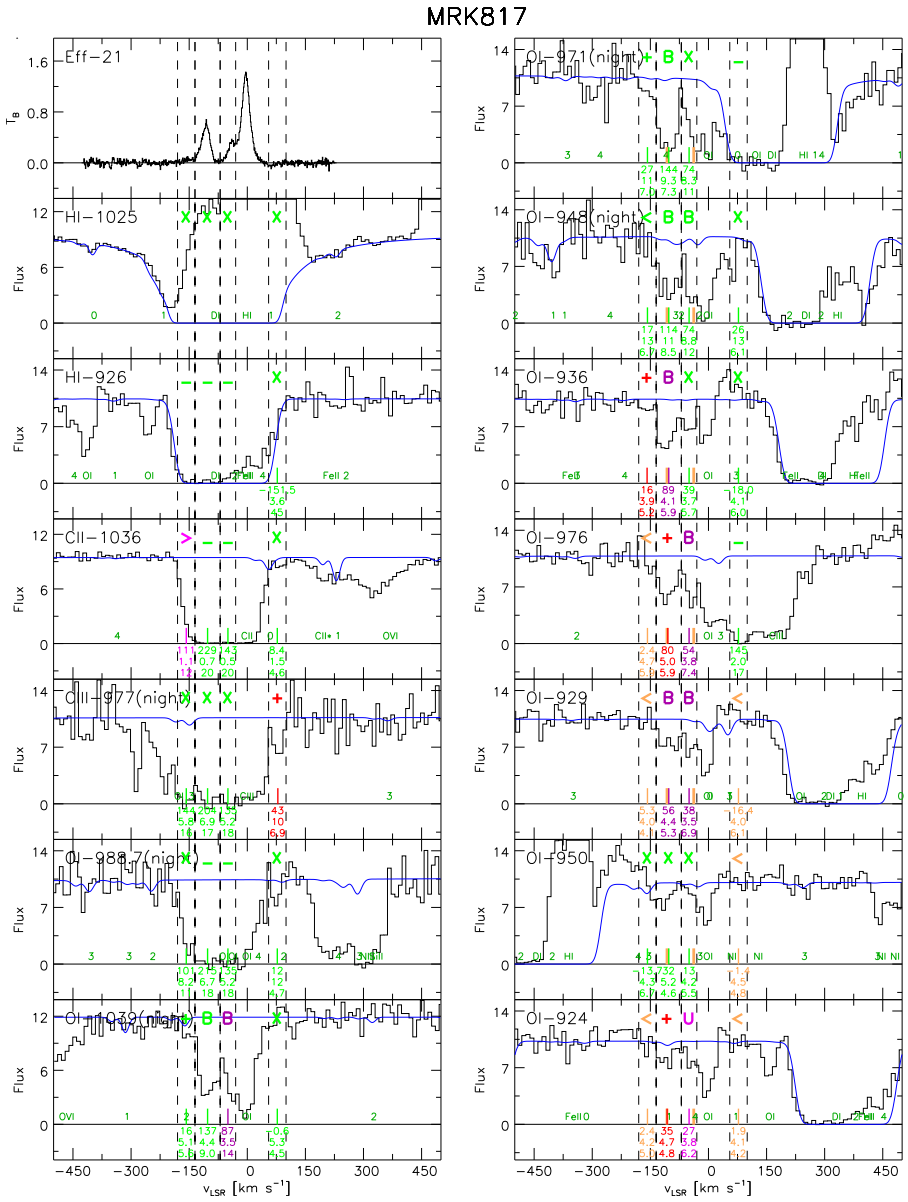

Figure 3.39 Cutouts of the Effelsberg 21 cm spectrum and selected UV spectra toward Mrk 817 highlighting ions and lines most relevant to the determination of the metallicity and depletion of each component.

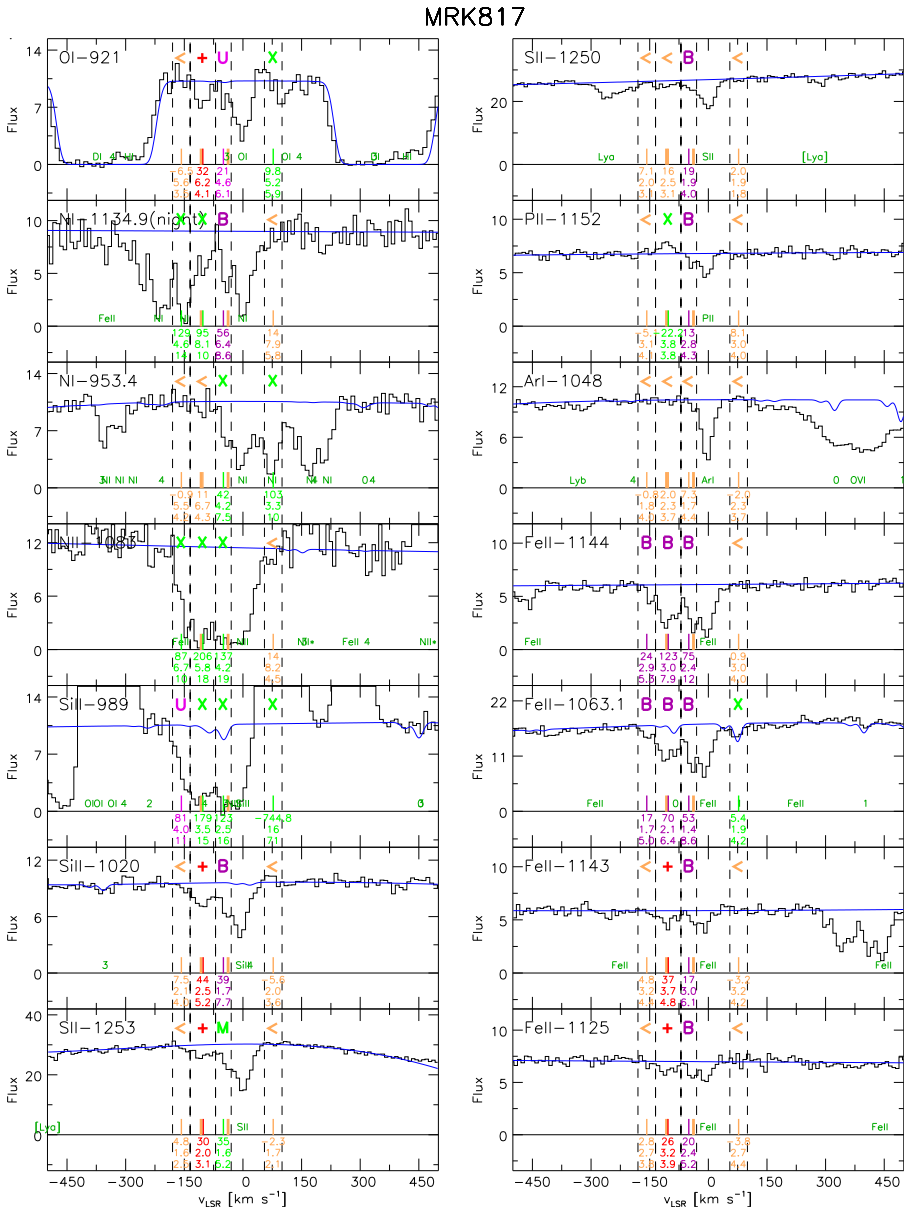

Figure 3.40 Cutouts of selected UV spectra toward Mrk 817 (continued).

(2004) used an interval of -160 km s^{-1} $\leq v_{\rm LSR} \leq -80$ km s^{-1} and Sembach et al. (2003) cite a single component with a velocity centroid of $v_{\rm LSR} = -109$ km s^{-1} in their respective studies of O VI in Complex C, although they did not derive low-ion abundances. Thus there are no previously published abundances for these two absorption components considered separately.

Giovanelli et al. (1973) designated the $v_{\rm LSR} = -157$ km s^{-1} component seen here "CIIIC", but we follow the convention of Wakker (2001a), who refers to it as "CIC" to distinguish it from a different core CIIIC seen along the line of sight toward, e.g., PG1259+593 (see Section 3.4.14). It is a non-detection in 21 cm spectra for which we find a 5σ noise limit of N(H I) $\leq 5.5 \times 10^{18}$ cm^{-2} or log N(H I) ≤ 18.74. The blue wing of the Lyman series H I absorption is best fit by a component with velocity centroid of -157 km s^{-1}, FWHM = 25 km s^{-1}, and N(H I) $= 3.5 \times 10^{18}$ cm^{-2}, or log N(H I) = 18.54. The velocity centroid and width are comparable to those of the O I λ936 line, whose width was used to set the integration range for this component in the UV spectra. We feel the H I column density obtained via the Lyman series H I fit is more robust than the 21 cm detection limit, so we adopt N(H I) $= (3.5 \pm 1.0) \times 10^{18}$ cm^{-2}, or log N(H I) $= 18.54^{+0.11}_{-0.15}$, for this component. The only undepleted ion we detect is O I, which gives a metallicity of [O I/H I] $= -0.74 \pm 0.24$ ($0.18^{+0.13}_{-0.08}$ $Z_{\odot}$), consistent with expectations for Complex C.

The less-negative-velocity Complex C component is identified with cloud CIA, for which Wakker (2001a) gives N(H I) $= (3.1 \pm 0.09) \times 10^{19}$ cm^{-2}, or log N(H I) $= 19.49 \pm 0.01$. Their only abundance measurement is Z(S II) =

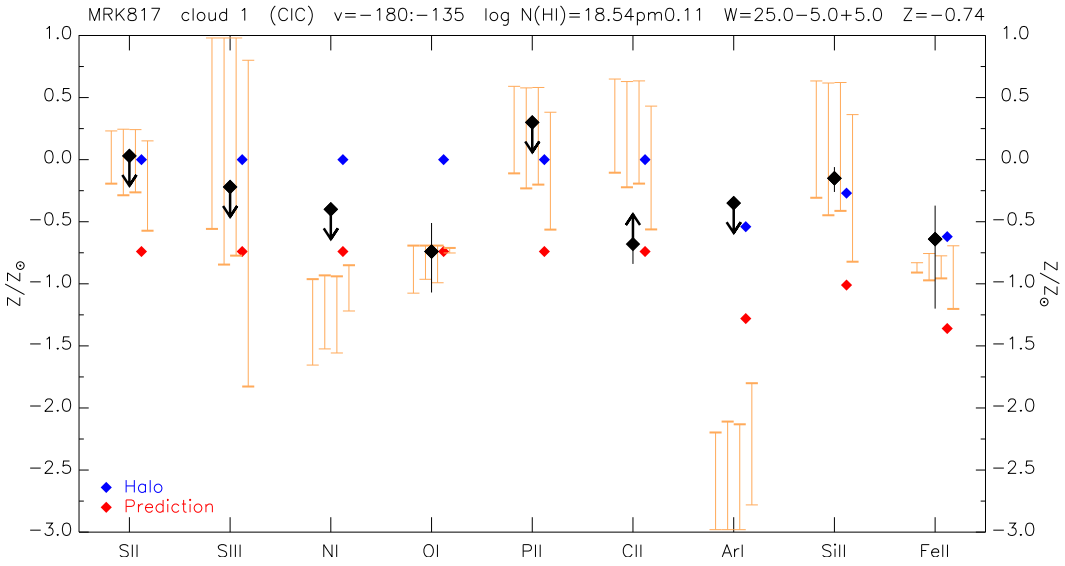

Figure 3.41 Abundance plot for Complex C toward Mrk 817 at −180 km s^{-1} $\leq v_{\rm LSR} \leq$ −135 km s^{-1}. The range of possible ionization corrections is shown for 3, 5, and 10 kpc (log ϕ = 5.51, 5.55, and 5.44) at densities between log n = −3 and −1, and for the extragalactic background (orange bars, left to right). A Halo depletion pattern is indicated with blue points for each ion, and predicted abundances with red points given our measured metallicity [O I/H I] = −0.74.

0.33 $Z_{\odot}$, at the upper end of the range of expected Complex C abundances for undepleted ions. Gibson et al. (2001) measured this sightline using *HST* GHRS/G160M and found log N(S II) = $14.27^{+0.51}_{-0.51}$ in the interval −140 km s^{-1} $\leq v_{\rm LSR} \leq$ −80 km s^{-1} on the basis of the equivalent widths of the λ1250 and λ1253 lines. They adopted Wakker's (2001) value of N(H I) to compute [S II/H I] = -0.48 ± 0.06 ($0.33^{+0.05}_{-0.04}$ $Z_{\odot}$), noting this result was incompatible with the results of Wakker et al. (1999a,b) who found an ionization-corrected value of [S/H] = -1.05 ± 0.12 in Complex C along the line of sight toward Mrk 290. They dismiss ionization corrections as accounting for the difference,

arguing that bringing their Mrk 817 abundance of S II in line with the abundance Wakker found toward Mrk 290 would result in an an unreasonably high predicted value for the Hα emission measure. They suggest that spatial H I substructure within Complex C below the resolution limit of available 21 cm data explains the disagreement between their S II abundance and that reported previously by Wakker. Collins et al. (2003) also used Wakker's (2001) value of N(H I) and set FWHM = $10.8^{+3.2}_{-2.2}$ km s^{-1} on the basis of multiple detections of lines of O I, Fe II, and S II. In the velocity interval -140 km s^{-1} $\leq v_{\rm LSR}$ ≤ -80 km s^{-1}, they found [S II/H I] = -0.34 ± 0.08 ($0.46^{+0.09}_{-0.08}$ $Z_{\odot}$) from the 1250Å line only, while noting that like in the case of Mrk 290, the true value may turn on the question of whether an ionization correction is required. The other undepleted species for which they quote an abundance is [O I/H I] = $-0.59^{+0.25}_{-0.17}$ ($0.26^{+0.20}_{-0.08}$ $Z_{\odot}$) from the 924Å line only, consistent with the upper limit they set for Mrk 290 in the same study. Shull et al. (2011) present *HST* COS/G130M data they integrate over a single velocity interval encompassing both of our Complex C components from -190 km s^{-1} $\leq v_{\rm LSR} \leq -70$ km s^{-1}, from which they derive [S II/H I] = -0.60 ± 0.10 ($0.25^{+0.07}_{-0.05}$ $Z_{\odot}$) and [O I/H I] = -0.47 ± 0.24 ($0.34^{+0.25}_{-0.14}$ $Z_{\odot}$). Their O I abundance is based on the Collins et al. (2003) column density, as Shull et al. found only an upper limit of log N(O I) $\geq$ 14.98. It differs from the Collins et al. (2003) abundance for the same column density as a result of using a different value of log N(H I), 19.50 ± 0.01, based on GBT 21 cm observations. The weighted mean of their reported O I and S II abundances is -0.56 ± 0.09 ($0.27^{+0.06}_{-0.05}$ $Z_{\odot}$). However we

note that their reported value of [S II/H I] is considerably lower than what we calculate given their N(S II) and N(H I), -0.35 ± 0.08 ($0.45^{+0.09}_{-0.08}$ $Z_{\odot}$), which is more consistent with their reported O I abundance. Together, they give a weighted mean metallicity of -0.38 ± 0.25 ($0.42^{+0.33}_{-0.18}$ $Z_{\odot}$).

The Effelsberg 21 cm spectrum of this component shows a profile asymmetry with a wing extending to the blue, although we note that this asymmetry does not match that seen in the UV line profiles. Nevertheless, we fit only a single Gaussian to the 21 cm data with $v_{\rm LSR} = -107$ km s^{-1} and FWHM = 26 km s^{-1}, for N(H I) = $(2.96 \pm 0.09) \times 10^{19}$ cm^{-2}, or log N(H I) = 19.47 ± 0.01. Adding an additional component to fit the wing does not change N(H I) within the uncertainty of a single component. Shull et al. (2011) measured a GBT spectrum toward Mrk 817, fitting a single Gaussian to the CIA component with $v_{\rm LSR} = -108$ km s^{-1}, FWHM = 27.5 ± 0.3 km s^{-1}, and N(H I) = $(3.17 \pm 0.05) \times 10^{19}$ cm^{-2}, or log N(H I) = 19.50 ± 0.01. A very broad component appears below -120 km s^{-1} and above $+30$ km s^{-1} that prevents the flux from going to zero between the HVC and the IVC in this sightline. We think this apparent component is not real, and that a bad baseline fit to their data accounts for the discrepancy relative to our N(H I) value.

We find [O I/H I] = -0.50 ± 0.10 ($0.32^{+0.08}_{-0.07}$) for CIA in this direction based on the detection of eight lines of O I. For S II, we detect only the 1253 Å line, as the intrinsically stronger λ1259 line is lost to a data dropout. Our measurement of the 1253 Å line gives an equivalent width of $30 \pm 2.0 \pm 3.1$ mÅ, log N(S II) = $14.32^{+0.05}_{-0.07}$ and [S II/H I] = -0.27 ± 0.05 ($0.54^{+0.07}_{-0.06}$ $Z_{\odot}$).

While our S II column density is within errors of other authors, we lack the leverage of the 1259 Å line and consider our S II abundance less reliable than O I. Therefore, we prefer our [O I/H I] value as the definitive metallicity for this cloud. We note, however, that given the effects of significant H I substructure in Complex C discussed previously, our metallicity result for this cloud may be overestimated. If this is true, it would revise our metallicity downward and bring it better in line with expectations for Complex C. Given the distance and direction of Complex C, the expected ionization correction for S II suggests that our measured value of [S II/O I] = +0.23 is consistent with the data.

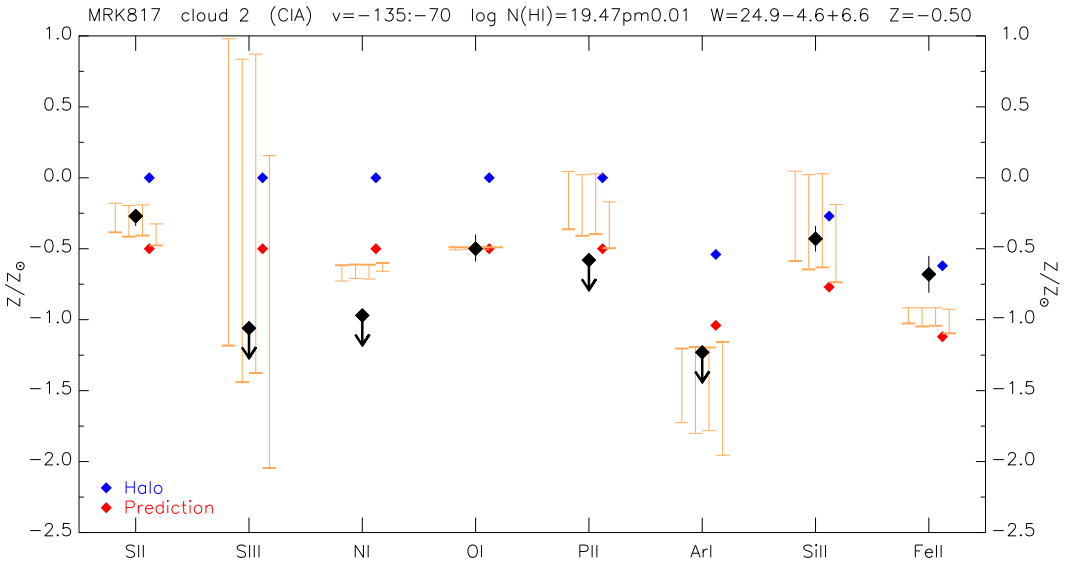

Figure 3.42 Abundance plot for Complex C cloud CIA toward Mrk 817 at -135 km s^{-1} $\leq v_{\rm LSR} \leq -70$ km s^{-1}. The plot parameters are the same as in Figure 3.41 but for our [O I/H I] metallicity of -0.50.

We detect lines of lines of N II, O I, Si II, S II, Fe II, and P II in the velocity range -70 km s^{-1} $\leq v_{\rm LSR} \leq -30$ km s^{-1}. The Mrk 817 sightline

passes through a region just off the edge of the IV Arch in H I maps (Wakker 2001a, Lehner et al. 2004), and we associate this absorption with IV Arch gas. All of the detected lines are blended to some degree with Galactic absorption at zero velocity. The UV detections correspond with a 21 cm feature in the Effelsberg spectrum to which we fit a single Gaussian at $v_{\rm LSR} = -39$ km s^{-1} with FWHM = 25 km s^{-1} and N(H I) = $(1.58 \pm 0.11) \times 10^{19}$ cm^{-2}, or log N(H I) = 19.20 ± 0.03. Among undepleted ions, we find [O I/H I] = -0.39 ± 0.20 ($0.41^{+0.24}_{-0.15}$ $Z_\odot$), [S II/H I] = $+0.13 \pm 0.14$ ($1.35^{+0.51}_{-0.37}$ $Z_\odot$), and [P II/H I] = $+0.09 \pm 0.18$ ($1.23^{+0.86}_{-0.32}$ $Z_\odot$). The abundance pattern is shown in Figure 3.43. We cannot immediately explain the discrepancy between the abundances of O I on the one hand and S II and P II on the other. The O I result is based on confident, blended detections of the 976 Å, 1039 Å, and 929 Å lines, and the less confident detection of two additional, weaker lines, 924 Å and 921 Å, whose blended detections are statistically significant but somewhat noisier and more dependent on continuum placement. Therefore, the formal error on N(O I) may be somewhat underestimated. While we do not find a literature O I measurement for this component against which to compare our measurement, we note that Richter et al. (2001c) report [O I/H I] = $-0.01^{+0.35}_{-0.27}$ through IV Arch gas toward PG1259+593; at the same time, our value of [S II/H I] is very similar to theirs ($+0.11^{+0.11}_{-0.08}$; $1.29^{+0.37}_{-0.22}$ $Z_\odot$). Using N(H I) and N(P II) in Lehner et al. (2004) for an IV Arch component toward Mrk 817 at $v_{\rm LSR}$ = -40 km s^{-1} with an unspecified velocity width, we compute [P II/H I] = $+0.16 \pm 0.16$ ($1.45^{+0.65}_{-0.45}$ $Z_\odot$) from their observations, well within errors of our

value. In Figure 3.43, it is clear that for a cloud at $z = 1$ kpc with log N(H I) = 19.2, the expected pattern is that S II and P II are less ionized than H I, since [S II/H I] is greater than [S/H] by ∼0.3 dex and [P II/H I] is greater than [P/H] by ∼0.4 dex. Assuming our measured metallicity log $Z \sim -0.4$, the predicted values of [S II/H I] and [P II/H I] are both ~ -0.1, while the measured abundances are $\sim +0.1$. If our O I measurement is reliable, the apparent underabundance of O I relative to the other undepleted ions along this sightline, while inconsistent with expectations for typical IVCs, may in fact be real.

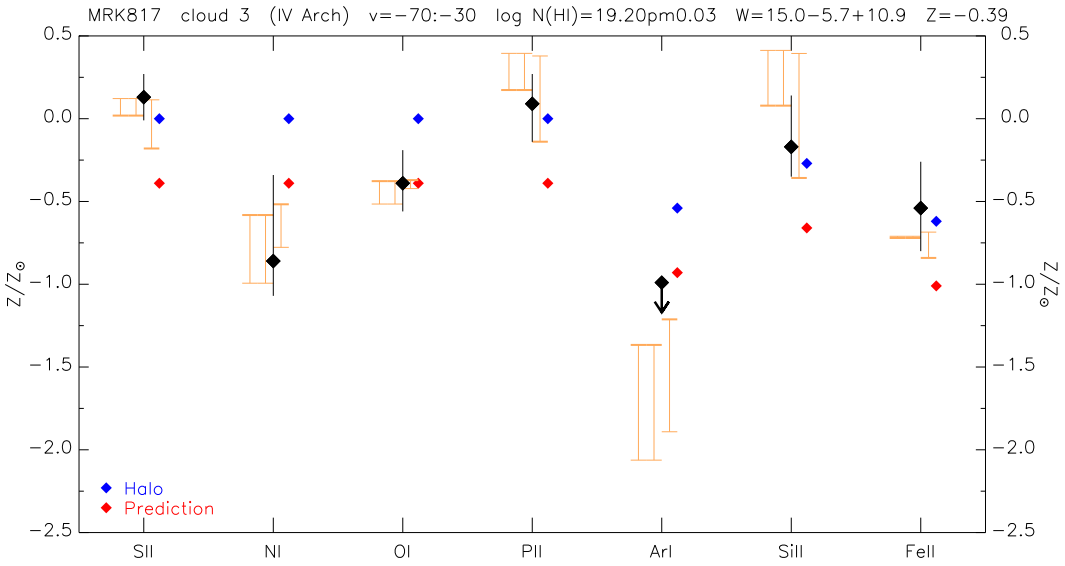

Figure 3.43 Abundance plot for the IV Arch toward Mrk 817 at -70 km s^{-1} $\leq v_{\rm LSR} \leq -30$ km s^{-1}. The plot parameters are the same as in Figure 3.41 but for our [O I/H I] metallicity of -0.39.

Finally, in this sightline we detect C III λ977 at $v_{\rm LSR} = +77$ km s^{-1} with a FWHM of 17 km s^{-1} and an equivalent width of $31.7 \pm 4.4 \pm 6.5$ mÅ.

From this we derive log N(C III) = $13.00^{+0.24}_{-0.45}$. The velocity range over which we detect this line does not match to any feature in the 21 cm spectrum toward Mrk 817, although it is coincident with the red wing of the H I Lyman series absorption in the UV. The 5σ noise limit of the 21 cm spectrum corresponds to N(H I) $\leq 5.4 \times 10^{18}$ cm^{-2}, or log N(H I) ≤ 18.73; however, the fit to the baseline in this spectrum is bad and we believe this N(H I) upper limit is not reliable. Attempts to find a lower limit by fitting the red wing of the Lyman series lines results in a value of N(H I) of $\sim 10^{14}$ cm^{-2}, far below the expected metal line detection threshold. Fox et al. (2006) detected this line at $v_{\rm LSR}$ = 75 ± 9 km s^{-1} and width 18 ± 3 km s^{-1}, quoting log N (C III) = $12.77^{+0.11}_{-0.15}$; they also note O VI absorption in this sightline at $v_{\rm LSR} = 71 \pm 9$ km s^{-1}. They conclude that such highly ionized HVCs have low H I column densities ($\lesssim 10^{18}$ cm^{-2}) and are formed under hot ($T \sim 10^6$ K) conditions conditions in Galactic outflows. If the component observed in C III and O VI toward Mrk 817 at this velocity is associated with this phenomenon, we would expect it to have near-solar metallicity. The existing data are insufficient to determine this.

In summary, toward Markarian 817 we detect two Complex C components: the CIC core at $v_{\rm LSR} \sim$ -160 km s^{-1}, for which we find $Z = -0.74$ (0.18 $Z_\odot$), and the CIA core at $v_{\rm LSR} \sim$ -100 km s^{-1} with $Z = -0.50$ (0.32 $Z_\odot$), consistent with previous measurements of Complex C. At lower velocities, we see absorption from the IV Arch at $v_{\rm LSR} \sim$ -50 km s^{-1}, which we argue has log $Z \sim -0.4$ (0.4 $Z_\odot$). Lastly, we note absorption in C III λ977 at $v_{\rm LSR} \sim 75$

km s^{-1} not associated with 21 cm emission and only weak absorption in the H I Lyman series, which we therefore left out of our abundance analysis for this sightline.

3.4.10 Markarian 876

The sightline toward Mrk 876 samples some of the lower-density gas (N(H I) $\sim 10^{19}$ cm^{-2}) in Complex C, and is one of several probing Complex C in which O VI absorption is seen (Wakker et al. 2003). Intermediate-velocity absorption is seen near -50 km s^{-1} in the Lower IV Arch cloud IV20 (Kuntz & Danly 1996), and at the lowest negative velocities the sightline intercepts the Draco Nebula, an object with properties between those of IVCs and Galactic molecular clouds. However, the Mrk 876 sightline passes through an exceptionally large column of Galactic H_2 (2.3×10^{18} cm^{-2}; Shull et al. 2000), resulting in strong contamination of many high-velocity absorption features. A representative sample of ions detected in our UV spectra is shown in Figures 3.44-3.46.

Absorption in the velocity range -205 km s^{-1} $\leq v_{\rm LSR} \leq -150$ km s^{-1} is attributed to the CD core of Complex C Wakker (2001a). Murphy et al. (2000) detected this component in early *FUSE* observations of Mrk 876, noting the first detection of O VI in an HVC. While they looked for absorption in a number of low ion lines, they report only the confident detection of Fe II λ1144, for which they derive log N(Fe II) = $13.67^{+0.13}_{-0.18}$. Given log N(H I) = $18.61^{+0.08}_{-0.09}$ from an Effelsberg 21 cm observation, they find [Fe II/H I] =

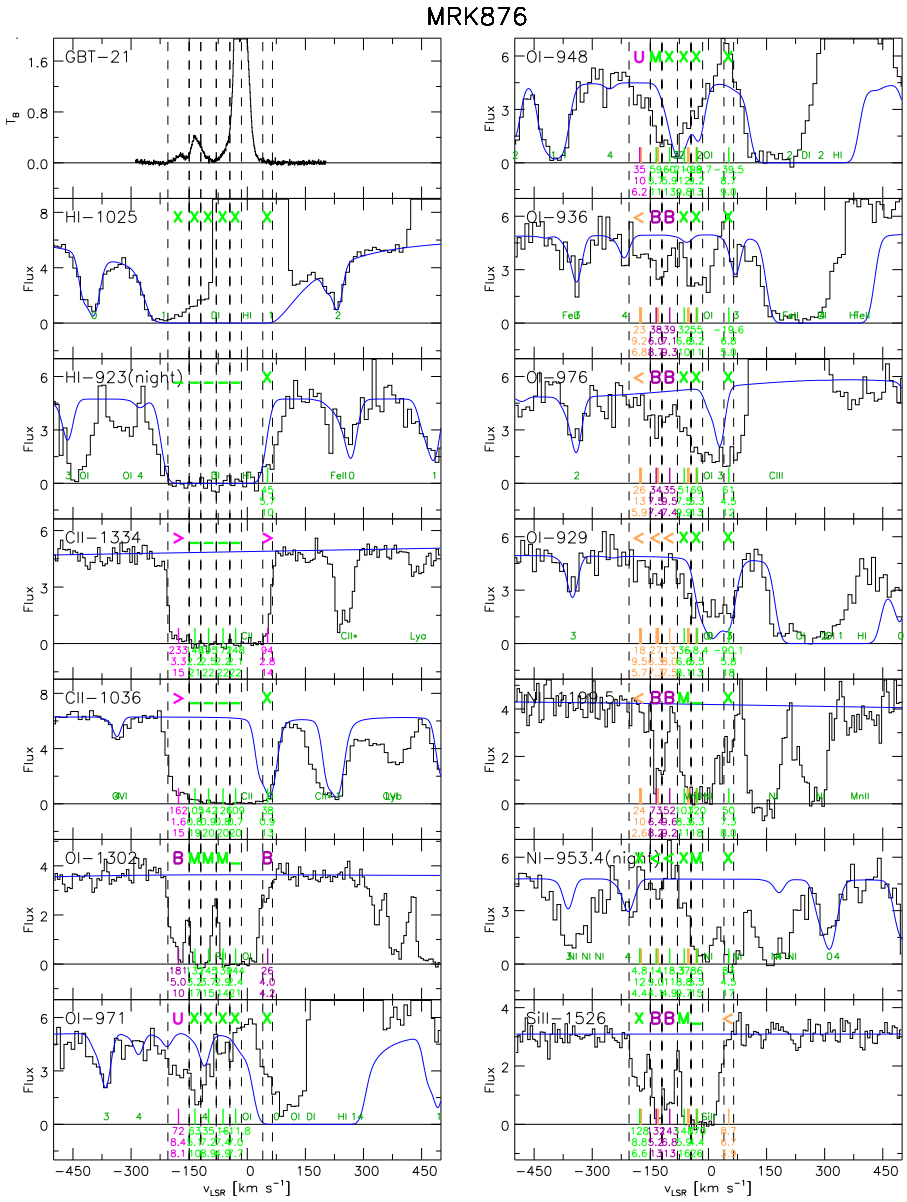

Figure 3.44 Cutouts of the GBT 21 cm spectrum and selected UV spectra toward Mrk 876 highlighting ions and lines most relevant to the determination of the metallicity and depletion of each component.

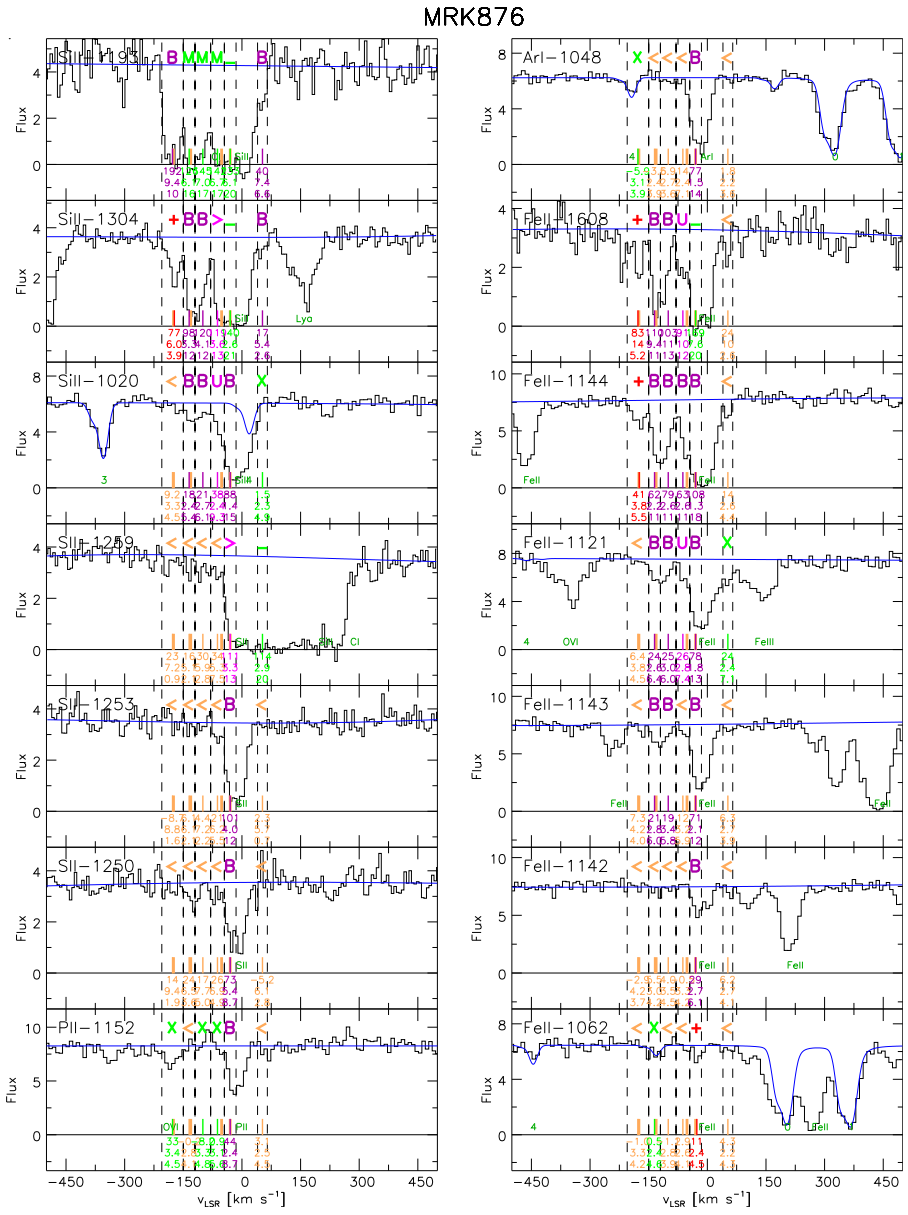

Figure 3.45 Cutouts of selected UV spectra toward Mrk 876 (continued).

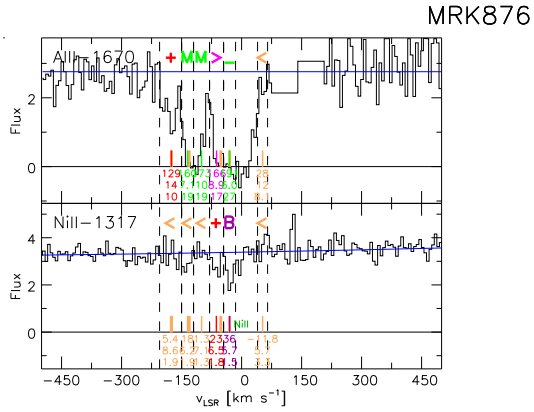

Figure 3.46 Cutouts of selected UV spectra toward Mrk 876 (continued).

-0.35 ± 0.14. Fe III λ1122 is absent in their spectrum, leading to a limit of N(Fe III)/N(Fe II) < 0.22. Sembach et al. (2003) noted the presence of O VI in their data at a centroid velocity of $v_{\rm LSR} = -173$ km s^{-1}, quoting N(O VI) $= 14.05 \pm 0.04 \pm 0.13$ over -200 km s^{-1} $\leq v_{\rm LSR} \leq -100$ km s^{-1}, taking into account all the Complex C gas in the sightline. Collins et al. (2007) made use of additional *FUSE* exposure time and better-quality *HST* STIS data in their study of this component, integrating absorption over -210 km s^{-1} $\leq v_{\rm LSR} \leq -155$ km s^{-1} for which they quote $b = 15.4^{+3.5}_{-2.5}$ km s^{-1} and [O I/H I] $= -0.70^{+0.18}_{-0.15}$. More recently, Shull et al. (2009) searched for Si II and Si III absorption this sightline with *HST* STIS and *FUSE*, reporting log N(Si II) $= 13.67^{+0.09}_{-0.07}$ and log N(Si III) ≥ 13.61 over -230 km s^{-1} $\leq v_{\rm LSR} \leq -155$ km s^{-1}. From these measurements they derive a range of possible ionization parameters, $-3.42 \leq \log U \leq -3.31$, and corresponding metallicites, $-2.31 \leq \log (Z/Z_{\odot}) \leq -1.10$. The CD core component is weakly detected in 21 cm H I emission, blended with the feature due to the CIB core, discussed

below. We fit a single Gaussian to spectrum centered at $v_{\rm LSR} = -175$ km s^{-1} with FWHM = 23 km s^{-1} and N(H I) = (5.6 ± 0.5) $\times 10^{18}$ cm^2, or log N(H I) = 18.75 ± 0.04. The corresponding UV lines show a distinct profile asymmetry with broad ($\Delta_v \sim 55$ kms) wings centered at $v_{\rm LSR} \sim -180$ km s^{-1} and a stronger core ($\Delta_v \sim 55$ kms) centered near the peak of the 21 cm emission. This structure is visible in Figures 3.44-3.46, particularly in O I λ1302, Si II λ1526, and Al II λ1670; other lines (e.g., Fe II λ1608) show the broad component only weakly relative to the strong core. This asymmetry is not indicated in 21 cm spectrum, likely indicating unresolved substructure below the angular resolution of the GBT. Multiple detections of lines of Si II and O I imply an intrinsic linewidth of FWHM = $27.1^{+11.5}_{-6.2}$ km s^{-1}, or Doppler $b = 16.3^{+6.9}_{-3.7}$ km s^{-1}, for the broad feature. Our inferred abundances for the CD core are shown in Figure 3.47. Among undepleted species, we only detect O I confidently, yielding a metallicity of [O I/H I] = -0.58 ± 0.38, or $0.26^{+0.48}_{-0.13}$ $Z_\odot$. While compatible with our expectation for Complex C ($Z \sim 0.1 - 0.3$ $Z_\odot$), unresolved H I structure in the GBT spectrum may bias our N(H I) value toward a lower column than actually exists for this component, and therefore our estimate of Z is likely an overestimate. The predicted abundances assume our measured [O I/H I] metallicity, but again are subject to revisions of N(H I).

The CIB core component near -133 km s^{-1} is more well-studied than the CD core. Some authors do not distinguished these components separately, setting velocity intervals for computing column densities as wide as -210 km

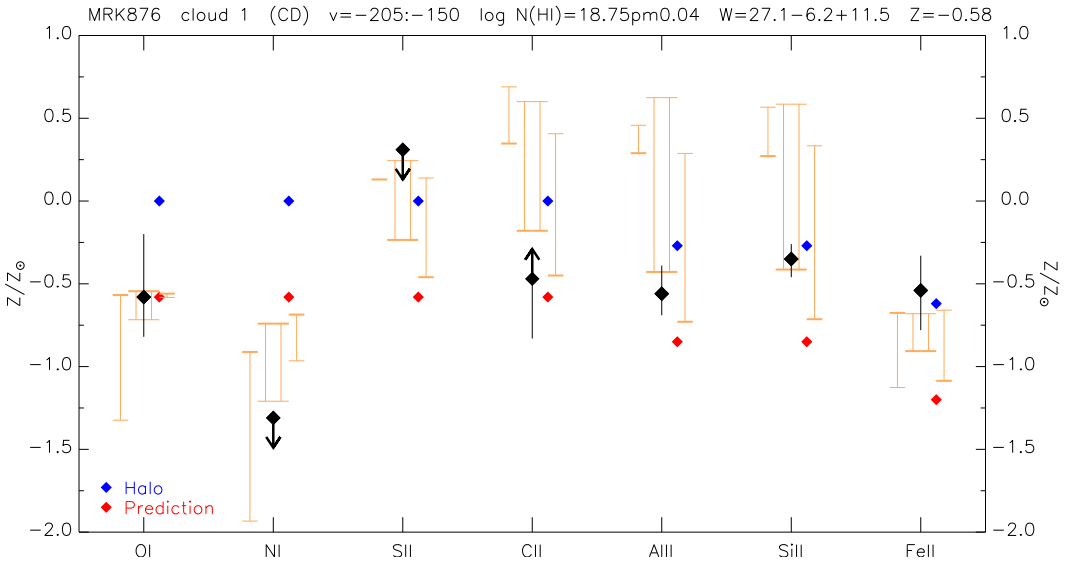

Figure 3.47 Abundance plot for the CD core of C-South toward Mrk 876 at -205 km s^{-1} $\leq v_{\rm LSR} \leq -150$ km s^{-1}. The range of possible ionization corrections is shown for 1, 5, and 10 kpc ($\log \phi = 6.66$, 5.55, and 5.55) and the extragalactic background at densities between $\log n = -3$ and -1 (orange bars, left to right). A Halo depletion pattern and predicted abundances with red points given our measured metallicity [O I/H I] $= -0.58$ are shown.

s^{-1} $\leq v_{\rm LSR} \leq -95$ km s^{-1} (Gibson et al. 2001, Collins et al. 2003, Sembach et al. 2003). There is little agreement as to the velocity width of the CIB core absorption in part because in both 21 cm emission and UV absorption it is strongly blended with the neighboring CD core lines. Previous studies have considered only a single velocity interval corresponding to the extent of the 21 cm emission, but we argue that the UV spectra show two strongly-blended but distinct components both belonging to CIB that we have designated CIB-1 (-150 km s^{-1} $\leq v_{\rm LSR} \leq -120$ km s^{-1}) and CIB-2 (-120 km s^{-1} $\leq v_{\rm LSR} \leq -80$ km s^{-1}). That the $v_{\rm LSR} \sim -133$ km s^{-1} absorption feature consists of

two blended components is most evident in Figures 3.44-3.46 in lines of N I (λ1199.5), Fe II (λ1608), and Si II (λ1526, 1193, 1304, and 989). Splitting our velocity integration window for CIB into two separate units makes direct comparison with previous authors' work difficult, but we can draw some general conclusions. Murphy et al. (2000) detected several low-ion species in the range -160 km s^{-1} $\leq v_{\rm LSR} \leq -100$ and infer $b = 12.1 \pm 5.6$ km s^{-1} from five Fe II lines. They find [N I/H I] $= +0.087 \pm 0.032$ and report limits for [P II/H I] $< +0.30$ and [Ar I/ H I] < -0.47, attributing the apparent low Ar I abundance to a photoionization effect. Collins et al. (2003) defined an interval -150 km s^{-1} $\leq v_{\rm LSR} \leq -95$ km s^{-1} in their *FUSE* and *HST* GHRS/STIS data roughly corresponding to CIB-1, from which they compute [O I/H I] $= -0.54^{+0.43}_{-0.29}$ and [N I/H I] $= -1.19^{+0.14}_{-0.12}$ assuming $b = 16.1^{+7.4}_{-3.9}$ km s^{-1} measured from all detected lines on a single COG. They revisited this component in Collins et al. (2007), updating the velocity integration interval to -155 km s^{-1} $\leq v_{\rm LSR} \leq -85$ km s^{-1}. They also revise their log N(H I) value for this component upward from $19.26^{+0.03}_{-0.03}$ to $19.30^{+0.03}_{-0.04}$ on account of the different velocity limits in each case. This slightly reduces their O I metallicity to $-0.59^{+0.22}_{-0.21}$, assuming their measured $b = 17.8^{+2.0}_{-1.8}$ km s^{-1}. The measurements of N(Si II) and N(Si III) in the range -155 km s^{-1} $\leq v_{\rm LSR} \leq -90$ km s^{-1} made by Shull et al. (2009) were used to constrain the range of implied ionization parameters for this component to $-3.34 \leq \log U \leq -3.26$ and the corresponding metallicites to $-1.52 \leq \log\,(Z/Z_{\odot}) \leq -0.53$. Shull et al. (2011) improved upon their earlier work with new data from *HST* COS, obtaining linewidth of $b = 20$

km s^{-1}and [O I/H I] $= -0.83^{+0.19}_{-0.19}$. CIB-1 is strongly detected in the GBT spectrum to which we fit a Gaussian centered at $v_{\rm LSR} = -131$ km s^{-1} with FWHM = 33 km s^{-1} and N(H I) $= (1.29 \pm 0.05) \times 10^{19}$ cm^{-2}, or log N(H I) $= 19.11 \pm 0.02$. We determined the intrinsic linewidth, FWHM $= 15.9^{+4.9}_{-2.6}$ km s^{-1}, or $b = 9.5^{+2.9}_{-1.6}$ km s^{-1}, from the clear detection of three lines of Si II. Abundances for this component are shown in Figure 3.48. The stronger lines of O I are too nearly saturated and blended with their comparably-strong CIB-2 counterparts to measure, but from the weaker lines λ936 and λ976 we find [O I/H I] $= -0.54 \pm 0.19$ ($0.29^{+0.16}_{-0.10}$ $Z_\odot$).

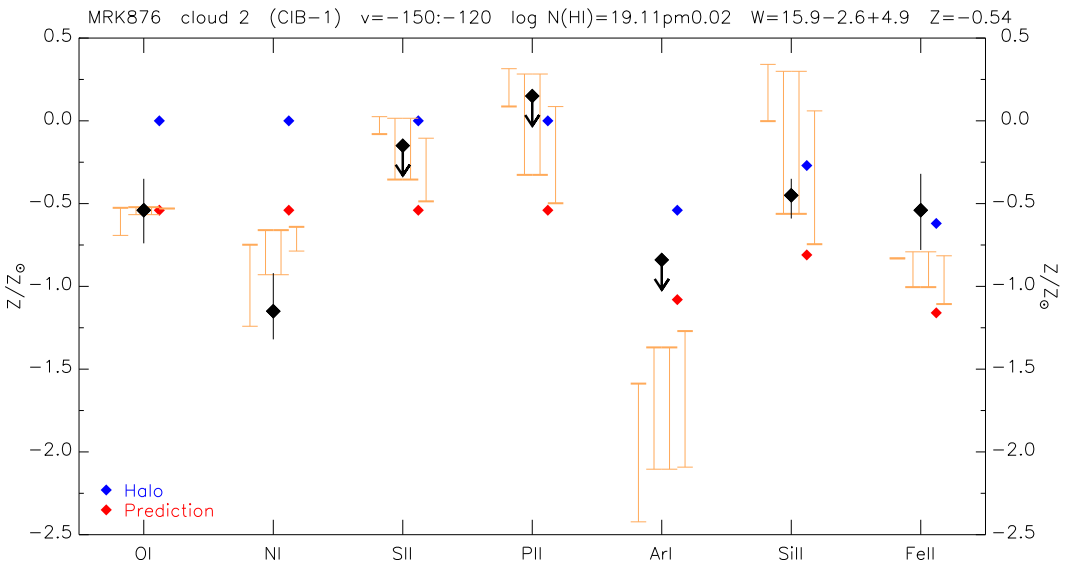

Figure 3.48 Abundance plot for the "CIB-1" core of Complex C toward Mrk 876 at -150 km s^{-1} $\leq v_{\rm LSR} \leq -120$ km s^{-1}. The range of possible ionization corrections is shown for 1, 5, and 10 kpc (log ϕ = 6.66, 5.55, and 5.55) and the extragalactic background at densities between log $n = -3$ and -1 (orange bars, left to right). A Halo depletion pattern and predicted abundances with red points given our measured metallicity [O I/H I] $= -0.54$ are shown.

CIB-2 also appears in the 21 cm data as a "shoulder" on the red wing of the CIB-1 component. We simultaneously fit a single Gaussian to this feature with the CIB-1 fit, centered at $v_{\rm LSR} = -120$ km s^{-1} with FWHM = 25 km s^{-1} and N(H I) = (9.5 ± 0.5) $\times 10^{18}$ cm^{-2}, or log N(H I) = 18.99 ± 0.02. Three lines of Si II were detected, sufficiently separated from the CIB-1 component to determine the intrinsic linewidth; we find FWHM = $16.5^{+4.4}_{-1.6}$ km s^{-1}, or Doppler $b = 16.3^{+6.9}_{-3.7}$ km s^{-1}. The resulting abundances are shown in Figure 3.49. We find a slightly higher metallicity for this component, [O I/H

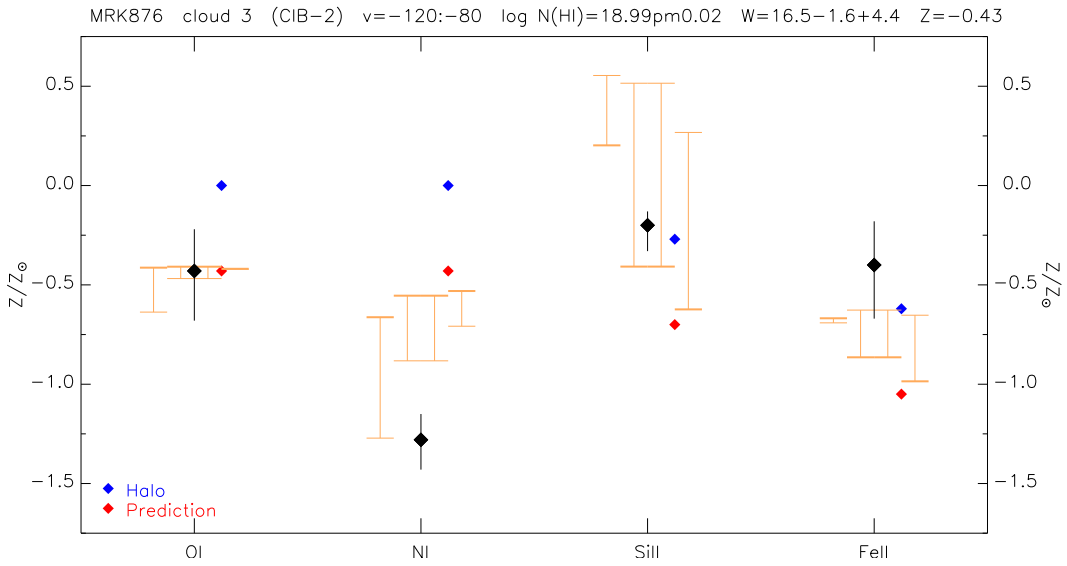

Figure 3.49 Abundance plot for the "CIB-2" core of Complex C toward Mrk 876 at -120 km s^{-1} $\leq v_{\rm LSR} \leq -80$ km s^{-1}. The range of possible ionization corrections is shown for 1, 5, and 10 kpc (log ϕ = 6.66, 5.55, and 5.55) and the extragalactic background at densities between log $n = -3$ and -1 (orange bars, left to right). A Halo depletion pattern and predicted abundances with red points given our measured metallicity [O I/H I] = -0.43 are shown.

I] = -0.43 ± 0.21 ($0.37^{+0.23}_{-0.14}$ $Z_\odot$), as compared to CIB-1 but the two values are

within measurement uncertainties of each other.

The sightline toward Mrk 876 likely intercepts some of the gas in the Lower IV Arch cloud IV20 ($\ell = 102°$, $b = +36°$; Kuntz & Danly 1996), which should show absorption lines around $v_{\rm LSR} = -50$ km s^{-1}. This velocity is separated by little more than ~ 10 km s^{-1} from the Draco Nebula, discussed below; no substantial abundance work has been previously done on either component to guide our selection of velocity integration intervals for each cloud. We initially thought that absorption from the two components was sufficiently indistinguishable among the UV spectra and defined a single velocity interval combining absorption from both sources over -65 km s^{-1} $\leq v_{\rm LSR} \leq -20$ km s^{-1}. This approach has the advantage of preserving as much 21 cm flux as possible in the Draco Nebula to result in the most reliable N(H I) estimate we can make, even though in principle it is contaminated by 21 cm flux from IV20. However, IV20 is not obviously detected in the GBT spectrum above the signal level in the wings of the Draco Nebula feature, which itself is stronger than the zero-velocity Galactic H I signal. Further examination of the UV data suggests that IV20, while strongly blended with the Draco signal, is distinct; this is most easily seen in, e.g., C II* λ1335, S II λ1253, Ni II λ1317, and the intrinsically stronger lines of Fe II. We therefore split the components at $v_{\rm LSR}$ $= -45$ km s^{-1}, setting the higher negative-velocity limit for IV20 at -80 km s^{-1} so as to be contiguous with the CIB-2 velocity integration window. The choice was not arbitrary; strong edges in the absorption profiles of several lines such as N I λ953.4, O I λ1302 and 1039, Si II λ1526 and 1304, and Al II λ1670

suggest placement of the division in velocity between the two components. Cutouts of the lines used to determine the velocity windows for IV20 and the Draco Nebula are shown in Figure 3.50.

There is no evident 21 cm emission within the stated velocity limits for IV20 above the wing of the strong Draco Nebula signal at $v_{\rm LSR} = -30$ km s^{-1}; we can therefore rule out a feature of N(H I) $\gtrsim 4.5 \times 10^{18}$ cm^{-2}, or log N(H I) $\gtrsim 18.65$, at the 5σ level, assuming a linewidth of 20 km s^{-1}. The IV20 velocity interval is completely saturated in the Lyman series H I lines, so we cannot derive a reliable lower limit for N(H I) by fitting them. We can estimate N(H I) by assuming a metallicity for this cloud. Wakker (2001a) gives $Z \sim 1\ Z_{\odot}$ for the Lower IV Arch along several sightlines. If IV20 in fact has solar metallicity, N(H I) would be about 8×10^{18} cm^{-2}, or log N (H I) $\gtrsim 18.80$, well above the detection threshold of the GBT spectrum. We therefore assumed the upper limit from the GBT spectrum and from five detected lines of O I we derive an intrinsic linewidth of FWHM = $16.0^{+6.6}_{-4.5}$ km s^{-1}, or $b = 9.6^{+4.0}_{-2.7}$ km s^{-1}. With this information, we find [O I/H I] $< +0.25$ ($< 1.78\ Z_{\odot}$); however, at this limit, the abundances of Si II, Fe II, and Ni II fall outside the ranges predicted by our ionization models. A compromise metallicity of log $Z = +0.1$ ($1.26\ Z_{\odot}$) brings these species along with O I in line with the models. Inferred abundances are shown in Figure 3.51 for this value. While we cannot rule out a lower metallicity for this cloud, the N(H I) detection limit suggests a slightly supersolar metallicity, consistent with a Galactic Fountain origin. It is notable that such a metallicity also brings N I

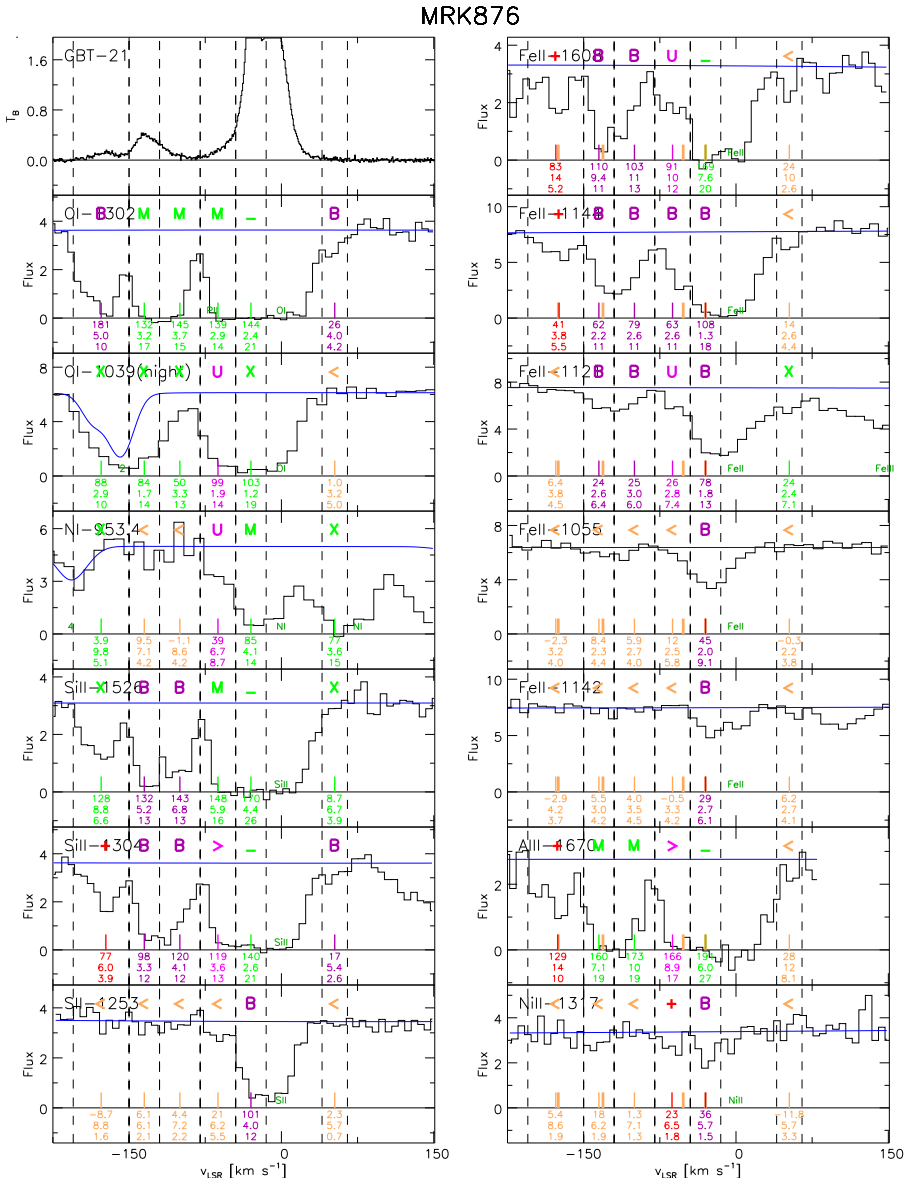

Figure 3.50 Cutouts of the GBT 21 cm spectrum and selected UV spectra toward Mrk 876 illustrating the lines used to determine the velocity integration limits for the IV20 and Draco Nebula components described in the main text.

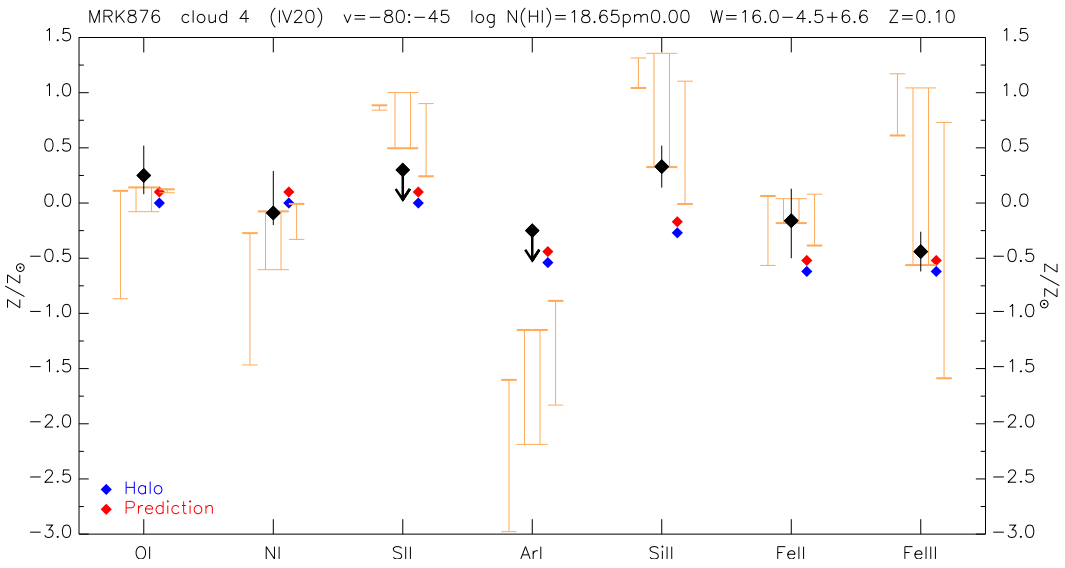

Figure 3.51 Abundance plot for IV20 toward Mrk 876 at -80 km s^{-1} $\leq v_{\rm LSR}$ ≤ -45 km s^{-1}. The range of possible ionization corrections is shown for 1, 5, and 10 kpc (log ϕ = 6.66, 5.55, and 5.55) and the extragalactic background (log ϕ = 4.53) at densities log $n = -3$ and -1 (orange bars, left to right). A Halo depletion pattern and predicted abundances with red points given our inferred metallicity (log $Z = +0.1$) are shown.

into agreement with the ionization models to within errors, suggesting it is less underabundant than expected; this may indicate the presence of secondary N in this cloud.

The Draco Nebula (LBN 406/415; Lynds 1965) is an optical reflection nebula found to be an H I 21 cm emission source by Goerigk et al. (1983), who noted its positional coincidence with faint, diffuse nebulosity in the original Palomar Observatory Sky Survey plates. It was the first high- latitude ($b \sim +38°$) nebula detected in molecular lines, including ^{12}CO, ^{13}CO, and H_2CO (Goerigk et al. 1983, Mebold et al. 1985) and was cataloged by IRAS

as part of the high-latitude "infrared cirrus" at 60 μm and 100 μm, indicating large columns of dust (Goerigk & Mebold 1986). Given the object's Galactic latitude, its appearance at optical wavelengths is likely due to backscattering of the integrated light of the Galactic plane (Mebold & Kalberla 1984). Kalberla et al. (1984) made 21 cm observations of the Draco Nebula with the Westerbork Synthesis Radio Telescope (WSRT) in which they interpreted a jet-like structure in H I emission emerging from an outlet in a low-velocity shock front between the Nebula and the surrounding gas as coincident with a high-velocity filament at $v_{\rm LSR} = -180$ km s^{-1}. They further argue that the observed soft X- ray emission in the vicinity of the Nebula is the result of thermal bremsstrahlung from the interaction of high-velocity gas and gas in the Nebula itself. A similar argument was made by Herbstmeier et al. (1993) on the basis of CO observations. Distance estimates in the literature range from $z > 180$ pc (Lilienthal et al. 1991) to $z < 2.5$ kpc (Mebold et al. 1985, Goerigk & Mebold 1986). Goerigk and Mebold suggested their distance limit is compatible with the upper limit of 2.1 kpc to the Complex C core CIIIC reported by Songaila et al. (1985), but more recent estimates of the distance to Complex C place it much higher off the Disk (Wakker et al. 2007). More recently, Richter et al. (2003) quote a disk height of 0.3 kpc $\leq z \leq$ 0.8 kpc and Wakker (2006) claims $\sim$ 0.5 kpc, which may place it near the thick disk/halo interface. UV-absorbing H I in the Nebula casts a "shadow" against the 0.25-keV X-ray background in the region (Snowden et al. 1991, Burrows & Mendenhall 1991); Moritz et al. (1998) interpreted the observed shadowing

as evidence for a bright, hot ($T \sim 10^6$ K) Galactic X-ray corona in its direction. The implication of hot gas at the distance to the Draco Nebula is borne out by observations of very highly-ionized oxygen by Shelton et al. (2010), who observed O VI, O VII, and O VIII absorption in hot gas near the Nebula. They found that reproducing the observed line ratios may require additional processes other than shock heating, including heat conduction, mixing, and radiative cooling of very hot ($T > 10^6$ K) gas. This cloud, low off the Disk and evidently interacting with hot gas there, may exemplify the last stage of the return flow of the Galactic Fountain before the gas returns to the disk (Richter et al. 2003). We therefore expect it to have supersolar metallicity.

While the Draco Nebula technically falls out of the scope of this work by virtue of its deviation velocity, we include it in our analysis because no previous abundance work on it exists in the literature. As described above, we set velocity integration limits of -45 km s^{-1} $\leq v_{\rm LSR} \leq -15$ km s^{-1}. At the low negative-velocity end of the integration range set by the UV absorption there is certainly Milky Way contamination leading to greater uncertainty in the measured column densities than we would obtain if it were further separated in velocity from the Galaxy. The Nebula is a strong source of 21 cm emission; we fit a single Gaussian to the data centered at -30 km s^{-1} with FWHM = 29 km s^{-1} and N(H I) = $(7.94 \pm 0.04) \times 10^{18}$ cm^{-2}, or log N(H I) = 19.90 ± 0.01. The Nebula is clearly detected, albeit blended with zero-velocity Galactic absorption, in most of the low ions (S II, P II, Ar I, Si II, Fe II, Ni II). It is completely saturated in C II and C III yet among the few

instances in our entire sample with measurable C II* at $N(\text{C II}^*) = 13.99^{+0.19}_{-0.64}$. S III and Al II λ1670 are fully saturated, as are the strongest lines of some species, e.g., N I (λ1199.5 and 1200.2), O I (λ1302, 988.7, and 1039), Fe II (λ1608), and Si II, of which only the λ1020 line is measurable. Fe III λ1122 is measurable though strongly blended with both IV20 and Galactic absorption. We found the intrinsic linewidth in the Nebula, FWHM = $14.9^{+7.3}_{-5.1}$ km s^{-1} ($b = 8.9^{+4.4}_{-3.1}$ km s^{-1}), from detections of multiple lines of Si II and Fe II; the resulting abundances are shown in Figure 3.52. There are no useful O I lines from which to measure a metallicity on account of strong H_2 contamination, but from two detected (but blended) S II lines (λ1253 and 1250) and one lower limit (λ1259) we find [S II/H I]= $+0.23 \pm 0.56$ ($1.70^{+4.47}_{-1.23}$ $Z_\odot$). Fe II is more strongly depleted than predicted, consistent with expectations given the amount of dust implied by far infrared observations. Si II may be similarly depleted but we cannot state this definitively given the measurement uncertainties on N(Si II), which is determined solely by the strongly blended detection of λ1020.

Weak absorption in a number of lines of both low and high ions appears in our spectra near +52 km s^{-1}, of which we find no previous mention in the literature. These lines include N I λ1199.5, O I λ1302, Si II λ1193, Al II λ1670, and Fe II λ1144 and 1121. It appears as a strong wing in C II λ1334 and Si III λ1206. Similar wings are indicated in O VI (λ1031 and 1037), C IV (λ1548 and 1550), and Si IV (1393). Given the detections among highly-ionized species, we neither expect nor observe 21 cm emission associated with this component in the GBT spectrum. The detected low-ion lines have linewidths of FWHM

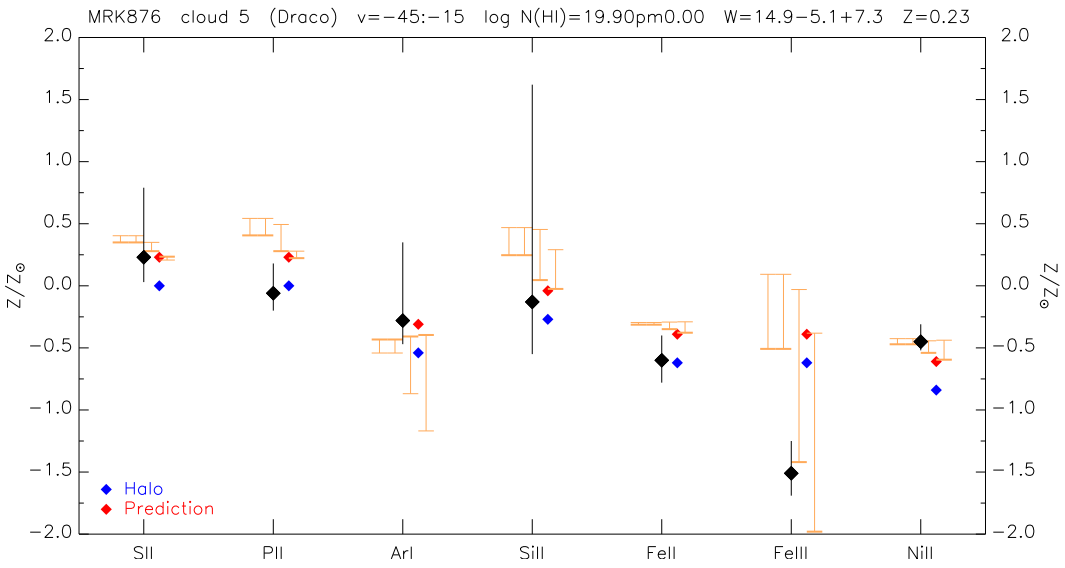

Figure 3.52 Abundance plot for the Draco Nebula toward Mrk 876 at -45 km s^{-1} $\leq v_{\rm LSR} \leq -15$ km s^{-1}. The range of possible ionization corrections is shown for 0, 1, and 2 kpc (log $\phi = 6.66$, 5.75, and 5.55) and the extragalactic background (log $\phi = 4.53$) at densities log $n = -3$ and -1 (orange bars, left to right). A Halo depletion pattern and predicted abundances with red points given our measured metallicity [S II/ H I] $= +0.23$ are shown.

~ 17 km s^{-1} ($b \sim 10$ km s^{-1}); given that information, we calculate a 5σ upper limit of N(H I) $< 8.4 \times 10^{17}$ cm^{-2}, or log N(H I) < 17.92. A component at about $+50$ km s^{-1} is required to adequately fit the red wing of the Lyman series H I lines, particularly λ923 and λ920 with a minimum N(H I) $\sim 1 \times 10^{17}$ cm^{-2}, or log N(H I) ~ 17.00. Assuming N(H I) is in the middle of this range, we find a value of $(5 \pm 4) \times 10^{17}$ cm^{-2}, or log N(H I) $= 17.70^{+0.26}_{-0.70}$. However, this result leads to [O I/ H I] $= -0.70 \pm 0.49$ ($0.20^{+0.42}_{-0.13}$ $Z_{\odot}$), well below the "typical" IVC metallicity $Z \sim 1$. If the actual metallicity of this IVC is close to solar, it would imply log N(H I) ~ 17.00, similar to the minimum H I column density required

to adequately fit the Lyman series line profiles. Therefore, we can only place very wide constraints on its metallicity of $0.13 \leq Z/Z_{\odot} \leq 1.10$. The reliability of this result is rendered highly uncertain because all of the detected lines are blended with absorption at slightly lower positive velocities. This material does not appear to be related to the zero-velocity Galactic absorption as it extends to positive velocities beyond the expected extent of the Galactic absorption wings. As a result, while we note the apparent IVC and quote the limits obtained above, we cannot claim a definitive judgment on the metallicity of this cloud. We also cannot clearly determine an ionization correction indicating the likely distance to this cloud from the Galactic plane, but note the strong lines of high-ions. Absent an independent distance estimate, we cannot distinguish among ionization mechanisms for this cloud and thus do not speculate on its origin or fate.

To summarize, the Mrk 876 sightline shows absorption from several distinct features at intermediate and high velocities. Three of these features relate to Complex C, each at an expected metallicity of a few-tenths solar. The core CD in the South extension of Complex C is seen at $v_{\rm LSR} \sim -177$ km s^{-1} and has a metallicity $Z \sim 0.3\ Z_{\odot}$. Two blended absorption units at $v_{\rm LSR} \sim -135$ and ~ -100 appear to be associated with the core CIB. They have metallicities of $Z \sim 0.3\ Z_{\odot}$ and $\sim 0.4\ Z_{\odot}$, respectively, but both values are within measurement errors of each other. At lower negative velocities, the sightline direction is coincident with the IV20 core of the Lower IV Arch near $v_{\rm LSR} \sim -50$ km s^{-1}, blended with absorption from the Draco Nebula at

$v_{\rm LSR} \sim -30$ km s^{-1}. While we find a metallicity of $Z \sim 1.25\ Z_{\odot}$ for IV20, that value is strongly driven by uncertainty in the value of N(H I) used to compute abundances and should be considered only approximate. The existing data do not allow us to rule out a subsolar abundance consistent with other published values among Lower IV Arch sightlines. The Draco Nebula itself is at sufficiently low negative velocity as to be partially blended with Galactic absorption. While not a proper IVC by definition, no previously published abundance for this enigmatic object exists. We find a distinctly supersolar abundance pattern near $Z \sim 1.7\ Z_{\odot}$, but this result is somewhat sensitive to depletion. Finally, we note the presence of a previously undescribed IVC near $v_{\rm LSR} \sim +50$ km s^{-1}, but are unable to derive a reliable abundance estimate for it.

3.4.11 NGC 1705

This sightline is among those in our dataset with the highest S/N ratio at 23 per resolution element in the *FUSE* spectra. NGC 1705 itself is an H I-rich dwarf galaxy with a systemic heliocentric velocity of $+628 \pm 9$ km s^{-1} (Meurer et al. 1992). York et al. (1990) observed lines of C IV and Si IV in its direction with *IUE* made especially prominent by a combination of relatively low spectral resolution and the large inherent velocity range of the absorption. They argued for a largely interstellar origin for the lines, rather than stellar absorption intrinsic to NGC 1705 itself. Sahu & Blades (1997) identify absorption near +230 km s^{-1} with the WW487 cloud (Bajaja et al.

1985, Wakker & van Woerden 1991). The NGC 1705 sightline falls less than 2° away from the position of WW487 in 21 cm maps (Sahu & Blades 1997), which is in turn $\sim 10°$ from the outermost H I contours that enclose both of the Magellanic Clouds (Sahu 1998). Sahu (1998) therefore proposed that WW487 is associated with the Magellanic Stream, implying an impact parameter of about 2 kpc. Heckman et al. (2001) observed this sightline with *FUSE* in a study of O VI absorption in the NGC 1705 outflow at $\sim +540$ km s^{-1}; they comment briefly on the WW487 contribution to their spectra, noting strong absorption at $v_{\rm LSR} = +270 \pm 15$ km s^{-1} in C III λ977, C II λ1036, and Lyman series lines of H I. Additionally, they saw broad (FWHM $= 100 \pm 15$ km s^{-1}) O VI absorption at $v_{\rm LSR} = +326 \pm 10$ km s^{-1} that they attribute to WW487, but here we argue that this absorption is associated with a velocity component distinct from WW487. Sembach et al. (2003) surveyed 100 extragalactic sightlines, including NGC 1705, for O VI absorption with *FUSE* finding two broad components in the range $+120$ km s^{-1} $\leq v_{\rm LSR} \leq +405$ km s^{-1} with linewidths $\sim$50 km s^{-1} they attribute to the Magellanic Stream. We see absorption by three distinct clouds at high velocities in our UV data, all of which are probably related to the Magellanic Stream. Comparison with previously published results, however, is difficult because of variations in the number and width of velocity integration windows defined by other authors. We note individual cases as appropriate. Furthermore, we see absorption due to an IVC at $v_{\rm LSR}$ ~ 100 km s^{-1} noted by previous authors whose association with the Magellanic Stream is unclear. A representative sample of ions detected in our UV spectra

is shown in Figures 3.53-3.54. H I in this sightline is significantly ionized. The high-velocity interstellar absorption components have no complementary detections in the LAB 21 cm spectrum, and absorption in the Lyman series of H I is strongly saturated. We have estimated N(H I) for each component from upper limits obtained from the LAB spectrum, lower limits from fits to the Lyman series absorption. Where possible, in the case of undepleted ions, we compare our estimates with the values implied by the expected metallicity of the gas.

A number of authors have noted an emission feature in 21 cm spectra toward NGC 1705 at $v_{\rm LSR} \sim +100$ km s^{-1}. Richter et al. (2003) saw emission at +87 km s^{-1} in Villa Elisa data, citing Arnal et al. (2000), but reports neither H_2 nor any ionic line absorption in *FUSE* data. The same 21 cm feature was noted by Sembach et al. (2003) and Lehner et al. (2004); however, neither group measured abundances from their UV spectra. Wakker (2006) reported no H_2 absorption in *FUSE* spectra in this direction at +88 km s^{-1} to a limit of log $N(H_2) < 14.00$. More recently, Collins et al. (2009) mention Si III absorption in an IVC in STIS E140M spectra toward NGC 1705 at velocities $+100\ {\rm km\ s^{-1}} \leq v_{\rm LSR} \leq +148\ {\rm km\ s^{-1}}$. They give $N({\rm Si\ III}) = 12.52^{+0.05}_{-0.06}$, but they do not derive an abundance with respect to H I. Finally, Shull et al. (2009) measured $N({\rm Si\ II}) \geq 14.63$ and $N({\rm Si\ III}) = 12.69^{+0.13}_{-0.09}$ in *FUSE* and STIS data in the range $+90\ {\rm km\ s^{-1}} \leq v_{\rm LSR} \leq +143\ {\rm km\ s^{-1}}$, citing a corresponding log N(H I) ≥ 19.67 from LDS 21 cm data.

We see a 21 cm emission feature at $\sim +97$ km s^{-1} in the LAB spectrum

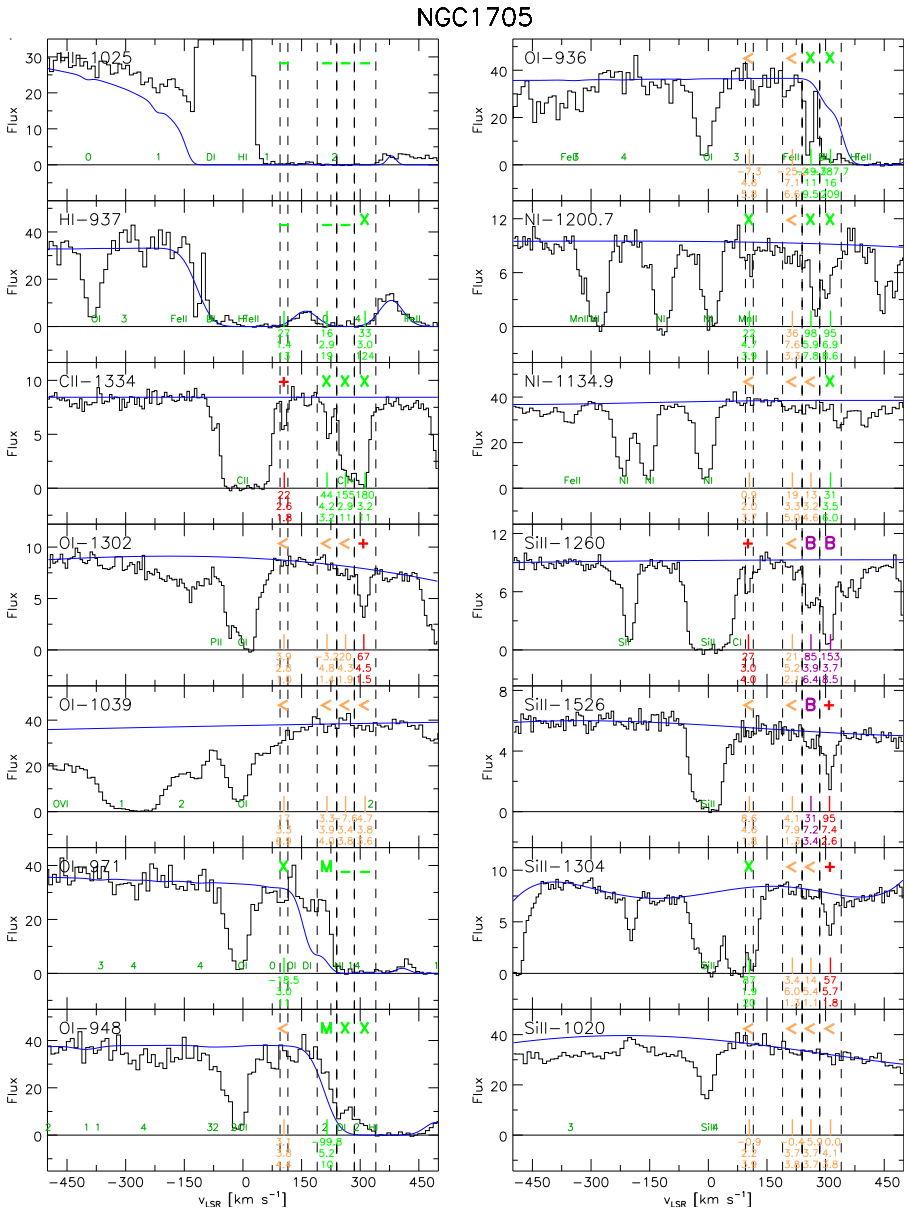

Figure 3.53 Cutouts of the LAB 21 cm spectrum and selected UV spectra toward NGC 1705 highlighting ions and lines most relevant to the determination of the metallicity and depletion of each component.

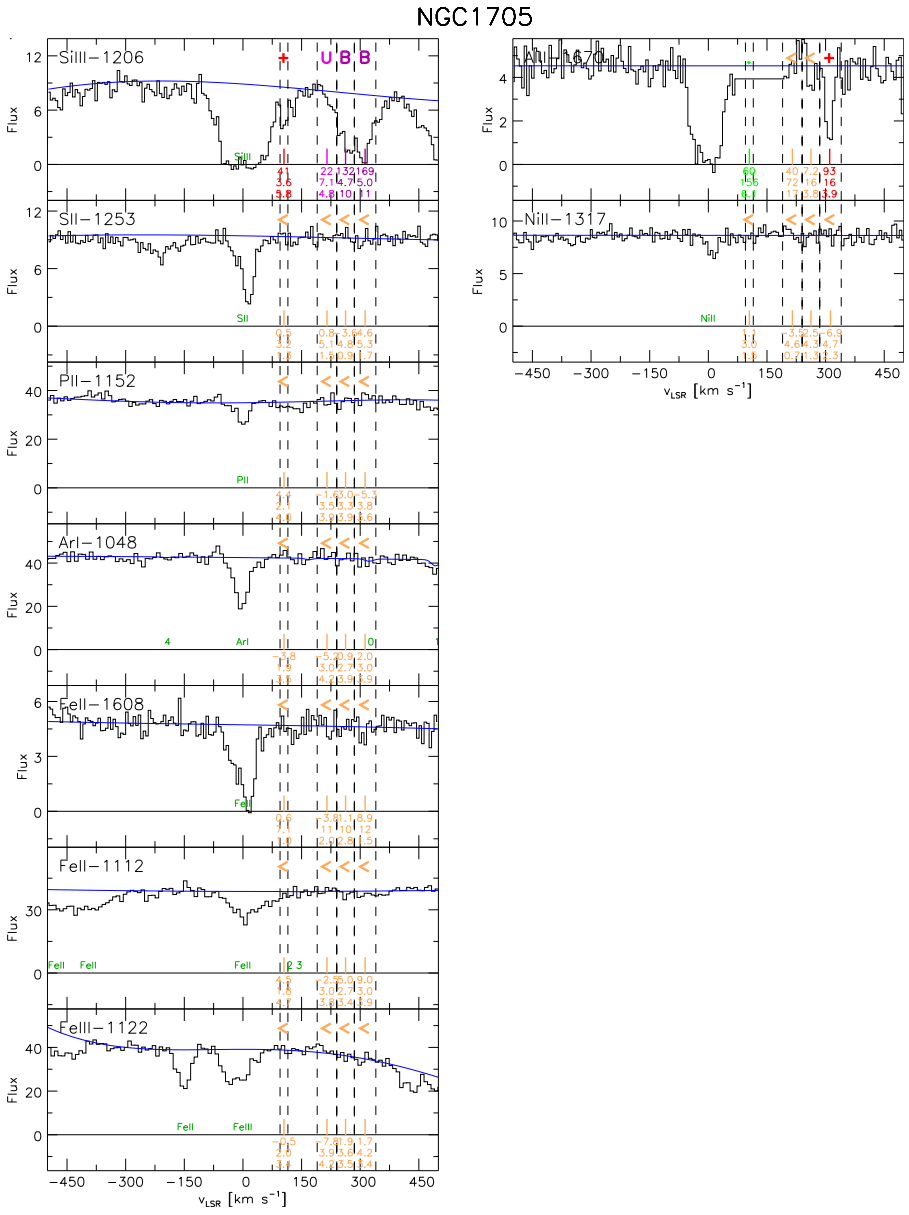

Figure 3.54 Cutouts of selected UV spectra toward NGC 1705 (continued).

that we believe is the same feature noted by previous authors at a slightly lower velocity. We fit a single Gaussian component of $N(\mathrm{H\ I}) = (6.6 \pm 0.7) \times 10^{18}$ cm^{-2}, or log $N(\mathrm{H\ I}) = 18.82^{+0.04}_{-0.05}$ to this feature, but caution that the data are very noisy. Weak, narrow absorption lines are seen in the UV data near this velocity in C II λ1334, Si II λ1260, and Si III λ1206 with line FWHMs of 11.2 ± 1.5, $14.0^{+1.3}_{-1.5}$, and 13.8 ± 2.2 km s^{-1}, respectively. The same feature is probably seen in C III λ977, but is too badly blended with both the zero-velocity Galactic absorption and the higher-velocity components to measure. Based on the visual extent of the lines and their measured widths, we chose a velocity integration interval of $+95$ km s^{-1} $\leq v_{\mathrm{LSR}} \leq +115$ km s^{-1} and a "typical" HVC intrinsic linewidth of 15 ± 5 km s^{-1}(Doppler $b = 9 \pm 3$ km s^{-1}). The resulting abundance pattern is shown in Figure 3.55. Our value of $N(\mathrm{Si\ III}) = 12.42^{+0.20}_{-0.12}$ is compatible with the Collins et al. and Shull et al. measurements despite our considerably smaller velocity integration range. We find $N(\mathrm{Si\ II}) = 12.29 \pm 0.22$, clearly discrepant with respect to the Shull et al. value, but again explained by the very different velocity integration ranges. While we do not observe any undepleted species in this component, we obtain abundance upper limits for C II, Si II, and Si III that are well below expectations for typical IVC and HVC metallicities given the $N(\mathrm{H\ I})$ value obtained from the LAB spectrum. The most likely explanation for this is an inaccurate estimate of $N(\mathrm{H\ I})$. If this cloud is physically associated with the higher-velocity gas in the sightline, which itself may be part of the Magellanic Stream, we would expect a metallicity like that of the LMC, $\sim 0.3\ Z_{\odot}$; see

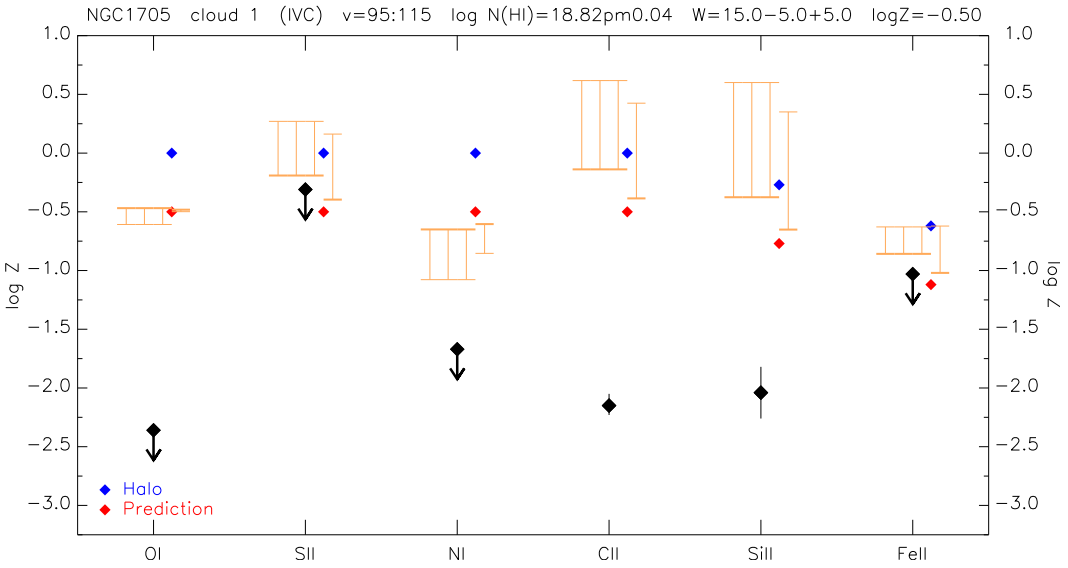

Figure 3.55 Abundance plot for ions in the IVC at +95 km s^{-1} $\leq v_{\rm LSR} \leq$ +115 km s^{-1} toward NGC 1705. The range of possible ionization corrections is shown as the orange bars for, left to right, 5, 10, and 20 kpc (log $\phi = 5.98$, 5.99, and 5.62), and the extragalactic background (log $\phi = 4.53$) at densities between log $n = -3$ and -1. A Halo depletion pattern is indicated with blue points for each ion, and predicted abundances with red points assuming an LMC-like metallicity of log $Z = -0.5$. The log N(H I) value used to make this plot likely includes signal from outside the NGC 1705 line of sight; log N(H I) $\sim$ 16 brings the data into agreement with ionization models at the indicated metallicity.

Section 3.5.4. This is similar to that of the present-day Small Magellanic Cloud (SMC), identified as the source of the gas now seen in the Stream (e.g., Fox et al. 2010). At the LAB-derived N(H I), the metallicity implied by ionization modeling (log $Z \simeq -2.5$) is more than a full dex below the lowest metallicites ever measured for HVCs. The large offset from predicted abundances at a metallicity of 0.3 solar is evident in Figure 3.55. We propose a solution to this apparent problem as follows: the relatively large LAB beam ($\sim 36'$) likely

samples intermediate-velocity gas that is unrelated to the NGC 1705 sightline. The abundance pattern can be reconciled with an LMC-like metallicity if log N (H I) ~ 16, a value like those inferred for other, higher-velocity clouds in this sightline that are not detected in the LAB spectrum. Given this combination of circumstances, and while we acknowledge the evident existence of this cloud, we are unable to make a robust estimate of its metallicity.

In the velocity range +190 km s^{-1} $\leq v_{\rm LSR} \leq$ +240 km s^{-1}, we see absorption in C II* λ1335, C III λ977, and Si III λ1206 in the form of a blue "wing" on the neighboring component centered on $v_{\rm LSR} = +262$ km s^{-1}. There is no H I emission feature in the LAB spectrum that corresponds to the apparent absorption at these velocities; from the data, we calculate a 5σ noise limit over this interval of N (H I) $\leq 8.4 \times 10^{17}$ cm^{-2} for a 20 km s^{-1} linewidth and $\leq 1.19 \times 10^{17}$ cm^{-2} for a 40 km s^{-1} linewidth, or log N (H I) ≤ 17.92 and ≤ 18.08, respectively. Despite strong blending from neighboring absorption, we fit a component to the Lyman series H I lines centered at +215 km s^{-1} with a FWHM of 32 km s^{-1}. The minimum value of N(H I) required to obtain a good fit is 1×10^{17} cm^{-2}, or log N(H I) = 17.00, representing a lower limit, but we note that this is highly uncertain. Since we do not have a good, independent estimate of the intrinsic H I linewidth, we take the larger upper limit for a 40 km s^{-1} wide line, settling on an estimate of N(H I) = $(8.5 \pm 3.5) \times 10^{17}$ cm^{-2}, or log N(H I) = $17.93^{+0.15}_{-0.23}$. As none of the detected species consisted of a sufficient number of lines to constrain the intrinsic linewidth, we used the width of the fit to the Lyman series lines, 30 ± 5 km s^{-1}(Doppler $b = 18 \pm 3$ km

s^{-1}). The resulting abundances with respect to H I are shown in Figure 3.56. All the detected ions in this component suffer some degree of depletion, so we

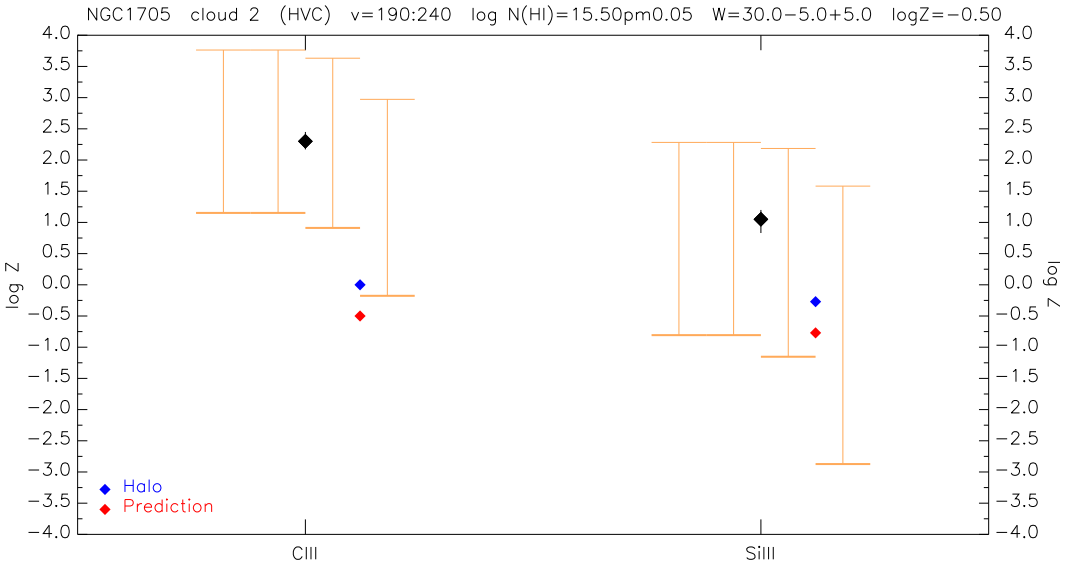

Figure 3.56 Abundance plot for ions in the HVC at +190 km $s^{-1} \leq v_{\rm LSR} \leq$ +240 km s^{-1} attributed to the Magellanic Stream toward NGC 1705. The range of possible ionization corrections is shown as the orange bars for, left to right, 5, 10, and 20 kpc (log $\phi = 5.98$, 5.99, and 5.62), and the extragalactic background (log $\phi = 4.53$) at densities between log $n = -3$ and -1. A Halo depletion pattern is indicated with blue points for each ion, and predicted abundances with red points assuming assuming the metallicity of the Magellanic Clouds (log $Z = -0.5$).

can make no definite pronouncement on its metallicity. However, since it is thought to be associated with the Magellanic Stream, we can draw some basic conclusions about it by assuming its undepleted metallicity is consistent with that of the Stream. In that case, the minimum value of N(H I) that brings the abundances of C III and Si III into agreement with the predictions of our ionization models is $(3.19 \pm 0.40) \times 10^{15}$ cm^{-2}, or log M(H I) = $15.50^{+0.05}_{-0.06}$.

Absent a more determination of N(H I), we argue that the metallicity of this cloud is consistent with that expected for the Magellanic Stream for a rather low H I column density.

We make a similar consistency argument for absorption seen in the data at $+240$ km s$^{-1} \leq v_{\rm LSR} \leq +285$ km s^{-1}, attributed to the cloud WW487. Sahu & Blades (1997) saw absorption in low-resolution, archival GHRS G140L spectra at $v_{\rm LSR} = +260$ km s^{-1} in Si II for which they quote $\log N$(Si II) = 13.60 without an uncertainty estimate. Heckman et al. (2001) claimed detection of ionic absorption in WW487 along the NGC 1705 sightline in early results from *FUSE*, but noted, for example, O I λ1302 at a velocity of $+326 \pm 10$ km s^{-1}, which is clearly part of our component discussed below centered at $v_{\rm LSR} = +312$ km s^{-1}. Other species, such as C III λ977 and C II λ1036, were observed around $+270$ km s^{-1} and are certainly associated with WW487. Their analysis of this sightline focused mainly on intrinsic abundances in NGC 1705, however. Wakker (2001a) quotes column density upper limits for a few ions at $+260$ km s^{-1} (Fe II, S II, Al II) and an accompanying value of $\log N$(H I) = 18.23 ± 0.10.

We detect lines of Si II λ1260 and 1526 and Si III λ1206 near $v_{\rm LSR} = +260$ km s^{-1}, all blended with neighboring components, as well as strongly saturated C III λ977. The λ1206 line shows structure within the component that may indicate contamination because the same structure is not seen in the other detected lines; the resulting Si II abundance reflects this possible contamination as a large random error. WW487 is an H I emission non-detection in the 21 cm LAB spectrum; we find 5σ upper limits of 5×10^{17}

cm^{-2} for a 20 km s^{-1} linewidth and 7.1×10^{17} cm^{-2} for a 40 km s^{-1} linewidth, or log N(H I) $\leq$ 17.70 and $\leq$ 17.85, respectively. Despite severe blending with neighboring components, the H I Lyman series lines are reasonably fit with N(H I) = $(1.2 \pm 0.1) \times 10^{18}$ cm^{-2}, or log N(H I) = $18.08^{+0.03}_{-0.04}$, and a FWHM of 25 km s^{-1}. Taking the higher linewidth value for the upper limit, we adopted N(H I) = $(4 \pm 3) \times 10^{17}$, or log N(H I) = $17.60^{+0.24}_{-0.60}$, for computing elemental abundances with respect to H I. We again took the H I linewidth of 30 ± 5 km s^{-1} (Doppler $b = 9 \pm 3$ km s^{-1}) to arrive at the abundances shown in Figure 3.57. As in the case of the cloud at $v_{\rm LSR}$ = +215 km s^{-1}, we cannot

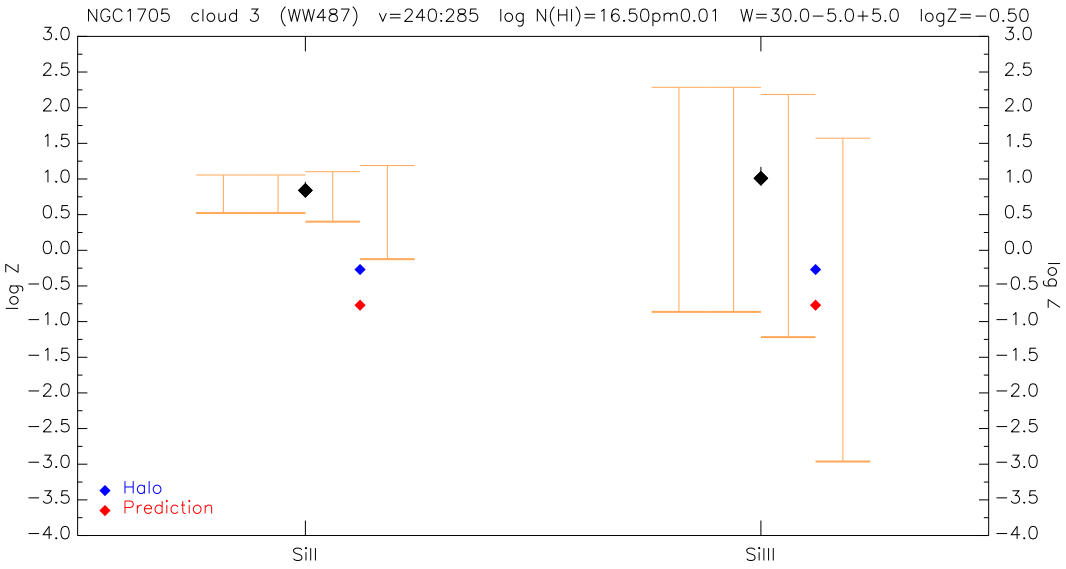

Figure 3.57 Abundance plot for ions in the cloud WW487 at +240 km s^{-1} $\leq v_{\rm LSR} \leq$ +285 km s^{-1} toward NGC 1705. The range of possible ionization corrections is shown as the orange bars for, left to right, 5, 10, and 20 kpc (log ϕ = 5.98, 5.99, and 5.62), and the extragalactic background (log ϕ = 4.53) at densities between log $n = -3$ and -1. A Halo depletion pattern is indicated with blue points for each ion, and predicted abundances with red points assuming the metallicity of the Magellanic Clouds (log $Z = -0.5$).

obtain a metallicity for WW487 free from the effects of depletion, and what at first seems to be an improbably low metallicity is thought to result from a poor initial estimate of N(H I). If we again assume the $\sim 0.3\ Z_{\odot}$ metallicity of the Magellanic Stream, we find the abundances of the detected species are within the limits specified by ionization corrections for N(H I) = (3.15 ± 0.05) $\times 10^{16}$ cm^{-2}, or log N(H I) = 16.50 ± 0.01.

Lastly, we identify an absorption component previously undescribed in the literature at $+285$ km s^{-1} $\leq v_{\rm LSR} \leq$ $+340$ km s^{-1} on the basis of several detected lines. O I λ1302 is cleanly detected with equivalent width $66 \pm 4.5 \pm 1.5$ mÅ; the next intrinsically strongest line, λ988, is contaminated, and by the third-strongest line, λ1039, the component registers only as an upper limit. It is seen clearly, blended with the WW487 absorption, in several of the strongest lines of Si II. As the strength of the WW487 lines decreases, the lines in this component become progressively less blended. We detect it in lines of C II, C III, and C II*, but in each case it is too strongly blended with WW487 to measure. Surprisingly, we see a strong line in Al II λ1670 of equivalent width $93 \pm 16 \pm 3.8$ mÅ. Its strength and FWHM (20.3 ± 7.5 km s^{-1}) are comparable to the detected Si II lines, which have a mean FWHM of 25.1 ± 2.8 km s^{-1}. We have no reason to believe it is the result of contamination from some other species.

Like the other components in this sightline thought to arise in the Magellanic Stream, there is no complementary H I emission feature in the LAB 21 cm spectrum, from which we compute N(H I) 5σ upper limits of 8.3×10^{17}

cm^{-2} for a 20 km s^{-1} linewidth and 1.17×10^{18} cm^{-2} for a 40 km s^{-1} linewidth, or log N(H I) of ≤ 17.92 and ≤ 18.07, respectively. In the Lyman series H I lines, this component is rather badly blended with intrinsic absorption in NGC 1705 at +555 km s^{-1}. However, we find an H I column of at least 9.5×10^{17} cm^{-2}, or log N(H I) = 17.98, is required to reproduce the observed line profile with a FWHM of 35 km s^{-1}. Taking the larger 21 cm upper limit for a 40 km s^{-1} line, we settled on a value of N(H I) = $(1.14 \pm 0.03) \times 10^{18}$ cm^{-2}, or log N(H I) = 18.05 ± 0.01, which we used to calculate abundances with respect to H I. The clean detection of two lines of Si II (λ1526 and 1304) and the blended detection of λ1260 is sufficient to constrain the intrinsic linewidth at $17.0^{+2.8}_{-1.9}$ km s^{-1}(Doppler $b = 10.2^{+1.7}_{-1.1}$), which compares well against the "canonical" HVC linewidth of 15 km s^{-1} we use frequently. The resulting abundances are presented in Figure 3.58. If this cloud originated in the Magellanic Stream, we would expect an undepleted metallicity of about 0.3 $Z_{\odot}$; we find [O I/H I] = -0.52 ± 0.09 ($0.30^{+0.07}_{-0.06}$ $Z_{\odot}$), which compares very well with our expectations. While we cannot definitively associate this component with the MS, its LSR velocity and measured O I metallicity are within the ranges seen in Stream gas

In summary, we see absorption due to four clouds along the line of sight toward NGC 1705. Three of the four, at $v_{\rm LSR}$ = +215, +263 (designated WW487), and +313 km s^{-1}, are thought to be associated with the Magellanic Stream and are expected to have metallicites of ~ 0.3 $Z_{\odot}$. WW487 and the cloud at +215 km s^{-1} are only detected in absorption by ions susceptible to

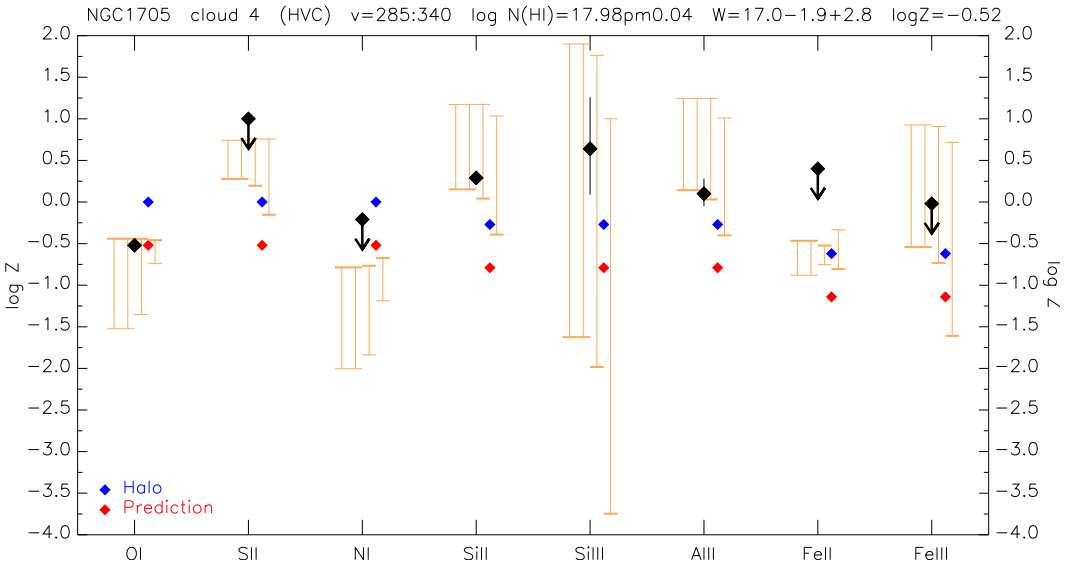

Figure 3.58 Abundance plot for ions in HVC at +285 km s^{-1} $\leq v_{\rm LSR} \leq$ +340 km s^{-1} attributed to the Magellanic Stream toward NGC 1705. The range of possible ionization corrections is shown as the orange bars for, left to right, 5, 10, and 20 kpc (log $\phi = 5.98$, 5.99, and 5.62), and the extragalactic background (log $\phi = 4.53$) at densities between log $n = -3$ and -1. A Halo depletion pattern is indicated with blue points for each ion, and predicted abundances with red points assuming the metallicity of the SMC (log $Z = 1.00$, or 0.1 $Z_{\odot}$).

depletion, but the cloud at +313 km s^{-1} is detected in O I at $Z \sim 0.3$ $Z_{\odot}$. Since this metallicity is similar to that of the Magellanic Clouds and other measurements of the Magellanic Stream (see Section 3.5.4), we conclude that at least the +313 km s^{-1} HVC is a member of that population of clouds. If the cloud at +215 km s^{-1} and WW487 are also physically related to the Stream, we expect they also have metallicities of about 0.3 solar. Making this assumption, we work backward to obtain N (H I) values for the two clouds and find they are well below the 21 cm detection threshold in the available LAB data. Given

the relatively large distance to the Stream ($\gtrsim 50$ kpc; see Section 3.5.4), all of the components above +200 km s^{-1} may suffer varying degrees of 21 cm beam smearing that result in highly uncertain N(H I) determinations. Finally, we detect C III and Si III in a cloud near +100 km s^{-1}, but it is unclear from the cloud's velocity that it is kinematically associated with the Stream. While a 21 cm emission feature is detected near the blue edge of the velocity window we define for this cloud, it is possible that spatially adjacent gas unrelated to the NGC 1705 sightline was detected in the relatively large LAB beam. Using N(H I) indicated by LAB results in an improbably small metallicity < 0.01 $Z_{\odot}$, while log N(H I) ~ 16 yields a metallicity in line with the Magellanic Stream. Absent a robust estimate of N(H I), we cannot quote a definitive metallicity for this cloud.

3.4.12 NGC 5253

This sightline is illuminated by NGC 5253, a small (diameter = 3.4 kpc), nearby ($z \sim 0.001$) irregular starburst galaxy in the Coma-Sculptor Group. Available UV spectra are generally of low S/N, and the continuum is shaped by underlying stellar lines in the galaxy, causing undulations in the spectrum and rendering analysis of these data difficult (Wakker 2006). Careful fitting of the continuum still results in higher systematic uncertainty in the measured equivalent widths of lines than that to which we are accustomed. Very strong intrinsic absorption appears near $v_{\rm LSR} = +404$ and +454 km s^{-1} further modifies the shape of the continuum. In the case of very strong lines

such as the Lyman H I series the intrinsic lines blend heavily with the zero-velocity Milky Way absorption, and toward the Lyman series limit the spectra are of essentially zero flux. Gas in this direction must be highly ionized, for it shows no emission at 21 cm, while highly ionized species such as O VI are observed (Wakker et al. 2003). All ions detected or providing useful limits in our UV spectra are shown in Figure 3.59.

The only absorption due to anomalous-velocity gas toward NGC 5253 unambiguously detected in our spectra is due to cloud WW154 in Complex WD (Wannier et al. 1972, Wakker & van Woerden 1991), for which there are no previously published abundance measurements. In determining the velocity integration window of this component, we made use of the only two lines clearly detected in the data: Fe II λ1144 and Si II λ1020. Each of these lines shows a narrow component roughly centered near +100 km s^{-1} with a FWHM of $\sim 32 \pm 3$ km s^{-1}, which we took as indicative of the intrinsic linewidth in the WW154 gas. On examination of these lines, we settled on a window of +75 km s^{-1} $\leq v_{\rm LSR} \leq$ +125 km s^{-1} for this component. From the LAB spectrum, we obtained a 5σ upper limit at the assumed linewidth of N(H I) $< 1.67 \times 10^{18}$ cm^{-2}, or log N(H I) = $<$ 18.22. Given the strength of the H I absorption in the Lyman series lines, we estimate a lower limit of N(H I) $> 7 \times 10^{17}$ cm^{-2}, or log N(H I) = $>$ 17.85, but we caution that this limit is not very robust due to the low S/N of the spectra. We therefore adopt N(H I) = $(1.19 \pm 0.49) \times 10^{18}$ cm^{-2}, or log N(H I) = $18.08^{+0.15}_{-0.23}$, for the purposes of computing abundances with respect to H I. In Figure 3.59 we show two lines

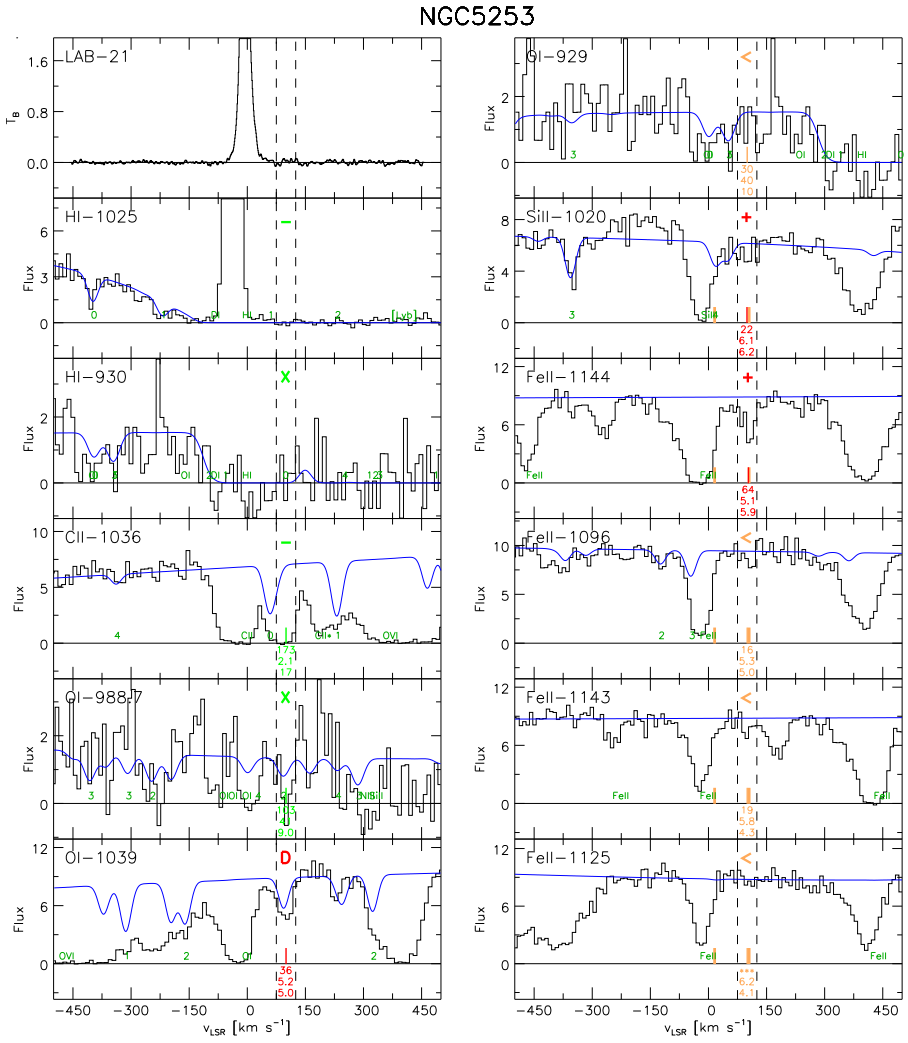

Figure 3.59 Cutouts of the LAB 21 cm spectrum and selected UV spectra toward NGC 5253 showing all detected ions and those providing useful upper limits.

of O I to illustrate our reasoning for the choice of line to use in determining the O I abundance. For certain wavelength ranges, the only available UV data are from the low-resolution STIS G140L grating ($R \sim 1000$), yielding spectra of insufficient resolution to meet the goals of our analysis. The strongest O I line, λ1302, falls in this category. Absorption due to WW154 is clearly indicated in O I λ1039, although it is significantly impacted by the intrinsic H_2 $5-0$ $P(1)$ line at λ1038.157, redshifted to the observed λ1039.55. We remove the contribution from the H_2 line using the method described in Section 3.3.5.4, finding a decontaminated equivalent width of $36.5 \pm 5.2 \pm 5.0$ mÅ. In the figure we also show O I λ988.7, although we ultimately decided against using the line in our analysis. While a detection is apparent in the spectrum, similarly impacted by redshifted, intrinsic H_2 $10-0$ $P(3)$ λ987.768, the resulting equivalent width ($103.4 \pm 41.0 \pm 9.0$mÅ) is highly uncertain. We felt uneasy allowing this uncertainty to propagate to the O I COG and ultimately to the inferred value of N(O I), therefore excluding it from the analysis. Still, we are confident that much of the absorption seen in the WW154 interval in O I λ988.7 is indeed attributable to this cloud, lending credence to the claimed detection of O I λ1039. Again assuming a linewidth of 30 km s^{-1}, we obtain log N(O I) = $14.68^{+0.10}_{-0.11}$, and given our adopted N(H I), we find [O I/H I] = -0.09 ± 0.17 ($0.81^{+0.39}_{-0.26}$ $Z_\odot$). Abundances for O I, Si II, and Fe II, along with limits for P II and Ar I, are presented in Figure 3.60. The only immediate point of comparison for this result is our study of the ESO265−G23 sightline in Section 3.4.3. In that direction, we found [O I/H I] = -0.81 ± 0.49 ($0.15^{+0.32}_{-0.10}$

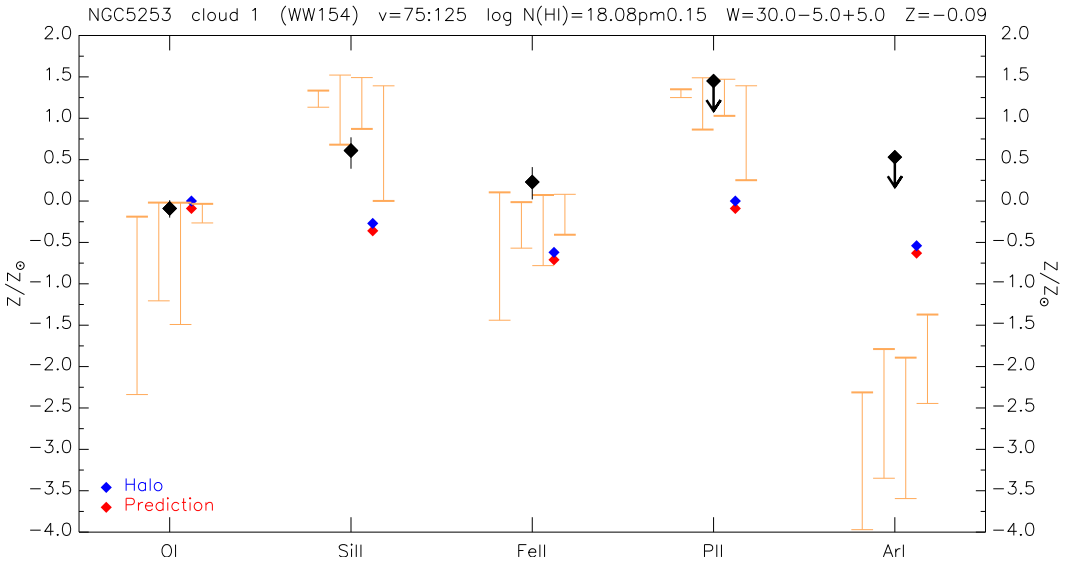

Figure 3.60 Abundance plot for WW154 (Complex WD) at $+75$ km s^{-1} $\leq v_{\rm LSR} \leq +125$ km s^{-1}. The range of possible ionization corrections is shown for 1, 2, and 5 kpc (log $\phi = 5.51$, 5.55, and 5.44) at densities between log $n = -3$ and -1, and for the extragalactic background (orange bars, left to right). A Halo depletion pattern is indicated with blue points for each ion, and predicted abundances with red points given our measured metallicity [O I/H I] $= -0.09$.

$Z_{\odot}$) for the cloud WW226 in Complex WD. Our claim of near-solar metallicity for WW154 hinges largely on the quality of the decontamination of the O I λ1039 line from interference by H_2. In the absence of additional metallicity measurements for Complex WD or more, higher-quality UV data on the NGC 5253 sightline, we are unable to conclusively tell whether this complex has either an approximately solar, or substantially subsolar, metallicity. A distance measurement toward this complex would contribute substantially to understanding this discrepancy. Wakker & van Woerden (1991) note that the relatively small deviation velocity of Complex WD suggests it may be "related

to the large-scale structure of the Galaxy." Putman et al. (2002) suggested that the resolved H I morphologies of various anomalous-velocity clouds in associations like Complex WD may be useful to classify objects thought to have common physical origins. Future H I interferometric surveys at higher angular resolution than presently available may help answer this question.

We see evidence of high-velocity gas near $v_{\rm LSR} = +200$ km s^{-1} but existing data are insufficient to obtain an abundance measurement. The basis for an HVC here is twofold. First, an H I component with a minimum column density of N(H I) $= 2 \times 10^{17}$ cm^{-2}, or log N(H I) = 17.30, is necessary to fit the observed Lyman series lines at this velocity. There is no corresponding detection in H I 21 cm emission; assuming a typical linewidth for HVCs of 15 km s^{-1}, the corresponding 5σ upper limit from the LAB spectrum is N(H I) $< 9.7 \times 10^{17}$ cm^{-2}, or log N(H I) = $<$ 17.99. If this component is real, it must be highly ionized. Second, weak absorption in Fe II λ1144 is indicated at roughly +150 km s^{-1} $\leq v_{\rm LSR} \leq$ +270 km s^{-1} with an equivalent width $32.3 \pm 9.4 \pm 5.1$ mÅ. From this apparent 3σ detection, assuming the same 15 km s^{-1} linewidth, we calculate log N(Fe II) = $13.45^{+0.11}_{-0.15}$. It is a clear non-detection in the next strongest Fe II line available, λ1096. Among other important ions that might trace this cloud such as O I, N I, and S II, the lines available in our data are either of insufficiently high S/N or are contaminated by intrinsic or zero-velocity Milky Way components or Galactic H_2. We might expect to see absorption by such a highly ionized cloud in higher ions. The Si III λ1260 line is only available in STIS G140L data, C III λ977 is very noisy and

contaminated by intrinsic O I λ976 in NGC 5253, and no data are available for, e.g., C IV, Si IV, and O VI. From the value of N(Fe II) above, we find that if this cloud is real, [Fe II/H I] = $+0.23^{+0.58}_{-0.37}$. Without additional information, particularly with respect to an expected ionization correction, we cannot make an informed estimate of the metallicity of this cloud among undepleted ions.

To summarize, in the NGC 5253 sightline, we clearly see absorption due to only one component: the cloud WW157 in the collection of HVCs known as Complex WD at $v_{\rm LSR} = +100$ km s^{-1}. We find for this cloud a metallicity of $Z = 0.81\ Z_{\odot}$, which we note conflicts strongly with the metallicity we found toward the Complex WD cloud WW226 in the direction of ESO265−G23 ($Z = 0.15\ Z_{\odot}$). This conflict precludes us from making a definitive claim concerning the metallicity of Complex WD. In addition, the presence of a previously undescribed HVC at $v_{\rm LSR} = +200$ km s^{-1} is indicated by weak absorption in a single line of Fe II and an adequate fit to the H I Lyman series lines requires a component at this velocity with $17.30 \leq \log N(\text{H I}) \leq 17.30$. If this cloud is real, we conclude its Fe II metallicity is probably > 0.72 solar, but can offer no further interpretation absent information about ionization conditions.

3.4.13 PG 1011−040

The line of sight toward the Seyfert 1 galaxy PG1011−040 passes through cloud WW92 (= HVC244+41+113) in Complex WB of the Wannier Clouds (Section 3.5.3.1). We analyzed data for this sightline from two sources: (1) the *FUSE* Cycle 2 Guest Investigator Program (ID B079) and (2) COS

G130M/G160M from *HST* Cycle 17 (ID 11524). Wakker et al. (2003) mention the (then-public) *FUSE* data but excluded them from their analysis in deference to the science goals of the Guest Observer under whose proposal the data were collected. The data are also referenced by van Woerden & Wakker (2004) with a preliminary abundance result for WW92 of $Z \gtrsim 0.1\ Z_{\odot}$, but a "probable value" of $\sim 0.7\ Z_{\odot}$. Fox et al. (2006) analyzed the as part of their survey of O VI/C III/H I in CHVCs; they identified two velocity windows of O VI absorption at $+100$ km s$^{-1} \leq v_{\rm LSR} \leq +240$ km s^{-1} and $+240$ km s$^{-1} \leq v_{\rm LSR} \leq +320$ km s^{-1}, but note that they did not find C III in either velocity range. For the latter window, they quote a value $\log N({\rm C\ III}) < 13.07$. A representative sample of ions detected in our UV spectra is shown in Figures 3.61-3.62.

An absorption feature is seen in several lines in this this direction in the velocity range $+60$ km s$^{-1} \leq v_{\rm LSR} \leq +100$ km s^{-1}. We find no previous mention of this feature in the literature, and it does not appear to be associated with any previously classified IVC. Its absorption lines suffer severe blending by both zero-velocity Galactic absorption and the lines of the neighboring WW92 component. Only one line (O I λ1039) is a clear, unblended detection. Several species are detected but the degree of blending is sufficient to render them useless in our abundance analysis; these include O I λ1302, C II λ1334, C III λ977, Si II λ1260, Si III λ1206, and Al II λ1670. The remaining, detected Si II lines (λ1526, 1193, 1190, and 1304) are blended but remain useful in the analysis. In the Green Bank 21 cm spectrum, this component is similarly

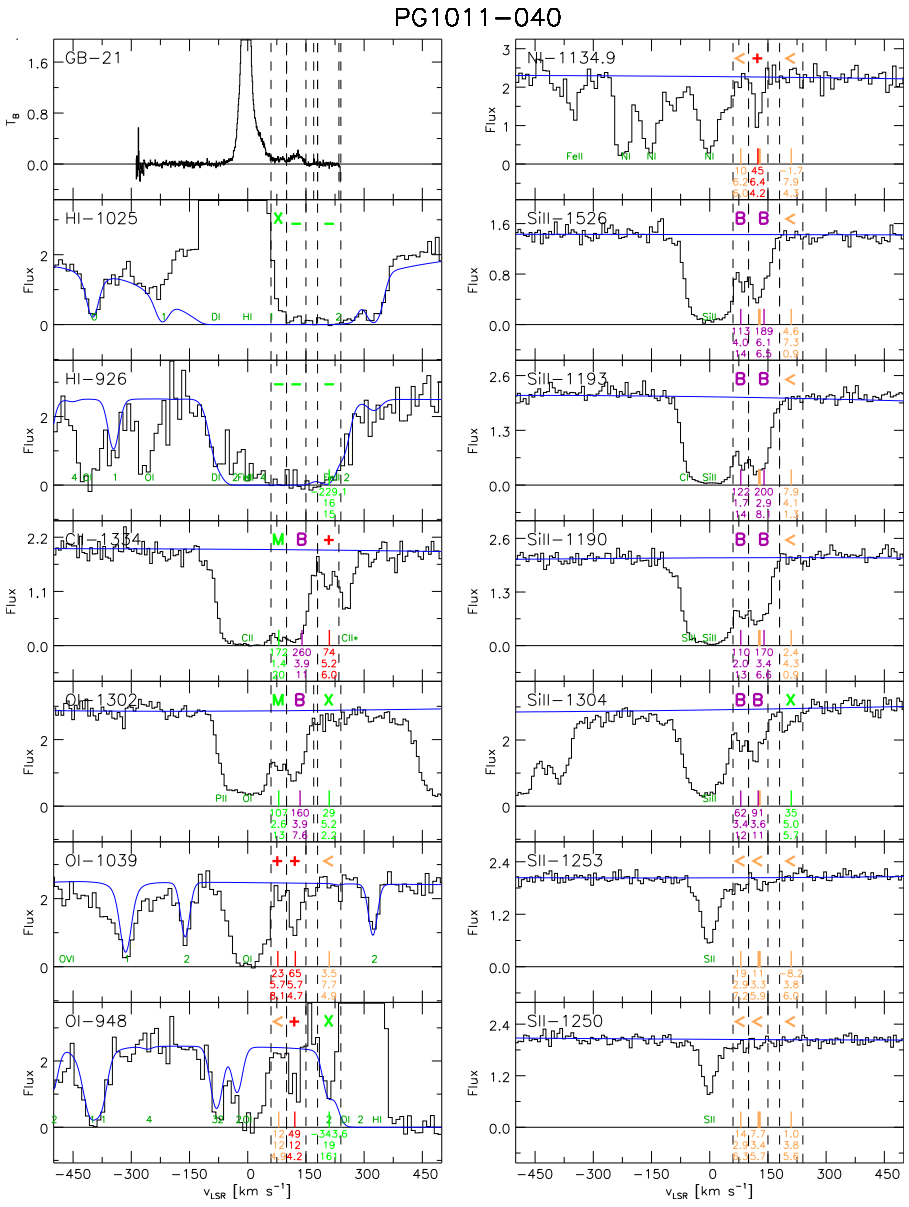

Figure 3.61 Cutouts of the Green Bank 21 cm spectrum and selected UV spectra toward PG1011-040 highlighting ions and lines most relevant to the determination of the metallicity and depletion of each component.

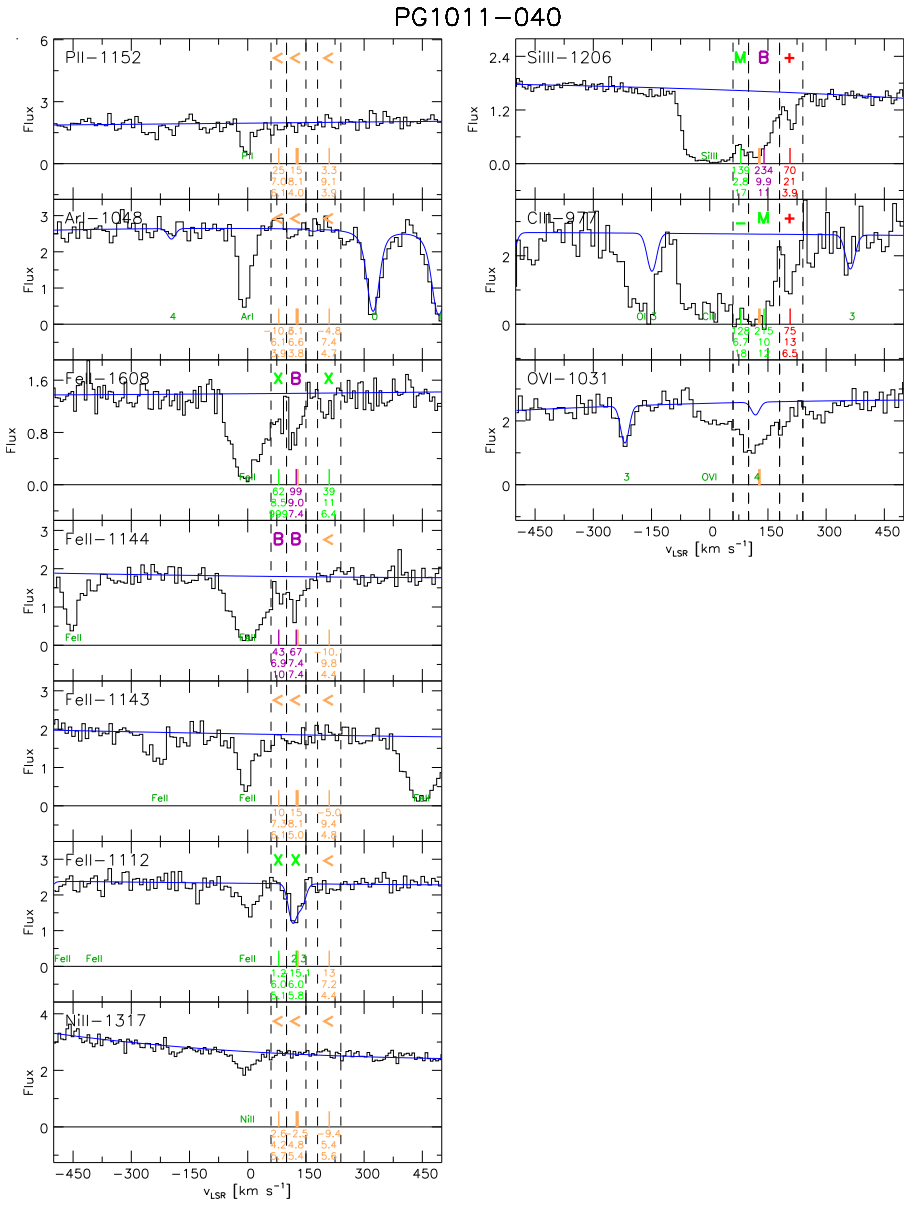

Figure 3.62 Cutouts of selected UV spectra toward PG1011-040 (continued).

situated between the Milky Way emission and the feature corresponding to WW92. Yet it is sufficiently distinct to fit a single Gaussian to the data centered at $v_{\rm LSR} = +83$ with FWHM = 34 km s^{-1} and N(H I) = $(5.4 \pm 1.4) \times 10^{18}$ cm^{-2}, or log N(H I) = $18.73^{+0.10}_{-0.13}$. The multiple (blended) lines of Si II we detected allowed us to estimate the intrinsic linewidth as $16.6^{+5.5}_{-4.2}$ km s^{-1} (Doppler $b = 10.0^{+4.0}_{-2.5}$ km s^{-1}). The resulting abundances are shown in Figure 3.63. Based on the O I λ1039 detection, we find [O I/H I] = -0.92 ± 0.23

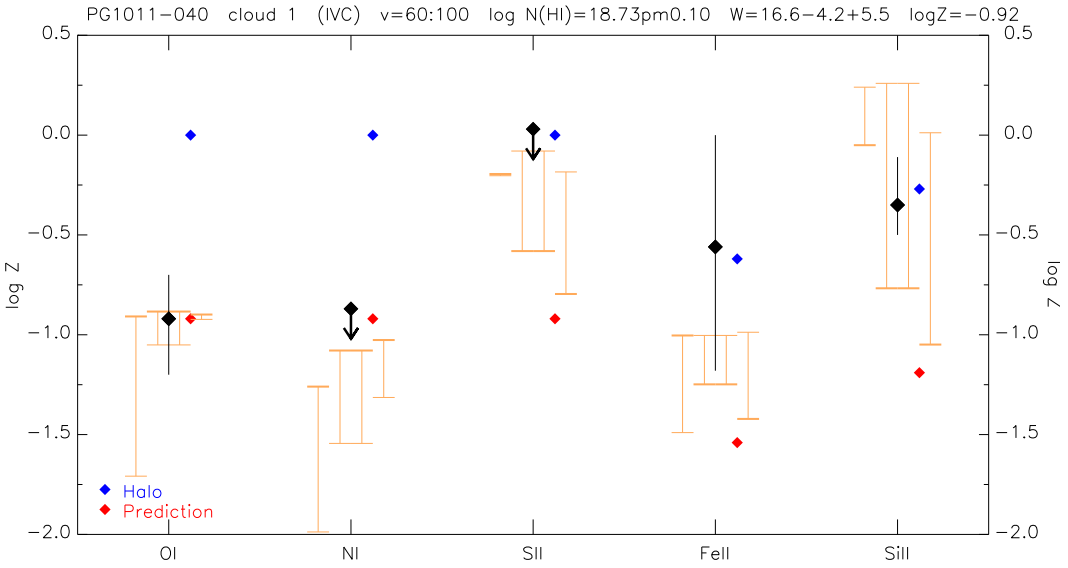

Figure 3.63 Abundance plot for a previously unreported IVC toward PG1011-040 at +60 km s^{-1} $\leq v_{\rm LSR} \leq$ +100 km s^{-1}. The range of possible ionization corrections is shown for 1, 5, and 10 kpc (log ϕ = 6.66, 5.51, and 5.51) at densities between log $n = -3$ and -1, and for the extragalactic background at log $\phi = 4.53$ (orange bars, left to right). A Halo depletion pattern is indicated with blue points for each ion, and predicted abundances in red points for our metallicity [O I/H I] = -0.92.

($0.12^{+0.08}_{-0.05}$ $Z_\odot$). This is lower than expected for an IVC enriched in metals

via the Galactic Fountain. No other undepleted species were detected against which the O I result can be compared, but the observed Si II abundance is consistent with ionization models for our measured N(H I) value, O I metallicity, and typical IVC distances. The Fe II abundance appears to disagree with the O I metallicity plus the ionization correction, although abundances allowed by the ionization models are within the large error bar on the Fe II measurement. This value is determined by the singular, blended λ1144 line, which is strongly impacted by blending with the neighboring absorption due to WW92. Alternately, this apparent overabundance of Fe II may simply indicate low depletion in this cloud, resulting in most of the Fe II being in the gas phase. In any case, the measured metallicity of this IVC is low enough as to preclude an origin in the Disk. Without more information, such as a distance, we cannot make a strong statement concerning an origin for this cloud.

Absorption due to the cloud WW92 is seen in the data at +100 km s^{-1} $\leq v_{\rm LSR} \leq$ +150 km s^{-1}; the detected lines are nearly all blended to some extent with the neighboring IVC discussed in the previous paragraph. This component is clearly indicated in the Green Bank 21cm data, to which we fit a single Gaussian centered at $v_{\rm LSR} = +126$ km s^{-1} with FWHM = 29 km s^{-1} and N(H I) = $(8.1 \pm 0.8) \times 10^{18}$ cm^{-2}, or log N(H I) = $18.91^{+0.04}_{-0.05}$. There is some variation in the observed widths of the lines in this component that depends on the particular ion one considers; we extended the velocity window to +170 km s^{-1} for O I λ1302 and to +180 km s^{-1} for C II λ1134 and 1036, C III λ977, all of the detected Si II and Si III lines except Si II λ1304, and Al II λ1670. We found

the variable velocity windows better captured all of the evident absorption without including excess continuum in other ions where the observed linewidth was lower. Detections of multiple lines of Si II suggest an intrinsic line FWHM of $27.0^{+3.3}_{-2.2}$ km s^{-1} (Doppler $b = 16.2^{+2.0}_{-1.3}$ km s^{-1}). In several instances (e.g, C II, Al II, Si III), only one strong, blended (but measurable) line was available; these often fall on the "critical" or "flat" part of the curve of growth in which significant changes to N have little effect on the measured line equivalent widths. As a result, the corresponding abundances with respect to H I have relatively large error bars, complicating their interpretation. The resulting abundances are presented in Figure 3.64. We find [O I/H I] $= -0.59 \pm 0.08$ ($0.26^{+0.05}_{-0.04}$ $Z_{\odot}$). The other detected ions fall well within the abundance ranges predicted by our ionization models, as seen in Figure 3.64 except for Fe II, suggesting that depletion onto dust is low in this cloud. Our absorption line bracketing work to determine distances to various HVCs gives a preliminary distance to WW92 between 12 and 22 kpc, placing it in the lower reaches of the Halo. At this distance it is unlikely the cloud has Disk origin.

We see absorption in the velocity range +240 km s^{-1} $\leq v_{\rm LSR} \leq$ +280 km s^{-1} due to another cloud which is not previously reported in the literature. It is attested by the presence of four clean detections: C II λ1334, C III λ977, Si III λ1206, and Al II λ1670. It is also suggested in Fe II λ1608, but we are not sufficiently confident in the reality of the feature seen there in the data to claim it as a detection. There is no corresponding feature in the Green Bank 21 cm spectrum to a 5σ upper limit of N(H I) $< 2.64 \times 10^{18}$ cm^{-2}, or log N(H

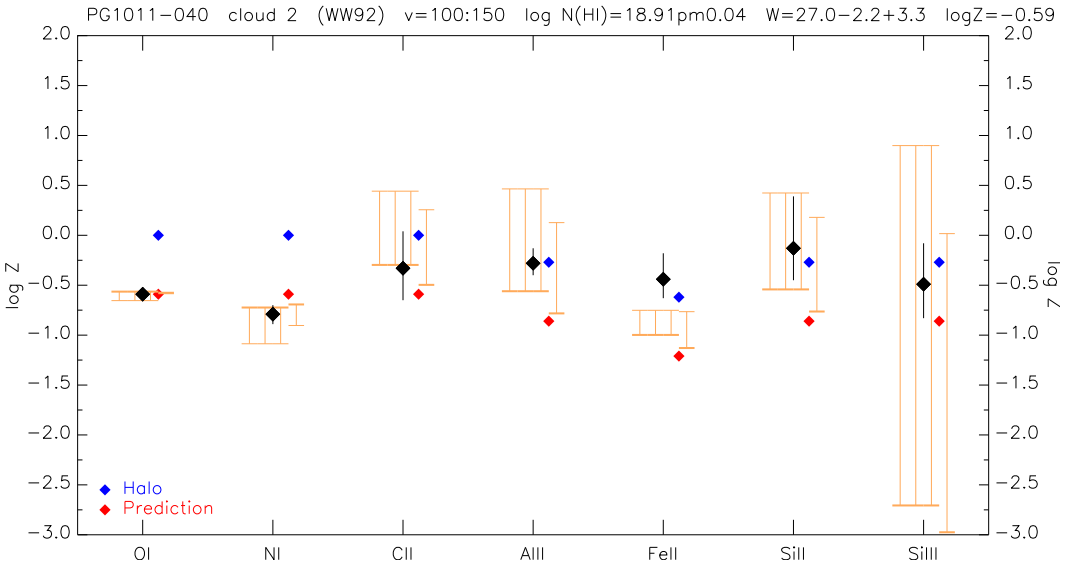

Figure 3.64 Abundance plot for the Complex WB cloud WW92 toward PG1011-040 at +100 km s^{-1} $\leq v_{\rm LSR} \leq$ +180 km s^{-1}. The range of possible ionization corrections is shown for 1, 10, and 50 kpc (log ϕ = 6.66, 5.51, and 5.51) at densities between log $n = -3$ and -1, and for the extragalactic background at log ϕ = 4.53 (orange bars, left to right). A Halo depletion pattern is indicated with blue points for each ion, and predicted abundances in red points for our metallicity [O I/H I] = −0.59.

I) < 18.42, assuming a line width of 40 km s^{-1}. However, the Lyman series H I line profiles are well fitted by a component centered at $v_{\rm LSR}$ = +205 km s^{-1} with FWHM = 30 km s^{-1} and N(H I) = (7±0.5) × 10^{16} cm^{-2}, or log N(H I) = 16.85±0.03. We used the FWHM of the H I fit component as an estimate of the intrinsic linewidth for the curves of growth, because we did not detect sufficient number of lines of any species to properly constrain it otherwise.The resulting abundances for the detected ions are shown in Figure 3.65. Since we do not detect any undepleted species in this component, we are unable to determine

its abundance in a way that is not model-dependent. Our ionization modeling yields a set of metallicity ranges that are relatively insensitive to distance given the value of N(H I) we obtained from fitting the Lyman series H I lines except for the case of very small distances and large distances at which the extragalactic ionizing background becomes dominates. The smallest distances ($d \sim 1$ kpc) are ruled out on the basis that the observed abundances can not be made to fit the model predictions within errors at any metallicity, while the range of predicted metallicities clusters around similar values for distances up to about 50 kpc. The extragalactic background allows for somewhat lower metallicities than ionization at distances consistent with those expected for HVCs. Models accommodating the spread of abundances in Figure 3.65 range over $-1.5 \leq \log Z \leq$ -0.1 ($0.03\ Z_{\odot} \leq Z \leq 0.79\ Z_{\odot}$). Abundances for all detected ions can be made to fit the ionization models within distance range 1 kpc $\leq d \leq$ 50 kpc for a much more restricted range of metallicities at this N(H I): $-1.5 \leq \log Z \leq$ -0.85 ($0.03\ Z_{\odot} \leq Z \leq 0.14\ Z_{\odot}$). We chose $\log Z = -1$ as the reference metallicity for Figure 3.65 as the measured abundances of the detected ions fit well within the ranges predicted by ionization modeling at this metallicity and N(H I). We can only say with any confidence that true metallicity of this cloud is probably about 0.1 solar, and a measurement of this cloud's distance would not help constrain this result any further. However, a large distance would argue for an unresolved small cloud, whose interior was cold and dense enough to explain the observed C II and Al II absorption with C III and Si III formed in an extended, ionized envelope. In this sense it could

be a CHVC, but the relative weakness of O VI λ1031 does not seem consistent with the highly-ionized HVCs (Section 3.5.3.4). It would be interesting to look at the strength of lines of C IV and Si IV but these lines are not present in data currently available. Therefore, we conclude that this cloud has an "HVC-like" metallicity of ~ 0.1 solar and probably represents infall from the Halo.

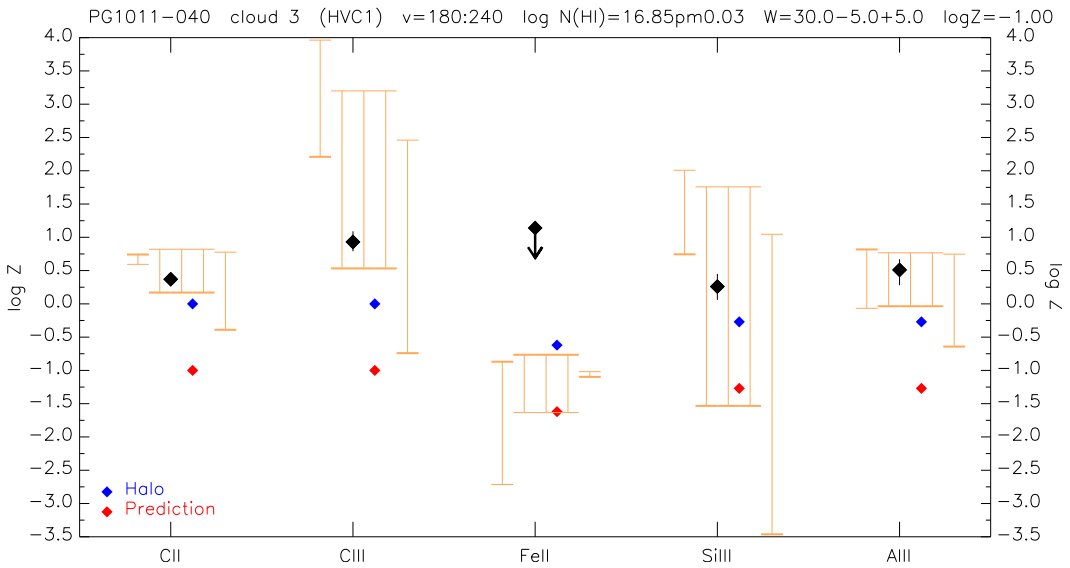

Figure 3.65 Abundance plot for a previously unreported HVC toward PG1011-040 at +240 km s^{-1} $\leq v_{\rm LSR} \leq$ +280 km s^{-1}. The range of possible ionization corrections is shown for 1, 5, 20, and 50 kpc (log ϕ = 6.66, 5.55, 4.93, and 4.99) at densities between log $n = -3$ and -1, and for the extragalactic background at log ϕ = 4.53 (orange bars, left to right). A Halo depletion pattern is indicated with blue points for each ion, and predicted abundances in red points for a metallicity of log Z = -0.85

Finally, we see the suggestion of C III λ977 absorption in the interval +240 km s^{-1} $\leq v_{\rm LSR} \leq$ +280 km s^{-1}, but this is not a confident detection given the noise. This range roughly corresponds to that of an H I absorption

component, centered at +265 km s^{-1} with FWHM = 30 km s^{-1} and N(H I) = (6 ± 2) × 10^{14} cm^{-2}, or log N(H I) = 14.78$^{+0.12}_{-0.18}$, required to adequately reproduce the observed profiles of the Lyman series H I lines. This component is most clearly evident in the H I λ1025, 972, and 937 lines, and to a lesser extent in λ949, which is partly contaminated by zero-velocity O I λ948. The C III feature is also coincident in velocity with O VI λ1031 absorption at +240 km s^{-1} ≤ $v_{\rm LSR}$ ≤ +320 km s^{-1}; we have included this O VI line in Figure 3.62 for reference. We also note an H I absorption component centered at +325 km s^{-1} with FWHM = 30 km s^{-1} and N(H I) = (8 ± 2) ×10^{14} cm^{-2}, or log N(H I) = 14.90$^{+0.10}_{-0.12}$, also necessary to fit the line profiles of the same H I lines as in the case of the +260 km s^{-1} component. Given its relatively low H I column density, it is not surprising the +325 km s^{-1} component is not seen in absorption in any of our other ionic lines. However, it is worth noting that there is also no corresponding O VI absorption at or near +325 km s^{-1}, given the typical association of H I and O VI absorption in IGM absorbers.

In summary, we see absorption toward PG1011−040 centered at $v_{\rm LSR}$ = +125 due to WW92 in Complex WB of the Wannier Clouds with a metallicity of ∼ 0.25 $Z_\odot$. This absorption component has been reported by other authors, but ours is the first abundance measurement for this cloud. We also find abundances for two other previously unreported components: an IVC at $v_{\rm LSR}$ = +80 km s^{-1} heavily blended with WW92 absorption with Z ∼ 0.1 $Z_\odot$, and an HVC at $v_{\rm LSR}$ = +210 km s^{-1} for which we also infer Z ∼ 0.1 $Z_\odot$ on the basis of ionization modeling. Lastly, we note the presence of two

additional absorption components in the data for which we were unable to derive abundances; both are required to reproduce the observed profiles of the Lyman series H I lines. One is centered at +260 km s^{-1}, consists of the singular detection of C III λ977, and generally matches a feature seen in O VI at +280 km s^{-1}, while the other, low-N(H I) component, centered at +325 km s^{-1}, matches no other absorption feature in the data, including O VI.

3.4.14 PG1259+593

This sightline is among those with the highest S/N ratio in our dataset, at 30 per resolution element. Two sources of intermediate/high-velocity absorption have been previously noted in this direction, identified with the CIIIC core of Complex C (Giovanelli et al. 1973, Wakker 2001a) and the IV Arch (Kuntz & Danly 1996). The sightline also passes through the IV Arch but is apparently unassociated with any particular cloud core. The Galactic H I emission in the direction of PG1259+593 ($\ell = 120\overset{\circ}{.}56$, $b = +58\overset{\circ}{.}05$) is comparatively low because this sightline is nearly coincident with the "Ursa Major Hole", a region with the smallest column of low-velocity H I in the northern sky (Lockman et al. 1986). The 21 cm emission associated with Complex C is stronger than both that of the IV Arch and Galactic ISM components. There is less confusion between Galactic absorption and intermediate/high-velocity gas than in most sightlines, and the contaminating effect of H_2 is relatively minimal; PG1259+593 has among the strongest 21 cm emission and least complicated velocity structure of any Complex C sightline. There are several

known intergalactic H I Lyα systems in this direction (e.g., Bahcall et al. 1993, Zuo & Lu 1993, Richter et al. 2004, Sembach et al. 2004, Richter et al. 2006b, Tripp et al. 2008, Danforth et al. 2010), but they are sufficiently separated in velocity from the Complex C and IV Arch components so as not to impact our analysis here. The CIIIC component also shows O VI absorption associated with Complex C (Richter et al. 2001c, Fox et al. 2004). A representative sample of ions detected in our UV spectra is shown in Figures 3.66-3.68.

PG1259+593 lies along the edge of the CIIIC core, seen in the Leiden-Dwingeloo Survey (LDS; Hartmann & Burton 1997) as a $\sim 1^\circ \times 2^\circ$ region of $N(\mathrm{H\ I}) = 3 \times 10^{19}$ cm^2 (Sembach et al. 2004). The fact that this sightline samples Complex C at relatively high $N(\mathrm{H\ I})$ is fortuitous because ionization effects are considerably less important than in the cases of sightlines that sample considerably lower column density. It is likely, however, that unresolved velocity structure within the CIIIC component adversely impacts abundance analysis, and previous work suggests that the Complex C absorption profile in this direction consists of more than one component. Richter et al. (2001c) note that the strong lines of O, Si, and Fe show asymmetries in the red wings of the absorption profiles, which they claim argues for a weak, blended absorption component around -110 km s^{-1}. Similarly, Sembach et al. (2004) found at least two velocity components for Complex C were necessary to adequately fit their *FUSE* and *HST* STIS spectra of O I, centered at $v_{\mathrm{LSR}} = -129$ km s^{-1} and -112 km s^{-1}; the -112 km s^{-1} component only contributes significantly to the overall absorption in the intrinsically-strongest λ1302.168 and

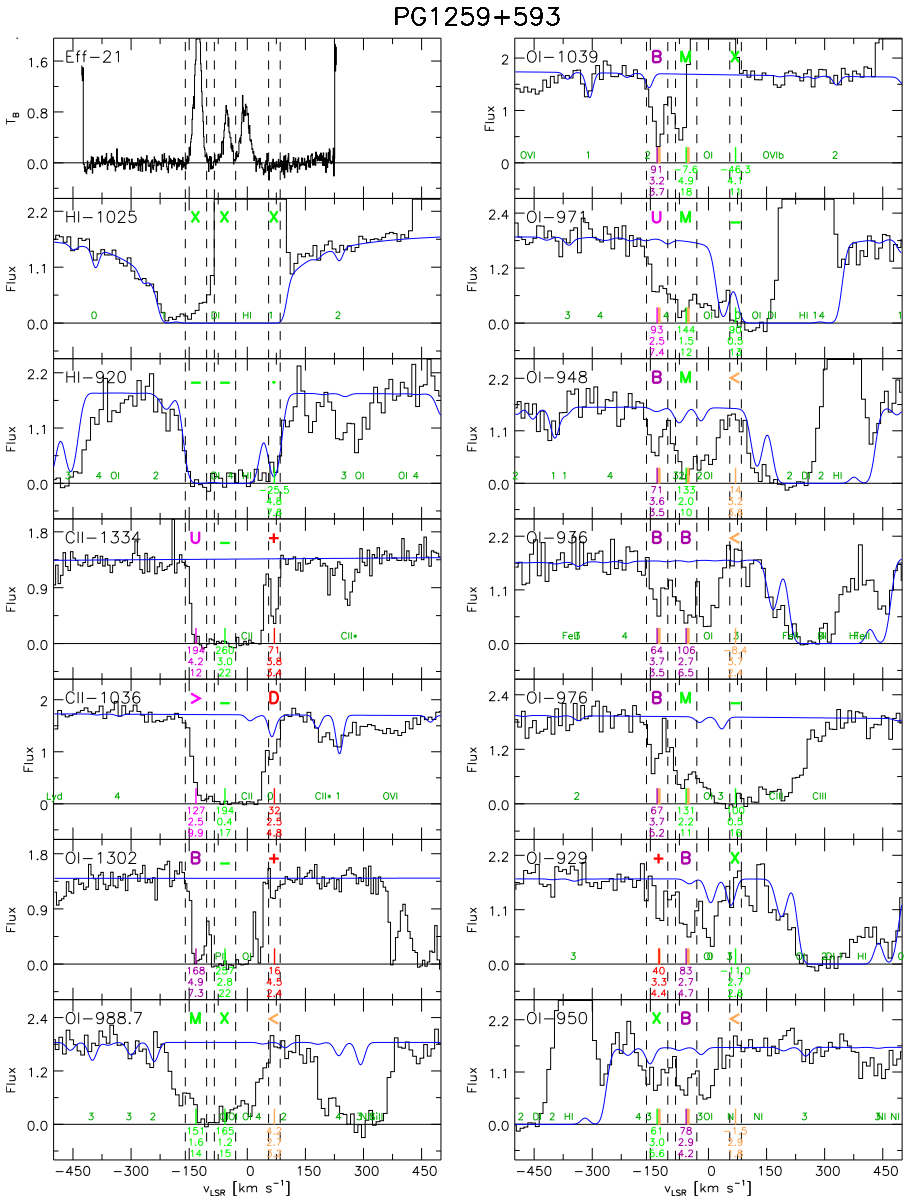

Figure 3.66 Cutouts of the Effelsberg 21 cm spectrum and selected UV spectra toward PG1259+593 highlighting ions and lines most relevant to the determination of the metallicity and depletion of each component.

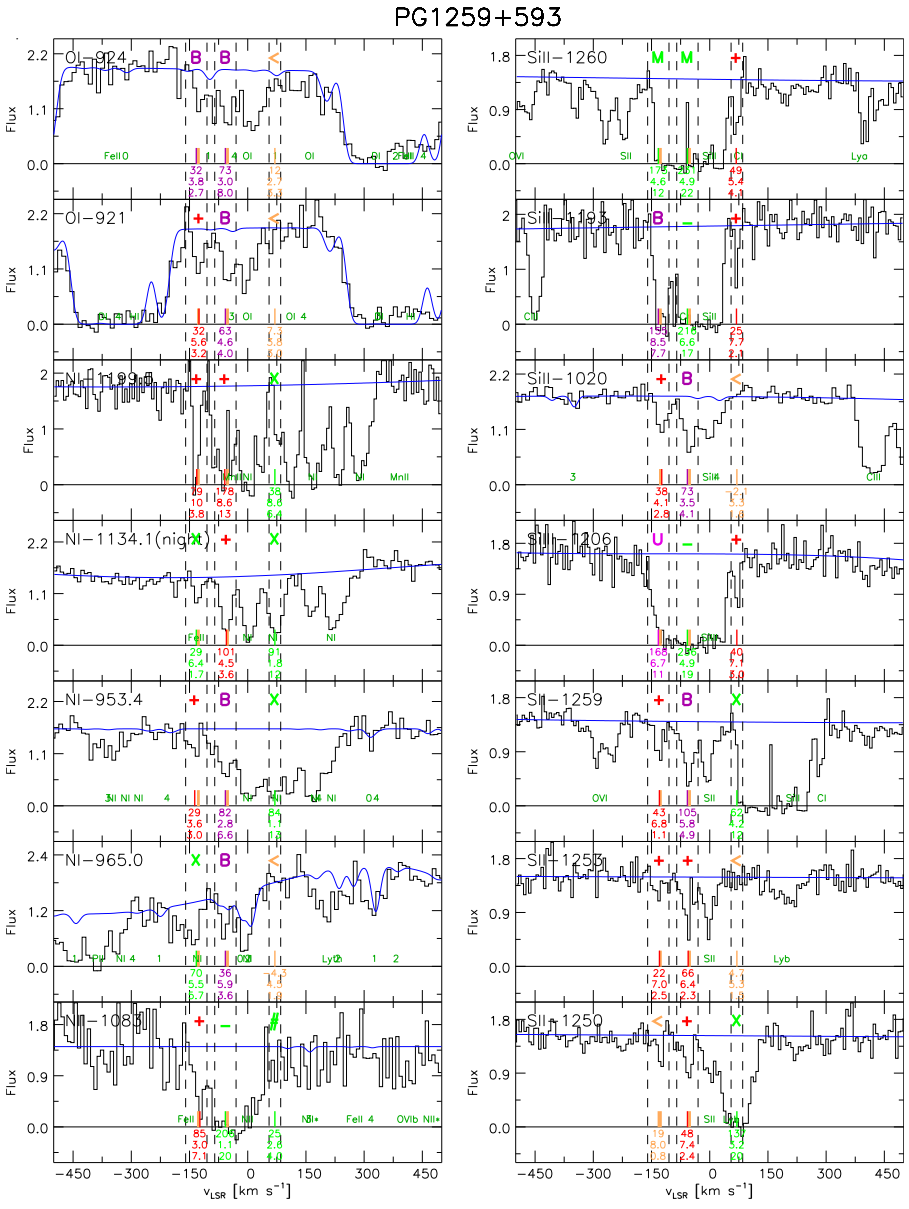

Figure 3.67 Cutouts of selected UV spectra toward PG1259+593 (continued).

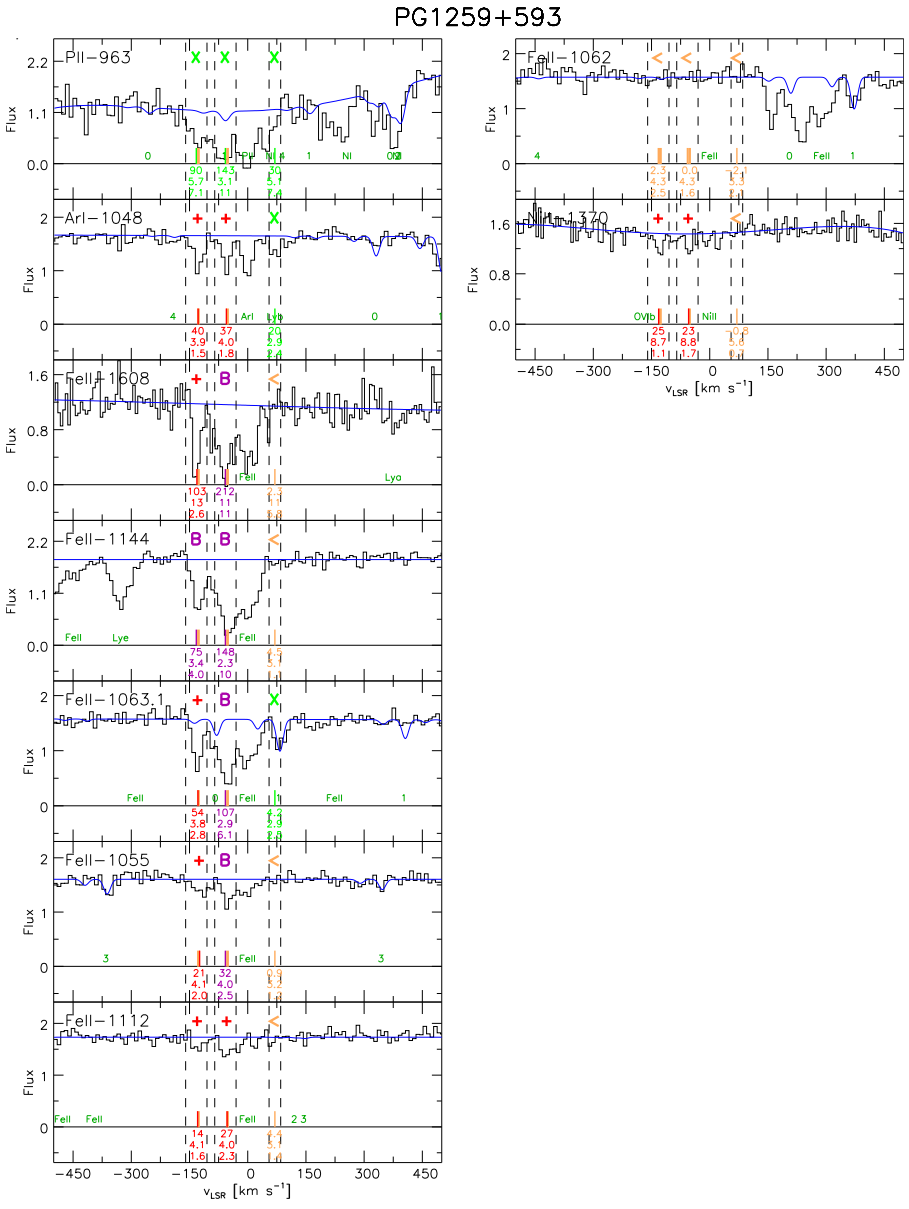

Figure 3.68 Cutouts of selected UV spectra toward PG1259+593 (continued).

λ1039.230 lines. Neither author attempts to disentangle the absorption from these components, treating them for purposes of deriving column densities and abundances as if they were single components centered at $v_{\rm LSR} = -130$ km s^{-1} and -128 km s^{-1}, respectively. However, the two-component fit obtained by Sembach et al. (2004) is better than a single component; this adjusts their derived value of N(O I) downward relative to the earlier measurements of Wakker et al., Richter et al., and Collins et al. The single- component value for N(O I) reported by Sembach et al. is $15.66^{+0.09}_{-0.06}$, assuming $b = 9.7 \pm 0.7$ km s^{-1}; this compares favorably with our measurement, N(O I) $= 15.72^{+0.30}_{-0.40}$, even though we used a higher FWHM. After Richter et al analyzed this sightline, $\sim$400 ks worth of additional data was taken for PG1259+593, allowing Collins et al. (2003) to refine the earlier abundances and obtain a measurement for Ar I, log N(Ar I) $= 13.10^{+0.12}_{-0.15}$. They used $b = 10.0^{+1.9}_{-1.5}$, based on multiple detections of lines of O I, Fe II, Si II, and S II. Lehner et al. (2004) report a few abundances based on the Ne IIpresented by Sembach et al. (2004), finding an unexpectedly low [P II/H I] ≤ 1.05 (3σ) that they attribute to a real abundance variation. Shull et al. (2011) do not comment on the details of the Complex C velocity structure in this sightline, other than to acknowledge the work of Sembach et al. and adopt their log N(O I).

We detect UV absorption in this component at -160 km s^{-1} $\leq v_{\rm LSR}$ ≤ -105 km s^{-1} and note that the corresponding 21 cm emission profile in the Effelsberg data is distinctly asymmetric, with a broad blue wing that suggests unresolved velocity substructure. Because we could not account for

the asymmetric line profile in an unambiguous way by fitting multiple Gaussian components, we fit the profile with a single Gaussian, resulting in a value of N(H I) = $(8.83 \pm 0.14) \times 10^{19}$ cm^{-2}, or log N(H I) = 19.95 ± 0.01. However, we note that Sembach et al. (2004) published a measurement of N(H I) from combining the Westerbork map (primary beam HPBW = 35°) in their Figure 3 with single-dish Effelsberg data centered on the QSO to yield a synthesized beam of 1′. We therefore adopt their value N(H I) = $(9.0 \pm 1.0) \times 10^{19}$ cm^{-2}, or log N(H I) = 19.95 ± 0.05, because it suffers much less from the effects of unresolved small-scale structure than the Effelsberg measurement alone. From multiple detections of lines of Fe II, Si II, N I, and O I, we find FWHM = $16.0^{+2.9}_{-2.2}$ km s^{-1}, which we note is higher than what previous authors have found. This would ordinarily have the effect of lowering our measured column densities. Excluding N I, among undepleted ions we find [O I/H I] = -1.07 ± 0.19 ($0.09^{+0.06}_{-0.03}$ $Z_{\odot}$) and [S II/H I] = -0.73 ± 0.10 (0.19 ± 0.04 $Z_{\odot}$). The S II abundance is determined by only two detections (λ1253 and 1259) and one upper limit (λ1250) and is therefore more poorly-constrained compared to our O I abundance, which is composed of nine detected lines. The result appears to make [S II/H I] enhanced relative to [O I/H I], but our O I measurements are certainly affected by small-scale structure in the O I lines. We do not believe the indicated enhancement is real but rather illustrative of systematic uncertainties associated with our method of assuming a single component. Our O I abundance is 0.2 dex lower than that found by Sembach et al. (2004), who account for apparent velocity substructure in their detailed

analysis of the O I lines. N I is cleanly detected in the λ1199.5 line; in λ1200.2, the CIIIC component appears to suffer some contamination from zero-velocity Galactic absorption. However, these lines appear to be more narrow and deep than detections in weaker lines such as λ953.4 (see Figure 3.66), and their contribution to the N I COG probably leads to an underestimate of N(N I). If we take the λ953.4 line alone, using the FWHM quoted above, we find log N(N I) $\sim$ 14.53, or about 0.18 dex higher than our derived value of $14.35^{+0.22}_{-0.33}$. In turn, that would make [N I/H I] = -1.20, which is still inconsistent with the expectation from the O I metallicity and ionization modeling. Thus, we confirm a subsolar N/O ratio from these observations. On the other hand, Ar I is much stronger than we expect from ionization modeling, but we see nothing wrong with the lines or the Ar I COG. We find log N(Ar I) = $13.34^{+0.07}_{-0.09}$, which disagrees with the values of $<$ 13.15 reported by Richter et al. (2001c) and $13.10^{+0.12}_{-0.15}$ by Collins et al. (2003). We believe the discrepancies are attributable to our analysis of higher-quality data obtained more recently, although we cannot explain the resulting apparent overabundance of Ar I.

We do not associated the H I emission in the direction of PG1259+593 with any particular core in the IV arch, although Richter et al. (2001c) note that this component is close to the IV Arch core IV19, for which Kuntz & Danly (1996) found a velocity range of -62 km s^{-1} $\leq v_{\rm LSR} \leq -42$ km s^{-1} from H I maps. Richter et al. assumed a single absorption component in the IV Arch velocity interval centered at $v_{\rm LSR} = -55$ km s^{-1} and measure log N(H I) = 19.48 ± 0.01 from the Effelsberg 21 cm spectrum. They de-

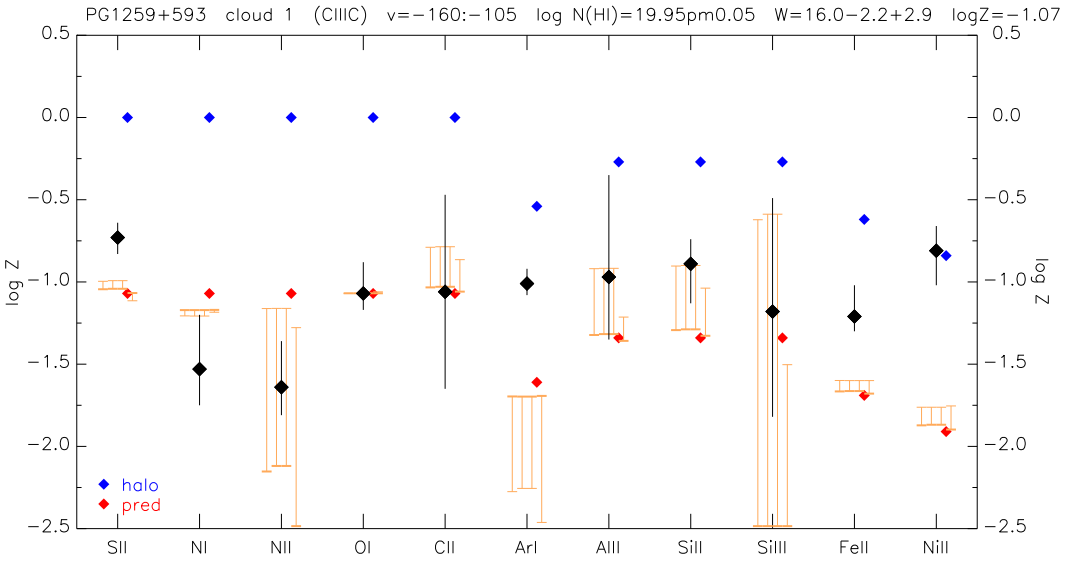

Figure 3.69 Abundance plot for the CIIIC core of Complex C toward PG1259+593 at -160 km s^{-1} $\leq v_{\rm LSR} \leq -105$ km s^{-1}. The range of possible ionization corrections is shown for 3, 5, and 10 kpc (log ϕ = 5.51, 5.55, and 5.55) at densities between log $n = -3$ and -1, and for the extragalactic background at log ϕ = 4.53 (orange bars, left to right). A Halo depletion pattern is indicated with blue points for each ion, and predicted abundances with red points given our measured [O I/H I] = -1.07.

termined FWHM = $10.2^{+5.7}_{-3.2}$ km s^{-1} from a curve of growth analysis, finding [O I/H I] = $-0.01^{+0.35}_{-0.27}$ ($0.98^{+1.21}_{-0.45}$ $Z_{\odot}$). They use their measured [S II/H I] = $+0.11^{+0.11}_{-0.08}$ to derive an ionization fraction of 0.24; they explain their low measured abundances of N I and Ar I as due to photoionization effects, which they note results in depressed abundances of these two species seen in other IVCs (Richter et al. 2001a). Their measured abundances of refractories such as Fe II and Si II suggest relatively minimal dust depletion in this component. Collins et al. (2003) acknowledged IV Arch in their study of the Complex C in the PG1259+593 sightline, specifically noting that their integration limits for

the higher-velocity gas specifically avoided contamination by the IV Arch, but they do not report any metallicity measurement for it. Lehner et al. (2004) measured abundances for Fe II, S II and P II in this component, which are largely in accord with those of other authors, and a line FWHM of ~ 30 km s^{-1} from their Fe II measurements. Similar to the case with the Complex C component in this sightline, Sembach et al. (2004) find three IV Arch velocity components ($v_{\rm LSR} = -81.9$, -54.5 and -29.0 km s^{-1}) are required to fit their O I absorption profiles, while noting that the components are not individually visible in 21 cm emission profiles. While they did not carry out an extensive abundance analysis for the IV Arch component, they report [O I/H I] ≈ -0.10 (0.79 $Z_{\odot}$) using log N(H I) = 19.48 from the Effelsberg 21 cm spectrum. Disagreement exists among the metallicities of undepleted ions reported previously. The abundances of O I and P II are generally in agreement at [X/H I] ~ 0.0 (1.0 $Z_{\odot}$). S II is about 0.1 dex supersolar relative to the other ions, and N I averages about 0.5 dex subsolar. O I and P II match the expected Halo depletion pattern, S II is slightly overabundant, and N I is significantly below expectations. Ionization may account for the observed deficit of N I in the case of the IV Arch, as we see strong saturation in the λ1083 line of N II; the IV Arch lies at a height $0.8 \leq z \leq 1.8$ kpc above the plane of the Milky Way (Wakker 2001a).

We detect the IV Arch in this sightline at -85 km s$^{-1} \leq v_{\rm LSR} \leq -30$ km s^{-1}. We fit a single component to the Effelsberg 21 cm spectrum and obtain N(H I) = $(2.81 \pm 0.13) \times 10^{19}$ cm^{-2}, or log N(H I) = 19.45 ± 0.02. The

same disagreement in the abundances among the undepleted ions reported in previous studies is present in our measurements. We used a line width FWHM $= 19.6^{+7.4}_{-5.3}$ km s^{-1} based on multiple detections of Fe II, O I, and N I, which we note is at odds with both previously published values. Two ions give slightly subsolar abundances, [N I/H I] $= -0.24 \pm 0.26$ ($0.58^{+0.90}_{-0.13}$ $Z_{\odot}$) and [O I/H I] $= -0.08 \pm 0.31$ ($0.83^{+0.87}_{-0.42}$ $Z_{\odot}$), while two give supersolar abundances, [S II/H I] $= +0.30 \pm 0.11$ ($2.00^{+0.46}_{-0.52}$ $Z_{\odot}$) and [P II/H I] $= +0.21 \pm 0.11$ ($1.62^{+0.72}_{-0.21}$ $Z_{\odot}$). Abundances for this component are shown in Figure 3.70. This pattern among undepleted species is remarkably similar to that for the IV Arch component seen toward Mrk 817, as detailed in Section 3.4.9, except offset to higher metallicity by a few tenths of a dex. Adopting the O I metallicity for the predicted abundances in Figure 3.70 brings N I, S II, and P II into line with the expectation after correcting for ionization at log N(H I) = 19.45 and $z =$ 1-5 kpc. Fe II and Ni II are slightly higher, implying 0.3 dex less depletion than the reference Halo value.

Finally, two authors report absorption in both low and high ions of several species at $\sim +65$ km s^{-1}. Richter et al. (2001c) saw absorption in O I, C II, C III, Al II, Si II, Si III, and Fe II near +60 km s^{-1}, but could not find a corresponding H I emission component in either Effelsberg or Green Bank 21 cm spectra. If the angular size of the absorber were small, beam smearing would prevent it from being detected in 21 cm surveys, but it should be visible in the higher Lyman lines of H I. However, they found blending with low-velocity Galactic absorption in their *FUSE* spectra which precluded

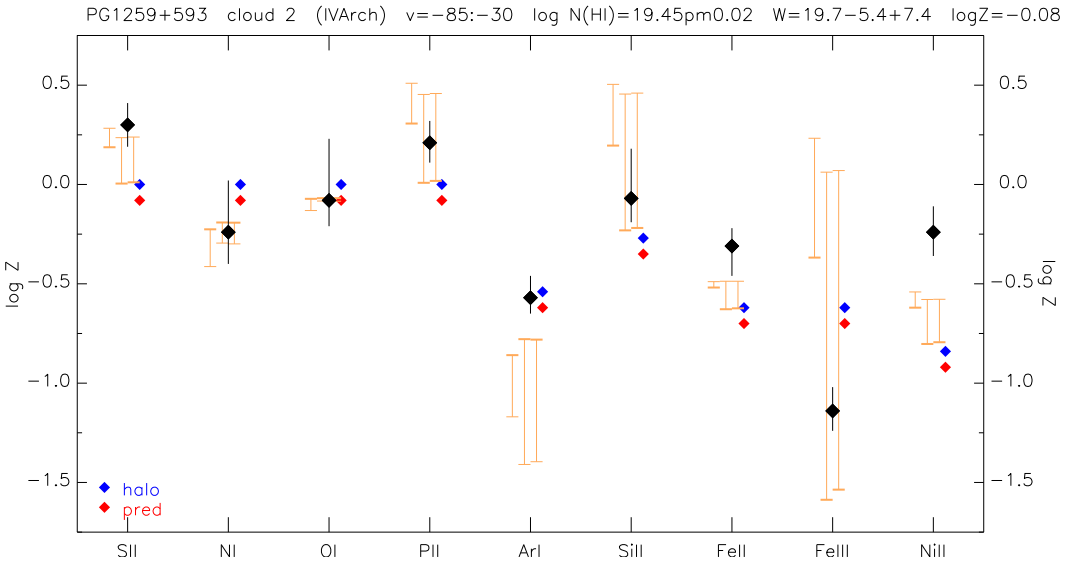

Figure 3.70 Abundance plot for the IV Arch toward PG1259+593 at −85 km s^{-1} $\leq v_{\rm LSR} \leq$ −30 km s^{-1}. The plot parameters are the same as in Figure 3.69 but for our [O I/H I] metallicity of −0.08 and a range of possible ionization corrections of 1, 2, and 5 kpc (log ϕ = 6.66, 5.51, and 5.55; orange bars, left to right).

unambiguous detection, rendering abundances with respect to H I impossible to measure. Sembach et al. (2004) note weak absorption in *FUSE* spectra at +69 km s^{-1} in the same lines reported by Richter et al. While similarly unable to determine N(H I) from either 21 cm spectra or fitting H I Lyman series absorption, they estimated it from their measurement of log N(O I) (= 13.43 ± 0.08). Assuming a solar abundance of oxygen, they derive log N(H I) = 16.69 ± 0.08.

This component is cleanly detected without blends in C II λ1334, O I λ1302, Si II λ1260, Si II λ1190, and Si III λ1206 in the velocity range +55 km s^{-1} $\leq v_{\rm LSR} \leq$ +85 km s^{-1}. These lines have a mean FWHM = 15.8±0.5 km s^{-1}.

Absorption at +70 km s^{-1} appears in Al II λ1670, but is adversely impacted by a data glitch slightly blueward of the line. Si II λ1193 is marginally detected at a lower FWHM (12.3 ± 7.5 km s^{-1}) in noisy data. Finally, C IIIλ977 is detected but strongly blended with zero-velocity absorption but appears to be of a strength comparable to Si III if unblended. As noted previously, this component is not detected in the Effelsberg 21 cm spectrum to a 5σ limit of N(H I) $\leq 3.19 \times 10^{18}$ cm^{-2}, or log N(H I) ≤ 18.50). However, the component is sufficiently separated in velocity from the Galactic H I absorption in the UV to permit an estimate of the lower limit of N(H I) $\geq (3.0 \pm 0.5) \times 10^{16}$ cm^{-2}, or log N(H I) $\geq 16.48^{+0.07}_{-0.08}$. We note that this is within a factor of $\sim$ 1.3 of the Sembach et al. estimate based on an assumption of solar metallicity, but in both cases is below the expected detection threshold for the metal ions. However, the component is best fit assuming a linewidth of 17 km s^{-1}, inconsistent with the derived FWHM of the metal ion lines. Without a better constraint on N(H I), it is impossible to argue in any convincing way for a particular metallicity for this cloud.

To summarize, in the direction of PG1259+593 we see absorption due to gas associated with the CIIIC cloud of Complex C centered at $v_{\rm LSR} = -132$ km s^{-1}, with a metallicity of $\sim 0.1\ Z_{\odot}$. The IV Arch is detected at $v_{\rm LSR} = -57$ km s^{-1} with $Z \sim 0.8\ Z_{\odot}$, following an abundance pattern similar to that seen in the IV Arch toward Mrk 817. Finally, we note absorption in several species at $v_{\rm LSR} \sim +70$ km s^{-1} unassociated with 21 cm emission and displaying weak absorption in the H I Lyman series insufficient to adequately constrain N(H

I). We therefore did not carry out an abundance analysis on this component.

3.4.15 PG 1626+554

The sightline toward PG1626+554 samples gas associated with the CIB core of Complex C, and has been analyzed in studies of Galactic O VI (Sembach et al. 2003, Fox et al. 2006, Collins et al. 2007). Wakker et al. (2003) note that O VI absorption in this sightline is also seen at Complex C velocities. The spectra available to us for analysis consist of *FUSE* observations supplemented by *HST* FOS G130H/G190H/G270H data taken shortly before the instrument was decommissioned; missing *FUSE* data for $\lambda < 1000$ Å results from an unintentional misalignment in the *FUSE* instrument for the associated observation. While PG1626+554 is one of the least complicated Complex C sightlines, much of the *FUSE* data is of marginal utility due to incomplete wavelength coverage and very low signal in many of the spectra. Continuua below 1000 Å among many lines of important diagnostic ions such as H I, O I, N I, and C III are near zero flux. Cutouts of the remaining lines with useful information are shown in Figure 3.71. As a result of these issues with the data, abundance determinations are strongly influenced by the small number of detections of most ions.

Absorption attributable to CIB is seen in the velocity range -150 km s$^{-1} \leq v_{\rm LSR} \leq -90$ km s^{-1}, but the interpretation of its metallicity involves some subtleties. The limits of this window are derived from the observed extent of a handful of lines detected in the available data, e.g., O I λ1039 and Fe II λ1144.

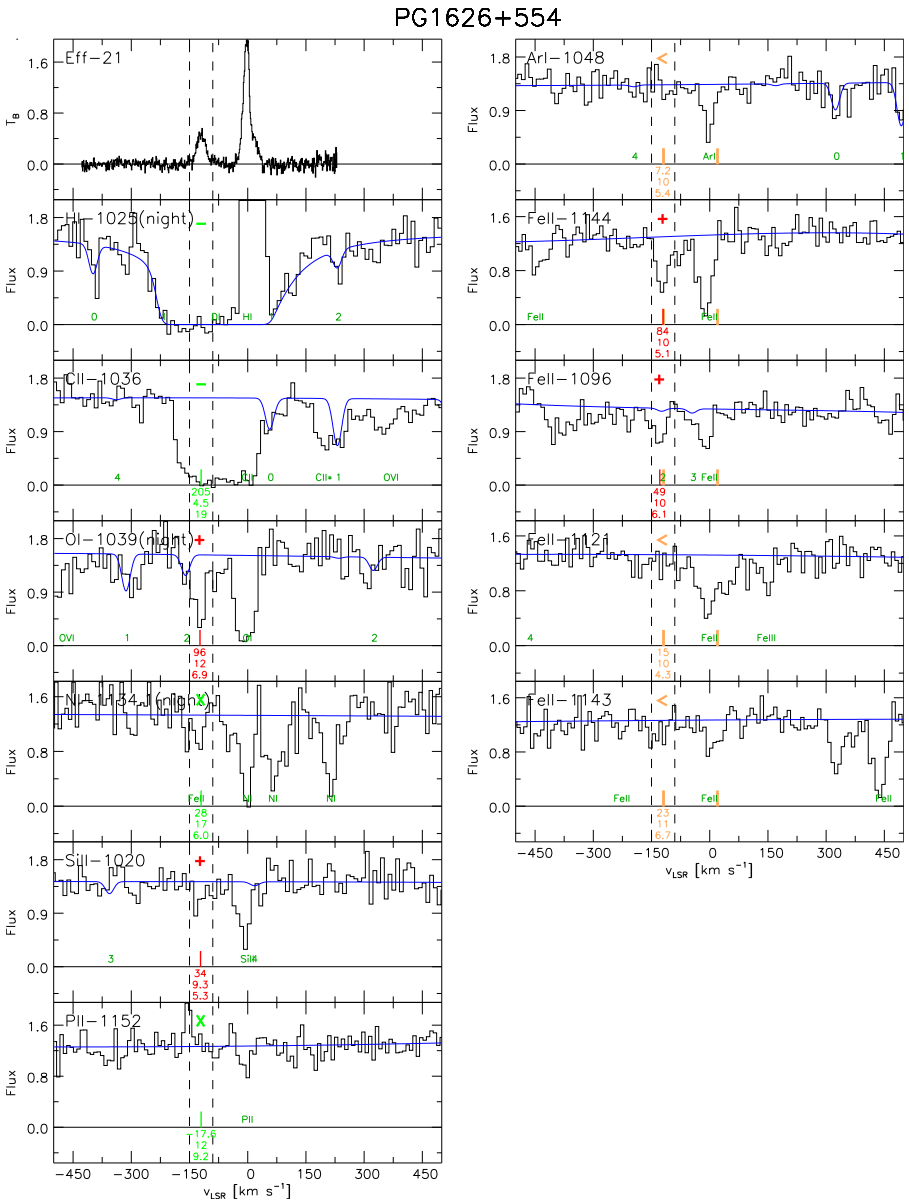

Figure 3.71 Cutouts of the Effelsberg 21 cm spectrum and selected UV spectra toward PG1626+554 highlighting ions and lines most relevant to the determination of the metallicity and depletion of each component.

These lines show indications of a weak, red "shoulder" extending perhaps as far as -50 km s^{-1}, which mirrors a similar shoulder in the Effelsberg 21 cm spectrum. We decomposed the 21 cm feature into two Gaussian components. The bulk of the observed H I emission is well fitted by a Gaussian centered at $v_{\rm LSR} = -119$ km s^{-1} with FWHM = 27 km s^{-1} and N(H I) = $(2.44 \pm 0.13) \times 10^{19}$ cm^{-2}, or log N(H I) = 19.39 ± 0.02. The shoulder of this feature, however, requires a Gaussian component with a much larger linewidth; we find the best fit centered at -110 km s^{-1} with FWHM = 70 km s^{-1} and N(H I) = $(1.92 \pm 0.01) \times 10^{19}$ cm^{-2}, or log N(H I) = 19.21 ± 0.01. Some authors, such Collins et al. (2003, 2007) extend the red limit of the window to -75 km s^{-1} in their analyses in an evident attempt to incorporate at least some of the UV absorption in the shoulder. The gas responsible for the shoulder may be a separate IVC, but we do not find the apparent UV absorption sufficiently convincing to target it for abundance analysis. As a result, for CIB in this direction, we adopt N(H I) as computed solely for the -120 km s^{-1} component, acknowledging that it must underestimate the actual H I column in the velocity range we define for obtaining CIB column densities. In lines of certain ions such as C II, the influence of the -110 km s^{-1} component is strong enough to render the CIB component useless for deriving N, but in the absence of useful data encompassing more lines of various ions, we feel this is the best approach in order to estimate the metallicity of CIB along this particular sightline.

Given that we do not detect a sufficient number of lines of any particular ion to constrain the intrinsic linewidth of the CIB component, we used the

best-fit value of 27 ± 5 km s^{-1} (Doppler $b = 15 \pm 3$ km s^{-1}) from the 21 cm spectrum for the COG analysis. The resulting abundances are shown in Figure 3.72. Based on the singular, but strong (7σ), detection of O I λ1039,

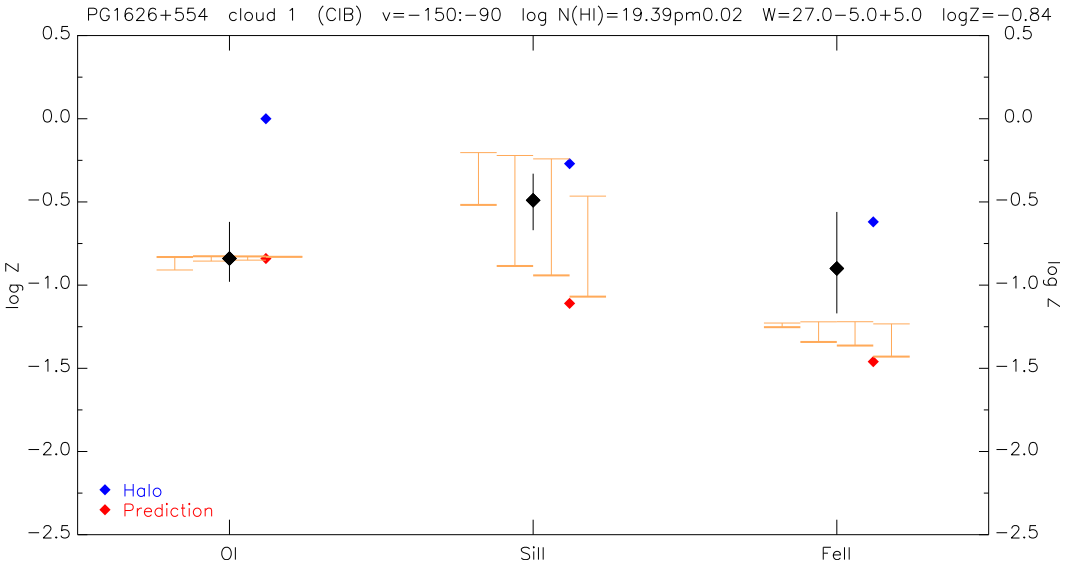

Figure 3.72 Abundance plot for the CIB core of Complex C toward PG1626+554 at -150 km s$^{-1} \leq v_{\rm LSR} \leq -90$ km s^{-1}. The range of possible ionization corrections is shown for 1, 5, and 10 kpc (log ϕ = 6.66, 5.77, and 5.60) at densities between log $n = -3$ and -1, and for the extragalactic background at log ϕ = 4.53 (orange bars, left to right). A Halo depletion pattern is indicated with blue points for each ion, and predicted abundances with red points given our measured [O I/H I] = -0.84.

we find [O I/H I] = -0.84 ± 0.22 ($0.14^{+0.10}_{-0.06}$ $Z_\odot$). No data are available for the intrinsically-stronger λ1302 line, and all other O I lines appearing in the present data set have near-zero flux. However, the implied O I metallicity is well within expectations for Complex C and reasonably consistent with the measurement of Collins et al. (2007), -0.79 ± 0.10 ($0.16^{+0.04}_{-0.03}$ $Z_\odot$) for an assumed

Doppler $b = 10.2$ km s^{-1}. We recognize that this is value disagrees with our H I linewidth obtained from 21 cm measurements, but we reiterate that their velocity integration window inevitably contains some significant amount of absorption due to the -110 km s^{-1} component. We believe this accounts for more of the difference in [O I/H I] between our measurement and theirs than do the disparate linewidths. Collins et al. also report an O I abundance of $-0.41^{+0.23}_{-0.20}$ ($0.39^{+0.27}_{-0.14}$ $Z_{\odot}$) for an assumed Doppler $b = 18.0$ km s^{-1} to illustrate the range linewidths resulting from abundance analyses of other Complex C sightlines. This is a larger value for b than can be justified by the data available to us for the PG1626+554 sightline. Relative to the range of Fe II abundances predicted by our ionization modeling, as shown in Figure 3.72, the measured value of [Fe II/H I] suggests low depletion in this cloud.

We also note a strong wing on the C II λ1036 line from the blue limit of the CIB window, -150 km s^{-1}, returning to the continuum level at about -200 km s^{-1}. This wing is not seen in any line of any other ion in the available data, but several important ions are either absent (Si III) or represented only by weak lines (Si II), or the data are of exceptionally low signal (C III). Wakker et al. (2003) suggests that O VI absorption may be present out to -210 km s^{-1}, but any such feature appears to be negatively impacted by the $(6-0)$ $P(3)$ line of H_2 at 1031.191 Å. There is no 21 cm detection in the Effelsberg spectrum at these velocities, nor is a component at this velocity required to adequately fit the Lyman series H I lines to an upper limit of N(H I) $\sim 10^{17}$ cm^{-2}, or log N(H I) ~ 17.00.

In summary, we measured the metallicity of the CIB core of Complex C along the sightline toward PG1626+554, finding $Z = 0.14\ Z_{\odot}$, in agreement with both expectations for Complex C and measurements of CIB toward Mrk 876. However, we note that the measurement toward PG1626+554 is evidently contaminated by a possible IVC near -110 km s^{-1}, leading to a potential overestimate of [O I/H I]. We did not find this IVC sufficiently distinguished from the CIB absorption to subject it to an abundance analysis. Finally, we note a possible HVC at -175 km s^{-1} based on the shape of the blue wing of C II λ1036, and place an upper limit of 0.4 $Z_{\odot}$ on its metallicity from ionization modeling. The final word on an inventory of metallicites of interstellar material in this sightline awaits better-quality data with larger wavelength coverage.

3.5 Results and Analysis: High Velocity Clouds

In this section, we broadly summarize the current state of knowledge each of the HVC/IVC complexes and/or individual clouds whose abundances we measured in the present work. The goal is to provide context for interpreting these new metallicities.

Table 3.6. Metallicity Results Summary

Sightline	Cloud	v_{cent} (km s^{-1})	N(H I) ($\times 10^{18}$ cm^{-2})	log N(H I)	Z ($Z_\odot$)	log Z	Ion(s)
3C273.0	–	+28	19.4 ± 2.2	19.29 ± 0.05	$1.3^{+1.2}_{-0.5}$	$0.1^{+0.3}_{-0.2}$	S II, Si II, Fe II
	–	+85	0.0035 ± 0.0005	$15.54^{+0.06}_{-0.07}$	> 0.14	> -0.85	C II, Si II
	–	+205	$< 1 \times 10^{-5}$	< 13.00	–	–	–
3C249.1	C	−120	0.025 ± 0.005	$16.40^{+0.08}_{-0.10}$	–	–	–
	IV Arch	−55	$58^{+1.5}_{-1.5}$	19.76 ± 0.01	$0.12^{+0.39}_{-0.29}$	$+0.05 \pm 0.13$	S II
ESO265-G23	WW226	+121	46.1^{+1}_{-1}	19.66 ± 0.01	$0.15^{+0.32}_{-0.10}$	-0.81 ± 0.49	O I
	–	+181	–	–	–	–	–
	MS	+262	≤ 3.07	18.15 ± 0.39	~ 1	~ 0	Si II, Si III
Mrk 106	A	−155	39.8 ± 0.6	19.60 ± 0.01	$0.23^{+0.21}_{-0.11}$	-0.64 ± 0.28	O I
	LLIVe	−43	22.4 ± 0.7	19.35 ± 0.01	~ 1	~ 0	N I, Si II, Fe II
	–	+60	0.74 ± 0.64	$17.87^{+0.27}_{-0.87}$	–	–	–
Mrk 153	M	−85	~ 1	~ 18.00	–	–	O I, Fe II
	IV Arch	−45	36.3 ± 1.4	19.56 ± 0.02	~ 0.8	~ -0.1	P II, Ar I, Fe II
	IVC157+56+70	+70	5.8 ± 0.7	$18.76^{+0.06}_{-0.05}$	$0.33^{+0.33}_{-0.17}$	-0.48 ± 0.30	O I
Mrk 205	WW84a	−202	14.9 ± 1.2	$19.17^{+0.03}_{-0.04}$	$0.05^{+0.33}_{-0.05}$	-1.27 ± 0.85	O I
	WW84b	−174	1.0 ± 0.7	$18.00^{+0.23}_{-0.52}$	$0.06^{+0.08}_{-0.03}$	-1.20 ± 0.34	O I
	C-South	−140	1.0 ± 0.7	$18.00^{+0.23}_{-0.52}$	$0.21^{+0.21}_{-0.09}$	-0.67 ± 0.27	O I
	LLIV	−63	41.2 ± 0.7	19.61 ± 0.01	$2.29^{+1.60}_{-0.88}$	$+0.36 \pm 0.22$	S II

Table 3.6 (cont'd)

Sightline	Cloud	v_{cent} (km s^{-1})	N(H I) ($\times 10^{18}$ cm^{-2})	log N(H I)	Z ($Z_\odot$)	log Z	Ion(s)
Mrk 279	C-South ("C1")	-188	$2^{+2}_{-1.2}$	$18.30^{+0.30}_{-0.40}$	$0.10^{+0.08}_{-0.04}$	-0.99 ± 0.25	O I
	CIII ("C2")	-143	19.2 ± 2.4	$19.28^{+0.05}_{-0.06}$	$0.17^{+0.17}_{-0.07}$	-0.78 ± 0.27	O I
	–	-113	$9.7^{+1.6}_{-1.6}$	$18.99^{+0.07}_{-0.08}$	–	–	–
	IV9	-83	$32.6^{+1.8}_{-1.8}$	19.51 ± 0.02	$1.66^{+1.43}_{-0.85}$	$+0.22 \pm 0.29$	S II
	LLIV	-45	49 ± 5.5	19.69 ± 0.05	$0.85^{+0.13}_{-0.18}$	-0.07 ± 0.08	S II
Mrk 509	–	-293	0.15 ± 0.07	$17.18^{+0.17}_{-0.27}$	< 0.55	< -0.26	O I
	–	-235	0.003 ± 0.001	$15.48^{+0.12}_{-0.18}$	–	–	–
	–	-125	0.02 ± 0.005	$16.30^{+0.10}_{-0.12}$	–	–	–
	g2a	$+55$	26.0 ± 0.5	19.41 ± 0.01	~ 0.5	~ -0.3	S II, P II, Si II, Fe II
	g2b	$+90$	4.3 ± 2.0	$18.63^{+0.17}_{-0.27}$	~ 0.5	~ -0.3	S II, P II, Si II, Fe II
	–	$+128$	0.01 ± 0.001	$16.00^{+0.04}_{-0.05}$	–	–	–
Mrk 817	CIC	-158	4.5 ± 1	$18.65^{+0.08}_{-0.11}$	$0.18^{+0.13}_{-0.08}$	-0.74 ± 0.24	O I
	CIA	-103	29.8 ± 0.9	19.47 ± 0.01	$0.32^{+0.08}_{-0.07}$	-0.50 ± 0.10	O I
	IV Arch	-50	$15.8^{+1.1}_{-1.1}$	19.20 ± 0.03	$0.41^{+0.24}_{-0.15}$	-0.39 ± 0.20	O I
	–	$+78$	–	–	–	–	–
Mrk 876	CD	-178	5.6 ± 0.5	18.75 ± 0.04	$0.26^{+0.37}_{-0.15}$	-0.58 ± 0.38	O I
	CIB-1	-135	12.9 ± 0.5	19.11 ± 0.02	$0.29^{+0.16}_{-0.10}$	$-0.54^{+0.19}_{-0.19}$	O I
	CIB-2	-100	9.7 ± 0.5	18.99 ± 0.02	$0.37^{+0.23}_{-0.14}$	-0.43 ± 0.21	O I
	IV20	-63	16.3 ± 3	$19.21^{+0.07}_{-0.09}$	~ 1.25	~ -0.1	O I, Si II, Fe II,Ni II
	Draco	-30	79.4 ± 0.4	19.90 ± 0.01	~ 1	~ 0	S II, P II, Si II, Fe II
	–	$+53$	0.5 ± 0.4	$18.70^{+0.26}_{-0.70}$	$0.20^{+0.42}_{-0.13}$	-0.70 ± 0.49	O I

3.5.1 Complex A

The sum total of distance, kinematic, and morphological information available about these clouds suggest that they are low-metallicity material accreting onto the Milky Way. Various distance estimates give the heliocentric distance to Complex A in the range of $2 - 10$ kpc, or about $1.5 - 7$ kpc in z-height above the Galactic plane (Wakker et al. 1996, Ryans et al. 1997a, van Woerden et al. 1999, Sembach et al. 2003, Wakker et al. 2003). This range of likely distances led van Woerden & Wakker (2004) to estimate the total H I mass of the complex as $\sim 10^6\ M_\odot$. A warm ionized gas component was reported by Tufte et al. (1998) in Hα observations with WHAM. Barger et al. (2012) estimate the total mass of the neutral hydrogen in Complex A at $1.6 - 2.3\ \times 10^6\ M_\odot$ and the mass of the warm ionized component at $1.3 - 2.5\ \times 10^6\ M_\odot$, also from WHAM data. Higher ions such as O VI, indicative of a hot ionized component, have been observed toward some Complex A sightlines; Sembach et al. (2003) measured log N(O VI) ~ 13.81 in the AVI core toward Mrk 106 but did not see it toward Mrk 116 to an upper limit of log N(O VI) < 13.49, noting the 2° angular separation of the two sightlines corresponds to a linear separation of $140 - 350$ pc at the assumed distance to Complex A.

Previous metallicity studies found sub-solar values for Complex A. Kunth et al. (1994) made pre-COSTAR GHRS observations of Mrk 116, finding [O I/H I] ~ -0.5 while cautioning that their result is subject to considerable measurement uncertainties, permitting possible metallicities ranging from $\sim 0.1\ Z_\odot$ up to slightly supersolar. Optical observations by Schwarz et al.

Table 3.6 (cont'd)

Sightline	Cloud	v_{cent} (km s^{-1})	N(H I) ($\times 10^{18}$ cm^{-2})	log N(H I)	Z ($Z_\odot$)	log Z	Ion(s)
NGC 1705	–	+105	~ 0.01	~ 16	–	–	C II, Si II
	–	+215	~ 0.003	~ 15.50	~ 0.3	~ -0.5	C III, Si III
	WW487	+263	~ 0.03	~ 16.50	~ 0.3	~ -0.5	Si II, siliii
	–	+313	0.95 ± 0.1	17.98 ± 0.01	$0.30^{+0.07}_{-0.06}$	-0.52 ± 0.09	O I
NGC 5253	WW154	+100	≤ 1.38	≤ 18.14	$0.81^{+0.39}_{-0.26}$	-0.09 ± 0.17	O I
	–	+210	≤ 0.97	≤ 17.99	–	–	–
PG1011-040	–	+80	5.4 ± 1.4	$18.73^{+0.10}_{-0.13}$	0.12	-0.92	O I
	WW92	+125	8.1 ± 0.8	$18.91^{+0.04}_{-0.05}$	0.26	-0.59	O I
	–	+210	0.07 ± 0.005	16.85 ± 0.03	~ 0.1	~ -1	C II, C III, Si III, Al II
	–	+260	–	–	–	–	C III
	–	+325	–	–	–	–	H I
PG1259+593	CIIIC	-133	90 ± 10	19.95 ± 0.05	$0.09^{+0.06}_{-0.03}$	-1.07 ± 0.19	O I
	IV-Arch	-58	28.1 ± 1.3	19.45 ± 0.02	$0.83^{+0.87}_{-0.42}$	-0.08 ± 0.31	O I
	–	+70	0.03 ± 0.005	$16.48^{+0.07}_{-0.08}$	–	–	C II, O I, Si II, Si II
PG1626+554	CIB	-120	24.4 ± 1.3	19.39 ± 0.02	$0.14^{+0.10}_{-0.06}$	-0.84 ± 0.22	O I

(1995) include the detection of Ca II toward Mrk 106 at $v_{\rm LSR} = -152$ km s^{-1}; as Ca is heavily depleted in the ISM, this result argues for a low dust content in Complex A.

Wakker et al. (1996) compile an exhaustive list of eleven possible origin scenarios for Complex A, although many (e.g., the "ghost" of nearby molecular clouds; representative of a supernova shell; a large z-height spiral arm) have fallen out of favor entirely as general explanations of the HVC/IVC phenomenon in the intervening years. In part because LLIV gas is seen in the same direction, a Galactic Fountain origin could not be ruled out, but they lean toward an explanation in which Complex A is comprised of low-metallicity gas being accreted by the Milky Way; in either case, metallicity is the key in discriminating between these scenarios. Wakker (2001a) argued for a metallicity of $0.05 - 0.1$ solar on the basis of the Kunth et al. observations.

Belokurov et al. (2007) report the discovery of a tidal stream that extends over $\sim 50^\circ$ in the north Galactic cap as a stellar overdensity in SDSS imaging data, which at first was not clearly associated with any known progenitor. This "Orphan Stream" lies along a great circle describing an orbit of Galactocentric radius ~ 25 kpc. The authors point out this great circle is coincident with both the long dimension defining the main structure of Complex A, as well as with the dwarf spheroidal (dSph) galaxy Ursa Major II (UMa II; Zucker et al. 2006). Belokurov et al. comment on the possible association of all three, noting the comment of Zucker et al. regarding the irregularity of UMa II's isophotes and "evidence of multiple concentrations," suggesting the

galaxy is in the process of tidal disruption. They explain the evident difference between the inferred orbital radius of the Stream and distance estimates to Complex A on the assumption that the two lie along different wraps of the same orbit. However, results reported by Newberg et al. (2010) on the orbit of the Orphan Stream refute the idea of a kinematic association with either Complex A or UMa II on the basis that the velocity of neither is consistent that that of the Stream; the N-body simulations of Sales et al. (2008) support this view. Recent metallicity measurements of stars in the Orphan Stream by Casey et al. (2013) support the idea that the Stream parent is a dSph, but note the Stream's metallicity is about 0.5 dex below the lowest metallicity estimates for Complex A. Therefore, while intriguing, it is unlikely that Complex A finds its origin in material tidally stripped from an accreted Milky Way dSph.

More recently, Barger et al. (2012) took a different approach to measure abundances in Complex A: rather than conduct a pencil-beam UV abundance study, they analyzed visible-wavelength spectroscopic data from WHAM, which was designed to detect faint optical emission from diffuse ionized sources. The data consist of deep, targeted observations in Hα, and several forbidden lines of low ions: [S II] λ6716, [N II] λ6584, and [O I] λ6300. In addition to estimating the total H I mass in the warm ionized component as described above, they derive N and S abundance limits for grids of temperature, metallicity, and cloud configurations assuming photoionization as the only source of ionization. For several Complex A cores, they find sub-solar abundances that imply temperatures $> 10^4$ K or gas with large fractions of singly- ionized N

and S. Their values, along with the Kunth et al. measurement of Mrk 116 and our new abundance value for Mrk 106 are collected in Table 3.8.

The quality of the data from which we obtained a measurement of the O I abundance of the AVI core toward Mrk 106 is superior to that of the GHRS spectra obtained by Kunth et al. (1994) and implies a somewhat lower metallicity, but we caution that it hinges on the detection of a single line of O I. However, we used an improved value of N(H I) which is less susceptible to the effect of small-scale structure than that reported by Kunth et al. We are certain that the metallicity of Complex A, to the extent that abundances in the AVI core are representative of the entire Complex, is certainly below solar and probably similar to that of Complex C. The observation of cold neutral and warm/hot ionized components suggests Complex A is being ionized by an interaction with hot Halo gas, and its metallicity excludes any origin scenario in the Disk.

3.5.2 Complex C

Complex C is a large (1600 deg^2) association of HVCs in the northern Galactic sky at velocities $200 > v_{\rm LSR} > 90$ km s^{-1} (Wakker 2001a, Lehner et al. 2004). It consists of several cores seen in 21 cm maps, which are identified individually; the following cores for which new measurements are presented here are listed in Table 3.9. CI (cores CIA, CIB, CIC) and CIII (cores CIIIA, CIIIB, CIIIC) were named by Giovanelli et al. (1973). We follow the convention of Wakker (2001a) in referring to the low-latitude side of Complex

Table 3.7. Complex A Abundances

Cloud	Sightline	v_{min}[a] (km s^{-1})	v_{max} (km s^{-1})	log N(H I)	Ion(s)	$[X/\mathrm{H\ I}]$	$Z/Z_\odot$	Reference
AIII	–	−250	−50	–	[N II]	~ -0.4	~ 0.4	Barger et al. (2012)
AIV	–	−250	−50	–	[S II]	~ -0.5	~ 0.3	Barger et al. (2012)
AVI	IZw 18[b]	–	–	19.32 ± 0.02	O I	$-0.49^{+0.70}_{-0.62}$	$0.32^{+1.30}_{-0.25}$	Kunth et al. (1994)
AVI	Mrk 106	−250	−50	–	[S II]	~ -0.15	~ 0.7	Barger et al. (2012)
		−205	−105	19.60 ± 0.01	O I	-0.64 ± 0.28	$0.23^{+0.21}_{-0.11}$	**This work**

Table 3.8. Measurements of Complex A abundances with literature comparison values.

[a] v_{min} without an accompanying v_{max} indicates a centroid velocity only. Entries with neither velocity signify situations in which no velocity limits were quoted.

[b] Also designated Markarian 116.

C as "C-South"; more precisely, he defined this as Complex C at $\ell > 101°$, $b < +48°$ and $80° \leq \ell \leq 100°$, and velocities $v_{\rm LSR} < -140$ km s^{-1} in the region of overlap with CI. Core CD is defined as the core at $\ell = 90°$, $b = +34°$, and $v_{\rm LSR} < -150$ km s^{-1} close to "Complex D" of Wakker & van Woerden (1991). Complex C is situated roughly 6-12 kpc above the plane of the Milky Way at a Galactocentric radius < 14 kpc. The best distance estimates for Complex C to date are those reported by our group in a series of two papers, Wakker et al. (2007) and Wakker et al. (2008). Individual measurements include cores CI ($z = 6.8 - 9.2$ kpc), CIIIA ($z = 6.4 - 11.2$ kpc), and a core at $\ell = 68°$, $b = +38°$ named alternately "C-extension" by Giovanelli et al. (1973) and "CeI" by Wakker (2001a); for the latter core, we found $z = 6.5 - 12.3$ kpc. Obtaining reliable distance brackets allows us to estimate the total mass of Complex C. We found $(3 - 14) \times 10^6$ $M_\odot$ which implies a mass flow of $0.1 - 0.25$ $M_\odot$ yr^{-1} toward the disk of the Milky Way. The total inflow rate of all other clouds with known distances is about half this much (Wakker 2012); therefore, we conclude the total cold gas accretion rate of the Milky Way is a few tenths of a solar mass per year, in line with estimates derived from other nearby galaxies (e.g., Sancisi et al. 2008).

In addition to absorption from low ions and H^+ (Tufte et al. 1998, Wakker et al. 1999a), highly ionized species such as C IV, Si IV, (Fox et al. 2004) and O VI (Murphy et al. 2000, Sembach et al. 2000, 2003) are seen in the direction of Complex C, suggesting a highly ionized boundary layer at the Complex margins attributable to its interaction with the hot, ambient medium

of the Galactic halo (Murphy et al. 2000, Sembach et al. 2000, Richter et al. 2001c). There is little or no dust in Complex C, inferred from the lack of significant depletion in ions such as Si (Murphy et al. 2000, Wakker 2001a, Collins et al. 2003, Tripp et al. 2003) and the nondetection of H_2 Murphy et al. (2000), Richter et al. (2001c). A high D/H value relative to the Milky Way ISM was ruled out by Sembach et al. (2004) in *FUSE* observations toward PG1259+593; however, they found a very different D/O value (0.28 ± 0.12) compared to the local ISM and Disk, which in the absence of N(H I) information argues for a subsolar metallicity. The abundances of N I, O I, Si II, and Fe IIand evident lack of dust led Wakker (2001a) to conclude there is no secondary nitrogen in Complex C (i.e., N/O < 0.5; see Section 3.3.10). This indicates that intermediate-mass stars have not contributed substantially to the enrichment of Complex C gas (Tripp et al. 2003). Wakker (2001a) also notes that the abundances toward Complex C are consistent with α-element enhancement (e.g., Si/O > 1), but Tripp et al. (2003) decided error bars on then-current measurements were too large to justify that conclusion. If the apparent α-element enhancement is shown to be true, and the claims of no secondary nitrogen and low iron-peak element abundance confirmed, it would strongly suggest that the heavy elements in Complex C were manufactured in a previous generation of massive stars that ended as Type II supernovae and that Complex C is not the site of relatively recent star formation (Wakker 2001a).

Gibson et al. (2001) argued that the apparent homogeneity of metal-

licity measurements along multiple Complex C sightlines favored an origin scenario in which its contents are considered mildly-enriched "waste" gas from the Milky Way or processed gas tidally stripped from a dwarf galaxy rather than low-metallicity Galactic "fuel". On the other hand, Collins et al. (2003) concluded that this complex may be the result of a mixture of infalling, low-metallicity gas with enriched material from the Galactic Fountain. Tripp et al. (2003) presented evidence that Complex C is intrinsically metal-poor, and its spatial pattern of low- and high-ion absorption indicates it is on a plunging orbit toward the Disk that is causing its leading edge to ablate and dissipate as it interacts with hot Halo gas. In their analysis, apparent metal enrichment along some sightlines through the complex is the result of outflowing Galactic Fountain gas that may be interacting with Complex C. Shull et al. (2011) founds that individual clumps of gas within Complex C appear to be virial near-equilibrium with pressure confinement, and that their masses are probably sufficiently large to survive dissipation by surface instabilities as the Complex interacts with the hot Halo medium.

Table 3.9. Complex C Abundances

Cloud	Sightline	v_{min}[a] (km s^{-1})	v_{max} (km s^{-1})	log N(H I)	Ion	$[X/\mathrm{H\ I}]$	$Z/Z_\odot$	Reference
				CI				
CIA	Mrk 817	−140	−80	19.48 ± 0.01	O I	$-0.59^{+0.25}_{-0.17}$	$0.26^{+0.20}_{-0.08}$	Collins et al. (2003)
					N I	< -0.96	< 0.11	
		−160	−80	19.48 ± 0.01	O I	$-0.50^{+0.25}_{-0.18}$[d]	$0.32^{+0.25}_{-0.11}$	Tripp et al. (2003)
		−160	−80	19.48 ± 0.01	O I	$-0.45^{+0.25}_{-0.17}$	$0.35^{+0.28}_{-0.11}$	Fox et al. (2004)
		−140	−80	19.51 ± 0.01	O I	$-0.54^{+0.16}_{-0.09}$	$0.29^{+0.13}_{-0.05}$	Collins et al. (2007)
					N I	< -1.17	< 0.07	
		−190	−70	19.50 ± 0.18	O I	-0.47 ± 0.24	$0.34^{+0.25}_{-0.14}$	Shull et al. (2011)
		−135	−75	19.47 ± 0.01	O I	-0.50 ± 0.10	$0.32^{+0.08}_{-0.07}$	**This work**
					N I	< -0.97	< 0.11	
CIB	Mrk 876	−150	−95	19.26 ± 0.03	O I	$-0.54^{+0.43}_{-0.29}$	$0.29^{+0.49}_{-0.14}$	Collins et al. (2003)
					N I	$-1.19^{+0.14}_{-0.12}$	0.06 ± 0.02	
		−155	−85	19.48 ± 0.01	O I	$-0.70^{+0.18}_{-0.15}$	$0.20^{+0.10}_{-0.06}$	Collins et al. (2007)
					N I	$-1.18^{+0.14}_{-0.12}$	$0.07^{+0.03}_{-0.02}$	
		−170	−100	19.39 ± 0.18	O I	$-0.82^{+0.17}_{-0.14}$	$0.15^{+0.07}_{-0.04}$	Shull et al. (2011)
		−150	−120	19.11 ± 0.02	O I	-0.54 ± 0.19	$0.29^{+0.16}_{-0.10}$	**This work**
					N I	-1.15 ± 0.23	$0.07^{+0.05}_{-0.03}$	
		−120	−80		O I	-0.43 ± 0.21	$0.29^{+0.16}_{-0.10}$	
					N I	-1.28 ± 0.13	$0.05^{+0.02}_{-0.01}$	
	PG1626+554	−155	−75		O I	< -0.79	< 0.16	Collins et al. (2003)

Table 3.9 (cont'd)

Cloud	Sightline	v_{min}[a] (km s^{-1})	v_{max} (km s^{-1})	log N(H I)	Ion	$[X/\mathrm{H\ I}]$	$Z/Z_\odot$	Reference
					N I	< -0.88	< 0.13	
		-155	-75	19.43 ± 0.12	O I	-0.79 ± 0.10	$0.16^{+0.04}_{-0.03}$	Collins et al. (2007)[b]
		-155	-75		O I	$-0.41^{+0.23}_{-0.20}$	$0.39^{+0.27}_{-0.14}$	Collins et al. (2007)[c]
		-150	-90	19.39 ± 0.02	O I	-0.84 ± 0.22	$0.14^{+0.10}_{-0.06}$	**This work**
CIC	Mrk 817	-180	-135	$18.54^{+0.11}_{-0.15}$	O I	-0.74 ± 0.24	$0.18^{+0.13}_{-0.08}$	**This work**
					N I	< -0.40	< 0.40	
				CIII				
CIIIC	PG1259+593	-130	–	19.92 ± 0.01	O I	$-1.03^{+0.37}_{-0.31}$	$0.09^{+0.13}_{-0.05}$	Richter et al. (2001c)
					N I	$-1.94^{+0.17}_{-0.21}$	$0.011^{+0.006}_{-0.004}$	
		-180	-105	19.92 ± 0.01	O I	$-1.00^{+0.19}_{-0.25}$	$0.10^{+0.05}_{-0.04}$	Collins et al. (2003)
					N I	$-1.82^{+0.20}_{-0.13}$	$0.015^{+0.009}_{-0.004}$	
		–	–		O I	$-0.91^{+0.20}_{-0.25}$[d]	$0.12^{+0.07}_{-0.05}$	Tripp et al. (2003)
					N I	$-1.83^{+0.22}_{-0.16}$	$0.015^{+0.010}_{-0.005}$	
		-130	–	19.92 ± 0.01	O I	$-0.85^{+0.37}_{-0.31}$	$0.14^{+0.19}_{-0.07}$	Fox et al. (2004)
		-180	-105	19.92 ± 0.01	O I	$-0.86^{+0.19}_{-0.25}$	$0.14^{+0.08}_{-0.06}$	
		-128	–	19.95 ± 0.05	O I	$-0.79^{+0.12}_{-0.16}$	0.16 ± 0.05	Sembach et al. (2004)
		–	–	19.95 ± 0.01	O I	$-1.00^{+0.21}_{-0.18}$	$0.10^{+0.06}_{-0.03}$	Collins et al. (2007)
					N I	$-1.81^{+0.25}_{-0.18}$	$0.015^{+0.012}_{-0.005}$	
		-170	-95	19.97 ± 0.19	O I	-0.81 ± 0.15	$0.15^{+0.06}_{-0.05}$	Shull et al. (2011)
					N I	-1.95 ± 0.12	$0.011^{+0.004}_{-0.003}$	

Table 3.9 (cont'd)

Cloud	Sightline	v_{min}[a] (km s^{-1})	v_{max} (km s^{-1})	log N(H I)	Ion	$[X/\mathrm{H\ I}]$	$Z/Z_\odot$	Reference
		-150	-105	19.95 ± 0.05	O I	-1.07 ± 0.19	$0.09^{+0.05}_{-0.03}$	**This work**
					N I	-1.54 ± 0.34	$0.03^{+0.03}_{-0.02}$	
(off core)	Mrk 279	-210	-165	$18.24^{+0.17}_{-0.28}$	O I	-0.99 ± 0.25	$0.10^{+0.08}_{-0.04}$	**This work**
					N I	< -1.26	< 0.05	
				CD				
	Mrk 876	-210	-95	19.48 ± 0.01	O I	< -0.32	< 0.48	Collins et al. (2003)
					N I	$-1.09^{+0.16}_{-0.15}$	$0.08^{+0.04}_{-0.02}$	
		-210	-155	$18.72^{+0.12}_{-0.17}$	O I	$-0.59^{+0.22}_{-0.21}$	$0.26^{+0.17}_{-0.10}$	Collins et al. (2007)
					N I	< -1.13	< 0.07	
		-205	-150	18.75 ± 0.04	O I	-0.58 ± 0.38	$0.26^{+0.48}_{-0.13}$	**This work**
					N I	< -1.31	< 0.05	
				"C-South"[e]				
	Mrk 205	-120	$-$	19.20 ± 0.06	S II	< -0.51	< 0.31	Lehner et al. (2004)
		-165	-125	$18.11^{+0.09}_{-0.11}$	O I	$-0.78^{+0.12}_{-0.13}$	$0.17^{+0.05}_{-0.04}$	Collins et al. (2007)
					N I	< -0.63	< 0.23	
		-165	-115	$18.00^{+0.23}_{-0.52}$	O I	-0.67 ± 0.27	$0.21^{+0.21}_{-0.09}$	**This work**
	Mrk 279	-180	-90	19.52 ± 0.06	O I	$-0.71^{+0.36}_{-0.25}$	$0.19^{+0.25}_{-0.09}$	Collins et al. (2003)
					N I	< -1.20	< 0.06	
		$-$	$-$		O I	$-0.59^{+0.36}_{-0.26}$[d]	$0.26^{+0.33}_{-0.11}$	Tripp et al. (2003)

We have made more measurements along individual sightlines toward this cloud complex than toward any other; these results are collected in Table 3.9 along with relevant literature values for purposes of comparison. Our measurements consist of a previously- unreported component in the direction of Mrk 279 that samples CIII off the main cores and six other components along five sightlines for which previous abundance measurements exist in the literature. In the latter case, our measurements agree with consensus values to within errors; this gives us confidence that our method for determining abundances is robust. To many of the Complex C sightlines with existing, published abundance information, we add abundances for ions without previous measurements.

We can draw some useful conclusions by looking at a few abundance ratios, shown in Table 3.11, in which we show values of Si/O, Fe/O, and N/O for the seven Complex C components included in our sample. We include these particular ratios in the table because they are indicative of the likely origin of the heavy elements we see in this cloud complex. As Wakker (2001a) pointed out, to the extent that dust depletion is not important in Complex C, the following criteria suggest past enrichment by Type II supernovae: (1) an enhancement of the α elements; (2) a low abundance of iron-peak elements; and (3) evidence of primary N production. We find evidence for all three criteria among our Complex C sightlines. The entries in Table 3.11 are arranged in rough order of increasing (ℓ, b); i.e., along the long axis of the Complex away from the Galactic plane. We find that the alpha element fraction, represented

Table 3.9 (cont'd)

Cloud	Sightline	v_{min}[a] (km s^{-1})	v_{max} (km s^{-1})	log N(H I)	Ion	$[X/\mathrm{H\ I}]$	$Z/Z_\odot$	Reference
					N I	< -1.1[f]	< 0.08	
		-180	-90	19.52 ± 0.06	O I	$-0.57^{+0.36}_{-0.25}$	$0.27^{+0.35}_{-0.12}$	Fox et al. (2004)
		-200	-120	19.27 ± 0.08	O I	$-0.95^{+0.14}_{-0.13}$	$0.11^{+0.04}_{-0.03}$	Collins et al. (2007)
					N I	$-1.83^{+0.14}_{-0.17}$	$0.015^{+0.006}_{-0.005}$	
		-135	-65	19.19 ± 0.03	O I	< -0.54	< 0.29	Collins et al. (2003)
					N I	< -0.34	< 0.46	
		-165	-120	19.17 ± 0.02	O I	-0.78 ± 0.27	$0.17^{+0.14}_{-0.08}$	**This work**
					N I	-1.87 ± 0.15	$0.017^{+0.007}_{-0.005}$	

Table 3.10 (cont'd)

[a]v_{min} without an accompanying v_{max} indicates a centroid velocity only. Entries with neither velocity signify situations in which no velocity limits were quoted.

[b]For Doppler $b = 10.2$ km s^{-1}

[c]For Doppler $b = 18.0$ km s^{-1}

[d]Quoted as total [O/H].

[e]The low-latitude side of Complex C; see main text for precise definition.

[f]Quoted as total [N/H].

Table 3.11. Complex C Abundance Ratios

Core	Sightline	v_{min} (km s^{-1})	v_{max} (km s^{-1})	Si/O	Fe/O	N/O
CD	Mrk 876	−205	−150	$1.70^{+3.43}_{-1.14}$	$1.10^{+3.17}_{-0.81}$	< 0.19
"CIB -1"	Mrk 876	−150	−120	$1.23^{+1.17}_{-0.60}$	$1.00^{+1.57}_{-0.61}$	$0.25^{+0.40}_{-0.15}$
"CIB -2"	Mrk 876	−120	−80	$1.70^{+1.54}_{-0.81}$	$1.07^{+1.81}_{-0.67}$	$0.14^{+0.17}_{-0.08}$
CIB	PG1626+554	−150	−90	$0.87^{+2.29}_{-0.63}$	$2.24^{+3.13}_{-1.31}$	–
CIA	Mrk 817	−135	−75	$1.17^{+0.64}_{-0.42}$	$0.66^{+0.46}_{-0.27}$	< 0.34
CIC	Mrk 817	−180	−135	$3.89^{+5.44}_{-2.27}$	$1.26^{+2.91}_{-0.88}$	< 2.19
C-South	Mrk 279	−165	−120	$1.95^{+5.13}_{-1.41}$	$0.68^{+1.37}_{-0.45}$	$0.08^{+0.13}_{-0.05}$
C-South	Mrk 205	−165	−125	$2.63^{+5.69}_{-1.80}$	< 4.27	< 12.59
CIII (off core)	Mrk 279	−210	−165	$3.24^{+5.47}_{-2.03}$	< 1.29	< 0.49
CIIIC	PG1259+593	−150	−105	$1.51^{+1.80}_{-0.82}$	$0.71^{+1.03}_{-0.42}$	$0.34^{+0.81}_{-0.24}$

by Si/O, is enhanced along each sightline. The most α-enhanced sightlines appear to be those on the low-latitude side of the Complex, but this is not an especially robust conclusion given the uncertainties of the individual measurements. The iron-peak abundance, represented by Fe/O, is generally $\lesssim 1$, indicating a deficit relative to what we might expect for Disk gas. Finally, our measurements confirm that most sightlines probing Complex C find N/O sufficiently low (< 0.5) to argue that the observed N has, generally, a primary nucleosynthetic origin and was not made in recent generations of stars (Lu et al. 1998a).

3.5.3 Other HVCs

While the distribution of high-velocity gas across the sky is seen to form coherent structures of major cloud complexes, a number of smaller clouds exist.

We collect them here and summarize their abundances in Table 3.12.

Table 3.12. Other HVC Metallicities

Cloud	Sightline	v_{min}[a] (km s^{-1})	v_{max} (km s^{-1})	log N(H I)	Ion	$[X/\mathrm{H\ I}]$	$Z/Z_\odot$	Reference
				Complex WB				
WW92		–	–	–	–	~ -0.3	~ 0.5	Wakker (2012)
PG1011−040		–	–	–	–	-0.42	0.38	Flack and Wakker (2004)[b]
		–	–	–	–	-0.47	0.34	Ojalvo & Wakker (2005)
		+100	+150[c]	$18.91^{+0.04}_{-0.05}$	O I	-0.59 ± 0.08	$0.26^{+0.05}_{-0.04}$	**This work**
					N I	-0.79 ± 0.10	$0.16^{+0.04}_{-0.03}$	
WW135		–	–	–	–	~ -0.3	~ 0.5	Wakker (2012)
				Complex WD				
WW582		–	–	–	–	~ -0.7	~ 0.2	Wakker (2012)
WW154	NGC 5253	+50	+150	$18.02^{+0.12}_{-0.17}$	O I	-0.09 ± 0.17	$0.81^{+0.39}_{-0.26}$	**This work**
WW226	ESO265−G23	+90	+152	19.66 ± 0.01	O I	-0.81 ± 0.49	$0.15^{+0.32}_{-0.10}$	**This work**
				Complex gp				
g2b	Mrk 509	+75	+105	$18.72^{+0.08}_{-0.09}$	O I	-0.47 ± 0.27	$0.34^{+0.29}_{-0.16}$	**This work**
					N I	-0.87 ± 0.19	$0.13^{+0.07}_{-0.05}$	**This work**
				Very High Velocity Clouds				
WW84a	Mrk 205	−220	−183	$19.17^{+0.03}_{-0.04}$	O I	-1.27 ± 0.85	$0.05^{+0.33}_{-0.05}$	**This work**
					N I	-1.40 ± 0.32	$0.04^{+0.08}_{-0.01}$	

3.5.3.1 The Wannier Clouds (Complexes WA, WB, WC, WD)

The Wannier Clouds are a group of positive-velocity HVCs in the third and fourth Galactic quadrants first reported by Wannier et al. (1972) and given designations Complex WA, Complex WB, Complex WC, and Complex WD; 64 individual clouds within these groups are identified by the prefix "WW" in the catalog of Wakker & van Woerden (1991). They are clearly separated from the major Complexes A and C by virtue of their positive velocities and considerably lower H I column densities. Wakker and van Woerden thought WB, WC, and WD might be related to the "large-scale structure of the Galaxy" on the basis of their small deviation velocities. Blitz et al. (1999) argued these Clouds are distant objects undergoing infall in the direction of the Local Group Barycenter, complementary to the Extreme Positive (EP) clouds seen in the direction of the Local Group anti- Barycenter, which implies low metallicities on the order of $Z \sim 0.1\ Z_{\odot}$, but the upper distance limit to Complex WB reported by Thom et al. (2006), ~ 9 kpc, seems to place them well within the Halo. This is consistent with the upper limit of 16 kpc for the extended, ionized envelope of gas surrounding Complexes WA and WB along the sightline toward PG 0914+001 measured by Lehner et al. (2012). Smoker et al. (2004) established lower distance limits of $\sim 1.4 - 2.5$ kpc to gas in Complex WB in the directions of EC 09470−1433 and EC 09452−1403.

Measured metallicities for members of this group span a considerable range. In Complex WB gas, Wakker and coworkers quote $Z \sim 0.5\ Z_{\odot}$ for clouds WW92 and WW135 (Wakker 2012) and $0.34 \leq Z \leq 0.38\ Z_{\odot}$ along

Table 3.12 (cont'd)

Cloud	Sightline	v_{min}[a] (km s^{-1})	v_{max} (km s^{-1})	log N(H I)	Ion	$[X/\mathrm{H\ I}]$	$Z/Z_\odot$	Reference
WW84b	Mrk 205	−183	−165	$18.00^{+0.23}_{-0.52}$	O I	-1.20 ± 0.34	$0.06^{+0.08}_{-0.03}$	**This work**
					N I	< -0.69	< 0.20	
Highly Ionized High Velocity Clouds								
GCN	Mrk 509	−340	−250	< 17.69	N I	$> +0.11$	> 1.29	Sembach et al. (1999)
		−335	−260	< 17.69	O I	> -0.73	> 0.19	Collins et al. (2004)
					N I	$> +0.06$	> 1.15	
		−325	−260	$17.18^{+0.17}_{-0.27}$	O I	< -0.26	< 0.55	**This work**
					N I	< 0.46	< 2.88	
		−250	−170	< 17.69	N I	> -0.08	> 0.83	Sembach et al. (1999)
		−260	−200	< 17.69	O I	> -0.88	> 0.13	Collins et al. (2004)
					N I	> -0.09	> 0.81	

[a] v_{min} without an accompanying v_{max} indicates a centroid velocity only. Entries with neither velocity signify situations in which no velocity limits were quoted.

[b] Private communication.

[c] Some ions/lines were integrated to +180 km s^{-1}; see Section 3.4.13.

the sightline toward PG1011−040 (Ojalvo & Wakker 2005). We found $Z = 0.26\ Z_\odot$ for WW92 toward the latter sightline. Complex WD gas seems to be of lower metallicity by comparison. We measured $Z = 0.15$ for the cloud WW226 in the direction of ESO265−G23, in accord with the figure of $Z \sim 0.2\ Z_\odot$ given by Wakker (2012) for WW582. However, our measurement of $Z = 0.8\ Z_\odot$ for WW154 toward NGC 5253 disagrees with both. Considering the range of implied distances, 1.4 kpc $\leq |z| \leq$ 16 kpc and a range of metallicities from near-solar to substantially subsolar, both the Galactic Fountain and Halo infall are consistent with the data. Probably both scenarios explain different components of the Wannier Clouds.

3.5.3.2 Cloud g2

This small, faint cloud is part of Complex gp, an association of intermediate velocity gas in the region $\ell = 30° - 70°$, $b = -45°$ to 20°. 21 cm maps indicate a comet-like head-tail morphology that suggests the interaction of a cold, dense core with surrounding, hot Halo gas. It is seen in the direction of Mrk 509 at moderate positive velocities as described previously in Section 3.4.8. In our analysis of Mrk 509 spectra, we decided to split the component usually defined around +30 km s^{-1} $\lesssim v_{\rm LSR} \lesssim$ +100 km s^{-1} into two pieces at +75 km s^{-1} based on indications of two distinct components in both the UV and H I 21 cm emission spectra. We call these components g2a (+35 km s^{-1} $\leq v_{\rm LSR} \leq$ +75 km s^{-1}) and g2b (+75 km s^{-1} $\leq v_{\rm LSR} \leq$ +105 km s^{-1}). On the assumption that both components represent the same

cloud, from the abundance patterns of g2a and g2b along with the predicted abundance ranges from ionization modeling, we find a systemic metallicity of ~ -0.3 ($\sim 0.5\ Z_{\odot}$) for g2. Given the 21 cm morphology of the cloud, it is probably located in the lower reaches of the Halo and made of fundamentally lower-metallicity material that is presently mixing with enriched gas from the Disk, diluting it to the measured value.

3.5.3.3 Very High Velocity Clouds (VHVCs)

Clouds with $|v_{\rm LSR}| \gtrsim 250$ km s^{-1} are categorized as Very High Velocity Clouds (VHVCs; e.g., Wakker & van Woerden 1997a and references therein) and are mostly found in the southern Galactic hemisphere around $\ell < 180°$. This places them in the vicinity of the tip of the Magellanic Stream, making them complementary to the EP Clouds at $\ell > 180°$ thought to coincide with the Leading Arm of the Stream. Given the fragmentary morphology of the Stream, Giovanelli (1981) argued the VHVCs are a population of these fragments, but interpreted this to result from the Stream leading the Magellanic Clouds, now known not to be the case (Jones et al. 1994). Wakker (1990) showed the observed scatter of velocities can be produced in a trailing-Stream scenario. The VHVCs must be distant (~ 50 kpc) if they are physically related to the tip of the Stream. However, many VHVCs show a two-velocity-component structure that the Stream does not, which argues against a physical relation (and, therefore, a common distance). The metallicity of this population, then, is a key factor in understanding these clouds' origin, particularly

in comparing it with both the Stream and the Magellanic Clouds themselves.

We observed the VHVC called WW84 in the direction toward Mrk 205 in two distinct velocity intervals which we called WW84a (-220 km s^{-1} $\leq$ $v_{\rm LSR}$ $\leq$ -183 km s^{-1}) and WW84b (-183 km s^{-1} $\leq$ $v_{\rm LSR}$ $\leq$ -165 km s^{-1}). Burton et al. (2004) found a distance bracket of $210 \leq D \leq 1100$ kpc for this object, making it among the most distant HVCs known, perhaps lying beyond the Magellanic Clouds themselves. We find very low metallicities for the two components of this cloud, $Z \sim 0.05$ and 0.06 $Z_{\odot}$, respectively; this cloud has the lowest metallicity of any HVC ever measured to date. Comparison with some Magellanic Stream values suggests these metallicities are relatively low but not inconsistent with previous measurements. Lu et al. (1998b) measured abundances in HVC 287.5+22.5+240, an EP Cloud likely in the leading tail of the Stream, and found [S/H] $= -0.60^{+0.11}_{-0.15}$ and [Fe/H] $= -1.48 \pm 0.07$, arguing that the metallicity and depletion of this cloud coupled with its position and velocity suggest that it originated from the Magellanic Clouds. Sembach et al. (2001a) measured the metallicity of the same cloud with *FUSE*, finding [Si/H] $= -0.81^{+0.09}_{-0.12}$, [P/H] < -0.42, [N/H] > -1.93, and [Fe/H] $= -1.51^{+0.09}_{-0.12}$. The first proper metallicity measurement of the Stream itself was made by Gibson et al. (2000), who found [Si II/H I] $= -0.55$. Lehner et al. (2008) measured the metallicity of the Magellanic Bridge as [O/ H] $= -0.96^{+0.13}_{-0.11}$ ($0.11^{+0.04}_{-0.02}$ $Z_{\odot}$). They found an overall metallicity of $Z = 0.10^{+0.02}_{-0.01}$ toward one sightline and $0.02 < Z < 0.13$ toward another. Fox et al. (2010) estimated [O/H] $= -1.00^{+0.05}_{-0.08}$ ($0.10^{+0.01}_{-0.02}$ $Z_{\odot}$) for the Stream from STIS and *FUSE* mea-

surements of NGC 7469 and Mrk 335. They note this is close to the Lehner et al. measurement for the Magellanic Bridge but is low relative to previously published values for the Stream by factors of 2-4, suggesting that the Stream originates specifically from the SMC. Our results for WW84 strongly suggest this cloud is more metal-poor than the lowest-metallicity measurements of either the Bridge or the Stream and therefore does not find its origin in either. Its metallicity is also below the present-day values of 0.1 and 0.3 $Z_{\odot}$ for the SMC and LMC (e.g., Matthews et al. 2009) but our measurement uncertainties do not preclude a metallicity consistent with the SMC, at least. Finally, our measurements of WW84 inform investigations into dust in the Magellanic Stream, if these clouds are indeed physically associated. Observations of high-velocity H_2 toward Stream sightlines are interpreted to indicate the presence of considerable amounts of dust (Richter et al. 2001b, Sembach et al. 2001a). However, our analysis shows no substantial depletion of refractory elements such as Si II relative to O I. We therefore conclude that WW84 must not be formed from the same gas representative of the Magellanic Clouds, Stream, or Bridge, on the basis of its particularly low metallicity and evident absence of significant dust. A more robust distance estimate would help clear up this picture.

3.5.3.4 Highly Ionized High Velocity Clouds (HIHVCs)

A subclass of the HVC population is seen in which there is (1) prominent absorption in high ions such as O VI, C IV, and Si IV and (2) weak or

absent H I 21 cm emission, implying log N(H I) $\lesssim$ 18, known as "Highly Ionized High Velocity Clouds" (HIHVCs). Being 21 cm non- detections, they are almost always discovered serendipitously in UV pencil-beam spectra of background sources. They sometimes show low-ion absorption, indicative of a multiphase structure. They were first reported by Sembach et al. (1995) and have since been investigated recently by a number of other authors (e.g., Sembach et al. 1999, Nicastro et al. 2003, Collins et al. 2003, Fox et al. 2004, 2005, Collins et al. 2005, Ganguly et al. 2005, Fox et al. 2006). Three origin scenarios have been proposed to explain them, each with its own characteristic predictions of metallicity and distance. First, they may form in a Fountain-like feedback process or even in a Galactic wind (Wakker 2004, Keeney et al. 2006), in which case we would expect them to have near- solar abundances and relatively small z-heights. An example may be the HIHVC within the Galaxy reported by Zech et al. (2008) toward the globular cluster Messier 5; they claim a low log N(H I), 16.50 ± 0.06, and a supersolar corresponding [O/H] $= +0.22 \pm 0.10$ ($1.66^{+0.43}_{-0.34}$ $Z_{\odot}$). They note that both photoionization and collisional ionization are required to explain all the observed properties of this cloud. Second, if they are more like "conventional" HVCs, they may represent material condensing out of the Halo and raining down toward the Disk and therefore ought to have low abundances ($\sim 0.1 - 0.3$ $Z_{\odot}$) and large distances ($\gtrsim$ 10 kpc). Fox et al. (2005) and Collins et al. (2005) assert the HIHVCs my simply be the low-N(H I) tail of the distribution of otherwise normal HVCs based on ionization and velocity arguments. Third, they may be extragalac-

tic, associated with a WHIM-like medium in the Local Group (Nicastro et al. 2002) and should therefore show low abundances ($\lesssim 0.1\ Z_{\odot}$) and distances ranging from beyond the outer reaches of the Halo up to as much as 1 Mpc. Small clouds at such extreme distances would be below the angular resolution of current radio interferometers, explaining their non- detection in H I emission. In an extragalactic context, the HIVHCs may be low-redshift analogs of QSO damped Lyα (DLA) systems (Sembach et al. 1999, Collins et al. 2004). Absent reliable information on the distances to these clouds, it is difficult to discern among ionization mechanisms and therefore the physical conditions in which the clouds exist; however, given their preferred ionization mechanism (photoionization by light with a relatively hard spectrum) and small derived thermal pressures compared to typical interstellar values, they conclude the HIHVCs are likely located in or just beyond the distant reaches of the Galactic Halo, possibly within a putative, hot Galactic Corona ($d \approx 30 - 200$ kpc). If they are at such large distances, they may be associated with the filamentary structures thought to compose the "Cosmic Web" in the nearby universe (e.g., Blitz et al. 1999).

Due to the observed degree of ionization among HIHVCs, abundance measurements inevitably rely heavily on photoionization models for which the ionizing source is unclear. N(H I) values are not at all well-constrained, in which case we are left with only limits on implied abundances. These statements are true of two clouds in the HVC Complex Galactic Center Negative (GCN; Wakker & van Woerden 1991) we observed in the direction of Mrk

509. The origin of the gas in this complex is still unclear. Sembach et al. (1995) called them "C IV HVCs" and distinguished them from "classical H I HVCs", likening the gas to the high-ionization metal line systems associated with quasar sightlines given that they show (1) strong C IV absorption and (2) essentially no detectable low-ion (e.g., C II and Si II) absorption or 21 cm emission to very low levels. Winkel et al. (2011) present new 21 cm observations which show a number of discrete, resolved cloudlets without an accompanying diffuse extended counterpart, which they note is unusual among HVC complexes. Their observations indicate Complex GCN is comprised of several different populations of clouds of different origins, and may be an example of warm-gas accretion onto the Milky Way in which clouds are unstable to interaction with the Halo, becoming ionized as they plunge inward toward the Disk. Individual clouds have a head-tail morphology matching expectations given the implied multiphase nature of many HIHVCs. The distance to Complex GCN has been recently estimated at ~ 20 kpc by Jin (2010), who described the complex as a stream extending over more than 50° across the Halo with an estimated mass of 10^5 $M_\odot$. It may therefore represent a tidal stream whose progenitor was a dwarf galaxy, but no counterpart is identified among the known stellar streams surrounding the Milky Way. In such a scenario, we would expect to see exceptionally low metallicities.

Despite the difficulties inherent in determining reliable N(H I) values for HIHVCs, the limits we obtain for the GCN clouds toward Mrk 509 allow us to place meaningful corresponding limits on their metallicities. We find O

I metallicities of $\gtrsim 0.1\ Z_{\odot}$ for both components in this sightline, which appears to rule out the very low values associated with Milky Way dSphs. Our metallicity measurements compare favorable with the only previously published values, from Collins et al. (2004). While we cannot completely rule out an extragalactic origin for this gas based on abundances, discriminating among the Fountain/wind and Halo "rain" models awaits a robust determination of corresponding upper N(H I) limits.

3.5.4 The Magellanic Stream

This association of clouds is the best direct evidence we have for the formation of some HVCs in the debris of gas tidally tripped from dwarf satellite galaxies orbiting the Milky Way. The Magellanic System is composed of the LMC, the SMC, the Magellanic Bridge (an H I filament linking the two), the Leading Arm, and the Magellanic Stream(Matthews et al. 2009). Mathewson et al. (1974) first reported the discovery of the Stream as "...a long filament of H I extend[ing] from the region between the Magellanic Clouds down to the south galactic pole," identified as the material remains of a close encounter between the SMC and the Milky Way $\sim 5 \times 10^8$ years ago. The nature of this gas was clarified by Giovanelli (1981) who discounted a Local Group origin, asserting the clouds were "shreds of Magellanic material." The Stream spans approximately $100^{\circ} \times 10^{\circ}$ of sky and contains as many as $2 \times 10^8\ M_{\odot}$ of neutral hydrogen (Putman 2000, Putman et al. 2003b). Observed velocities of the gas range over large positive and negative values, reaching zero velocity as the

Stream crosses near the South Galactic Pole (Sembach et al. 2003). The gas is significantly ionized, which (Putman et al. 2003b) explain may be the result of the interaction of the Stream with Halo gas.

Two main ideas are proposed to explain how the Stream became separated from the SMC: (1) ram-pressure stripping of gas from the SMC on its last passage through the ionized disk of the Galaxy (Moore & Davis 1994, Mastropietro et al. 2005), and (2) tidal disruption of gas by the Galaxy during the most recent perigalacticon passage by the SMC (Connors et al. 2006). It is also possible some combination of both mechanisms are involved (Heller & Rohlfs 1994). A more controversial theory involve the blowouts of supergiant shells in either the LMC or SMC that were dispersed into the Stream and Leading Arm by a combination of tidal and ram pressure forces (the "Blowout Hypothesis"; Nidever et al. 2008, Nidever 2009). At the same time, recent work by Kallivayalil et al. (2006b,a), Besla et al. (2007) involving proper motion measurements for the Magellanic Clouds and follow-up suggests that none of the existing ideas adequately explains the formation of the Stream. They argue the entire Magellanic System is either on its first passage through the immediate environment of the Milky Way or that its orbital period and apogalacticon distance are larger than previously believed.

Metallicity measurements suggest values consistent with those of the present-day Magellanic Clouds. Lu et al. (1998b) measured abundances in HVC 287.5+22.5+240 and found [S/H] $= -0.60^{+0.11}_{-0.15}$ and [Fe/H] $= -1.480.07$, arguing that the metallicity and depletion pattern of this cloud, taken in con-

sideration with its position and velocity, implied an origin in the Magellanic Clouds. Gibson et al. (2000) made what they refer to as "the first metallicity determination for gas in the Magellanic Stream", finding [S II/H I] = −0.55. Based on the proximity of one of their MS sightlines, Fairall 9, to the SMC and the generally disrupted appearance of the SMC, they concluded that the MS originated there. Sembach et al. (2001a) reported additional measurements of HVC 287.5+22.5+240 with FUSE, reporting [Si/H] = $-0.81^{+0.09}_{-0.12}$, [P/H] < −0.42, [N/H] > −1.93, and [Fe/H] = $-1.51^{+0.09}_{-0.12}$. The observed depletion pattern matched that of warm gas in the SMC. They also observed more than 30 lines of H_2 in MS material, finding log $N(H_2) = 16.80 \pm 0.10$; this implies a considerable amount of dust in the environment where the H_2 formed. However, they reason that the H_2 may have formed in the SMC and survived the process by which the MS was tidally stripped from the SMC. Richter et al. (2001b) offered an alternative explanation in which the H_2 formed in situ on dust grains during the 2 Gyr in which the MS material is thought to have been orbiting the Milky Way, suggesting that it traced a more extensive (but undetected) molecular gas phase in the Halo that could be linked to star formation. Lehner et al. (2008) report an overall metallicity measurement of log $(Z) = -1.02 \pm 0.07$ for the Magellanic Bridge, suggesting a different (and lower) metallicity for the Bridge compared to the Stream. Not all measurements of the Stream metallicity find this discrepancy; for example, Fox et al. (2010) report [O/H] = $-1.00 \pm 0.05 \pm 0.08$ in *FUSE* measurements of the Stream toward NGC 7469 and Mrk 335. They note this is close to the Lehner

et al. value for the Bridge, but that it is low relative to previously published values for the MS by factors of 2-4. While it is possible a large variation in metallicity exists with the Stream, Fox et al. note that their measurement is the first derived from O I, which is less sensitive to ionization corrections than, e.g., Si II. Assuming that $Z = 0.1\ Z_{\odot}$ is the "true", underlying metallicity of the Stream, it becomes increasingly evident that its gas originated in the SMC ($Z \sim 0.1\ Z_{\odot}$) rather than the LMC ($Z \sim 0.3\ Z_{\odot}$).

We measured abundances of three clouds thought to be associated with the MS toward NGC 1705 at velocities +285 km s^{-1} $\leq v_{\rm LSR} \leq$ +340 km s^{-1}. The direct measurement of the highest positive-velocity cloud indicates $Z = 0.30\ Z_{\odot}$, higher than found in the present-day SMC and, in fact, somewhat more consistent with the present-day LMC. On the other hand, while less well-constrained, measurements of the other two clouds are also consistent with 0.3 $Z_{\odot}$ for reasonable (but low) values of N(H I). While the metallicity of the $v_{\rm LSR} = +312.5$ km s^{-1} component disagrees with expectations based on S II measurements of other authors, given ionization effects, we argue that it is a robust value. The strong, unambiguous detection of the λ1302 line drives an O I abundance that is higher than in SMC gas and resistant to ionization corrections.

Table 3.13. Magellanic Stream Abundances

Sightline	v_{min}[a] (km s^{-1})	v_{max} (km s^{-1})	log N(H I)	Ion	$[X/\mathrm{H\ I}]$	$Z/Z_\odot$	Reference
NGC 7469	-500	-200	18.60 ± 0.02	Mg II	-1.51 ± 0.11	0.03 ± 0.01	Gibson et al. (2001)
III Zw 2	-400	-320	< 18.70	Mg II	$\gtrsim -1.3$	$\gtrsim 0.05$	Gibson et al. (2000)
Fairall 9	$+170$	$-$	$-$	S II	$\lesssim -0.05$	$\lesssim 0.89$	Lu et al. (1994)
				Si II	$\gtrsim -0.70$	$\gtrsim 0.20$	
	$+210$	$-$	$-$	S II	$\lesssim -0.52$	$\lesssim 0.30$	Lu et al. (1994)
				Si II	$\gtrsim -1.15$	$\gtrsim 0.07$	
	$+125$	$+250$	18.97 ± 0.02	S II	$-0.55 \pm 0.06(^{+0.17}_{-0.21})$	0.28 ± 0.04	Gibson et al. (2000)
NGC 1705	$+190$	$+240$	~ 15.50	C III, Si III[b]	~ -0.5	~ 0.3	**This work**
	$+240$	$+285$	~ 16.50	Si II, Si III[b]	~ -0.5	~ 0.3	**This work**[c]
	$+285$	$+340$	18.05 ± 0.01	O I	-0.52 ± 0.09	$0.30^{+0.07}_{-0.06}$	**This work**

3.6 Results and Analysis: Intermediate-Velocity Clouds

3.6.1 IV Arch

This association of intermediate-velocity gas clouds was first described by Wesselius & Fejes (1973), and a catalog of cores was presented by Kuntz & Danly (1996). The Arch lies at a height 0.2 kpc $\leq z \leq$ 6.2 kpc from the plane (Kuntz & Danly 1996, Wakker 2001a, Smoker et al. 2004, Welsh et al. 2004) and consists of a number of individual, condensed clumps, many of which appear to be surrounded by a thinner envelope of gas; these clumps are arranged on an overall axis in which clouds with the highest velocities are seen on the axis and cloud velocity decreases with increasing distance from it. The Arch shows a coherent structure in velocity and column density, particularly at the highest velocities, that implies it is of a single nature rather than an unrelated collection of small clouds approaching the Galactic disk (Kuntz & Danly 1993). Weak H_2 absorption is seen in the gas, implying the presence of dust and a relatively high metallicity (Richter et al. 2001b). This evidence points to the Galactic Fountain as the origin of the gas, although it is unclear how likely it is that such a large, ordered body of gas can be produced via the mechanism implicated in the Fountain model. Wakker (2001a) pointed out that there are significantly more IVCs in the northern Galactic polar region than in the southern polar region; Welsh et al. (2004) offer an interpretation for this apparent asymmetry in the form of an evacuated cavity into the inner Halo associated with the "Local Chimney" providing a preferred direction of gas flow from a past explosive event in the Disk that propelled the gas we

Table 3.13 (cont'd)

Sightline	v_{min}[a] (km s^{-1})	v_{max} (km s^{-1})	log N(H I)	Ion	$[X/\mathrm{H\ I}]$	$Z/Z_\odot$	Reference
LMC	–	–	–	S II	-0.57 ± 0.10	$0.27^{+0.07}_{-0.06}$	Russell & Dopita (1992)
	–	–	–	Si II	-0.53 ± 0.22	$0.30^{+0.19}_{-0.12}$	Welty et al. (1999)
SMC	–	–	–	S II	-0.68 ± 0.16	$0.21^{+0.09}_{-0.06}$	Russell & Dopita (1992)
	–	–	–	Si II	-0.57 ± 0.17	$0.27^{+0.13}_{-0.09}$	Welty et al. (1997)
Bridge	–	–	–	O I	$-0.96^{+0.13}_{-0.11}$[d]	$0.11^{+0.04}_{-0.02}$	Lehner et al. (2008)
	–	–	–	O I	$> -1.36 \pm 0.30$[e]	$0.04^{+0.04}_{-0.02}$	
	–	–	–	O I	$-1.00 \pm 0.05 \pm 0.08$	0.10 ± 0.03	Fox et al. (2010)

Table 3.14 (cont'd)

Note. — MS sightlines are ordered according to v_{LSR} values of the gas they probe from negative to positive.

[a]v_{min} without an accompanying v_{max} indicates a centroid velocity only. Entries with neither velocity signify situations in which no velocity limits were quoted.

[b]A consistency argument was made to obtain N(H I) by assuming an LMC-like metallicity ($\sim 0.3\ Z_\odot$).

[c]This component is also known as WW487.

[d]Sightline toward DI 1388.

[e]Sightline toward DGIK 975.

now see as the IV Arch. Furthermore, evidence exists that there may be some physical association with gas in the Complex C core CIII (Kuntz & Danly 1996).

Table 3.15. IV Arch Metallicities

Sightline	v_{min} (km s^{-1})	v_{max} (km s^{-1})	log N(H I)	Ion	[X/H I]	$Z/Z_\odot$	Reference
3C249.1	−80	−30	19.76 ± 0.01	S II	$+0.05 \pm 0.13$	$1.12^{+0.39}_{-0.29}$	**This work**
				N I	-0.71 ± 0.64	$0.19^{+0.66}_{-0.15}$	
Mrk 153	−60	−25	19.56 ± 0.02	P II	$+0.19 \pm 0.09$	$1.23^{+0.68}_{-0.44}$	**This work**
				N I	-0.41 ± 0.22	$0.39^{+0.52}_{-0.06}$	
PG1259+593	−55	–	19.48 ± 0.01	O I	$-0.01^{+0.35}_{-0.27}$	$0.98^{+1.21}_{-0.45}$	Richter et al. (2001c)
				S II	$+0.11^{+0.11}_{-0.08}$	$1.29^{+0.37}_{-0.22}$	
				N I	$-0.68^{+0.50}_{-0.29}$	$0.21^{+0.45}_{-0.10}$	
	−54	–	19.50 ± 0.06	S II	$+0.07^{+0.09}_{-0.10}$	$1.17^{+0.27}_{-0.24}$	Lehner et al. (2004)
				P II	$+0.10^{+0.09}_{-0.10}$	$1.26^{+0.29}_{-0.26}$	
	−82	−29	19.48 ± 0.01	O I	~ -0.10	~ 0.79	Sembach et al. (2004)
	−85	−30	19.45 ± 0.02	O I	-0.08 ± 0.31	$0.83^{+0.87}_{-0.42}$	**This work**
				S II	$+0.30 \pm 0.11$	$2.00^{+0.58}_{-0.45}$	
				P II	$+0.21 \pm 0.11$	$1.62^{+0.47}_{-0.36}$	
				N I	-0.24 ± 0.26	$0.58^{+0.47}_{-0.26}$	
Mrk 817	−40	–	19.33 ± 0.06	P II	$+0.16 \pm 0.21$	$1.45^{+0.90}_{-0.55}$	Lehner et al. (2004)
	−70	−30	19.20 ± 0.03	O I	-0.39 ± 0.20	$0.41^{+0.24}_{-0.15}$	**This work**
				N I	-0.86 ± 0.52	$0.14^{+0.32}_{-0.10}$	
				S II	$+0.13 \pm 0.14$	$1.35^{+0.51}_{-0.37}$	
				P II	$+0.09 \pm 0.18$	$1.23^{+0.86}_{-0.32}$	

A summary of IV Arch metallicities obtained in the course of this work is presented in Table 3.15 along with literature references for comparison, where available. The table entries include the first abundance measurements of IV Arch gas in the direction of Mrk 153 and limits toward Mrk 876. Two conclusions about the Arch emerge from the table. First, among undepleted ions along every included sightline, the gas has near-solar metallicity and is thus enriched in metals to the extent predicted in the Fountain model. Second, a underabundance of O relative to other undepleted species such as S and P is indicated in at least two sightlines (PG1259+593 and Mrk 817). The magnitude of the effect is strongest toward Mrk 817, for which we present the first O I metallicity obtained for the IV Arch in this direction.

3.6.2 LLIV Arch

The LLIV Arch lies between 0.6-1.2 kpc above the plane in the gap between the Perseus and Local spiral arms of the Milky Way at a deviation velocity of -20 to -30 km s^{-1} (Wakker 2001a, Richter et al. 2001a). In the plane of the sky, it crosses Complex A such that both are probed along certain sightlines. Given the distance constraint, Wakker (2001a) estimates its mass at 1.5-6 $\times 10^5$ $M_\odot$. He also notes gas at similar velocities along sightlines off the main bulk of the structure are referred to as the "LLIV Arch Extension" and is probably spatially close to the Arch proper at $z < 0.9$ kpc. O VI and C IV at Arch velocities are seen toward PG 0804+761 (Richter et al. 2001c) and SN 1993J (de Boer et al. 1993), indicating an ionization fraction of around

Table 3.15 (cont'd)

Sightline	v_{min} (km s^{-1})	v_{max} (km s^{-1})	log N(H I)	Ion	$[X/\mathrm{H\ I}]$	$Z/Z_\odot$	Reference
Mrk 876[b]	-80	-45	< 18.65	O I	$\sim +0.1$	~ 1.25	**This work**
PG0953+414	–	–	19.36	S II	$+0.04^{+0.07}_{-0.09}$	1.1 ± 0.2	Wakker (2001a)

Table 3.16 (cont'd)

[a] v_{min} without an accompanying v_{max} indicates a centroid velocity only. Entries with neither velocity signify situations in which no velocity limits were quoted.

[b] Abundances are for the cloud IV20.

20%.

Metallicities for LLIV Arch sightlines, including those of the present work, are collected in Table 3.17. To the handful of previously- published metallicities for the LLIV Arch we have added two new sightlines (Mrk 106 and Mrk 279). We find metallicities generally solar or greater. Exceptions include the subsolar value we find toward Mrk 279 (0.9 $Z_{\odot}$, respectively) and $Z \sim 0.9$ $Z_{\odot}$ reported by Lehner et al. (2004) toward HD 233622 in the Extension. We note these sightlines probe gas well off the main axis of the Arch (as seen in, e.g., Figure 15 of Wakker 2001a), which may therefore be a diffuse, low-metallicity envelope surrounding the main, metal-enriched bulk of the Arch itself. The aggregate of metallicities listed in Table 3.17 along with the above considerations leads us to affirm the basic picture of the LLIV Arch laid out by Wakker (2001a): these clouds appear to be condensing out of a return flow of the Galactic Fountain, enriched in metals compared to Disk material.

3.6.3 Other IVCs

A few special cases exist of intermediate-velocity gas which does not seem to fit into any of the established IVC complexes, which we consider here. Their metallicities are collected in Table 3.19.

One important result of the present work is the first abundance determination of the Draco Nebula detailed in Section 3.4.10. Given its low height off the Disk ($z \sim 0.5$ kpc) and evident interaction with hot gas in situ argues that this cloud is an example of the final stage of the process by which mate-

Table 3.17. Low-Latitude Intermediate Velocity (LLIV) Arch Metallicities

Sightline	v_{min}[a] (km s^{-1})	v_{max} (km s^{-1})	log N(H I)	Ion	$[X/\mathrm{H\ I}]$	$Z/Z_\odot$	Reference
Mrk106	-65	-20	19.35 ± 0.01	N I, Fe II, Si II	~ 0	~ 1	**This work**
Mrk 205	-45	–	19.71 ± 0.06	S II	$+0.39^{+0.27}_{-0.19}$	$2.45^{+2.12}_{-0.87}$	Lehner et al. (2004)
	-90	-35	19.61 ± 0.01	S II	$+0.36 \pm 0.22$	$2.29^{+1.60}_{-0.88}$	**This work**
				P II	$+0.10 \pm 0.20$	$1.26^{+1.14}_{-0.30}$	
				N I	-0.57 ± 0.77	$0.27^{+2.13}_{-0.20}$	
Mrk 279	-60	-30	19.23 ± 0.11	S II	-0.03 ± 0.12	$0.93^{+0.30}_{-0.23}$	**This work**
PG0804+761	-70	-30	19.54 ± 0.01	O I	$+0.01 \pm 0.23$	$1.02^{+0.71}_{-0.42}$	Richter et al. (2001a)
HD 233622	-40	–	20.12 ± 0.08	S II	$-0.15^{+0.08}_{-0.09}$	$0.71^{+0.14}_{-0.13}$	Lehner et al. (2004)
				P II	-0.21 ± 0.09	$0.62^{+0.14}_{-0.12}$	
SN1993J (M81)	-45	–	–	Zn II	$+0.20^{+0.10}_{-0.12}$	1.6 ± 0.4	de Boer et al. (1993)

Table 3.18. Measurements of LLIV Arch abundances with literature comparison values.

[a] v_{min} without an accompanying v_{max} indicates a centroid velocity only.

Table 3.19. Other IVC Metallicities

Cloud	Sightline	v_{min} (km s^{-1})	v_{max} (km s^{-1})	log N(H I)	Ion	$[X/\mathrm{H\ I}]$	$Z/Z_{\odot}$	Reference
Draco Cloud	Mrk 876	-65	-20	19.85 ± 0.02	S II	$+0.28 \pm 0.64$	$1.91^{+6.41}_{-1.47}$	**This work**
					P II	-0.01 ± 0.25	$0.98^{+0.76}_{-0.43}$	

rial in the Galactic Fountain returns to the disk. We find a clearly supersolar metallicity consistent with this picture, and a depletion of refractory elements (e.g., Fe II) matching the observed warm dust emission seen in 60 and 100 μm imagery.

3.7 Summary

In the current study, we have measured metallicities for HVCs and IVCs from UV spectroscopy along the lines of sight to ten background continuum sources in a mixture of new and archival data. The sources were targeted for spectroscopy based on their spatial coincidence with high- and intermediate-velocity H I has in 21 cm emission data, which was also used to obtain H I column densities to which to refer our abundance measurements. Of the twenty-six discreet absorption components we measured across the ten sightlines, nineteen are identified as HVCs and seven as IVCs, of which it appears twelve HVC components and four IVC components are previous unpublished. In cases where metallicites of particular components were previously published, the similarities between our results and those reported by other groups leads us to believe that our measurement method is robust and yields reliable values. In those cases where multiple sightlines trace the same association of gas, such as in Complex C, spatial variations in the abundances we measure are consistent with spatial trends identified by other authors.

In Complex C, we measured abundances along six previously published sightlines (Mrk 279, Mrk 817, Mrk 876, Mrk 205, and PG1259+593) through

cores CIA, CIB, CIIIC, CD, and the low-latitude side of the Complex that we call "C-South". Our results are broadly compatible with those reported of previous studies, in which metallicities average around 0.1 $Z_{\odot}$. We add one new Complex C component, an off-core cloud in the velocity range -210 km s^{-1} $\leq v_{\rm LSR} \leq -165$ km s^{-1} toward Mrk 279, for which we find $Z = 0.10$ $Z_{\odot}$. Our measurement is the first to definitively separate this gas from that in C-South, which is usually subsumed into this component by other authors. We confirm the apparent metal enrichment of two cores relative to the "global" average of Complex C: the CIA core along the Mrk 817 sightline, whose metallicity we find to be $Z = 0.32$ $Z_{\odot}$, and the CD core toward Mrk 876, which has $Z = 0.29$. We take ratios of Si, Fe, and N with respect to O along these sightlines, and make the following broad observations about Complex C: (1) it is slightly enhanced in α elements, and this enhancement may be more pronounced along the edge of the Complex closest to the Galactic plane; (2) it is generally deficient in iron-peak elements, but this apparent deficiency decreases along the short axis of the Complex as one moves away from the Galactic plane; and (3) to within errors, there is no evidence for significant N enrichment through the "secondary" nucleosynthetic pathway. From these observations and our previous efforts to place meaningful limits on its distance, we conclude that Complex C is an association of clouds condensing out of the Halo which has not been significantly polluted by metals from Type II supernovae in the Disk.

Our dataset samples two sightlines that pass through the "Wannier Clouds", a loose grouping of discrete clouds near $v_{\rm LSR} \sim 100$ km s^{-1} at

lower northern Galactic latitudes. These provide the first measurements of the metallicites of the clouds WW154 and WW226 in the collection of clouds called Complex WD. We find a surprisingly large variation between them: WW154 has $Z = 0.81\ Z_{\odot}$, while WW226 is considerably lower at $Z = 0.15$. Even when measurement errors are taken into account, there is no overlap in these values. It is likely that there exists more than one explanation for the origin of these clouds in particular, and more broadly, for all the groups among the Wannier Clouds.

We measured metallicities for two components of the small cloud known as "g2" in Complex gp, for which there are no published values in the literature. While it has been previously defined on the basis of H I velocities over the interval $+30$ km s^{-1} $\lesssim v_{\rm LSR} \lesssim$ $+100$ km s^{-1}, we split into two pieces ('g2a"; $+35$ km s^{-1} $\leq v_{\rm LSR} \leq +75$ km s^{-1} and "g2b"; $+75$ km s^{-1} $\leq v_{\rm LSR} \leq +105$ km s^{-1}) based on the shape and extent of the UV absorption. We find a metallicity of ~ -0.3 ($\sim 0.5\ Z_{\odot}$) for this cloud.

Among the class of objects known as the Very High Velocity Clouds (VHVCs), we report the first measurements for the cloud WW84. As in the previous case of cloud g2, we split the absorption due to this cloud into two parts, "WW84a" (-220 km s^{-1} $\leq v_{\rm LSR} \leq -183$ km s^{-1}) and "WW84b" (-183 km s^{-1} $\leq v_{\rm LSR} \leq -165$ km s^{-1}). For both clouds, we find particularly low metallicities: $Z = 0.04\ Z_{\odot}$ and $0.06\ Z_{\odot}$, respectively. Furthermore, we find essentially no depletion of, e.g., Si II and Fe II relative to O I indicating no substantial dust content. The VHVCs are believed to relate to the Magellanic

Stream given their position and velocity, but our measurements of WW84 seem to refute that idea. Furthermore our measurements fall below even the metallicity of the Magellanic Bridge. We are tempted to conclude that WW84 must not have originated in the Magellanic System, but would require a reliable distance measurement to support that claim.

Three discrete components of the Magellanic Stream appear in the sightline toward NGC 1705, none of which have previously published metallicities. For one of these three in the velocity range +285 km s^{-1} $\leq v_{\rm LSR} \leq$ +340 km s^{-1}, we obtain a metallicity of $Z = 0.25\ Z_{\odot}$ based on the strong detection of O I λ1302. This is the first O I metallicity measured for the Stream; previous reports in the literature involve measurements of S II, which is less resistant to ionization effects than O I. While there exists a wide range in earlier measurements of [S II/H I], our O I metallicity for this component is similar, suggesting that ionization is not a particularly important concern in the NGC 1705 sightline. A value of 0.25 $Z_{\odot}$ is closer to that of the LMC, but is not incompatible with the metallicity of the SMC, from which the Magellanic Stream is thought to originate. We also see two other components toward NGC 1705 without literature comparison values at +190 km s^{-1} $\leq v_{\rm LSR} \leq$ +240 km s^{-1} and +240 km s^{-1} $\leq v_{\rm LSR} \leq$ +285 km s^{-1} (also known as cloud WW487). While we detect no undepleted species in these two clouds, the results of our CLOUDY modeling along with reasonable constraints on the values of N (H I) for each cloud suggest the depleted abundances of C III, Si II, and Si IIIare consistent with an undepleted metallicity of $\sim 0.1\ Z_{\odot}$.

Among IVCs, we have measured the metallicity or provided an upper limit for the IV Arch group of clouds along four sightlines (Mrk 153, Mrk 817, Mrk 876, and PG1259+593), and the Low-Latitude Intermediate Velocity (LLIV) Arch along two (Mrk 205 and Mrk 279). Toward the IV Arch, the measurement for Mrk 153 is the first ever made; however, the only undepleted ion we detect in the Arch is P II, which suffers more from the effects of ionization than O I and S II. From ionization modeling, the measured abundances imply a metallicity of about 0.8 solar, well within the range of previously-published metallicity measurements for Arch sightlines. Toward Mrk 817, we measured the O I metallicity of the Arch for the first time, finding $Z = 0.41$ $Z_{\odot}$. This value is strongly at odds with the P II metallicity of $Z = 1.45$ reported by Lehner et al. (2004) in the same direction. In consideration of the values of [S II/H I] and [P II/H I] we measure and the expectation from ionization modeling, we are led to conclude that the true metallicity of the Arch in this direction is $\sim 1.0-1.3$ $Z_{\odot}$and the apparent underabundance of O I is real. It is possible that the pencil- beam sampling this particular sightline through the Arch intercepts a cloud that has a different composition than others in the same association. There is some indication this is also true in the Arch component toward PG1259+593, where the O I abundance is also lower than the S II and P II abundances by about 0.4 dex. The detection of gas in the LLIV Arch toward Mrk 279 is the first such report for that sightline; there we find an S II metallicity of $Z = 0.93$ $Z_{\odot}$. Our measurement of [S IIH I] = +0.36 in LLIV Arch gas toward Mrk 205 agrees very well with the value of +0.39

reported by Lehner et al. (2004). Other than the unexplained apparent deficit of O I toward two IV Arch sightlines, the generally supersolar metallicities we see among these IVC complexes support an origin in the Galactic Fountain.

Finally, we report the first abundance measurements ever made for the Draco Nebula, also known as LBN 406/415, an object whose velocity, z-height above the Galactic plane (~ 0.5 kpc), and direct detection in warm dust emission at far-IR wavelengths suggest a heavily enriched Fountain cloud on its final plunge toward the Disk. The metallicity is difficult to precisely constrain because of uncertainty in the determination of N(H I) and the magnitude of ionization corrections, but we believe it to be $\sim 2\ Z_{\odot}$. Given that Draco has been detected in lines of molecules such as CO and H_2CO, it is possible that it is an otherwise ordinary molecular cloud found at an unusually large disk height. In the final analysis, it may represent some hybrid of Fountain and purely Disk material, encouraging further study.

Chapter 4

The Astrochemistry Of The High-Mass Protostellar Objects NGC 7538 IRS 9 and IRS 1

J. Barentine and J. Lacy, *Astrophysical Journal* **757**, 111 (2012)

John Lacy obtained the telescope time for this study as PI of successful observing proposals at Gemini and the IRTF, built the instrumental apparatus, and wrote the software used to obtain and reduce the data. I was responsible for the entirety of the data collection, reduction, modeling, and analysis, and I wrote the text.

4.1 Introduction

Details of the pre-Main Sequence (pre-MS) life cycles of low-mass stars such as the Sun ($M \sim 1M_{\odot}$) have been gleaned from decades of research; see McKee & Ostriker (2007) for a recent review. This is thanks in part to the relative amenability of low-mass protostellar objects to study. However, details of high-mass ($M > 8M_{\odot}$) star formation are not as well understood at present, in part because high-mass stars are not generally forming near the solar neighborhood and remain deeply embedded during their pre-MS evo-

lution. An important unresolved issue is whether high-mass stars form in a manner resembling a scaled- up version of low-mass star formation (Keto & Zhang 2010, Johnston et al. 2011) or through other mechanisms uncharacteristic of the low-mass case such as collisions/mergers (Bonnell et al. 1998, Bonnell & Bate 2005, Bally & Zinnecker 2005) and competitive accretion in clusters (Bonnell et al. 2001, 2004). Clearly, the environments in which high-mass star formation takes place seem to influence the formation process itself. Massive stars are most often seen to form in large groups ("OB associations") near the edges of dense clumps in giant molecular clouds (GMCs; Zinnecker & Yorke 2007). Elmegreen & Lada (1977) first suggested that spatially distinct subgroups of stars within OB associations trigger waves of self-propagating star formation in GMCs via shock/ionization fronts that progress from the outside in. This process may account for observations of OB subgroups that lie in linear arrangements along the Galactic plane, showing a monotonically-increasing sequence of ages (Blaauw 1964, 1991). Rapid improvements in both observational capabilities and theoretical sophistication in recent years are advancing our knowledge of the circumstances of massive star formation and enabling these fundamental questions to be addressed.

The origin of these stars is of particular interest due to their role in the Galactic ecosystem. In addition to serving as the principal sites of heavy element nucleosynthesis, the violent end of massive stars in supernovae injects considerable mechanical energy into the interstellar medium (ISM) while enriching it with metals (Arnett 1996). The debris are reconstituted in molecular

clouds from which new stars form, often accompanied by circumstellar disks (Jiang et al. 2008). These disks are evidently the source of accretion onto high-mass stars as they approach the MS in the Hertzsprung-Russell diagram and ignite hydrogen burning, then continue to accrete their final masses, moving parallel to the MS (Zinnecker & Yorke 2007). Relatively little is known about the structure and chemical composition of massive protostellar envelopes, and even less about how they evolve in time. Ready comparison with envelope models for low-mass objects is instructive but only of limited use, in part due to the radically different radiation environment in the high-mass case. The composition and structure of the envelope are of interest as they determine the final mass of the star through an accretion mechanism whose details are still unclear. Piecing together the components of protostellar envelopes is complicated by the observation that most objects are deeply embedded, particularly early in the formation process. Spectroscopy of molecules is useful in delineating physical structures at high extinction where other methods are limited. Pure rotational transitions of molecules in the millimeter probe a sufficiently low energy regime but such observations are typically of low spatial resolution. Better resolution is achieved in the infrared where many ro-vibrational molecular lines are located.

We present high resolution, mid-infrared spectra of a number of molecules toward an embedded infrared source in the NGC 7538 starforming complex, NGC 7538 IRS 9, and compare the results to a previous study of the nearby source NGC 7538 IRS 1 (Knez et al. 2009). Both sources are presumed to har-

bor high-mass protostellar objects in their interiors. Their proximity to one another suggests that, having formed within the same molecular cloud, the starting chemical abundances for each object should have been substantially similar. A comparison of their current states provides insights about differences in their ages and/or divergence in their individual evolutionary histories.

Weak free-free emission (≤ 60 μJy at 3.6 cm; Sandell et al. 2005) is observed toward IRS 9. Further evidence for the comparatively primitive nature of the envelope of IRS 9 is given by the detection of various ices in its *Infrared Space Observatory* (ISO) spectrum (Whittet et al. 1996; Gibb et al. 2004). These ices are not seen toward IRS 1, which appears to be in a relatively advanced point in its pre-MS evolution. It is a considerably stronger source at centimeter wavelengths and shows evidence of both ionized and molecular components in a bipolar outflow originating in a disk seen nearly edge-on (Sandell et al. 2009, Qiu et al. 2011). IRS 1 also shows signs of a circumstellar disk and an emerging compact H 2 region; it is thought to be a forming late O star undergoing active accretion, suggesting a more advanced evolutionary state (Lacy & Jaffe 2007, Beuther et al. 2012). Sandell et al. (2009) further note that the system is heavily accreting ($\dot{M} \sim 2 \times 10^{-4}$ $M_{\odot}$ yr^{-1}) and that the accretion may be episodic in nature. On the basis of GHz line observations, Surcis et al. (2011) conclude that the accretion appears to be the result of radial infall from a "torus" thousands of Astronomical Units (AU) in size, traced by H_2O and CH_3OH masers, instead of the Keplerian disk favored by Pestalozzi et al. (2004).

Until recently, estimates of the distance to NGC 7538 placed it at ∼3.0 kpc (Heyer et al. 2001, Brunt 2003, Foster & Routledge 2003, Balog et al. 2004, Reid & Wilson 2005, Kameya 2006, Araya et al. 2007). However, we adopted the distance of Moscadelli et al. (2009), who find a value of $2.65^{+0.12}_{-0.11}$ kpc from trigonometric parallax measurements. The total luminosity of IRS 9 is about 3.5×10^4 $L_\odot$ (Sandell et al. 2005, corrected to the Moscadelli et al. distance) and it is a bright IRAS 12 μm source at ∼60 Jy (Beichman et al. 1988). A zero-age Main Sequence (ZAMS) star with this luminosity would have a spectral type of B0.5, an effective temperature T_{eff} = 26200 K (Panagia 1973), and a mass of ∼13 $M_\odot$ (Ekström et al. 2012). Boogert et al. (2004) suggest the existence of an inner, warm molecular emission region with a radius of ∼70 AU; the dust temperature a tthis distance for an object of IRS 9's luminosity would be ∼1000 K depending on the dust mass opacity. Millimeter data show that IRS 9 is a site of active, massive star formation (Sandell et al. 2005) in which young stellar objects (YSOs) are driving a set of bipolar molecular outflows on a dynamical timescale of $\leq$ 20,000 years. At least one of these outflows appears to be highly energetic. Mitchell & Hasegawa (1991) report the discovery of an outflow in IRS 9 with a velocity of 110 km s^{-1}, which they interpret to have emerged as recently as 1,200 years ago, perhaps indicating the beginning of a recent episode of accretion.

Observations of these protostellar objects are broadly consistent with the Elmegreen & Lada (1977) picture of sequential high-mass star formation, as elaborated on by others in the particular case of NGC 7538 (Werner et al.

1979, Fischer et al. 1980, Dickel et al. 1981). The Campbell & Thompson (1984) model of NGC 7538 holds that a first generation of massive stars caused the visible H 2 region, which expanded and impinged on the neighboring molecular cloud; this compressed the cloud and generated shocks that caused the observed near-infrared fluorescent H_2 emission northwest of IRS 1. In this picture, high-mass star formation is progressing toward the southeast, and IRS 9 belongs to a second wave of star formation as it is placed further along the direction of propagation of the shock front. These objects then represent two snapshots of the evolution of a massive young protostellar object in a particular cloud and are useful in addressing temporal evolution questions.

This paper is organized as follows. In Section 4.2 we give details concerning how we obtained and reduced the data, followed by a detailed description in Section 4.3 of the molecular species detected. The data analysis is described in Section 4.4 with emphasis on spectral modeling, and we give some interpretation to the results in Section 4.5. We summarize these results and draw some conclusions in Section 4.6.

4.2 Observations and Reductions

We observed NGC 7538 IRS 9 with the Texas Echelon Cross (X) Echelle Spectrograph (TEXES; Lacy et al. 2002) on the Gemini North 8 m telescope in 2007 October. Similar observations of IRS 1 were carried out with TEXES at the NASA Infrared Telescope Facility (IRTF) 3 m telescope in 2001 June, 2001 November, 2002 September, 2002 December and 2005 November. Cir-

Table 4.1. Circumstances of TEXES observations of NGC 7538 IRS 9

UT Date	Telescope	Wavenumber Center (cm^{-1})	Included Features
2001 June 15	IRTF	768	C_2H_2 ν_5 R(15,16)
		780	[Ne II] ($^2P_{1/2} \rightarrow {}^2P_{3/2}$), C_2H_2 ν_5 R(21,22), HCN ν_2 R(22,23)
2001 June 18	IRTF	744	C_2H_2 ν_5 R(5,6), HCN ν_2 R(10)
2001 June 26	IRTF	761	C_2H_2 ν_5 R(12,13), HCN ν_2 R(15,16), HD, $H^{13}CN$ ν_2 R(18)
2001 June 28-29	IRTF	734	C_2H_2 ν_5 R(1), HCN ν_2 R(6,7)
2007 October 21	Gemini	828	HNCO ν_4 P-branch, $^{14}NH_3$ ν_2 sP(7,K)
		1308	$^{12}CH_4$ ν_4 R(0), $^{13}CH_4$ ν_4 R(1)
2007 October 25	Gemini	930	$^{14}NH_3$ ν_2 aQ(J,K)
		743	C_2H_2 ν_5 R(5,6)
2007 October 26	Gemini	853	$^{14}NH_3$ ν_2 aP(4,K)
		1323	$^{12}CH_4$ ν_4 R(2), $^{13}CH_4$ ν_4 R(4), C_2H_2 $\nu_4 + \nu_5$ P(1-3)
2007 October 27	Gemini	2055	OCS ν_2 P(12-22), ^{12}CO v=1-0 P(21,22), ^{13}CO P(11,12), $C^{18}O$ P(10,11), $C^{17}O$ P(16)
2007 October 28	Gemini	730	C_2H_2 ν_5 Q-branch
2007 October 30	Gemini	2085	^{12}CO v=1-0 P(14-15), ^{13}CO P(3,4), $C^{18}O$ P(2,3), $C^{17}O$ P(8,9)

cumstances for all IRS 9 observations are given in Table 4.1. IRTF observations of IRS 1 form the basis for the work of Knez et al. (2009). Additional observations of IRS 1 were made at Gemini in 2007 October to supplement previous TEXES data taken at the IRTF.

TEXES is a cross-dispersed grating spectrograph designed to operate at high spectral resolution (R = 75,000-100,000) over a range of mid- infrared wavelengths from 5 to 25 μm. Light diffracts off a coarsely-ruled "echelon"

grating (Michelson 1898) at a large incidence angle with respect to normal at order $n \sim 1500$. The light then diffracts off a cross-dispersion grating and is imaged onto a 256 $\times$ 256 pixel Si:As detector as a series of orders. At a given spectral setting between five and ten cross-dispersed orders are imaged onto the detector for a spectral coverage of about 0.5%. The continuity of orders is wavelength-dependent; below 11 μm order overlap is sufficient to yield continuous coverage over an entire spectral setting. At wavelengths longer than 11 μm there are gaps between adjacent orders.

On Gemini the pixel scale of TEXES was $\sim$0.″14 while at the IRTF it was $\sim$0.″36. The pixel scales also compare favorably with the diffraction limit at 10 μm of each telescope, 0.″70 and 0.″26 at the IRTF and Gemini, respectively. In both cases the seeing disc is, at worst, critically sampled under good seeing conditions. All observations were made at a resolving power $R \simeq$ 80,000, or $\Delta v \sim$ 3-4 km s^{-1} and the spectral coverage at each spectral setting was $\Delta\lambda \approx$ 0.06 μm. The spectral sampling of the TEXES array is about 1.0 km s^{-1}. Slit widths were 0.″5 at Gemini and 1.″4 at the IRTF. The slit length was $\sim$4″ on Gemini and $\sim$10″ on the IRTF, varying with wavelength. We alternated the telescope pointing between two positions on the sky in the slit direction, separated by $\sim$ 1-5″, during an exposure sequence. Subtraction of adjacent "nod" positions removes the contribution to the signal from night sky emission. The separation of points in the nod, or "nod throw", is determined by the slit length.

To correct for telluric atmospheric absorption we observed comparison

objects whose spectra are close to blackbody over the wavelength range of observation. At wavelengths beyond ~ 8 μm, asteroids meet this requirement while providing the most flux of available object types. Toward 5 μm, most asteroids provide insufficient flux to achieve a high signal-to-noise (S/N) ratio, so we used bright, hot Main Sequence stars such as Vega (α Lyr), Fomalhaut (α PsA) and Mirfak (α Per) as divisors. We aimed to observe the divisor for a given target at nearly the same airmass as the target observation for better divisions. Differences in airmass at the times of observations may be corrected after data reduction by taking the divisor spectrum to the power of the ratio of the airmasses. Residual structure in divided spectra was removed by fitting and subtracting low-order polynomials.

Finally, given the high spatial resolution of the Gemini observations, we considered the possibility that TEXES might resolve the emitting/ absorbing region around IRS 9 if it were spatially extended. We obtained a series of spatial-spectral scan maps of IRS 9 that allow us to place an upper limit on the linear size of any resolved structure. The approach and results are discussed in detail in Section 4.5.5.

4.2.1 Data Reduction

Our data reduction pipeline is described in detail in Lacy et al. (2002). Flux calibration is based on the approach of calibrating millimeter and submillimeter data in the manner of Ulich & Haas (1976). A typical sky calibration cycle involves collecting data on the sky and object with two positions of a ro-

tating chopper blade mounted just above the entrance window to the TEXES Dewar: one painted flat black and one low- emissivity, polished aluminum ("shiny") surface. The result of dividing by the black-sky difference removes atmospheric absorption and serves as both a spatial and spectral flat field image provided that the black position, sky, and telescope temperatures are approximately equal. We quote the Lacy et al. (2002) expression for the object intensity as a function of frequency,

$$I_\nu(object) \approx S_\nu(object - sky)\frac{B_\nu(T_{tel})}{S_\nu(black - sky)} \tag{4.1}$$

where S_ν is the measured signal and B_ν is the blackbody function at the telescope temperature T_{tel}. In the approximation that I_ν(black)-I_ν(sky) = $B_\nu(T_{tel})e^{-\tau_{sky}}$, this procedure corrects for sky absorption. Wavelength calibration is achieved by using the known wavelengths of night sky emission lines; expressed in velocity units, this method is accurate to $\sim$1 km s^{-1}.

Pipeline software written in FORTRAN performs the reduction steps resulting in a wavelength- and flux-calibrated object spectrum along with an estimate of the noise, the sky transmission spectrum, and the 2-D unextracted slit image. The program also corrects for optical distortion, removes cosmic ray spikes and fixes bad pixels. The systematic accuracy of radiometric calibrations is $\sim$25%, ignoring telescope pointing uncertainties.

4.3 Description of the Data

We observed IRS 9 in the lines of seven molecules at the settings summarized in Table 4.1. The selection of settings was motivated by the desire to include as many species and individual lines as possible given the severity of telluric atmospheric absorption at a particular setting. In particular, variations in the H_2O column over Mauna Kea often influenced the settings observed on a particular night, as many of the settings are sensitive to the intensities of telluric water lines. The systemic velocity of IRS 9 and motion of the Earth with respect to the Local Standard of Rest (LSR) were taken into account in choosing settings in which certain lines were shifted either into or away from nearby telluric absorption features, and in many cases required trade-offs in order to maximize efficiency and scientific return. Details of the observations for specific molecules follow.

4.3.1 C_2H_2

At Gemini, two lines in the acetylene ν_5 symmetric bending mode R branch were observed (J=5,6) along with approximately ten lines in the ν_5 Q branch. The R-branch lines are shown in Figure 4.1, while Figure 4.2 shows the Q-branch spectrum along with a simple LTE fit at a single rotational temperature of 100 K. This is discussed further in Section 4.4. Each acetylene line appears to consist of a single component. The $R(5)$ line is stronger than $R(6)$, as is expected due to its three-times-greater nuclear statistical weight. $R(6)$ appears to have a weak redshifted emission component at an LSR velocity

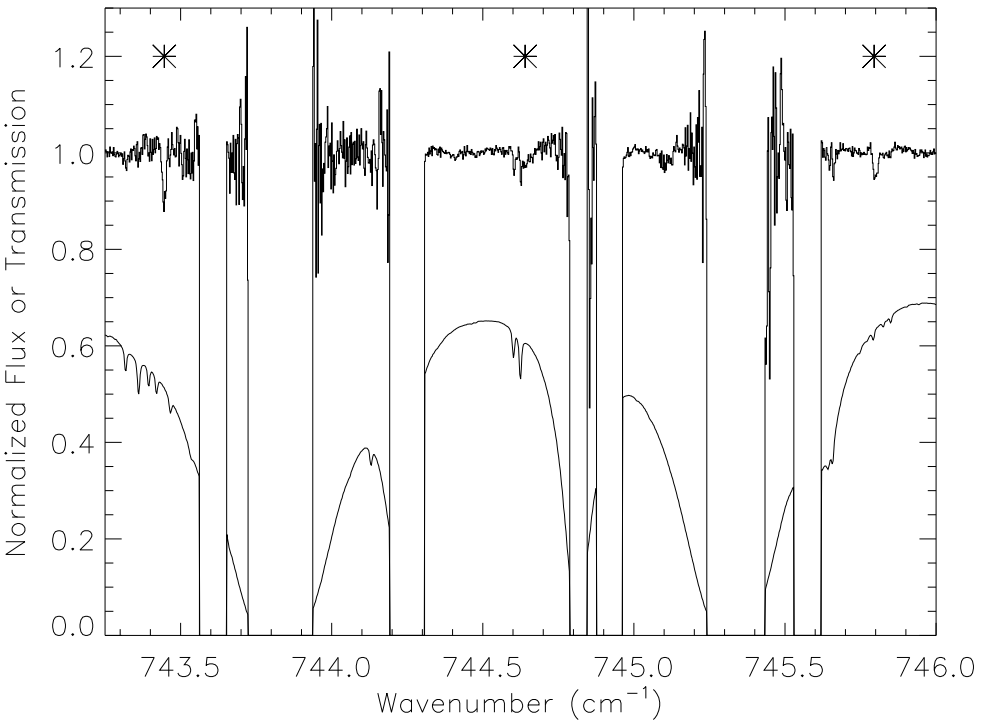

Figure 4.1 TEXES spectrum toward NGC 7538 IRS 9 showing features due to C_2H_2 and HCN. From left to right, the asterisks mark the positions of C_2H_2 ν_5 $R(5)$, HCN ν_2 $R(10)$, and C_2H_2 ν_5 $R(6)$. The upper trace shows the data, while the lower curve indicates the relative atmospheric transmission on the same scale. The HCN ν_2 $R(10)$ line is a detection despite the telluric lines at that wavenumber not completely dividing out. Gaps in the spectrum occur between echelon grating orders and where the telluric absorption is too great to be divided out.

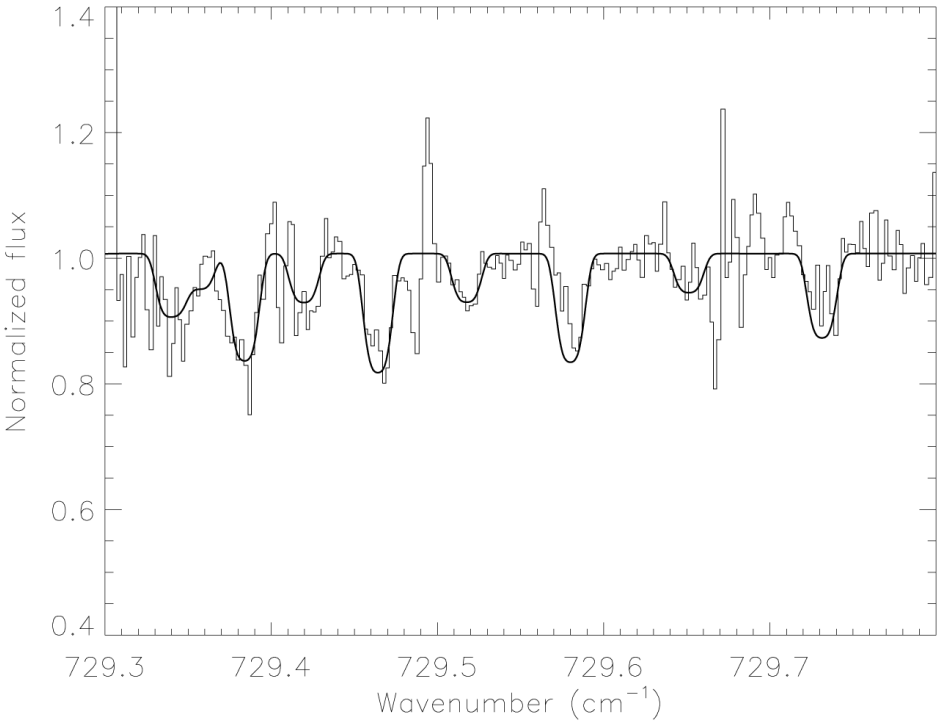

Figure 4.2 Spectrum of the ν_5 Q branch of C_2H_2 observed with TEXES toward NGC 7538 IRS 9 (thin lines). A fit is superimposed from an LTE pure absorption model with $T = 100$ K, $b = 1$ km s^{-1}, and $N(C_2H_2) = 2 \times 10^{15}$ cm^{-2} (thick line). The synthetic spectrum has been convolved with the TEXES instrumental line shape function.

of -54 km s^{-1} although this effect may be due to a poor fit to the continuum there. This component can be more easily seen in the top-center panel of Figure 4.10. Earlier IRTF observations of the ν_5 $R(1)$ line (wavenumber center 734 cm^{-1}) in 2001 June revealed a positive detection, but more importantly, higher J settings $R(15,16)$ (768 cm^{-1}) and $R(21,22)$ (780 cm^{-1}) were non-detections. The latter setting included the $^2P_{1/2} \rightarrow {}^2P_{3/2}$ fine structure line of [Ne II]; consistent with the weak free-free emission observed toward IRS 9, this line was also a non-detection and is discussed in detail in Section 4.4.4. Finally, although the positions of lines of the $^{13}C^{12}CH_2$ isotopologue fell in some of our spectral settings, we did not detect any.

We also did not detect any lines in the $2\nu_5 - \nu_5$ "hot bands" of acetylene toward IRS 9. However, the hot-band lines in the spectral settings observed were not particularly favorable for detection, so we cannot draw any strong conclusions about the ν_5 population from these observations. The observation of $\nu_4 + \nu_5$ combination mode lines, shown in Figure 4.3, is of particular interest. This is because it allows a measurement of the C_2H_2 abundance with intrinsically weaker lines at different wavelengths from the ν_5 band lines. Since the $\nu_4 + \nu_5$ line strengths are $\sim$5 times weaker than the ν_5 line strengths, absorption in the $\nu_4 + \nu_5$ lines may be dominated by high column density clumps of gas.

An energy level diagram indicating relevant vibrational levels of C_2H_2 is shown in Figure 4.4. The ν_5 mode is the symmetric bending mode in which the H atoms move together. In the ν_4 antisymmetric bending mode, they move in

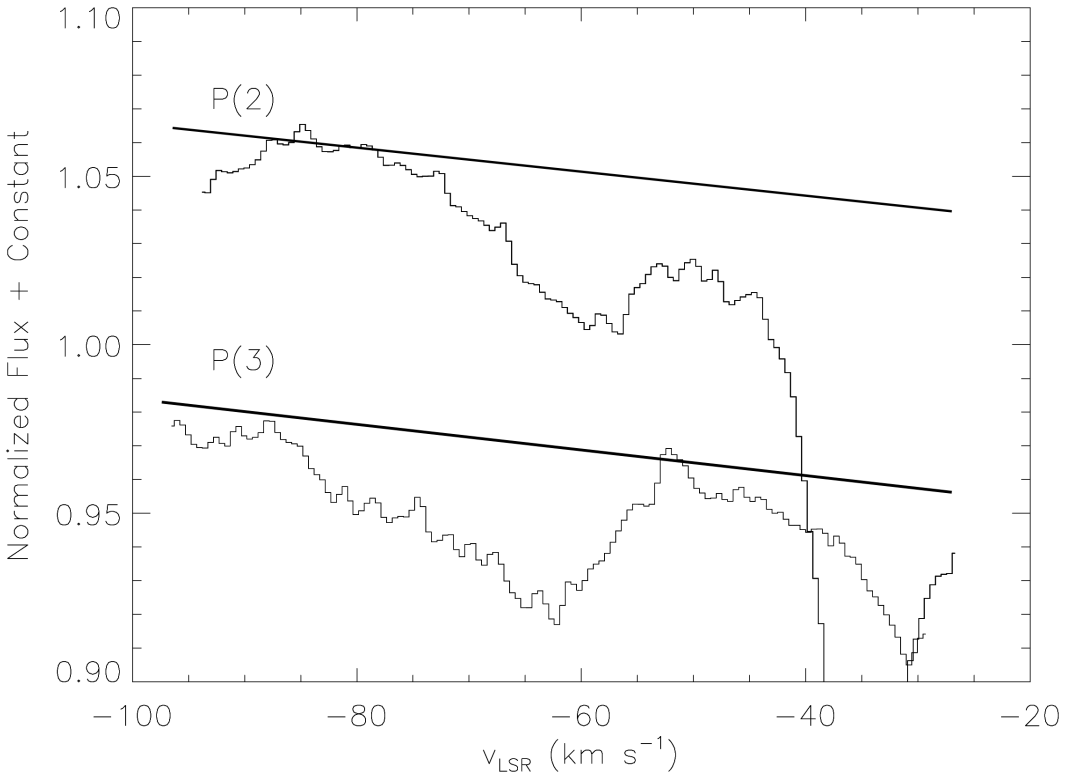

Figure 4.3 Spectra of two P-branch lines of the $\nu_4 + \nu_5$ combination mode of C_2H_2 shown on an LSR velocity scale. The two spectra have been offset vertically for clarity, and the continuua are indicated with heavy straight lines. Both spectra are affected by strong, poorly-corrected telluric absorption at small blueshifts.

opposition, resulting in no dipole moment. Therefore, transitions that change the ν_5 quantum number are relatively strong, with $A_{ul} \sim 10\ s^{-1}$. These include the ν_5, $2\nu_5 - \nu_5$ (between $2\nu_5$ and ν_5), and $\nu_4 + \nu_5 - \nu_4$ (between $\nu_4 + \nu_5$ and ν_4) transitions. Transitions that only change ν_4 do not occur radiatively, but transitions changing both ν_4 and ν_5, including $\nu_4 + \nu_5$ and $\nu_5 - \nu_4$, do occur although they are ~ 10 times weaker than those which only change ν_5. Because

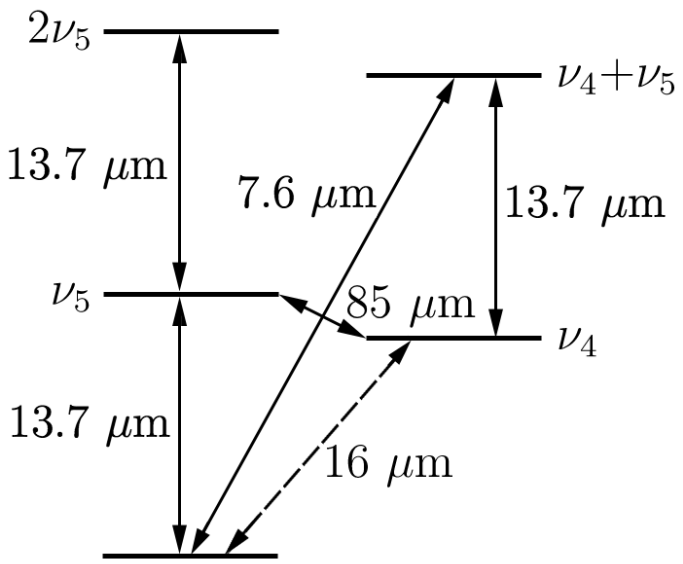

Figure 4.4 Energy level diagram for some mid-infrared-active, ro-vibrational transitions of C_2H_2. Radiatively-allowed transitions are denoted with solid lines and collisionally-allowed-only transitions with dashed lines. The excited vibrational levels are split by interactions between the rotational angular momentum and the angular momentum of the bending-mode vibration; however, the energy differences between these levels are too small to be seen at the resolution of the diagram.

of these selection rules, 7.6 μm photons can be absorbed in $\nu_4 + \nu_5$ lines, but molecules excited into the $\nu_4 + \nu_5$ level most often decay to the ν_4 level from which they can only decay to the ground vibrational level collisionally.

The ratio of the $\nu_4 + \nu_5$ $P(3)$ and $P(2)$ lines is difficult to determine due to poor telluric division, but appears to be less than the 9:2 ratio expected from their rotational and nuclear statistical weights. This probably indicates saturation of the lines in spite of their intrinsic weakness relative to the ν_5 transitions. We also note that the spectral region containing the $\nu_4 + \nu_5$ lines is contaminated by dense forests of HNO_3 and SO_2 lines, giving the superficial appearance of bad flat-fielding. Another difference between the ν_5 and the $\nu_4 + \nu_5$ transitions involves the shapes of the lines; the $\nu_4 + \nu_5$ lines are more asymmetric, with blue wings extending to nearly -90 km s^{-1}. In this regard they resemble the P Cygni-like shapes of the CO lines we observed toward IRS 9 (see Section 4.3.5). The $\nu_4 + \nu_5$ lines may result from absorption in a high column density component with a small covering factor that is strongly saturated. Or they may be formed in highly dust-obscured gas that is more visible at 7.6 than 13 μm due to the lower dust opacity off of the silicate absorption feature. The presence of the similar -80 km s^{-1} absorption feature in the CO lines supports this possibility. Alternately, the $\nu_4 + \nu_5$ line strengths relative to the ν_5 lines may be affected by other radiative transfer effects, as we discuss in Section 4.5.3.

4.3.2 HCN

Three of our spectral settings contain R-branch lines of the ν_2 bending mode of HCN with centers at 734 cm^{-1} ($6 \leq J \leq 7$), 745 cm^{-1} (J=10), and 761 cm^{-1} (J=16). The $R(6)$ line fell into a region where atmospheric transmission is not favorable, and $R(7)$ appears to be a marginal detection because of a weaker, nearby atmospheric feature. $R(10)$ (Figure 4.1) is a probable detection. $R(16)$ falls close to the $R(13)$ line of C_2H_2 but is sufficiently separated from the acetylene line to prevent blending and is the only clean HCN line detected. The $R(15)$ line of HCN fell just outside the first order of the 761 cm^{-1} setting. The S/N of the HCN observations is generally lower than that of C_2H_2 ν_5 R branch, but the HCN lines are clearly the broader of the two. The mean full width at half maximum (FWHM) of the four C_2H_2 R-branch lines is 6.5±1 km s^{-1}, whereas the HCN $R(16)$ line FWHM is ∼15 km s^{-1}. Finally, lines of the H^{13}CN isotopologue are also found in these settings but not detected: $R(9)$ in 734 cm^{-1} and $R(18)$ in 761 cm^{-1}. $R(18)$ falls into a gap between orders and $R(9)$ was affected by poor atmospheric transmission.

4.3.3 CH_4

We obtained data on three ν_4 R-branch lines of CH_4: the $R(0)$ line at 1311.43 cm^{-1} and the two $R(2)$ lines at 1322.083 cm^{-1} and 1322.152 cm^{-1}. In addition, the settings for these lines contained the positions of the $R(1)$ and $R(4)$ lines of $^{13}CH_4$, but both of these lines were clear non-detections. The $^{12}CH_4$ lines show clear asymmetries indicative of multiple velocity components.

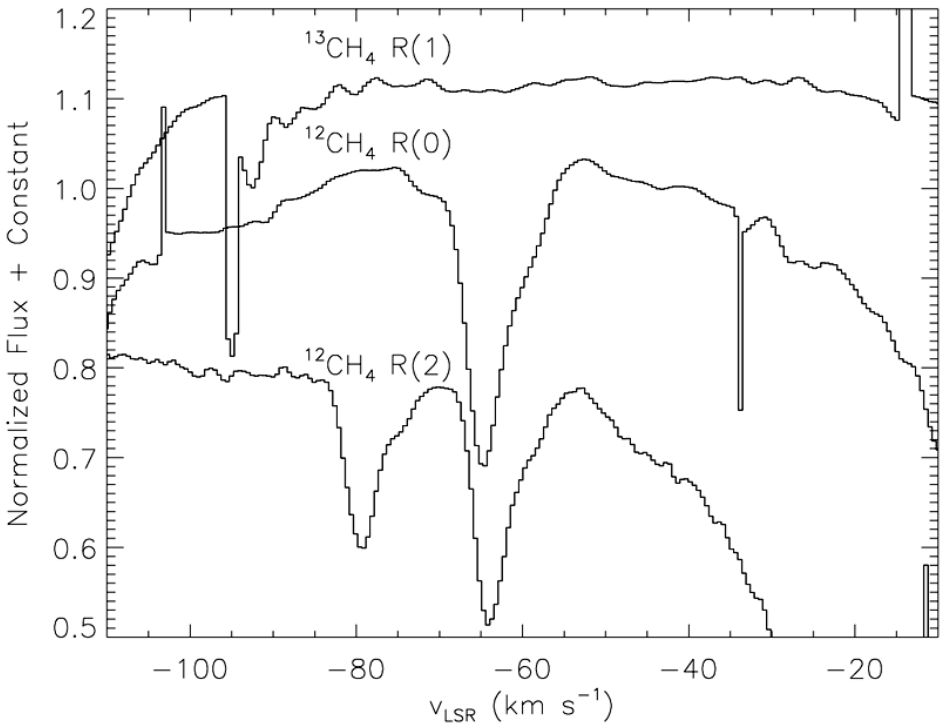

Figure 4.5 Spectra of three features in the ν_4 band of CH_4 toward IRS 9, shown on an LSR velocity scale. For the spectrum containing the $R(2)$ lines, the velocity scale has been set to the LSR value for the stronger component (rest frequency 1322.085 cm^{-1}). The individual spectra have been offset vertically for clarity.

Each feature has a principal component corresponding to greatest absorption at v_{LSR} = -65.0 km s^{-1} with additional components on the red wing of this feature separated in velocity by up to 6.5 km s^{-1}. The spectra are plotted in Figure 4.5.

4.3.4 NH_3

Two spectral settings observed contain a total of ten P-branch lines of ammonia, three in the ν_2 "umbrella" mode antisymmetric $P(4,K)$ group and seven in the ν_2 symmetric $P(7,K)$ group. Of the possible lines in these settings, only a$P(4,2)$ was not observed because of its proximity to a strong telluric atmospheric feature. Almost all of the NH_3 lines share a characteristic P Cygni-like profile, with an emission peak near the systemic velocity, around -60 km s^{-1}, and weak blueshifted absorption separated in velocity by 2.5 to 10 km s^{-1}. This may be compared to the -56.5 and -59.8 km s^{-1} absorption components seen in mid-infrared NH_3 absorption transitions toward IRS 1 (Knez et al. 2009) and a value of -60.0 km s^{-1} for the (3,3) rotational transition of NH_3 in Very Large Array (VLA) observations of IRS 1 at centimeter wavelengths (Henkel et al. 1984). The degree of absorption toward IRS 9 relative to emission varies as well; the highest K lines in the s$P(7,K)$ series show no absorption at all despite the fair S/N of the data. Finally, we observed a setting near 930 cm^{-1} containing the positions of the ν_2 aQ-branch lines ($1 \leq J \leq 9$); the data show weak absorption features at some of the indicated points in Figure 4.6. For comparison, a similar plot of the s$P(7,K)$ branch spectrum is also shown in the figure. We did not observe lines in the ν_2 R-branch of NH_3 because of their proximity to regions of significant telluric atmospheric absorption. Also, the R-branch lines are located in a spectral region of rapidly increasing absorption due to the 9.7 μm silicate dust feature. This fact significantly impacts our interpretation of the NH_3 P- and R-branch lines, as we

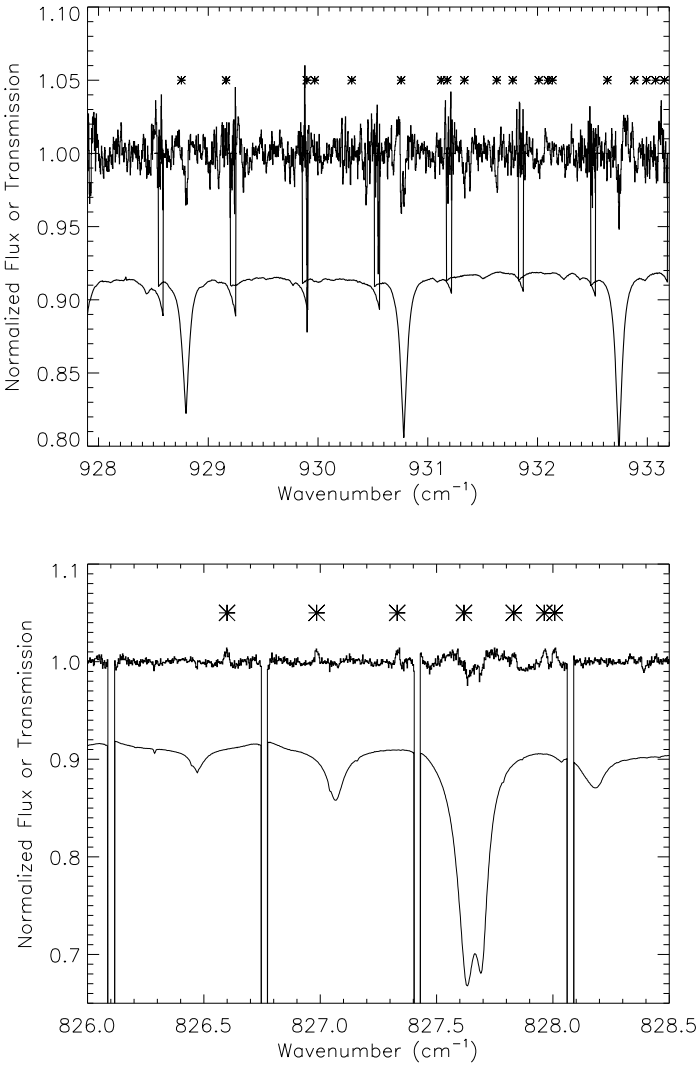

Figure 4.6 TEXES spectra toward NGC 7538 IRS 9 at the position of the $^{14}NH_3$ ν_2 antisymmetric Q branch (top panel) and symmetric $P(7,K)$ branch (bottom panel). The upper curve in each plot shows the data, while the lower curve in each shows the relative atmospheric transmission on the same scale. Asterisks mark positions of the NH_3 lines. Both spectra have been corrected for the Earth's motion relative to the LSR, and the position of the NH_3 line markers shifted to the systemic LSR velocity of approximately -60 km s^{-1}.

discuss in Section 4.5.3.

4.3.5 CO

We observed two settings in the 5 μm v = 1-0 band of CO, which included a number of P-branch lines of several isotopologues. These settings were centered approximately at 2055 cm^{-1} and 2085 cm^{-1}. Strongest among the detected features were the ^{12}CO lines with $J = 14$, 15, 21 and 22. Each line exhibited a strong P Cygni profile with emission and absorption components separated by $\sim$20 km s^{-1}. Each component was broader than those of any line of any other molecular species we observed, with line widths of 10-20 km s^{-1}. In each case the strength of the emission was approximately equal to the strength of the absorption. The features are consistent with an expansion or outflow and have been previously interpreted as such by Mitchell & Hasegawa (1991). Observations of IRS 1 were also made at these settings; we find a different profile altogether with a double-bottomed absorption feature in ^{12}CO, weaker absorption on the blue wing and a slight emission bump on the red wing of each feature. Spectra of both objects are shown in Figure 4.7.

Four ^{13}CO P-branch lines with J = 3, 4, 11, and 12 were also detected in the spectrum of IRS 9. Of these, $P(11)$ was a clear detection near the middle of a spectral order and away from contamination by telluric atmospheric lines, $P(12)$ was noisy and found very near the edge of a spectral order, and $P(8)$ and $P(9)$ are clearly detected, but blended slightly with two nearby C^{18}O features. Additional ^{13}CO lines, $P(11)$ and $P(12)$, are located

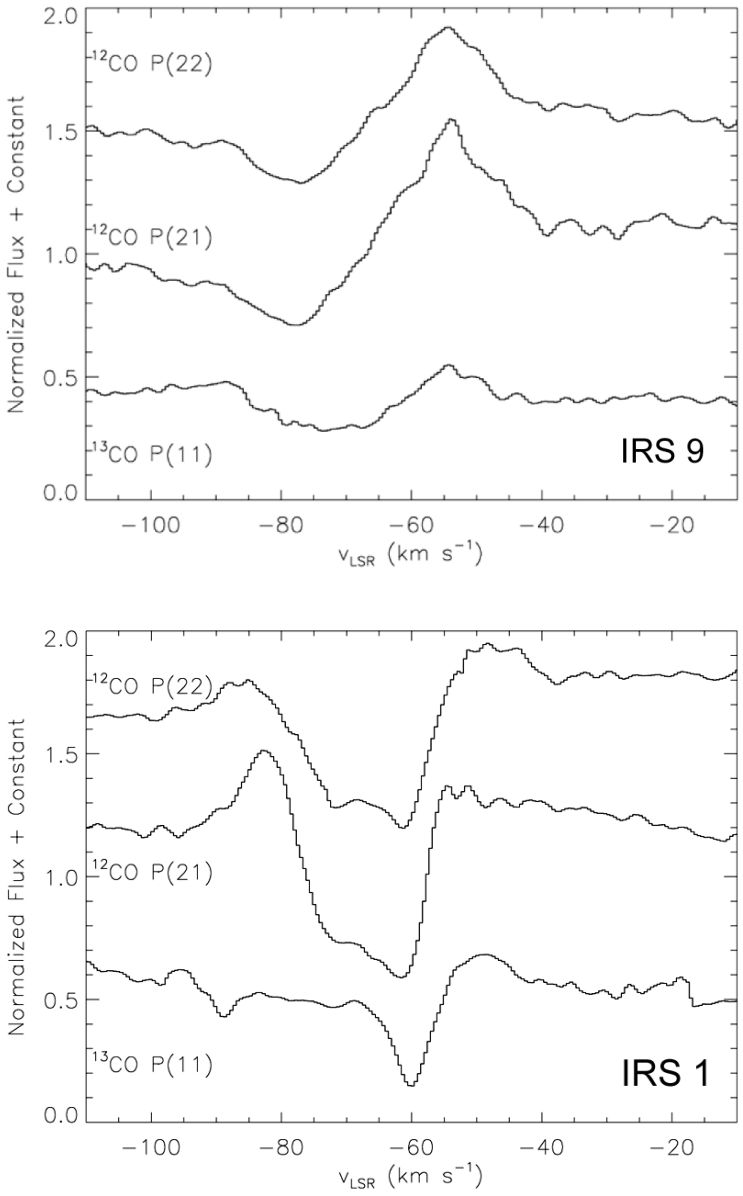

Figure 4.7 The upper panel shows spectra of two P-branch lines of ^{12}CO and one P-branch line of ^{13}CO toward IRS 9 obtained with TEXES. The lower panel shows the same spectral settings observed toward IRS 1. In both cases the motion of the Earth with respect to the LSR has been removed from the velocity scales.

in the spectral setting at 2055 cm^{-1} but occur in regions of strong telluric atmospheric absorption and thus were not detected. We also searched for lines attributable to $C^{17}O$ but did not confidently detect any; this is not surprising given the low expected abundance of $C^{17}O$. For reference, Smith et al. (2009) quote $N(^{12}C^{16}O)/N(^{12}C^{17}O)$ of 2800±300 toward the T Tauri star VV CrA, obtained at a spectral resolution similar to our TEXES observations. They compare this to the Local ISM value of 2005±155 (Wilson 1999)

The CO lines seen toward both IRS 9 and IRS 1 have different line shapes in ^{12}CO and ^{13}CO. In the case of IRS 1, the ^{13}CO features show only single components in the deepest absorption, while toward IRS 9 the ^{13}CO $P(11)$ line and ^{12}CO lines show the pronounced P Cygni profiles. The ^{13}CO lines in the 2085 cm^{-1} setting clearly show multiple components suggestive of P Cygni profiles in which emission is weak relative to absorption, and there are at least two distinct absorption units. In turn, the strongest absorption components show a weak, double-bottomed structure like the ^{12}CO lines in IRS 1. The multiple absorption units may appear in the profiles of the ^{12}CO features in the same spectral setting; weak "shoulders" on the blue wing of the absorption component are consistent with additional absorption suffering contamination by the primary components. Such shoulders are also noticeable on the red wings of the emission features of ^{12}CO . These details can be seen in Figure 4.8.

The detection of ^{13}CO toward IRS 9 with line depths comparable to those of ^{12}CO strongly indicates saturation of both isotopologues. Useful

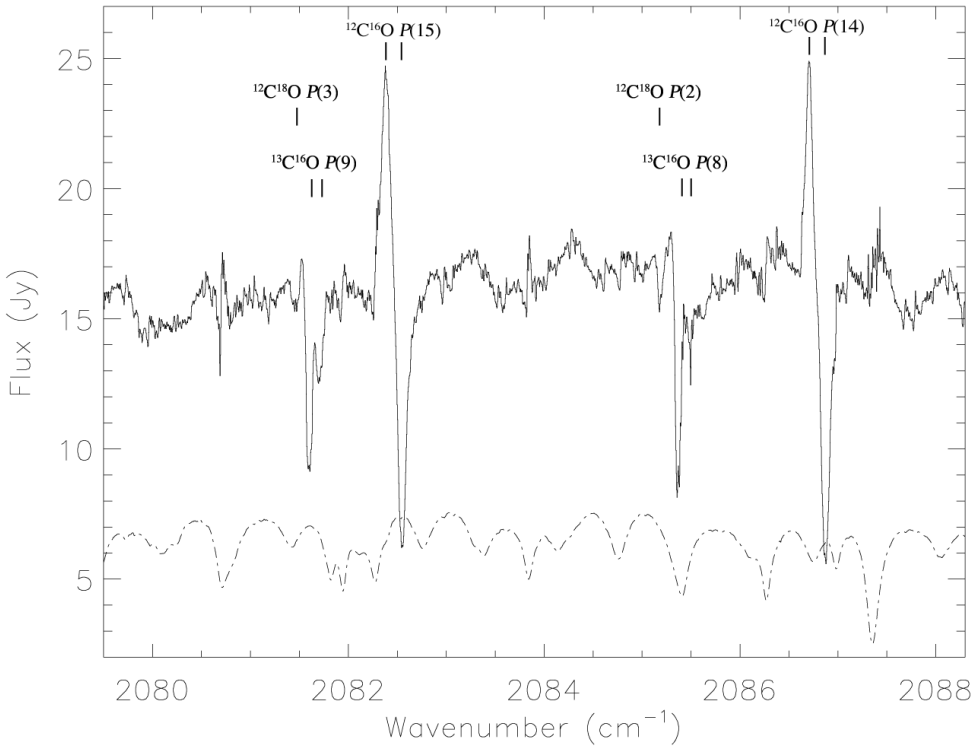

Figure 4.8 TEXES spectrum toward NGC 7538 IRS 9 centered near the 5 μm rotational lines of several isotopologues of CO. The data are shown in the upper trace (solid line) and the relative atmospheric transmission in the lower trace (dot-dashed line) multiplied by a factor of 10. Some line identifications are shown.

columns may however be obtained from rarer variants such as $C^{18}O$, but these lines are too weak to be measured accurately in the present spectra. It would also be of interest measure the $^{12}C/^{13}C$ ratio toward IRS 9 for comparison with the value of 45 toward IRS 1 reported by Knez et al. (2009). As we did not observe the ^{13}C isotopologue of C_2H_2 in our spectra of IRS 9, the CO observations would offer a way to measure the ratio if the lines were not saturated.

4.3.6 OCS

The ^{12}CO setting at 2055 cm^{-1} we observed also contains the positions of a number of P-branch lines of the ν_2 stretching mode of OCS ($12 \leq J \leq 22$), but we cannot confidently claim detections of any of them toward IRS 9. Periodic structure in the continuum of our 5 μm spectra may be broad OCS features, although it is more likely the structure results from flat- fielding residuals. For reference, we have overplotted the locations of the rest-frame OCS line centers over the data in Figure 4.9. It is unclear whether we should have observed lines of OCS in the gas phase, given the strong detections of CO nearby. Low temperatures may inhibit desorption of OCS from grains, but the theoretical grounds for predicting OCS abundances are questionable (Doty et al. 2004). The signature of an outflow in the spectra of CO hints at possible excitation through shocks. We might expect that OCS would be similarly excited but there is no support for this in our data. This is contrasted with the results of Evans et al. (1991), who detected gas-phase OCS toward

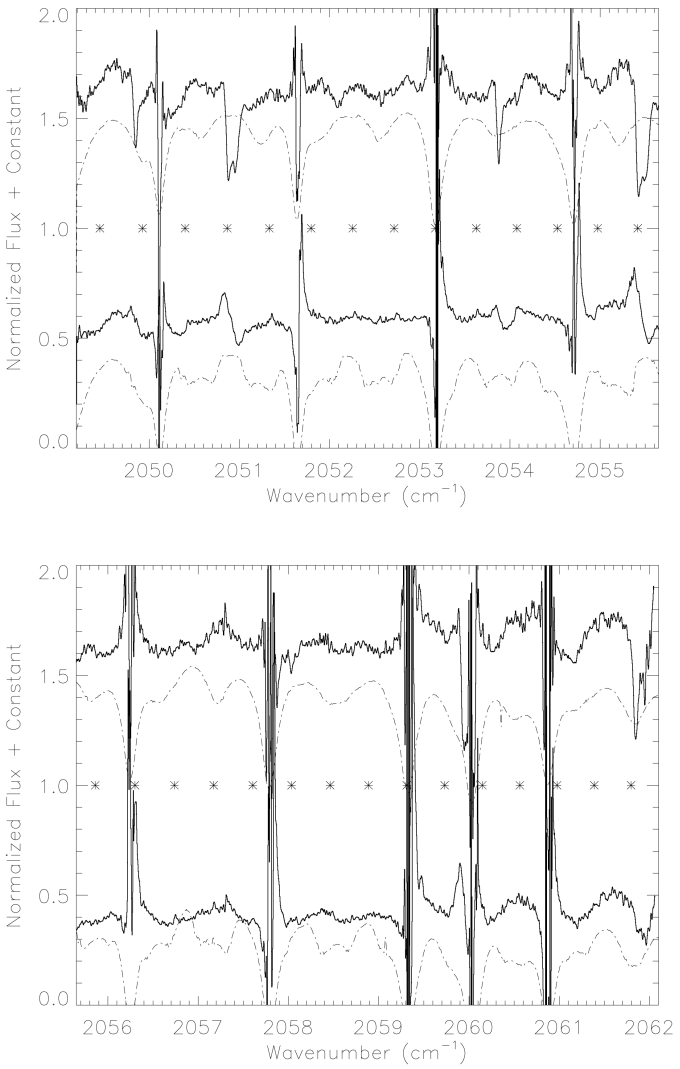

Figure 4.9 The TEXES spectra of NGC 7538 IRS 1 (top) and IRS 9 (bottom) near features in the P-branches of ^{12}CO and ^{13}CO; heavy solid lines are the object spectra and light dot-dash lines are the sky spectra offset for clarity. The wavenumber scale has been corrected to a velocity reference at rest in each object's frame, and the line centers of OCS features, marked with asterisks, have been velocity shifted appropriately.

Orion IRc2; for reasons given in Section 4.5, it is impossible to know whether this is due to temperature differences or real abundance variations between the IRS 9 and IRS 1.

4.3.7 HNCO

We looked for ν_4 bending mode HNCO IL-0 P-branch lines toward IRS 9 in the TEXES spectral setting that included s(7,K) lines in the P branch of ammonia. None of the three lines included in this setting ($2 \leq J \leq 4$) was detected, although there may be HNCO Q-branch absorption at 827.7 cm^{-1}, obscured by telluric interference. Given the strong observed ice absorption at 4.62 μm toward IRS 9 (Pendleton et al. 1999), now commonly attributed to OCN^-, and a lack of gas-phase HNCO absorption, it seems most likely that temperatures in the outer envelope of IRS 9 are sufficiently low to prevent OCN^- desorbing from grains in detectable quantities. Alternately, gas-phase OCN^- might exist at H (or H_2) abundances insufficient to result in considerable HNCO production.

4.4 Analysis and Modeling

We fit synthetic spectra to the TEXES data to derive excitation parameters and column densities for the various molecular species observed. A two-step process was devised in which rough estimates of the parameters were made from "by eye" fits of synthetic spectra to our data; these values were then used as the initial guesses in our fitting program which iterates values

of hundreds parameters to achieve the best fit to the data by minimizing χ^2. While our χ^2 code is robust in finding solutions even when starting far from the global minimum, convergence is achieved faster by using good initial guesses. This approach was best suited to our method of spectral analysis.

4.4.1 Simple Synthetic Spectrum Fitting

In order to get approximate parameters for the gas-phase lines we observed, we first fit synthetic spectra to the data using a fitting method commonly referred to as "chi by eye." This approach allowed us to get quick initial estimates of parameters such as excitation temperature and column density for the various molecules that were used as inputs to a more sophisticated non-linear least squares code to obtain optimal values of the parameters. The simple method also allowed us to determine the number, width and velocities of line components.

The equivalent width of an optically-thin line is the product of the line strength, α, and the column density, N. We obtained values of α for each molecular species observed from the GEISA database[1] of laboratory molecular data (Jacquinet-Husson et al. 2005). The GEISA coefficients are specified for a fiducial temperature $T_o = 296$ K; we corrected them to an assumed temperature T via the formula

$$\alpha(T) = \alpha(T_o) \exp\left[E_l \left(\frac{1}{k_B T_o} - \frac{1}{k_B T}\right)\right] \left(\frac{T_o}{T}\right)^{\beta} \tag{4.2}$$

[1] http://ether.ipsl.jussieu.fr/ether/pubipsl/geisa_iasi_raie_frame_2003_uk.jsp

where E_l is the energy of the lower state of a transition, k_B is Boltzmann's constant, and $\beta = 1$ for linear molecules and $\frac{3}{2}$ for non-linear molecules. Here the temperature dependence of the vibrational partition function and the stimulated emission correction are neglected as both are of order unity. For Gaussian lines, the line-center optical depth is calculated according to

$$\tau_l = \frac{N\alpha}{b\sqrt{\pi}} \tag{4.3}$$

where b is the Doppler b parameter in wavenumber units. The run of optical depth with frequency over the line is computed with

$$\tau(w) = \tau_l \exp \frac{-(w - w_o)^2}{b^2} \tag{4.4}$$

in which w is the wavenumber and w_o is the line-center wavenumber. The optical depths are converted to intensities by taking the exponential of $\tau(w)$; the continuua are normalized to unity. We assume that the rotational states are in local thermodynamic equilibrium (LTE). Our radiative transfer model also assumes pure absorption for fitting the observed absorption lines. Re-emission by the absorbing molecules is neglected. Emission features are treated as separate components, which are modeled as negative absorption. Populations of excited vibrational states are not calculated. Temperatures are arbitrarily held fixed at 200 K; this value is consistent with temperatures around IRS 1 derived from TEXES data. The exception was the Q-branch of C_2H_2 where a number of observed J states allowed the temperature to be constrained to 100 K. Column densities and velocities derived using this method are shown

in Table 4.2. Fits to the individual lines are shown in Figures 4.10 through 4.12.

Table 4.2. Molecular absorption parameters derived from simple synthetic spectrum fitting in LTE

Molecule/Band	Line	n[a]	T (K)	v_1[b] (km s^{-1})	v_2	v_3	b_1 (km s^{-1})	b_2	b_3	N_1[c] (cm^{-2})	N_2	N_3
C_2H_2 ν_5	$R(1)$	1	100	-62.0	–	–	3.3	–	–	1.0(15)	–	–
	$R(5)$	1	100	-62.0	–	–	2.4	–	–	4.5(14)	–	–
	$R(6)$	1	100	-65.5	–	–	2.4	–	–	4.5(14)	–	–
	Q branch	1	100	–	–	–	1.0	–	–	2.0(15)	–	–
C_2H_2 $\nu_4+\nu_5$	P(2)	1	100	-61.0	–	–	6.8	–	–	2.5(16)	–	–
	P(3)	1	100	-62.0	–	–	5.7	–	–	1.0(16)	–	–
HCN ν_2	$R(16)$	1	200	-64.5	–	–	7.9	–	–	1.2(16)	–	–
$^{12}CH_4$ ν_4	$R(0)$[d]	4	200	-65.0	-54.0	-61.0	2.3	2.7	4.6	7.5(16)	-4.0(15)	6.0(16)
	$R(2)$	2	200	-65.5	-61.5	–	2.3	2.5	–	6.0(16)	3.3(16)	–
	$R(2)$	–	–	–	–	–	2.5	2.3	–	6.3(16)	1.5(16)	–
$^{14}NH_3$ ν_2	a$P(4,0)$	2	200	-64.0	-70.0	–	4.6	3.9	–	-2.5(15)	5.0(14)	–
	a$P(4,1)$	2	200	-62.0	-72.0	–	5.3	3.9	–	-3.8(15)	2.5(14)	–
	a$P(4,3)$	2	200	-62.0	-70.0	–	2.8	3.9	–	-1.0(15)	1.0(15)	–
	s$P(7,0)$	2	200	-60.0	-69.0	–	2.9	2.9	–	-1.5(15)	1.2(15)	–
	s$P(7,1)$	2	200	-62.0	-70.0	–	1.8	4.0	–	-2.0(15)	7.5(14)	–
	s$P(7,2)$	2	200	-61.0	-62.5	–	3.3	2.9	–	-6.0(15)	4.5(15)	–
	s$P(7,3)$	2	200	-58.5	-64.0	–	1.8	2.9	–	-1.2(15)	1.5(15)	–
	s$P(7,4)$	2	200	-60.5	-63.0	–	1.8	1.8	–	-2.5(15)	2.0(15)	–
	s$P(7,5)$	1	200	-56.0	–	–	4.4	–	–	-7.0(15)	–	–
	s$P(7,6)$	1	200	-57.0	–	–	4.4	–	–	-4.0(15)	–	–

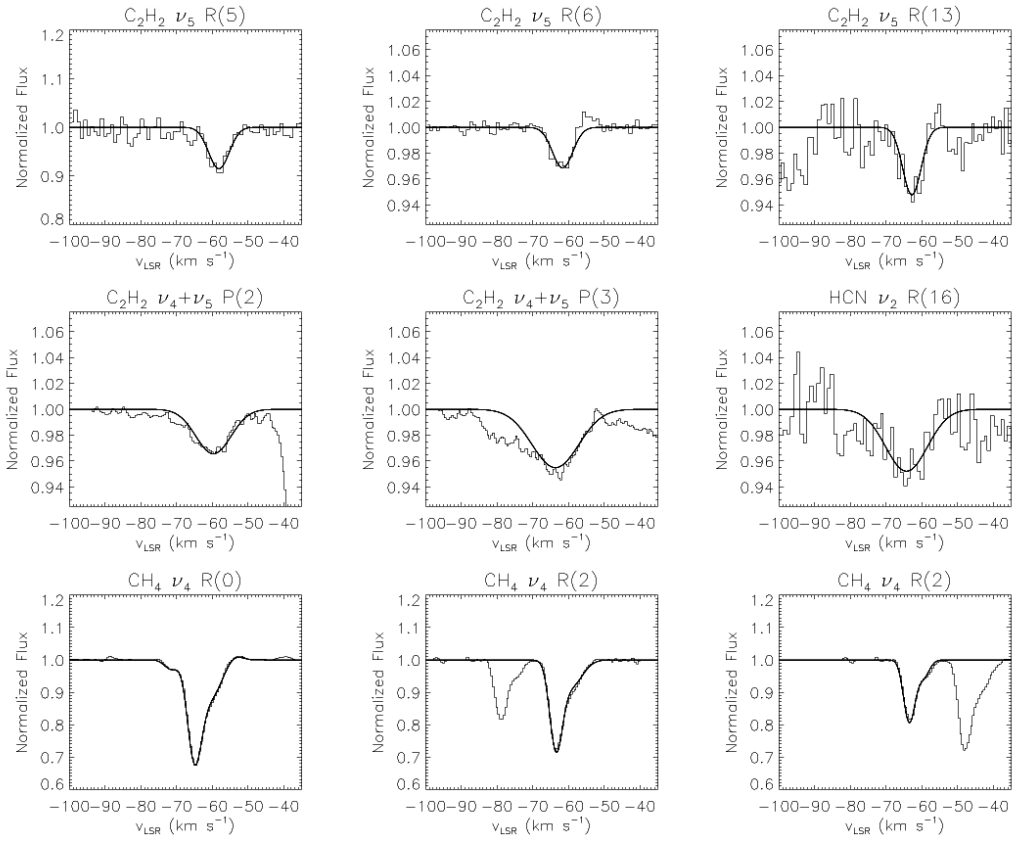

Figure 4.10 TEXES spectra of NGC 7538 IRS 9 (thin lines) and synthetic spectra computed using the simple LTE fitting method described in Section 4.4.1 (thick lines). The continuum in each spectrum has been normalized to unity and the spectra are plotted on a velocity scale referred to the LSR. Features shown are C_2H_2 ν_5 $R(5)$, $R(6)$ and $R(13)$; C_2H_2 $\nu_4 + \nu_5$ $P(2)$ and $P(3)$; HCN ν_2 $R(16)$; and CH_4 ν_4 $R(0)$ and the two components of $R(2)$.

4.4.2 χ^2 Minimization Spectral Fitting

Our spectral fitting code, `FITSPEC`, uses the Levenberg-Marquardt method of inverting the second derivative matrix to minimize χ^2 as in Bevington & Robinson (2003) for up to four unique absorbing or emitting units, or "clouds,"

Table 4.2 (cont'd)

Molecule/Band	Line	n[a]	T (K)	v_1[b] (km s^{-1})	v_2	v_3	b_1 (km s^{-1})	b_2	b_3	N_1[c] (cm^{-2})	N_2	N_3
$^{12}C^{16}O$ v=1-0	$P(14)$	3	200	-55.0	-64.5	-88.5	2.4	6.5	7.2	-1.0(16)	-1.1(17)	3.0(17)
	$P(15)$	3	200	-51.5	-63.5	-88.5	3.6	9.4	7.2	-2.5(16)	-2.2(17)	3.0(17)
	$P(21)$	2	200	-54.5	-77.5	–	10.9	10.9	–	-8.0(17)	5.5(17)	–
	$P(22)$	2	200	-55.0	-77.0	–	8.0	10.2	–	-6.0(17)	6.0(17)	–
$^{13}C^{16}O$ v=1-0	$P(3)$	3	200	-60.5	-70.5	-89.0	4.3	4.3	1.4	-9.0(17)	8.0(18)	7.0(17)
	$P(4)$	3	200	-61.5	-71.5	-86.0	3.6	5.0	6.5	-7.0(17)	6.8(18)	3.4(18)
	$P(11)$	2	200	-54.0	-75.0	–	5.8	10.2	–	-8.0(17)	2.7(18)	–
	$P(12)$	2	200	-54.0	-73.0	–	5.9	10.2	–	-3.5(17)	6.5(18)	–
$^{12}C^{18}O$ v=1-0	$P(2)$	2	200	-68.0	-72.0	–	2.9	3.6	–	7.5(18)	7.5(18)	–
	$P(3)$	2	200	-66.0	-71.0	–	4.3	4.3	–	3.0(18)	3.0(18)	–

[a]Number of velocity components fit.

[b]All velocities are referred to the LSR.

[c]Column densities are given in the form $A(B) = A\times10^{B}$. Negative values of A indicate components in emission. "Column density" includes all rotational states, assuming $T = 200$ K.

[d]The best fit to this line required four components. The remaining component not in the table is v_4 = -71.5 km s^{-1}, b_4 = 2.3 km s^{-1}, N_4 = 5.0(15)cm^{-2}

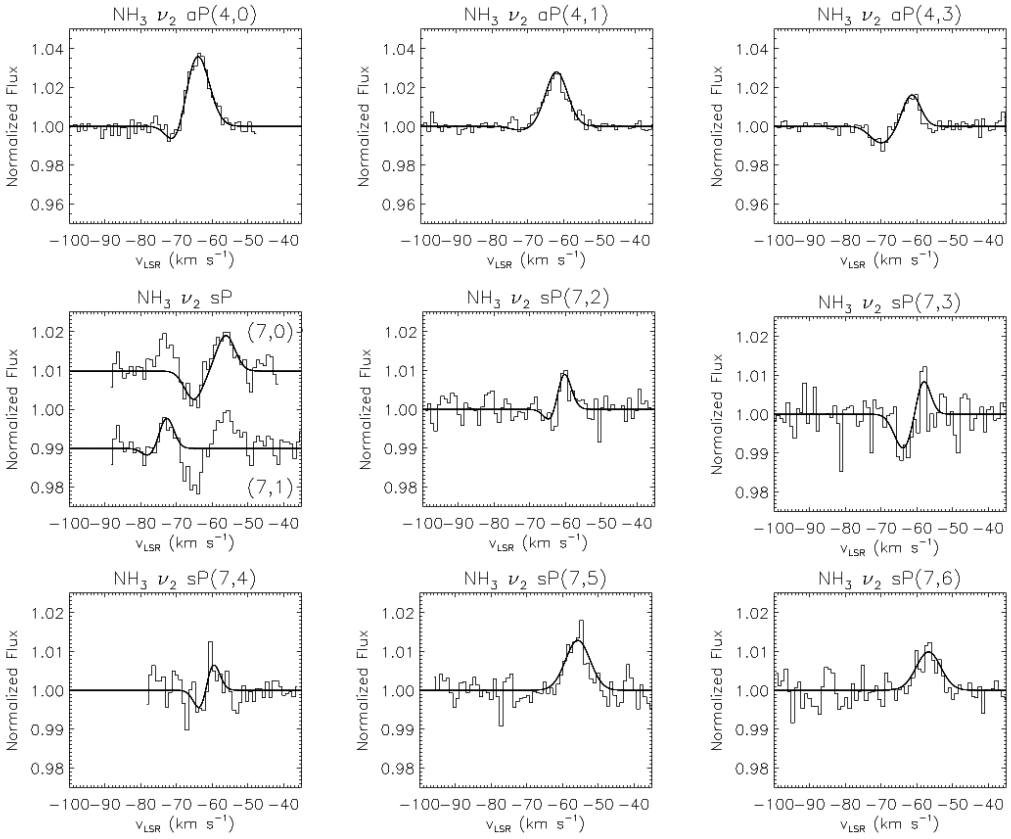

Figure 4.11 TEXES spectra of NGC 7538 IRS 9 (continued). Features shown are NH_3 ν_2 aP(4,0), aP(4,1), aP(4,3), sP(7,0), sP(7,1), sP(7,2), sP(7,3), sP(7,4), sP(7,5) and sP(7,6). The sP(7,0) and sP(7,1) lines are shown together in a single panel using the velocity scale for sP(7,0), and are offset slightly for clarity.

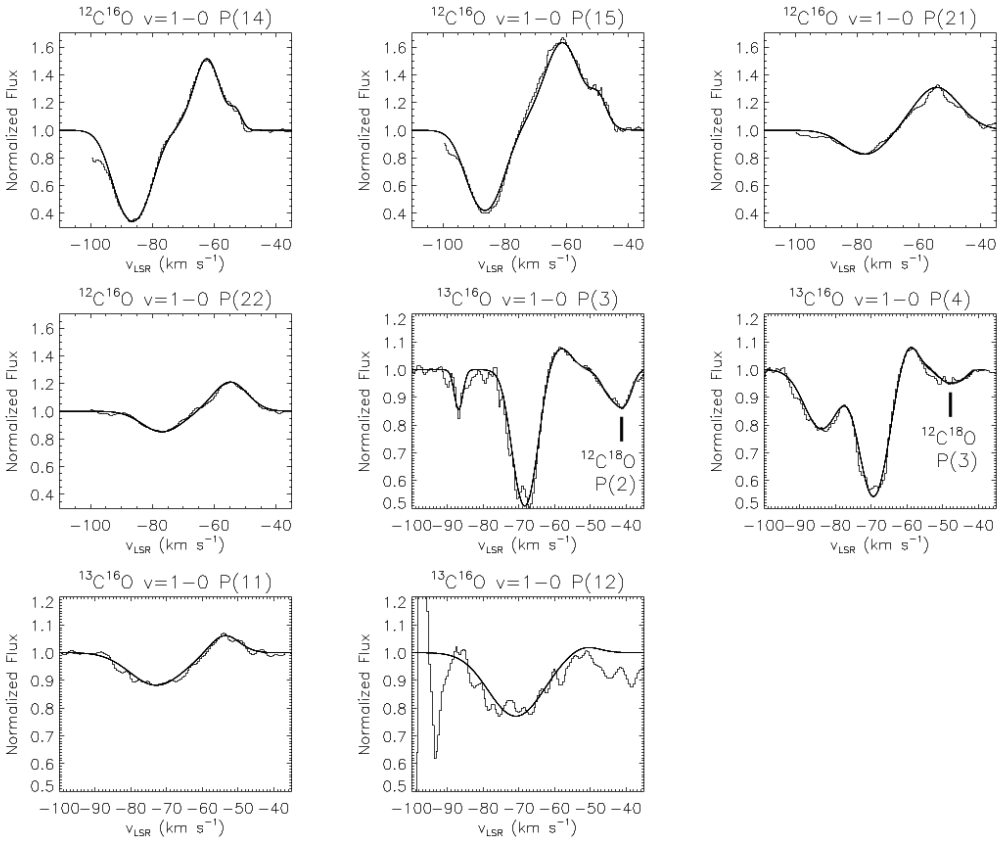

Figure 4.12 TEXES spectra of NGC 7538 IRS 9 (continued). Features shown are $^{12}C^{16}O$ v=1-0 $P(14)$, $P(15)$, $P(21)$ and $P(22)$; $^{13}C^{16}O$ v=1-0 $P(3)$ / $^{12}C^{18}O$ v=1-0 $P(2)$; $^{13}C^{16}O$ v=1-0 $P(4)$ / $^{12}C^{18}O$ v=1-0 $P(3)$; and $^{13}C^{16}O$ v=1-0 $P(11)$ and $P(12)$.

along the line of sight. The 1-D radiative transfer model assumes rotational LTE of all molecules with a single excitation temperature. As in our "by eye" fitting, re-emission by absorbing molecules is neglected and emission features are modeled as negative absorption. The total number of free fitting parameters depends on the number of molecules in the fit and the number of echelon orders in a particular spectral setting. Although there is a large number of free parameters in the fit, most of them are "uninteresting," such as baseline coefficients. The "interesting" parameters in the fit are Doppler shift, Doppler b parameter, column density, temperature, and covering factor for each cloud and for each molecule. The details of the program are discussed in Knez et al. (2009). For our observed molecules, we chose a number of absorbing clouds consistent with the number of velocity components seen in the TEXES spectra, allowing `FITSPEC` to independently determine their parameters. When available, we included data indicating the non-detection of certain lines, such as high-J C_2H_2 near 13 μm, to better constrain the fit parameters.

The success of `FITSPEC` requires accurate molecular transition data to compute synthetic spectra against which to fit the data. We relied on the calculations in Evans et al. (1991), giving information including the line center, the energy of the transition either in units of $J(J+1)$ (which is then multiplied by the molecule's rotational constant B) or E in units of cm^{-1}, and the rotational line strengths (Hönl- London factors) in units of cm^{-1} $(10^{16}$ cm$^{-2})^{-1}$. The program uses guesses of the starting parameter values to compute the initial model spectrum, and then iterates the fit by varying those values until

a convergence criterion is satisfied. The requirement is

$$\sum_i \left(\frac{\Delta p_i}{\sigma_{p_i}} \right)^2 \leq 0.01 \tag{4.5}$$

where Δp_i is the change in the value of parameter i and σ_{p_i} is the uncertainty in the parameter i, allowing all other parameters to vary.

The output of the program consists of the best-fit parameter values, uncertainty estimates and a synthetic spectrum having the properties of the best fit. The intensity of the synthetic spectrum is calculated by taking $I = I_o e^{-\tau}$ of each absorbing unit along the line of sight and adding any optically thin emission as

$$I_{obs} = I_0 \prod_{n=1}^{N} [1 - C_n(1 - e^{-\tau_n(\nu)})] + S_{em} C_{em} \tau_{em}(\nu) \tag{4.6}$$

where N is the number of absorbing clouds in the fit, I_0 is the intensity of radiation from the background continuum source (set to unity since the spectra are normalized), $C_n = \Omega_n/\Omega_0$ and τ_n are the covering factors and optical depths of the absorbing clouds, S_{em} and $C_{em} = \Omega_{em}/\Omega_0$ are the source function and covering factor of the emitting material, and Ω_0 is the solid angle of the continuum source. The right-hand term represents an optically-thin emitting cloud; since it only depends on the product of S_{em} and C_{em}, we scale C_{em} by S_{em}/I_0 and drop S_{em} from the formula. The product term in Equation 4.6 assumes that the absorbing clouds overlap randomly. That is, if two clouds each have covering factors of 0.1, 1/10 of each lies along the line of sight to the other.

Knez et al. (2009) used the same approach and note this results in greater absorption in saturated lines than would result if the optical depths were added first and then the transmission spectrum were calculated from the optical depth spectrum. The resulting fits to the data are better than those obtained by summing the optical depths first and then taking the exponential. This fitting approach, however, is not without drawbacks. Emission lines may not be thermally excited, but rather could be due to resonantly scattered light; we have no way of discriminating between these processes. We assume that upward transitions in the molecules we observe are not followed by re-emission of that radiation; in reality, most absorptions should be followed by re-emission, although in a direction uncorrelated with the incoming radiation, so the extent to which re-emission fills in the absorption depends on the distribution of the re-emitting gas around the continuum source.

The results of our `FITSPEC` runs on the IRS 9 data are summarized in Table 4.3 where they are compared with results from fitting TEXES data of IRS 1 with the same procedure in Knez et al. (2009).

4.4.3 Column Density Upper Limits For Non-Detections

We calculate column density upper limits from the lines that were not detected in the spectrum of IRS 9 by convolving the data with a Gaussian line shape function whose properties are consistent with those of detected lines. We begin by assuming a normalized spectrum containing a single absorption

Table 4.3. Molecular absorption parameters determined from χ^2 minimization spectral fitting

Species	v_{LSR} (km s^{-1})	T_{ex} (K)	b (km s^{-1})	$N(X)$[a] (10^{16} cm^{-2})	C %
			IRS 9 (this work)		
C_2H_2	-58.9(1.4)	195(57)	4.0(1.3)	-0.2(0.1)	52(189)[b]
	-63.9(1.0)	205(49)	4.0(1.1)	2.3(0.7)	16(9)
HCN	-58.7(1.7)	200(68)	4.0(1.3)	0.5(0.7)	52(193)[b]
	-63.8(2.9)	204(76)	4.0(1.4)	3.9(4.3)	11(6)
NH_3[a]	-57.3(0.5)	365(47)	5.1(0.7)	-1.1(0.1)	52(195)[b]
	-61.6(0.6)	201(43)	5.9(1.1)	4.8(0.8)	8(8)
HNCO[c]	-58.9(0.0)	195(0)	4.0(0.1)	0.1(-0.5)	52(0)
	-63.9(10.0)	205(50)	4.0(1.0)	0.9(-1.6)	16(10)
			IRS 1 (Knez et al. 2009)		
C_2H_2	-55.7(0.3)	225(20)	0.6(0.1)	3.0(0.6)	6(0.6)
	-59.4(0.3)	191(10)	0.6(0.1)	2.8(0.2)	24(1)
HCN	-56.3(0.3)	256(30)	0.8(0.1)	5.6(2.8)	8(1)
	-60.0(0.3)	456(127)	1.0(0.4)	1.3(1.2)	68(50)
NH_3	-57.3(0.3)	278(31)	0.9(1.0)	5.2(1.5)	9(1)
	-60.1(0.3)	248(32)	0.4(0.1)	2.8(0.8)	16(4)
HNCO	-57.2(0.3)	319(27)	1.8(0.2)	0.4(0.3)	4(0.3)
	-60.2(0.2)	171(79)	0.7(0.4)	0.1(0.3)	97(11)

Note. — Quantities in parentheses are the 1σ uncertainties on the adjacent figures in the same units unless otherwise indicated.

[a]Negative column densities indicate components in emission. Column densities for the emission components are $C_{em}\tau_{em}(\nu)$ converted to N and do not represent a real column densities.

[b]Unable to be constrained in the fit, assuming lines are optically thin.

[c]All HNCO parameters other than the column density were fixed equal to those of C_2H_2 because an insufficient number of HNCO lines were observed to constrain them.

line has the functional form

$$F_\nu = 1 - ae^{-x^2/b^2} \tag{4.7}$$

where $a > 0$ is the depth of the line and b is the Doppler b parameter. The observed spectrum is convolved with a Gaussian of the form ne^{-x^2/b^2} where n is a normalization factor here chosen to be $1/\sqrt{\pi}b$ such that the integral of the Gaussian is unity. The convolution is given by

$$F_\nu \otimes ne^{-x^2/b^2} = \int F_\nu ne^{-x^2/b^2} d\nu, \tag{4.8}$$

where $x = \nu - \nu'$. The upper limit of the equivalent width, W_{max}, of a line not detected is proportional to the peak value of the convolved spectrum according to

$$W_{max} = \sqrt{\pi} P b \tag{4.9}$$

in which P is the peak. We used $b = 3.5$ km s^{-1} in making the calculations, a value consistent with those derived by spectral fitting methods described previously. The column density limit for species X was then computed from

$$N(X) = \frac{W_{max}}{\alpha} \tag{4.10}$$

where α is the line strength. We used the GEISA line strengths where available and corrected them to a uniform temperature of 200 K as described previously. Results for our non-detections are given in Table 4.4.

We derived upper limits for all lines of a particular molecular species available in a given spectral setting, as indicated in the table by the number

Table 4.4. 3σ upper limits to column density of molecules in the upper state for selected non-detections

Species/Mode	Line	n[a]	N_{limit}(X) (cm^{-2})
$^{13}CH_4$ ν_4[b]	$R(1)$	1	4.1×10^{16}
	$R(4)$	4	3.1×10^{16}
OCS ν_2	P branch	34	2.9×10^{15}
HCN ν_2	$R(15)$	1	1.8×10^{16}
	$R(22)$	1	8.5×10^{16}
	$R(23)$	1	1.1×10^{17}
C_2H_2 ν_5	$R(12)$	1	8.5×10^{15}
	$R(21)$	1	9.4×10^{15}
	$R(22)$	1	3.5×10^{16}
C_2H_2 $2\nu_5-\nu_5$	Q branch	15	2.1×10^{17}

Note. — A uniform temperature of 200 K was assumed for all species.

[a]Number of lines/components in the attempted fit.

[b]The given values of $N(^{13}CH_4)$ are for the isotopologue only rather than the total CH_4 column density.

of lines parameter n. In cases where $n > 1$, the equivalent width and column density upper limits given are simple averages. All limits are given with respect to the total number of molecules along the column, irrespective of isotopic composition except for $^{13}CH_4$; here we have divided the derived column density by the terrestrial $^{12}C/^{13}C = 89$ ratio built into GEISA to recover the column density specifically for $^{13}CH_4$.

4.4.4 An Upper Limit to the Ionizing Flux in IRS 9

The $^2P_{1/2} \rightarrow {}^2P_{3/2}$ fine structure line of [Ne II] at 780.42 cm^{-1} is often used as a diagnostic of ionized gas at our wavelengths. The non-detection of this line in the spectrum of IRS 9 places a constraint on the amount of ionizing flux being emitted by the embedded central source.

The Lyman continuum luminosity (N_{Lyc}) can be calculated from the [Ne II] luminosity since both are proportional to the square of the density integrated over volume. The [Ne II] volume emissivity is given by

$$j_{[NeII]} = n_e n_{Ne^+} q_{lu} h\nu \frac{n_c}{n_e + n_c} \tag{4.11}$$

where n_e is the electron density, n_{Ne^+} is the density of ionized neon, q_{lu} is the rate coefficient for collisional excitation ($q_{lu}h\nu = 8.4 \times 10^{-22}$ erg s^{-1} cm^3), and $n_c = A_{ul}/q_{ul}$ ($= 4.9 \times 10^5$ cm^{-3} at an electron temperature $T_e = 10^4$ K) is the critical density in the two-level approximation, using the values in Osterbrock & Ferland (2006). The hydrogen recombination rate per unit volume is given by $n_{recomb} = \alpha_B n_e n_p$ where α_B ($= 2.6 \times 10^{-13}$ cm^3 s^{-1}) is the recombination rate for "case B" recombination, and n_p is the proton density. The ratio of N_{Lyc} to the [Ne II] luminosity is then given by

$$\frac{N_{Lyc}}{L_{[NeII]}} = \frac{n_{recomb}}{j_{[NeII]}} = \frac{n_{H^+}}{n_{Ne^+}} \frac{\alpha_B}{q_{lu} h\nu} \tag{4.12}$$

assuming $n_e \ll n_c$. The Ne^+/H^+ ratio is given by the product of the Ne abundance and the singly-ionized fraction for Ne, f_+. We take the value of f_+ = 0.3 from Figure 3 in Ho & Keto (2007) using for the radiation temperature

that of a ZAMS star with IRS 9's luminosity (T_r = 26200 K) and a ratio of the dilution factor for blackbody radiation, Γ, to the electron density of Γ/n_e = 10^{-19} cm^3. From this we adopt a Ne^+ / H^+ ratio to be 3×10^{-5}.

Without knowing the width of the [Ne II] line, it is difficult to place a strong upper limit on its flux, but an emission equivalent width of $W_\nu = 0.01$ cm^{-1} can be ruled out unless the line is wider than 0.2 cm^{-1}, or 77 km s^{-1}. This corresponds to a line flux limit of $F_{[NeII]} < 2.0 \times 10^{-13}$ erg s^{-1} cm^{-2} and a luminosity limit of $L_{[NeII]} = 4\pi d^2 F_{[NeII]} < 1.7 \times 10^{32}$ erg s $^{-1}$. We then calculate $N_{Lyc} < [3.3 \times 10^4 \times 2.6 \times 10^{-13}/8.4 \times 10^{-22}] \times 1.7 \times 10^{32} = 1.7 \times 10^{45}$ photons s^{-1}. For reference, Tielens (2005) gives the Lyman continuum luminosity of a main sequence B0 star as $N_{Lyc} = 1.4 \times 10^{48}$ photons s^{-1}. Apparently IRS 9 emits a small fraction of the Lyman continuum luminosity of a main-sequence star of its bolometric luminosity. The radiation environment of IRS 1 is considerably more intense, by comparison. From infrared and millimeter data, the exciting source is inferred to be of spectral type earlier then O7.5, total luminosity $L > 8 \times 10^4$ $L_\odot$, and Lyman continuum luminosity $N_{Lyc} > 10^{48}$ s^{-1} (Hackwell et al. 1982, Akabane et al. 2001, Lugo et al. 2004). The inferred radiation field of IRS 1 is more intense than that of IRS 9 and results in a different set of conditions under which chemistry proceeds.

4.5 Interpretation of the Spectroscopic Results

4.5.1 Assumptions and Caveats

Interpretation of our results requires caution, given the underlying assumptions of the radiative transfer model in `FITSPEC`. The program assumes a single continuum source behind all absorbing material and a constant temperature characterizing the material in each of up to four absorbing "clouds" along the line of sight. We also add an optically-thin emitting cloud, but neglect re-emission by the absorbing gas and absorption by the emitting gas. The column densities we report do not represent the entire column down to the embedded luminosity source, but rather the column only to an effective "dust photosphere" interior to which the continuum optical depth is large at a given wavelength. Consequently, our observations at 5 μm and 8 μm likely probe to greater depth than those at 13 μm. The optical depth may be higher at longer wavelengths due to silicate opacity, and the colder, outer layers of the dusty region are likely too cool to emit significantly at 5 μm. Comparison of results at different wavelengths is therefore difficult. We also did not take into account emission by molecules following absorption of photons, except as approximated by our "negative absorption" method of treating emission lines. Furthermore, we ignored emission following radiative excitation. We assumed either pure absorption or optically-thin emission. However, the neglect of emission from a radiatively excited molecule should not be valid; at any plausible gas density the collisional de-excitation rate should be far below the radiative rate. Critical densities for vibrational transitions are typically

greater than 10^{12} cm^{-3}, and almost all absorption events should be followed by emission, not collisional de-excitation. For two of our molecules, NH_3 and C_2H_2, we were able to observe lines of more than one vibrational band or rotational branch, and the comparison of the observed line depths provides evidence that re-emission following absorption is an important effect.

For NH_3, we observed weak emission in P-branch lines at wavelengths near 12 μm and possibly weak absorption in Q- branch lines near 10.5 μm. R-branch lines were not observed due to the silicate and telluric O_3 absorption at their wavelengths. We explain the differences between the P- and Q-branch lines based on the differing continuum radiation fields due to their differing proximity to the silicate dust feature. The NH_3 R branch is centered on the 9.7 μm silicate feature, the Q branch falls on its long wavelength shoulder, and the P branch is mostly between the 9.7 and 18 μm features. If the radiation field seen by a molecule is due to silicate emission either because the molecule is exposed to radiation from an optically thin external dust cloud or because it is immersed in a cloud of warm silicate dust, there will be more upward radiative transitions (i.e. more absorption) in the Q and R branches than in the P branch. The branching ratio between P-, Q-, and R-branch transitions from a given vibrationally-excited state depends on the K rotational quantum number, but is similar in the three bands. Consequently, if all absorption events are followed by an emission, absorptions will outnumber emissions in the R branch and emissions will outnumbers absorptions in the P branch, resulting in net emission in the P-branch lines, as we observe. In

Section 4.5.3 we describe a simple model involving purely radiative transitions in NH_3 incorporating upward and downward line strengths and assuming that the incident radiation field is proportional to the strength of the silicate feature at the wavelengths of the various lines. The model is time-independent and assumes the NH_3 gas is optically thin. More detailed and quantitative models will follow in a future paper.

4.5.2 C_2H_2, HCN, HNCO, OCS, and CO

We find that excitation temperatures for various molecules are basically consistent toward IRS 9 and IRS 1 with the exception of the hotter of the two NH_3 components toward IRS 1. That value of T_{ex} has a rather large uncertainty so it may in fact lie closer to $\sim$250 K. The column densities are also similar in the two sources, though again with particular exception in the case of HCN. Knez et al. (2009) had the benefit of more observed HCN lines, but we find a lower column toward IRS 9. Most striking is the disagreement between the two sources in terms of the intrinsic line widths; although the thermal broadening should be similar, turbulence or systematic velocity variations along the line of sight to IRS 9 are greater than toward IRS 1. At the least, we can say that the spectral lines observed in the direction of IRS 9 are generally less saturated than those seen toward IRS 1, and this has important consequences for the accuracy of the IRS 9 column densities we obtain.

An example in which saturation of lines becomes important is CO. Knez et al. (2009) derived fractional abundances relative to CO for a variety

of molecules seen in absorption toward IRS 1, attempting to compensate for badly saturated ^{12}CO lines by using the value of $N(^{13}\mathrm{CO})$ in Mitchell et al. (1990) and adopting $^{12}\mathrm{C}/^{13}\mathrm{C} = 45$ on the basis of their observations of C_2H_2. The value of $N(^{13}\mathrm{CO})$ for IRS 9 reported by Mitchell et al. was based on their measurement of ^{12}CO lines and assumed the terrestrial ratio $^{12}\mathrm{C}/^{13}\mathrm{C} = 89$. Boogert et al. (2004) confirm the saturation of the ^{12}CO lines observed toward IRS 9. From observations of lines of ^{13}CO and $^{12}\mathrm{C}^{18}\mathrm{O}$ in upper J levels of 7-15 they derive an optical depth $\tau_{12} = 13 \pm 4$ assuming $^{12}\mathrm{C}/^{13}\mathrm{C} = 80$ from Boogert et al. (2002). However, they argue that reliable values for $N(^{12}\mathrm{CO})$ can be obtained, since the ^{13}CO lines remain optically thin; they quote a value $N(^{12}\mathrm{CO}) = (3.2\pm1.0)\times10^{18}$ cm^{-2}. While we may argue with their choice of $^{12}\mathrm{C}/^{13}\mathrm{C}$ and with their conclusion that the ^{13}CO lines are optically thin, their value of the CO column density is probably more realistic for IRS 9 than that obtained from the lower-resolution observations of Mitchell et al. (1990). Abundance ratios for some of the molecules we observed with TEXES, relative to this column of CO, are shown in Table 4.5.

Similarly, an estimate of the abundance of various molecules with respect to H_2 can be made given a measurement of the quantity of dust along the line of sight and a value for the gas-to-dust ratio in a typical protostellar envelope. Knez et al. adopted an H_2 column density toward IRS 1 of 7.5×10^{22} cm^{-2} based on the 9.7 μm optical depth measured by Willner et al. (1982) to calculate fractional abundances of other molecules. Using the same method, we derive $N(H_2) = 5.2 \times 10^{22}$ cm^{-2} toward IRS 9 and present the resulting

Table 4.5. Abundances in IRS 9 and IRS 1 with respect to CO and H_2

	IRS 9 (this work)		IRS 1 (Knez et al. 2009)	
Molecule	$N(X)/N(CO)$	$N(X)/N(H_2)$	$N(X)/N(CO)$	$N(X)/N(H_2)$
C_2H_2	7.7(-3)	3.3(-7)	5.7(-3)	7.7(-7)
HCN	1.4(-2)	5.8(-7)	6.9(-3)	9.2(-7)
NH_3	1.9(-2)	7.9(-7)	3.6(-2)	4.8(-6)
CH_4	9.9(-2)	4.2(-6)	3.6(-2)	4.8(-6)
HNCO	<3.0(-3)	<1.3(-7)	5.0(-4)	6.0(-6)

Note. — All values are given in the notation $A(B) = A \times 10^B$. The column densities toward IRS 1 adopted for CO and H_2 were $N(^{12}CO) = 1{\times}10^{19}$ cm^{-2} (Knez et al. 2009) and $N(H_2) = 7.5{\times}10^{22}$ cm^{-2} (Willner et al. 1982). For IRS 9 the ^{12}CO column density used was $N(^{12}CO) = 3.2{\times}10^{18}$ cm^{-2} (Boogert et al. 2002) and the H_2 column density was the same as that used by Knez et al. (2009).

abundances in Table 4.5. The pattern of relative abundances differs between the objects according to both the molecular species and whether the abundance of a given species is referred to CO or to H_2. The latter observation indicates that either the abundance ratio of CO to H_2 or the gas-to-dust ratio varies between objects.

The assumptions made in calculating the values in Table 4.5 – that the CO column density is comparable along both lines of sight and that the dust distribution and gas-to-dust ratio are similar in both cases – may not be unreasonable given that both objects are along nearby sightlines toward the same molecular cloud. Given this caveat, it is worth noting that the fractional abundances of all molecules relative to both CO and H_2 are broadly consistent

with each other, except for HNCO with the values given for IRS 9 properly unconstrained by `FITSPEC` because no HNCO lines were detected. C_2H_2, HCN, and NH_3 are generally less abundant in IRS 9 than IRS 1, although this is only a suggestion in light of the assumptions.

Some kinematic information about IRS 9 is available in the line shapes. In combination with the varying effective depths to which sightlines probe at different wavelengths, line shapes give a sense of the distribution of various molecules along the line of sight. The P Cygni line profiles of our CO observations, for example, clearly indicate an outflow known previously. CH_4 absorption toward IRS 9 was known previously as well, but the TEXES data reveal the structure of the lines in more detail than the Keck+NIRSPEC spectra of Boogert et al. (2004) and the IRTF+Irshell spectra of Lacy et al. (1991).

In contrast to the circumstellar disk model of IRS 1 presented in Knez et al. (2009) based on TEXES observations, we cannot conclusively establish the presence of a disk in IRS 9. However, our fitting program preferred relatively small covering factors, similar to those in the best- fit synthetic spectra for the lower velocity component of IRS 1. Knez et al. interpret this as the signature of a near edge-on disk, acting as a source of continuum radiation that is only partially covered by the absorbing material. Given the high-velocity outflow in IRS 9 reported by Mitchell & Hasegawa (1991), we might rather be observing an accreting system nearly face-on in which the outflow both sweeps out a region near the continuum source and entrains material into the flow that only partially covers the source. This picture would account for the methane

observations of Boogert et al. (2004) in which cold, solid-phase methane is seen in the outer envelope, becomes depleted in the outflow, and is seen in the gas phase in the inner envelope, all along a single sightline. We develop this model further in Section 4.5.6.

Non-detections of molecules also furnish some interpretable information. Carbonyl sulfide (OCS) is a molecule that commonly occurs in ices along sightlines through molecular clouds and indicates the presence of sulfur-bearing precursor species such as H_2S and SO_2 (Ferrante et al. 2008). Gibb et al. (2004) detected solid-phase OCS toward IRS 9 with *ISO*, finding a column density of $(5.5\pm4.4) \times 10^{15}$ cm^{-2}, and Knez et al. (2009) speculate that gas-phase OCS should be observable toward IRS 9 as indicated in some chemical models. We find an upper limit of $N(\mathrm{OCS}) \leq 2.9 \times 10^{15}$ cm^{-2} in the gas phase, which is compatible with the Gibb et al. result to within errors; we therefore conclude that any OCS near IRS 9 is firmly sequestered as an ice. Tielens (2005) cites an OCS ice abundance of 0.1% relative to H_2O ice toward IRS 9 given a water ice column density of 1×10^{19} cm^{-2}. That figure may be compared to a CO ice abundance of 10%. In interstellar ices, OCS is commonly found in association with hydrogenated species such as H_2O and CH_3OH (Palumbo et al. 1997; Dartois et al. 1999). Laboratory results reported by Collings et al. (2004) indicate that OCS in an H_2O mixture desorbs at $\sim$150 K, implying that significant quantities of this molecule may be frozen out in cold envelopes. However, C_2H_2 is seen toward both IRS 1 and IRS 9, for example, and according to the same study desorbs at only a slightly lower

temperature. The relative columns of OCS and C_2H_2 may then reflect real differences in their abundances rather than their desorption temperatures. Alternately, OCS might only be abundant in the colder, outer envelope of IRS 9, explaining its apparent absence in the gas phase. Knez et al. (2009) did not observe OCS in the gas phase toward IRS 1 and Gibb et al. (2004) only cite an upper limit of 1×10^{15} cm^{-2} for the column density in the solid phase. Other sulfur-bearing molecules desorb from grains at a relatively low temperature of $\sim$70 K, well below the temperatures in both objects. It is difficult, then, to understand why high-J lines of CS were observed toward IRS 1 by Knez et al. (2009) when recent models by Wakelam et al. (2011) *underpredict* the abundance of CS relative to other S-bearing molecules at temperatures above 100 K. The IRS 1 CS gas-phase column density is comparable to the solid-phase column density of OCS toward IRS 9, so if IRS 1 began with a comparable OCS abundance it may indicate a reaction route preference for forming CS as opposed to, e.g., SO_2. However, Wakelam et al. (2004) do not associate OCS and CS but rather assume CS exists in the gas of the pre-evaporative phase. We did not search for CS or SO_2 toward IRS 9 on the basis of their presumed low abundances, and thus are unable to comment on the likelihood of any OCS/CS association.

The occurrence of isocyanic acid (HNCO) may be tied to the presence of the cyanate ion (OCN^-), where OCN^- is formed on grains by irradiation of solid HNCO in ices by UV in the presence of NH_3 (van Broekhuizen et al. 2004). Once evaporated from grains, OCN^- may then undergo hydrogenation

to become HNCO again. We speculate, however, that the hydrogenation of OCN^- takes place *before* desorption, since the charge an ion induces while on a grain would result in a relatively high desorption temperature. Knez et al. (2009) observed dozens of HNCO lines toward IRS 1 and infer a column density of 5.4×10^{15} cm^{-2}; this and the value of other gas parameters from their spectra led them to conclude that gas-phase HNCO may originate from evaporation of grain mantles by way of OCN^-. A low column density compared to the value expected from the observed abundance of OCN^- is interpreted as evidence that only a fraction of the available OCN^- desorbed from grains becomes HNCO, the remainder forming other molecules in gas-phase chemistry. Interpretation of observations is difficult, however, as Knez et al. point out that most chemical models do not currently include HNCO in their networks. All of the HNCO lines in the various TEXES settings we observed were non-detections. Our fitting program preferred column densities of $(0.1\pm0.5) \times 10^{16}$ cm^{-2} and $(0.9\pm1.6) \times 10^{16}$ in the two presumed absorbing units, although a clear lack of detected lines make these values limits at best. We cannot, therefore, confidently distinguish between scenarios in which HNCO has a very low abundance in all phases and those in which it is effectively locked up in ices and unavailable to spectroscopy at our wavelengths.

4.5.3 Radiative Excitation and Radiative Transfer

In order to explain the observed pattern of NH_3 absorption and emission in our spectra of IRS 9, we invoke a radiative transfer effect that emerged from

our modeling efforts. We begin with gas in a shell of thickness t around the continuum source with an NH_3 density n_{NH_3}. The rotational levels (J,K) of the ground vibrational state are assumed to be populated thermally at temperature T. Electric dipole transitions to and from an upper vibrational level proceed according to the selection rule that $\Delta K = 0$, $\Delta J = \pm\ 1$ or 0. In ammonia there is also a doubling of each vibrational level into symmetric and antisymmetric (s,a) inversion states, and the requirement that $s \leftrightarrow a$. Transitions are labeled by the inversion symmetry of the lower level. This gives the permitted transitions a/s $R(J_u\text{-}1,K)$, a/s $Q(J_u,K)$ and a/s $P(J_u\text{+}1,K)$. We obtain absorption coefficients α for each of these transitions from GEISA.

The absorption optical depth corresponding to α is

$$\tau(w) = \alpha N(\mathrm{NH_3})\phi_w \tag{4.13}$$

in which $N(NH_3)$ is the radial column density through the shell and ϕ_w is the line shape function, taken to be a Gaussian. Molecules are excited to the upper state along all branches at a rate

$$r_{up} = \sum_{P,Q,R} \int \frac{L_w}{hcw} \tau(w) dw \tag{4.14}$$

per second assuming $\tau \ll 1$ through the shell, where L_w is the incident continuum luminosity. The rate at which photons are emitted on a given branch is determined by the rate of transitions populating the upper level and the branching ratio of the Einstein A coefficients, e.g.,

$$r_{down}(P) = r_{up}(P) \frac{A_P}{A_P + A_Q + A_R} \tag{4.15}$$

for the P branch. We calculate values for the A coefficients according to

$$A_{ul} = \frac{8\pi c}{\lambda^2}\alpha(T)\frac{Q_r}{g_u}e^{E_l/kT} \tag{4.16}$$

where λ is the wavelength of the transition, Q_r is the rotational partition function, g_u is the statistical weight of the upper state, and E_l is the energy of the lower state.

We consider the $aP(4,K)$, $aQ(3,K)$, and $aR(2,K)$ lines that go to the $J = 3$ rotational level of the $s\nu_2$ vibrational level. We use the branching ratios to compute the expected emission flux in a given line l with wavenumber center w from

$$F_l = \frac{A_l}{A_P + A_Q + A_R}\frac{hcw}{4\pi d^2}\sum_{P,Q,R}\frac{L_w}{hcw}N\alpha(T). \tag{4.17}$$

To calculate the net flux in a line we also need the amount of absorption. We require the relative intensity of the 10 μm dust emission feature at the frequency of each of the branches in order to compute the absorption line flux. We use mid-infrared spectra of the young stars DI Cep and DK Tau obtained by Hanner et al. (1998) to which they fit models of optically-thin silicate dust emission. From these spectra we calculate relative intensities of 0.52, 0.78 and 1.00 for the continuum at the 11.7, 10.7, and 9.7μm wavelengths of the aP, aQ, and aR lines for which $J_u = 3$, respectively. The intensities are normalized to the value on the aR branch as it is nearest to the peak of the 10 μm silicate feature. The observed continuum flux near the P-branch lines, $\sim$60 Jy, is turned into a luminosity at the source by multiplying by $4\pi d^2$, where d is the distance to NGC 7538 (2.65 kpc). We corrected for extinction using the 10

μm optical depth measurement of Willner et al. (1982), which implies $A_{11.7\mu m}$ $\sim$ 2.2 magnitudes and $A_{9.7\mu m} \sim 4.4$ magnitudes toward IRS 9.

The extinction-corrected luminosity $\sim 1.5 \times 10^{35}$ erg s^{-1} cm^{-1} at the position of the P-branch lines is scaled to the other branches according the values above. We assume throughout that the lines are sufficiently broad that they remain optically thin, leading to uncertainty in the covering factor. Only the product of column density and covering factor is meaningful under such circumstances, so we used the sum of this product for the two NH_3 components rather than the sum of the NH_3 column densities themselves in calculating F_l. We considered the possibility that the optically thin case might result in uncertainties propagating to the line fluxes, and to this end we carried out additional runs of `FITSPEC` in which we deliberately held the value of the covering factor fixed equal to 1. This resulted in a variation of the product of column density and covering factor of $< 20\%$ compared to allowing the covering factor to vary. We therefore retained the assumption of the optically thin case, and opted to use the lower value for the product of column density and covering factor of 8.52×10^{15} cm^{-2} in place of N in Equation 4.17. For $\alpha(T)$, we chose an excitation temperature of 200 K, consistent with the `FITSPEC` results for the -61.6 km s^{-1} component. Finally, the assumed extinction was re-introduced at the end of the calculation to realistically predict the line fluxes observed at Earth.

The line fluxes we compute are given in Table 4.6. The predicted fluxes are the differences of the strengths of the predicted emission and absorption

Table 4.6. Predicted fluxes for the aP, aQ, aR lines of ν_2 transitions of NH_3 ($J_u = 3$) and measured fluxes for the corresponding aP-branch lines from TEXES spectra.

	Predicted			Observed
K	F_{aP}	F_{aQ}	F_{aR}	F_{aP}
0	5.55	–	-1.94	1.80
1	2.64	0.03	-0.95	1.35
2	2.03	0.02	-0.73	–
3	2.11	-0.87	–	0.90

Note. — All fluxes are given in units of 10^{14} erg s^{-1} cm^{-2}. Positive flux values indicate net emission while negative values indicate net absorption in a given line.

components of each line and show an overall pattern of emission on the P branch, weak absorption or no lines on the Q branch, and absorption on the R branch. The P-branch fluxes compare favorably with the integrated line fluxes from our data implying that our explanation is at least plausible. This suggests that the dust and NH_3 are in close proximity to one another, if not actually mixed.

In the case of acetylene, we observed lines of the ν_5 Q and R branches at 12.5-13.7 μm and the $\nu_4 + \nu_5$ P branch near 7.5 μm. The ν_5 Q and $\nu_4 + \nu_5$ P-branch lines are of low S/N, due to telluric interference, but clearly lead to higher C_2H_2 column densities than the ν_5 R-branch lines when the observations are interpreted with the pure absorption model. The $\nu_4 + \nu_5$ lines appear to

require at least an order of magnitude more C_2H_2 than do the ν_5 R-branch lines. The radiative transfer effects discussed for NH_3 may also be relevant for C_2H_2, and may explain a part of the discrepancy between the C_2H_2 bands. But the bands are farther from the silicate feature and the wavelength separation between the branches of the C_2H_2 bands is smaller than for NH_3, so the effects should be smaller. The greater column density derived from the $\nu_4 + \nu_5$ lines could instead be due to the smaller extinction at 7.5 μm allowing a greater column of gas to be probed. This explanation was suggested by Evans et al. (1991) to explain a similar effect seen toward Orion IRc2, but it is difficult to understand how it could explain more than a factor $\sim$ 2 discrepancy, given the ratio of extinction at the different wavelengths.

We propose a different explanation for the variation between the column densities derived from the C_2H_2 ν_5 and $\nu_4 + \nu_5$ lines. Vibrational excitation caused by a ν_5 band photon is almost always followed by emission of another ν_5 band photon, although possibly in a different branch. (Due to the C_2H_2 selection rules, P- or R-branch absorption can be followed by either P- or R-branch emission, but Q-branch absorption must be followed by emission in the same branch.) However, 7.5 μm $\nu_4 + \nu_5$ absorption is most often followed by a $\nu_4 + \nu_5 - \nu_4$ transition at $\sim$ 13.7 μm to the ν_4 level. Since radiative decay from the ν_4 level is forbidden, the ν_4 excitation energy is then eventually lost in a collision. The result of this series of transitions is that there is little $\nu_4 + \nu_5$ emission canceling the $\nu_4 + \nu_5$ absorption, and these lines are probably reasonably well treated with the pure absorption model that we used. In

contrast, the ν_5 absorption lines may be largely cancelled by emission, leading to an underestimate of the C_2H_2 column density. The amount of re-emission into our beam is very dependent on the (unknown) source geometry, which determines whether our line of sight has more or less than the average for the gas surrounding the source. Assuming the $\nu_4 + \nu_5$ lines can be treated with a pure absorption model to give a fair measure of the abundance along our line of sight, the required correction to the column densities derived from the ν_5 lines is approximately a factor of 10. The required correction to the column densities of our other observed molecules may be similar.

4.5.4 Abundance Trends and Relative Ages

In Figure 4.13 we present a graphical comparison of the column densities of C_2H_2, HCN, NH_3, HNCO, and CH_4 we obtain toward IRS 9 with those derived for IRS 1 in Knez et al. (2009). Column densities for each of the two components with similar LSR velocities (-57 km s^{-1} and -61 km s^{-1}) toward each object are shown. We reach rather different conclusions for the two velocity components; IRS 1 appears to be clearly enhanced in all molecules except for HNCO at -57 km s^{-1}, whereas the column densities are essentially the same to within errors at -61 km s^{-1}. HNCO is the exception at the higher negative velocity, but we again stress that the cited values for IRS 9 are those preferred by our fitting program despite HNCO being an evident non-detection in our data. It is therefore not strictly reliable in comparison with the firm detection of HNCO toward IRS 1. Also, we do not have any evidence *a priori* that

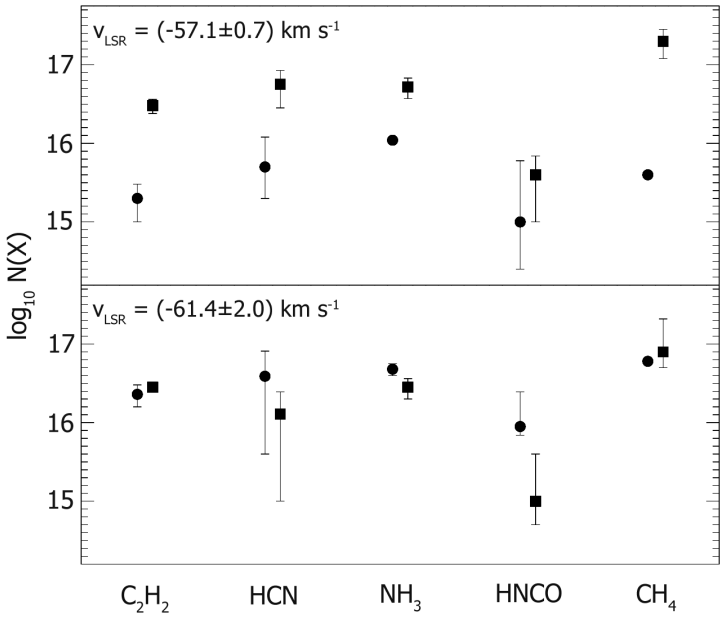

Figure 4.13 Log column densities for the main molecular species detected in this study for the two principal velocity components toward each target. IRS 9 values (this work) are shown as filled circles and IRS 1 values from Knez et al. (2009) as filled squares. The symbols for a given molecule are slightly offset for clarity.

these two velocity components are kinematically related. Knez et al. (2009) claim the two components seen toward IRS 1 are real but may not be separate; they may instead represent a non-Gaussian velocity distribution. If the latter situation is true, then such a velocity distribution may be systemic in other parts of NGC 7538. Regardless, the pattern that emerges from Figure 4.13 is suggestive of real differences in the gas-phase abundance of these molecules, which we attribute to differing thermal conditions in the environment of each object. If the molecular abundances in all phases were the same to begin

with, the gas-phase abundances we see at the present time are indicative of a difference in the relative ages of IRS 9 and IRS 1.

Several other lines of evidence also argue in favor of a younger age for IRS 9. First, a number of molecules (e.g., H_2O, CH_3OH, HCOOH, and OCN^-) are seen in the solid phase in the spectrum of IRS 9 that are either in the gas phase or apparently absent toward IRS 1. CO and CH_4 are seen both in the solid and gas phases, toward IRS 9 although the gas-phase lines probably form in the shocked outflow material. Second, a fairly strong ionizing radiation field exists near IRS 1, whereas our non-detection of the 12.8 μm line of [Ne II] discussed in Section 4.4.4 argues for a much weaker field toward IRS 9. In addition, IRS 1 has an ionized component to its outflow, probably driven by a wind; IRS 9 shows no similar outflow component. Third, the chemistry of IRS 1 resembles the "hot core" phase in which ices desorb from dust grains, leading to a short-lived ($\sim 10^4$-10^5 yr) high-temperature gas-phase chemistry and the synthesis of complex organic molecular species (van der Tak 2005). Some species, such as HNCO, are clear detections toward IRS 1 but appear to be absent toward IRS 9; we cannot rule out an intrinsic abundance effect in explaining this difference, but a simpler explanation is that the IRS 9 core is not yet sufficiently warm to evaporate it.

Knez et al. (2009) claim an age of $\sim 10^5$ yr for IRS 1 based on their chemical models. However, there is significant uncertainty in that value. Abundances of the molecules they detected indicate an age closer to $\sim 10^4$ yr, but for other molecules the chemical model predictions disagree with the observed

values, suggesting ages in the range of 2×10^3 to 2×10^6 yr. They explain this large range as a result of insufficiently detailed models. The models of Doty et al. (2002) predict enhancements in the abundances of C_2H_2, HCN, and CH_4 for temperatures above about 800 K at late times ($\geq 10^5$ yr); the enhancements are similar to those observed toward IRS 1, but the temperatures derived by Knez et al. (2009) are considerably lower than this. The fractional abundance of HCN in the Doty et al. model for 200 K quickly turns down at times $> 10^5$ yr whereas those of C $_2H_2$ and CH_4 increase through at least $10^{5.5}$ yr; N(HCN) is in fact slightly higher toward IRS 1 compared to IRS 9 by a factor of about 1.4. This may both support the argument that IRS 1 is the older object of the two and suggest an upper limit for its age, since the HCN abundance has not begun the predicted decline, but this conclusion is tentative since our value of N(HCN) for IRS 9 is determined by the singular detection of the ν_2 $R(16)$ line. Lastly, an additional age constraint from chemistry is provided by the non-detection of the molecule CCS by Hoffman & Seojin Kim (2011) in EVLA data, suggesting an age $\geq 10^4$ yr. Given that we find IRS 9 to be in an evidently more primitive chemical state than IRS 1, the upper limit to its age is probably $\sim 10^4$ yr. Detailed, robust chemical modeling, using our observations as inputs, may help more firmly constrain this value.

Our results, when considered in the context of the earlier work on IRS 1, qualitatively support a picture of an evolutionary sequence of cores in NGC 7538 consistent with the models of Elmegreen & Lada (1977) and Campbell & Thompson (1984) in which a wave of shock/ ionization fronts from a previous

generation of stars caused the sequential collapse of the cores that became IRS 1 and IRS 9, respectively. As the wave continues to propagate toward the southeast, it should initiate the collapse of cores found in progressively more primitive states. The 'IR-quiet' protostellar object NGC 7538 S is likely the next youngest object in the region after IRS 9 (Pestalozzi et al. 2006). Such a sequence, including NGC 7538 IRS 11 among the youngest objects, is supported by the maser observations of Hutawarakorn & Cohen (2003). It is tempting to assume that the wave has left the IRS 1 region already, but several newly-discovered submillimeter sources within 0.35 pc of IRS 1 reported by Qiu et al. (2011), presumably harboring forming intermediate- or high-mass stars, may be younger than IRS 9 and contemporaneous with NGC 7538 S. However, they may also be fragments, along with IRS 1, of a common progenitor. The star formation history of NGC 7538 may therefore be more complex than can be represented with a simple, monotonically-increasing series of protostellar ages.

4.5.5 Spatial Resolution of IRS 9

We checked whether IRS 9 is spatially resolved in TEXES data by obtaining spatial-spectral maps of IRS 9 and μ Cep, a mid-infrared- bright standard star that was used as a PSF reference for spatial deconvolution. To generate the maps, the TEXES slit was stepped across each object and spectral information gathered at each step, building up data cubes in which there are two spatial dimensions and one spectral dimension. Additional steps

were included at both the beginning and end of the scans to sample the sky for removal. The data are handled by our reduction pipeline in a manner substantially similar to the method of processing the nodded observations, treating a scan as a series of 2-D spectrograms.

IRS 9 and μ Cep were observed with identical scan parameters including scan direction, length, and step size, and were observed at comparable zenith angles. After reducing the raw data, different spectral windows were selected from which to form reconstructed images of each object by summing the data in the spectral direction. For IRS 9, we chose a window centered at about 745.88 cm^{-1}, near the position of the C_2H_2 ν_5 $R(6)$ line in the rest frame of the object. The window was 0.35 cm^{-1} wide. We selected this frequency range to search for spatial extent in the IRS 9 map as we noted absorption in the $R(6)$ line in nod-mode spectra. For the deconvolution reference, we chose a nearby spectral region apparently free from telluric and stellar photospheric absorption centered at 744.43 cm^{-1} and 0.25 cm^{-1} in width. The observed FWHM for each object was $0\farcs67$ for IRS 9 and $0\farcs63$ for μ Cep at each object's respective spectral setting. The deconvolution was performed using the maximum entropy method (Bryan & Skilling 1980; Narayan & Nityananda 1986), with results shown in Figure 4.14. The deconvolved image of IRS 9 in the C_2H_2 feature appears pointlike with some possible weak extension toward the NE. We do not believe this indicates that the envelope or other structure of IRS 9 is spatially resolved, and we carried out our other TEXES observations exclusively in nod mode.

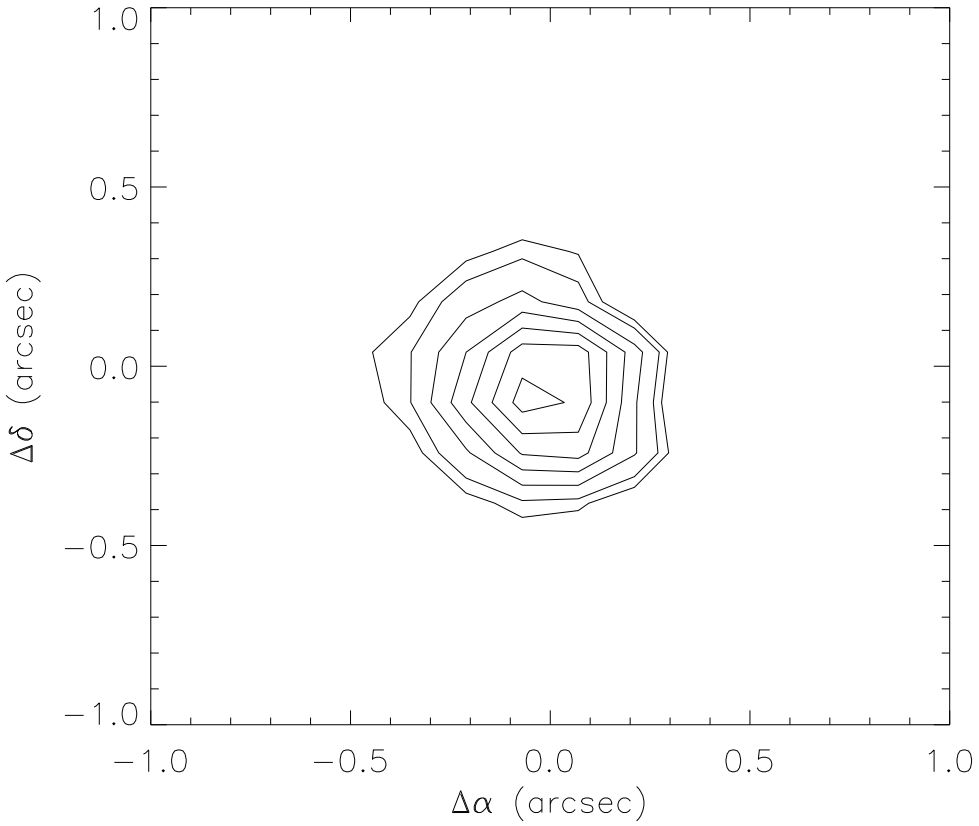

Figure 4.14 Contour plot of the TEXES scan map of NGC 7538 IRS 9 at 745.8 cm^{-1} after maximum entropy deconvolution. The PSF reference for the deconvolution was a scan map of the mid-infrared standard μ Cep made with the same parameters as the IRS 9 scan. North is up and east at left and contours are plotted at flux densities of 25, 50, 100, 150, 200, 250 and 300 Jy. The plot origin is approximately the location of the source peak intensity.

This approach to imaging and deconvolution should be interpreted cautiously. Poor seeing during a scan, for example, might distort the PSF on time scales shorter than the time required to scan across an object. However, we felt sufficiently convinced that IRS 9 presents itself as a point source in the mid-infrared that we did no further scans. Given the distance to NGC 7538 and the spatial resolution of our observations, we conclude that spatial structure of IRS 9 is unresolved on scales $\leq$ 2000 AU. This limit is consistent with the inferred sizes of disks detected around protostars with 10^3 - 10^5 $L_\odot$ (Patel et al. 2005, Schreyer et al. 2006, Rodríguez et al. 2007, Franco-Hernández et al. 2009, Galván-Madrid et al. 2010) and places a constraint on physical models of massive protostars in NGC 7538, which often include disks thought to be hundreds of AU in size (e.g., Sandell et al. 2009, Surcis et al. 2011).

4.5.6 A Structural Model Of IRS 9

Based on the conclusions we reach from kinematic indications in the data, we compose a toy model of the IRS 9 system to show its essential structure and a guess at the viewing geometry. This model is shown in Figure 4.15. In this view, the central, perhaps accreting object is shown in cross-section with a surrounding disk. The known bipolar outflow is indicated by the evacuated regions above and below the disk and by arrows showing the direction of the flow. A lighter shading above and below the disk represents the remaining envelope that has not been accreted or become part of the outflow. In order to account for seeing certain molecules under presumed LTE conditions while

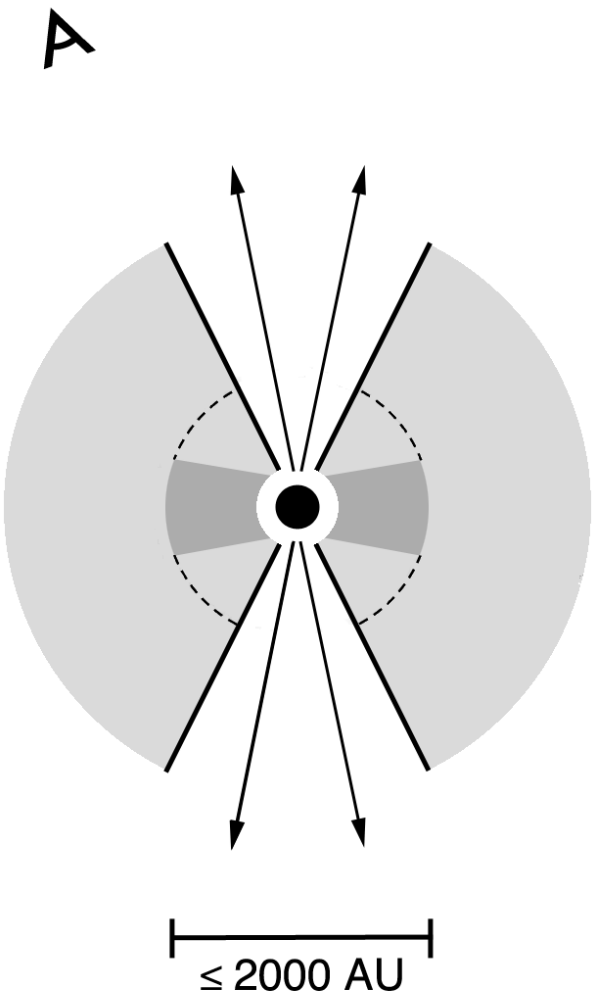

Figure 4.15 A cartoon rendering for a proposed model of NGC 7538 IRS 9 based on TEXES data. A central, embedded source (or sources) has at least partially cleared cavities in a bipolar outflow while significant dust remains in a spherical distribution (light gray shading). An inner disk may exist (dark gray shading). To account for our observations, the line of sight samples both scattered light in the outflow as well as a "dust photosphere" (dashed lines) where the dust becomes opaque at a mid-infrared wavelengths. The inferred viewing angle is shown, and a scale bar is provided based on the constraints discussed in Section 4.5.5. Note that the envelope and outflow cavities as depicted are not shown to this scale.

not observing the exciting source directly, we suggest a "dust photosphere" at a radius from the source at which the emission from the dust becomes optically thick, as indicated by dashed lines in the figure. It is this effective source of radiation against which we see most of our absorption lines. Since we do not resolve spatial structure in the molecular absorption region above the dust photosphere, we interpret the size scale constraint discussed in the previous section (2000 AU) as an upper limit to the radius of the dust photosphere itself. This value also represents an upper limit of the size of the disk, because a larger, optically-thick disk should have been detectable by virtue of its spatial extent. Our data do not permit a constraint to be placed on the size of the surrounding envelope or the outflow cavities.

The inclusion of a disk in this picture is tentative, given that the lifetime of disks around massive stars is thought to be particularly short, of order 10^{-4} the lifetime of the host star (Mann & Williams 2009). The evolutionary state of IRS 9 may be sufficiently early in its history, well before the embedded protostar is visible, to retain a disk. Knez et al. (2009) argue for a disk around IRS 1 whose surface is observed at near- grazing incidence; a sightline through the disk atmosphere is proposed to explain their observations.

We propose a viewing angle based on the following. First, the broad CO lines with their large, Doppler-shifted velocity separations suggest formation in the bipolar outflow. Second, the apparent radiative "pumping" of the NH_3 transitions, discussed in Section 4.5.3, requires continuum light from the direction of the dust photosphere. Third, the other molecular species we

observed in absorption also require a background continuum source, though the range of excitation conditions we derive is insufficient to definitively locate them in the envelope or the turbulent edge of the outflow cavity. The C_2H_2 combination mode may be an exception and could shock-excited in the outflow. Consequently, we place the viewing angle such that the observer is looking nearly along the edge of the outflow cavity and sees light from both sources. This model appears to account for all aspects of our observations in at least a qualitative way. It is also consistent with the conclusion of Sandell et al. (2005), based on HCO^+ $J = 2 \rightarrow 1$ observations showing deep, redshifted self-absorption, that the molecular outflow is viewed nearly pole-on.

4.6 Summary

We have presented the method and results of a study of the embedded high-mass protostellar object NGC 7538 IRS 9 and compared our findings to a similar investigation of the related object NGC 7538 IRS 1. We obtained high resolution, mid-infrared spectra of these objects in 46 ro-vibrational transitions of the fundamental bands of the molecules C_2H_2, CH_4, HCN, NH_3 and CO and a number of their isotopologues. We also detected two lines of the $\nu_4 + \nu_5$ combination mode of C_2H_2. From these observations we draw some broad conclusions.

1. IRS 9 appears to be a spatially-unresolved object on a scale of $\sim$2000 AU.

2. With the exception of CO, whose lines are saturated, we did not

observe ^{13}C isotopologues of any organic molecules. This may indicate a particularly large value of the $^{12}C/^{13}C$ ratio, or the ^{13}C isotopologue lines were simply below our threshold of detection.

3. There is no discernible, consistent trend in the abundance variations of C_2H_2, HCN, NH_3, and CH_4 with respect to either CO or H_2 between IRS 9 and IRS 1. Column density variations between the two objects are an order of magnitude or less in each case.

4. The observation of gas-phase CS absorption toward IRS 1 and the evident non-detection of sulfur-bearing species like OCS in the gas phase toward IRS 9 may reflect a real S abundance variation between the two objects but can also be explained by different thermal conditions in each case. A similar abundance discrepancy involving HNCO may indicate sufficiently low temperatures in the IRS 9 envelope to retain it as an ice and explain its detection in the solid phase by Gibb et al. (2004). If the abundances in all phases are actually comparable between the two sources, a relatively weak heating source is implied in the case of IRS 9. While this is at odds with the somewhat higher inferred abundances of the other molecules toward the warmer environment of IRS 1, the suggested sightline in that direction through a disk atmosphere subjects those molecules to direct irradiation by protostellar UV. This may drive photochemistry that lowers abundances of certain molecules as they are converted to other kinds.

5. However, the relative abundances of various molecular species with respect to CO and H_2 can also be explained by variations in the CO/H_2 ratio

or the gas-to-dust ratio between the two objects. Choosing between these interpretations would require better determining the CO and H_2 abundances toward both objects.

6. Lines of many species observed toward IRS 9 have higher Doppler b values than those toward IRS 1, resulting in lines toward IRS 9 being less saturated than those toward IRS 1.

7. Given the non-detection of Ne II in our data and the continuum flux density at the expected wavenumber of the line (70±10 Jy), we find a corresponding upper limit of $\sim 10^{45}$ photons s^{-1} for the Lyman continuum flux in IRS 9. This value is well below both the expected flux of a ZAMS star with the same luminosity and the ionizing flux of IRS 1 ($> 10^{48}$ photons s^{-1}).

8. The observed pattern of emission and absorption components of ammonia lines in our spectra can be explained by a non-LTE radiative transfer effect involving "pumping" of lines on the R-branch by light from the 9.7 μm silicate dust feature. Predictions of the strength of this effect compare reasonably well with observed fluxes in P-branch lines.

9. Our data are consistent with a simple model of the IRS 9 system in which the sightline probes both a high-speed outflow and a quiescent envelope illuminated from behind by a "dust photosphere" such that line formation depth is wavelength-dependent. The possibility of seeing the turbulent flow along the wall of the outflow cavity is supported by the broad, blueshifted wing of the C_2H_2 $\nu_4 + \nu_5$ combination band that may arise in a shock. A disk is

included in the model given the system's inferred young age and the presence of a kinematically-indicated disk toward the (presumably) older IRS 1.

10. Observed differences in the abundance of various molecular species toward IRS 9 and IRS 1 imply an upper limit to the age of IRS 9 of $\sim 10^4$ yr, whereas IRS 1 may be an order of magnitude older. This conclusion is consistent with the triggered star formation models of Elmegreen & Lada (1977) as applied to NGC 7538 by Campbell & Thompson (1984) and others.

Chapter 5

Discovery of a Pseudobulge Hidden Inside the "Box-Shaped Bulge" of NGC 4565

J. Kormendy and J. Barentine, *Astrophysical Journal* **715**, L176 (2010)

John Kormendy contributed the idea and text of this paper, and wrote the analysis software that was used. I obtained imagery from data archives, calibrated the data, and performed the analysis.

5.1 Introduction

Figure 5.1 compares the prototypical Sb galaxies NGC 3351 and NGC 4565. NGC 3351 is more nearly face-on and shows three main components – a bulge, a bar, and a disk. In contrast, NGC 4565 is edge-on; it shows only two components, a box- shaped bulge and disk. As long as we thought that boxy structure was a secondary property of normal bulges, a galaxy morphologist (Sandage 1961) would just use the bulge-to-total luminosity ratio $B/T \simeq 0.4$ (Simien & de Vaucouleurs 1986) to classify NGC 4565 as an Sb. However, we now know that "boxy bulges" are not bulges at all; rather, they are edge-on bars (Combes & Sanders 1981). So the SBb galaxy NGC 3351 shows a disk, a bar, and a bulge, but the SBb galaxy NGC 4565 shows only a disk and a bar.

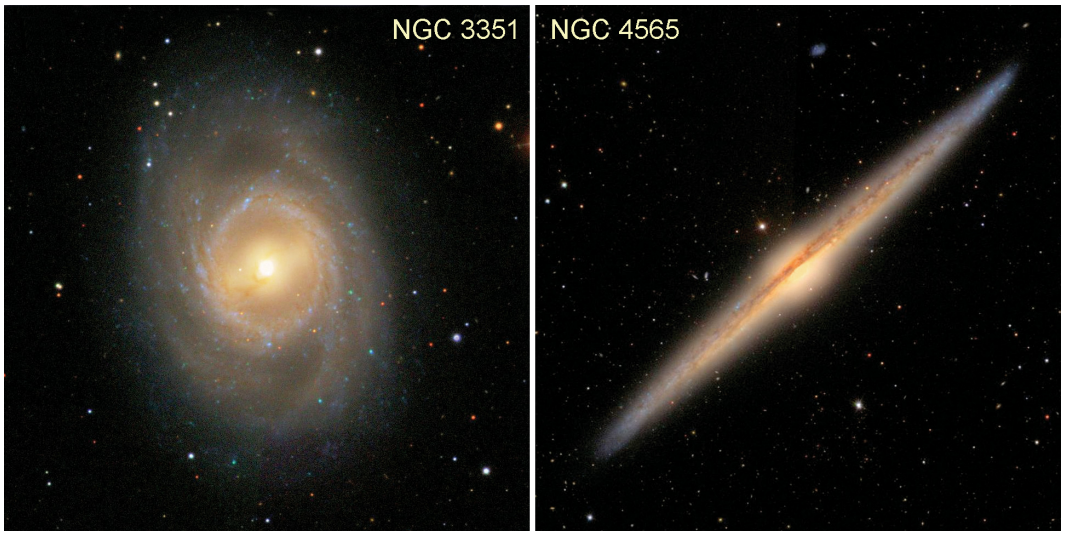

Figure 5.1 (left) NGC 3351 and (right) NGC 4565 in *gri* composite color images from the Sloan Digital Sky Survey (courtesy `http:// www.wikisky.org`). Simien & de Vaucouleurs (1986) estimate that $B/T = 0.1$ in NGC 3351; this is smaller than $B/T \simeq 0.4$ in NGC 4565 in part because they do not include the bar as part of the bulge.

Where is the bulge in NGC 4565?

Boxy bulges like that in NGC 4565 are a fundamental feature of edge-on disk galaxies (Sandage 1961; Buta et al. 2007). Their identification as edge-on bars is a well known result. The Combes & Sanders (1981) N-body model demonstration that bars heat themselves vertically by a combination of buckling instabilities and resonant star scattering has been confirmed and extended many times (Combes et al. 1990, Pfenniger & Norman 1990, Pfenniger & Friedli 1991, Raha et al. 1991, Athanassoula & Misiriotis 2002a, Athanassoula 2005, Shen et al. 2010 and many others). Cylindrical rotation is observed in N-body bars and in boxy bulges (Kormendy & Illingworth 1982, Jarvis 1990,

Shaw et al. 1993, Bettoni & Galletta 1994, Fisher et al. 1994, D'Onofrio et al. 1999, Falcón-Barroso et al. 2004) but not in classical, elliptical-galaxy-like bulges (Illingworth & Schechter 1982, Kormendy & Illingworth 1982, Binney et al. 1990, de Zeeuw et al. 2002, Verolme et al. 2002, Copin et al. 2004, Emsellem et al. 2004) this further cements the connection between boxy bulges and edge-on bars. Finally, a splitting of gas rotation velocities in edge-on boxy bulges (a "figure 8" shape of spectral emission lines) also is a robust signature of gas flow in an edge-on bar (Kuijken & Merrifield 1995a, Merrifield 1996, Merrifield & Kuijken 1999, Bureau & Freeman 1999). There is little doubt that the "boxy bulge" of NGC 4565 is not the real bulge of the galaxy. Does the galaxy contain a bulge at all? That is, does it contain a dense, central component that we would identify as a bulge in addition to the bar if the galaxy were seen face-on?

We care for two reasons, both involving galaxy formation:

Background: Early galaxy evolution was dominated by hierarchical gravitational clustering of density fluctuations that resulted in galaxy collisions and mergers (White & Rees 1978); these scrambled disks into ellipticals (Toomre 1977). Enormous energy has been invested in studying hierarchical clustering; there is little danger that the picture is fundamentally wrong (Binney 2004). However, it is incomplete. Recent work has established that hierarchical clustering is gradually giving way to a complementary suite of evolution processes that shape *isolated* galaxies. They evolve by rearranging energy and angular momentum; one consequence is the growth of central

components that masquerade as classical bulges but that, in general, formed slowly ("secularly") out of disks (see Kormendy 1993 and Kormendy & Kennicutt 2004 for reviews). We call them "pseudobulges" to distinguish them from merger remnants. They come in at least two varieties. As reviewed above, "boxy bulges" are believed to be edge-on bars. Our Galaxy contains one (Dwek et al. 1995). Another variety is grown out of disk gas that was transported inward by nonaxisymmetries such as bars; we call them "disky pseudobulges" here, because thery are often highly flattened, but we emphasize that they are not always flat (Kormendy 1993, Kormendy & Kennicutt 2004; Section 5.2). Then:

Reason 1: Confidence in our conclusion that the boxy center of NGC 4565 is an edge-on bar would be increased if we also observed a (pseudo)bulge as we do in face-on galaxies (Fig. 5.1). As long as face-on and edge-on galaxies appear to show physical differences, we cannot be sure that we understand them.

Reason 2: If the box in NGC 4565 is a bar, then it is part of the disk and B/T is smaller than we thought. If in addition the galaxy contains a pseudobulge and not a hidden classical bulge, then B/T is even smaller – possibly zero. This is hard to understand in the context of hierarchical clustering, which essentially always makes substantial bulges in giant galaxies (see Peebles & Nusser 2010 and Kormendy et al. 2010 for theoretical and observational reviews).

5.2 Dissecting NGC 4565 Using Mid-Infrared Images

Fundamental plane correlations tell us the low-luminosity bulges are small and dense, not large and fluffy (Djorgovski & Davis 1987, Faber 1987, Bender et al. 1992, Kormendy et al. 2009). So a (pseudo)bulge in NGC 4565 could only hide behind the dust lane. We use *Spitzer Space Telescope* IRAC archive images at 3.6 μm and 8 μm to look through the dust and measure the light profile of NGC 4565. The images are shown in Figure 5.2, The contrast and brightness ("stretch") in the top panel emphasize the boxy pseudobulge. A lighter stretch in panel (b) reveals two new features that are hidden at optical wavelengths. First, the galaxy shows an "inner ring" like those associated with bars (Sandage 1961, Buta et al. 2007). The 3.6 μm image shows starlight at the reddest wavelength that is free from dust emission, and the wavelength is long enough so that dust absorption is small. Still, there is a small danger that the ring looks dark inside because of absorption. But the 8 μm image in panel (c) shows PAH emission from dust. The ring is bright, implying active star formation. But there is no emission from inside the ring except at the center. We conclude that NGC 4565 is an almost-edge-on SB(r) galaxy. It is similar to NGC 2523, which is shown in Figure 5.2(d) scaled to match the ring size in NGC 4565 and with an orientation similar to the one that we infer for NGC 4565, with the bar almost along the line of sight. Our understanding of vertical bar thickening implies that NGC 2523, oriented as in Figure 5.2(d) but seen more nearly edge-on, would resemble NGC 4565.

The second new feature shown in Figure 5.2(b) proves to be the "miss-

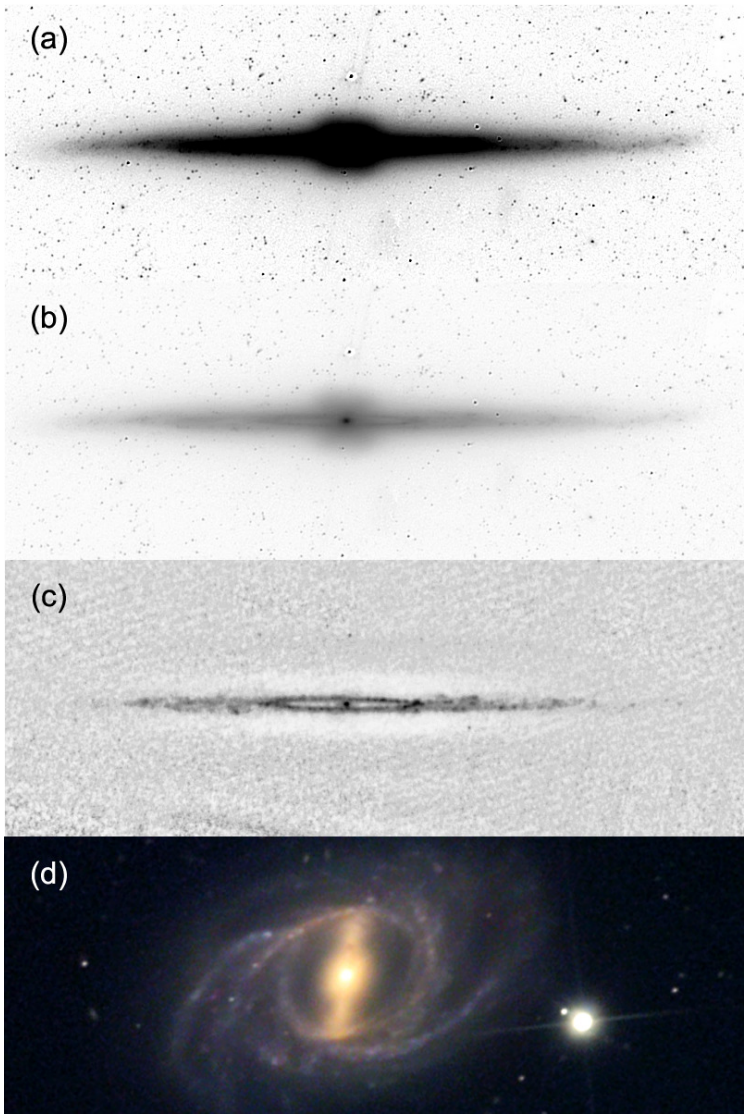

Figure 5.2 (a and b) PSF-deconvolved Spitzer/IRAC 3.6 μm negative images of NGC 4565 shown at different stretches that emphasize (a) the boxy bar and (b) an inner ring and pseudobulge. The newly detected pseudobulge is the tiny bright spot at the galaxy center. Its scale height is smaller than that of the outer disk. (c) Spitzer/IRAC 8 μm negative image showing PAH emission and therefore star formation from the inner ring and outer disk.

ing" pseudobulge. It is the tiny bright region at the galaxy center. It is compact – as expected – and it appears clearly distinct from the much lower surface brightness bar. To check whether it really is distinct from the bar and to see whether it is a small classical bulge or a pseudobulge, we measured its surface brightness profile along the major and minor axes of the galaxy. The minor-axis profile is shown in Figure 5.3. *Spitzer* resolution is poor, so we supplemented the *Spitzer* profile at small radii by measuring a *Hubble Space Telescope* (HST) NICMOS F160W archive image. Brightness cuts were extracted along the major and minor axes of NGC 4565. We used the minor-axis profile only on the side of the galaxy that is less affected by absorption. All profiles were zeropointed to the K_s bandpass of the 2MASS Large Galaxy Atlas (Jarrett et al. 2003).

The minor-axis brightness profile is plotted in Figure 5.3 against $r^{1/4}$ so the profile of a classical bulge is nearly a straight line. The profile consists of three separate segments, an outer halo, an intermediate-r profile that describes the boxy structure (see Kormendy & Bruzual 1978), and the dense central component. The latter components have concave-downward profiles, so they are Sérsic (1968) functions with indices $n \ll 4$. We therefore made a three-component decomposition into an outer exponential and two Sérsic functions. The intermediate-radius profile of the boxy bar proves to be exponential, $n = 1$. The central profile has $n = 1.33 \pm 0.12$ along the minor axis and $n = 1.55 \pm 0.07$ along the major axis. Both values are robustly less than 2. Classical bulges have $n \gtrsim 2$ whereas most pseudobulges have $n \lesssim 2$ (e. g.,

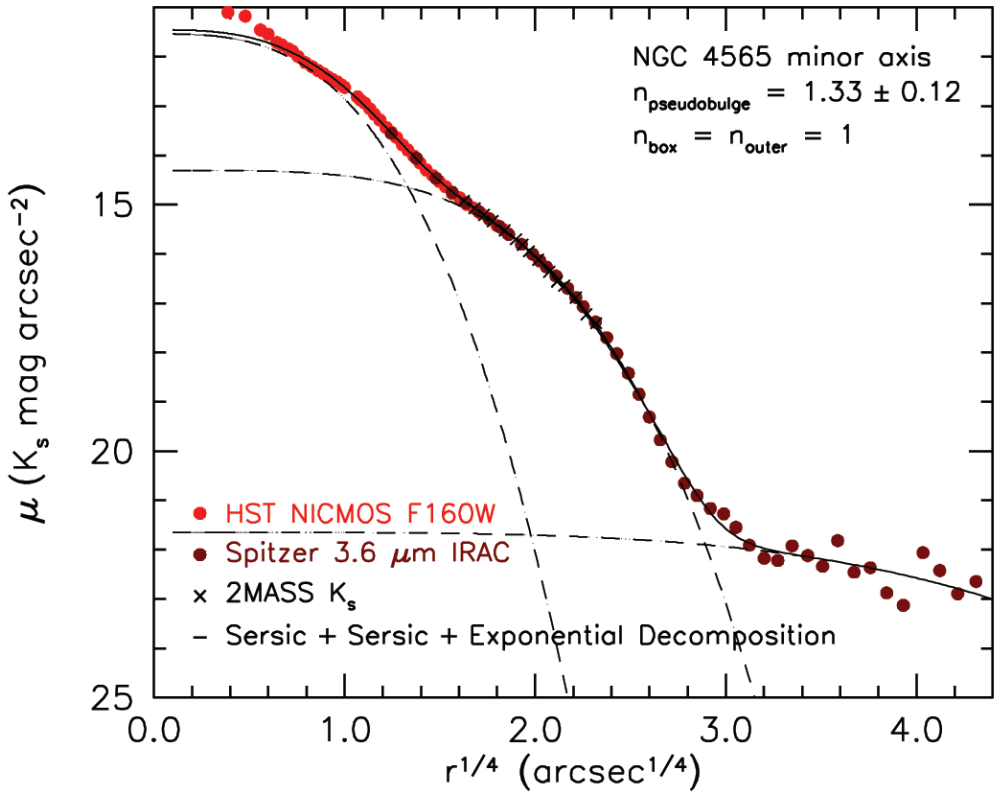

Figure 5.3 Minor-axis profile of NGC 4565 from HST NICMOS F160W (red points) and Spitzer IRAC 3.6 μm (brown points). A profile (black crosses) calculated from the 2MASS Large Galaxy Atlas image (Jarrett et al. 2003) provides the K_s-band zeropoint. The dashed lines show a decomposition of the profile into components in order of increasing radius: a Seyfert nucleus (Ho et al. 1997) or nuclear star cluster that is not included in the fit, the pseudobulge (Sérsic), box-shaped bar (Sérsic), and outer halo (exponential, but our data do not constrain the functional form). The solid line is the sum of the components.

Fisher & Drory 2008). Thus both the boxy structure and the inner bright region are pseudobulges, and NGC 4565 contains both subtypes of pseudobulge. However, the disky pseudobulge – the central component – is not flat: it has an axial ratio of ~ 0.8 to 0.9.

Remarkably, the smallest scale height of any structural component in the galaxy is that of the pseudo*bulge*. The decomposition in Figure 3 gives its exponential scale height as $\sim 1\farcs2 \simeq 90$ pc (we adopt a distance to NGC 4565 of 14.5 Mpc from Wu et al. 2002). We measure an exponential scale height of boxy bar plus disk of $10\farcs5 \simeq 0.74$ kpc. The scale heights of the thin and thick disk have been measured by many authors (e. g., van der Kruit & Searle 1981, Jensen & Thuan 1982, Shaw & Gilmore 1989 and Wu et al. 2002, who also tabulate previous results). Seven measurements of the thick disk scale height average to $14\farcs6 = 1.03$ kpc with a dispersion of $2\farcs3$. Eight measurements of the scale height of the thin disk average $8\farcs0 = 0.56$ kpc with a dispersion of $0\farcs9$. The middle component in Figure 5.3 has a scale height intermediate between that of the thin and thick disk, as expected, given that it includes thin disk, thick disk and boxy bulge along the line of sight. But the pseudobulge has a scale height that is smaller than that of the thin disk.

Simien & de Vaucouleurs (1986) find a bulge-to-total light ratio of $B/T = 0.4$. However, B refers to the boxy bar – not the pseudobulge within. Figure 5.2 shows that the pseudobulge is much less luminous than the boxy structure. If NGC 4565 were seen face-on, what we identify as a box-shaped bulge would be recognized as a bar and would not be included in the bulge

light inventory. Previously measured B/T ratios of edge-on galaxies with box-shaped bulges are therefore overestimated.

For the central pseudobulge, we measure a K_s magnitude of 9.09 ± 0.15. Jarrett et al. (2003) find that the total K_s magnitude of the galaxy is 6.060 ± 0.017. So the (inner) pseudobulge-to-total luminosity ratio is $PB/T = 0.061^{+0.009}_{-0.008}$, similar to $B/T = 0.1$ in NGC 3351 (Fig. 1). We see no sign of a classical bulge component.

Indeed, a normal classical bulge with $B/T \sim 0.06$ in V band would have an absolute magnitude of $M_{V,\mathrm{bulge}} \simeq -18.4$ and an effective radius of $r_e \simeq 0.7$ kpc $= 10''$ (Kormendy et al. 2009). It would be very obvious. We conclude that $B/T \ll 0.06$. In other words, NGC 4565 is effectively bulgeless.

5.3 Conclusion

The interpretation of boxy bulges in edge-on Sb galaxies as bars is more believable if we also find (pseudo)bulges like those associated with bars in face-on Sb galaxies. Our discovery of a pseudobulge in NGC 4565 that is distinct from the boxy bar increases confidence in our picture of secular evolution.

Furthermore, B/T ratios in edge-on galaxies with boxy bulges are smaller than previously believed. In NGC 4565, the detection only of a central pseudobulge means that we see no sign of a major merger remnant. Moreover, NGC 4565 rotates at 255 km s^{-1} interior to the outer warp (Rupen 1991). NGC 4565 has grown very massive while remaining a pure-disk galaxy. We

do not know how this can happen in a Universe dominated by the dynamical violence of hierarchical clustering.

Chapter 6

A Photometric Study of the Two Pseudobulges in the "Boxy Bulge" Galaxy NGC 5746

J. Barentine and J. Kormendy, *Astrophysical Journal* **754**, 140 (2012)

This chapter was published as a follow-on to the study of NGC 4565 presented in Chapter 5. The idea, analysis, and writing are mine alone. Kormendy is credited as an author for the use of his analysis and plotting software and in courtesy for his supervision of my work.

6.1 Introduction

The ΛCDM paradigm is based on the observation of dark matter concentrations ("halos") into which baryons fall, cool, and form stars. Galaxies are built by the hierarchical merging of smaller halos in a bottom-up fashion (White & Rees 1978). This implies frequent "major" mergers in the early Universe between objects of comparable mass. Mergers are understood to scramble disks into elliptical galaxies (Toomre 1977, Schweizer 1990) and are accompanied by cold-gas dissipation and starbursts in the smaller galaxies but not in the biggest galaxies that can hold onto X-ray gas (see Kormendy et al.

2009 for a review). The rate of major mergers peaked at $z \sim 1.2$ (Ryan et al. 2008), and since that time, the Universe has been in transition from merger-dominated galaxy evolution to slow ("secular") internal evolution (Kormendy et al. 2009).

In spite of the large amount of merger violence at early times, almost 2/3 of the most massive galaxies in the nearby universe (field environments like the Local Group) show no classical bulge at all (Kormendy et al. 2010, Fisher & Drory 2011; see Peebles & Nusser 2010 for a review). Thus most field galaxies show no sign that they experienced a major merger at least since the time of the merger rate peak. It is difficult to understand how stellar disks that were already in place at $z \sim 1$ survived until today without being converted into – or at least augmented by – a classical bulge (Kormendy et al. 2010). Here, it is important to note that we do not have the freedom to postulate bulges whose properties make them easy to hide. Bulges satisfy well defined "fundamental plane" parameter correlations (see Kormendy & Bender 2012 for the most recent version). Low-luminosity classical bulges are small, but they have high surface brightnesses and are described by Sérsic functions (Sérsic 1968) with indices $n \simeq 2.5$ that make them hard to hide and easy to identify. Thus we can be confident that, while ΛCDM performs well on large scales, the large fraction of nearby, giant galaxies which show little evidence of major mergers presents a challenge to our understanding of galaxy evolution on 10-kpc scales (e. g., Abadi et al. 2003, Governato et al. 2010, Kormendy et al. 2010, Peebles & Nusser 2010).

The magnitude of this challenge is underestimated if effectively bulgeless galaxies are undercounted because pseudobulges are mistaken for classical bulges. Prior to the development of the secular evolution picture (especially Kormendy 1993, Kormendy et al. 2009), this routinely happened even for face-on galaxies with dynamically disky pseudobulges (e. g., NGC 4736; see the above references). But identification of classical bulges in edge-on galaxies is particularly tricky. "Box-shaped bulges" such as that in NGC 4565 (Kormendy & Barentine 2010) are made of old stars and clearly bulge out above and below the edge-on disk plane. It is understandable that, in early papers, they were thought to be classical bulges which happen to have a box-shaped peculiarity in their structure. But now we know that box-shaped bulges are galaxy bars that are seen edge-on (Combes & Sanders 1981, Combes et al. 1990, Pfenniger & Norman 1990, Pfenniger & Friedli 1991, Raha et al. 1991, Athanassoula & Misiriotis 2002b, Athanassoula 2005, Shen et al. 2010). Bars form by gravitational instabilities in galaxy disks. The above papers show that, once a bar is well formed, it buckles vertically and rapidly turns into a thick structure that looks like a box-shaped bulge when seen edge-on. Heating of stars whose vertical motions are in resonance with the bar density wave further contributes to the thick, boxy- distorted structure. Also, a splitting of gas rotation velocities in edge-on boxy bulges (a "figure 8" shape of spectral emission lines) is a robust signature of gas flow in an edge-on bar and further cements our view of these boxy structures as bars (Kuijken & Merrifield 1995b, Merrifield 1996, Merrifield & Kuijken 1999, Bureau & Freeman 1999). Thus,

a "boxy bulge" in an edge-on object would be identified as the galaxy's bar if it were seen more face-on. Since it is really a part of the disk, we call such structures "boxy pseudobulges". This means that the true classical-bulge-to-total luminosity ratios of galaxies such as NGC 4565 are much smaller than the values $\sim 1/3$ that are measured (e. g., Simien & de Vaucouleurs 1986) when the boxy structure is identified as the bulge.

We demonstrated this effect for the nearly edge-on spiral NGC 4565 in Kormendy & Barentine (2010). Its center has a boxy photometric signature previously identified as a classical bulge (Simien & de Vaucouleurs 1986). But we found that this component is well fitted by a Sérsic function with index $n = 1$. This demonstrates that it does not have the characteristics of a merger-built classical bulge (Kormendy et al. 2009, Fisher & Drory 2008). It is consistent with a bar seen nearly end-on. Mid-infrared observations penetrate the thick midplane dust, revealing the true central component in this galaxy. It is a pseudobulge whose scale height is smaller than that of the outer disk. Its small pseudobulge-to-total (PB/T) ratio, $0.061^{+0.009}_{-0.008}$, means that the disk and its secularly-built structures completely dominate this galaxy. NGC 4565 is a massive galaxy; its rotational speed is $\sim$255 km s^{-1} interior to its outer warp (Rupen 1991). This result is especially hard to understand because it is easier to make bulgeless galaxies via feedback mechanisms (Governato et al. 2010) when the resulting galaxy is a dwarf. Thus NGC 4565 and galaxies like it are problematic in the context of hierarchical assembly models.

We know that galaxies like NGC 4565 are not rare (Kormendy et al.

2010, Fisher & Drory 2011). Previous efforts to measure B/T ratios of galaxies by way of light profile decompositions may have resulted in overestimates of the bulge contribution in galaxies at moderate to high inclinations. This could mask the true number of essentially bulgeless galaxies in the Universe. The problem of apparently bulgeless galaxies becomes more acute because most decomposition work is now done in an automated fashion and in two dimensions. It is difficult for these analyses to cope with patchy internal obscuration. Here, we use carefully constructed one-dimensional light profiles to address this problem.

The aim of this paper is to determine for NGC 5746, i. e., an additional normal, edge-on disk galaxy with a boxy bulge, the fraction of the total galaxy luminosity that is contributed by the boxy structure and by any additional, disky pseudobulge near the center. This requires making a clear photometric distinction between structural components in circumstances compromised by strong dust absorption. To this end, we determine the pseudobulge-to-total luminosity ratio PB/T and the pseudobulge scale height. In Section 6.2 we describe the selection of this galaxy and outline the method by which we constructed minor- and major-axis light profiles from photometric data spanning a range of wavelengths from the optical to the mid-infrared. We present the profiles in Section 6.3 and compare them with previous studies. The galaxy's PB/T ratio is calculated using these profiles, after subtracting fits to the other structures seen in the profiles. We show that NGC 5746 is a massive disk galaxy in which the bulge does not dominate the light profile at any radius.

We summarize our results in Section 6.4.

6.2 Method

6.2.1 Target Selection

We searched various lists of edge-on galaxies and applied the following selection rules: candidate objects must (1) be nearby (distance $D \lesssim 75$ Mpc); (2) be highly inclined (inclination $i \gtrsim 85°$); (3) show minimal, if any, indication of recent interaction with other galaxies; (4) have available data over a wide range of wavelengths and resolutions; and (5) be relatively free of dust. NGC 5746 ($\alpha_{2000.0}$=$14^h44^m56\overset{s}{.}005$, $\delta_{2000.0}$=+01°57′17″.06) meets essentially all of these requirements. It is classified as an SAB(rs)b? in the Third Reference Catalog of Bright Galaxies (RC3; de Vaucouleurs et al. 1991). Measurements reported in the literature give a mean distance of 27.6 Mpc with a 1σ dispersion of 2.5 Mpc (Tully 1988; Willick et al. 1997; Rand & Benjamin 2008; Tully et al. 2008; Springob et al. 2009a; Springob et al. 2009b; Tully et al. 2009). The galaxy is inclined to the line of sight by 83.9° and has a rather large maximum circular velocity of 318.5 ± 9.8 km s^{-1}. The inclination and velocity were obtained from HyperLEDA[1] and the circular velocity is corrected for inclination. While not as highly inclined as we would prefer, the observed angle has the benefit of reducing the effect of the dust in the central region. This galaxy also has the largest amount of archival photometric data of the candidate objects we considered.

[1]The Lyon-Meudon Extragalactic Database; `http://leda.univ-lyon1.fr/`

NGC 5746 has been shown previously to contain kinematic evidence for the presence of a bar (Kuijken & Merrifield 1995b, Bureau & Freeman 1999), manifesting itself in the apparent box-like shape of the "bulge" in optical images. We confirm the existence of the bar in observations reported here. The question remains: if the apparent bulge is actually the photometric signature of the bar, then where is the bulge in this galaxy?

6.2.2 Data and Calibrations

In many edge-on disk galaxies other than S0's, extinction at optical wavelengths is very large along sightlines through the disk midplane and could hide structures with scale heights smaller than that of the dust. Observations in the near- and mid-infrared can help overcome this problem. To see through the dust, we used 3.6 μm images made with the Infrared Array Camera (IRAC; Fazio et al. 2004) aboard the *Spitzer Space Telescope* to measure the minor- and major-axis light profiles NGC 5746. The spatial resolution of IRAC is insufficient to extend the light profiles to the smallest radii, so in the innermost region we augmented the profile with H-band data from the *Hubble Space Telescope* Near Infrared Camera Multi Object Spectrometer (NICMOS; Thompson 1994). At large radii, where dust is less of a problem and maximizing the signal-to-noise ratio (S/N) becomes more important, we used data from two large sky surveys: the Two Micron All-Sky Survey (2MASS; Skrutskie et al. 2006) and the Sloan Digital Sky Survey (SDSS; York et al. 2000). Filters, pixel scales, and fields of view of each telescope and instrument are

Table 6.1. Properties of Data Sources

Telescope	Instrument	Field Of View (′)	Scale (″ pix^{-1})	Filters
Spitzer 0.85m	IRAC	5.22 × 5.22	1.2 × 1.2	Channel 1 (3.6μm)
HST 2.4m	NICMOS	0.3 × 0.3	0.076 × 0.075	F160W (1.6μm)
2MASS 1.3m	2MASS Camera	8.5 × 8.5	2.0 × 2.0	K_s
SDSS 2.5m	Imager	13.51 × 8.98[a]	0.4 × 0.4	g, r, i

[a]Dimensions are given for a single image frame.

given in Table 6.1. We briefly summarize the calibration procedures for each data source.

The IRAC data were reduced by the Spitzer Science Center (SSC) using software pipeline version S14.0.0. The reduction steps include subtracting the bias level and dark current, flat fielding, and performing sky subtraction. We used the final, mosaicked versions of the images containing all pointings of the telescope at a given location and time of observation.

NICMOS data were calibrated using version 4.4.0 of the CALNIC reduction pipeline (Bushouse 1997). The code applies basic corrections to the data, including dark current subtraction, corrections for detector non-linearity, and flat fielding. After all images in an "association" of data are processed in this manner, a second stage creates mosaics of overlapping images and subtracts a scalar background ("sky") value. However, proper sky subtraction of images of extended sources is severely impacted by the instrument's small field of view. NGC 5746 overfills the NICMOS frame such that at no location is

the true sky level reached; the automated data reduction procedures typically overcorrect for sky by subtracting a value higher than the true sky level, resulting in negative pixel values in the corners of frames. We accounted for this by locating NICMOS frames from other programs taken as close in time as possible to our galaxy observations, typically within one day, and measuring real sky values from frames that did not contain large, extended objects. The "sky" value recorded in the headers of our galaxy images removed by CALNIC is added back to the pixels in our images and the measured sky value subtracted off.

The 2MASS data were calibrated nightly during survey operations by observing standard star fields at regular intervals. Photometry of the standard stars was used to derive the extinction coefficients and photometric zeropoints in each of the three survey passbands as a function of time throughout a given night. The survey observations did not permit absolute calibration of the 2MASS photometric system. However, Cohen et al. (2003) offer a calibration tied to Vega on the "Cohen-Walker-Witteborn" system from computation of relative spectral response curves. To place our fluxes on the 2MASS system, we used the zeropoints computed by the reduction pipeline and written into the image headers.

Photometric data from SDSS were calibrated using the PHOTO pipeline (Lupton et al. 2001) which gathers astrometric data, obtains the extinction and photometric zeropoint on the night the data were collected, renders the drift-scan images into a series of postage stamps, and estimates the flat field vectors,

bias drift, and the sky level for each. Corrected frames are produced using this information. We did not make use of SDSS-generated PSF or Petrosian-fitting photometry, but rather performed our own surface photometry on corrected frames.

6.2.3 Surface Photometry

Images from a given source were first prepared by correcting for any background gradients and cleaning contaminating pixels from sample regions. Systematic variations in the background were removed with the IRAF[2] task `mscskysub`, which fits a polynomial or spline of arbitrary order to a 2D surface. We specifically used second-order polynomials. Contaminants consisting of cosmic rays, foreground stars, and background objects were removed by computing the median of pixels in a user-defined region around the source; pixels varying from the median by more than 1.5σ were replaced by the median. This cleaning was done carefully by hand, and individual, problematic pixels were replaced on a case-by-case basis. Extended objects were treated by interpolating over pixels in a user-defined box around an object with a second-order polynomial and replacing the pixel values in the box with those of the fit. This approach works well for moderately bright stars but breaks down for the brightest objects; the affected pixels were edited out of the extracted 1D light profiles by hand.

[2]IRAF is distributed by the National Optical Astronomy Observatory, which is operated by the Association of Universities for Research in Astronomy (AURA) under cooperative agreement with the National Science Foundation.

We performed surface photometry on NGC 5746 by taking rectangular cuts along its minor and major axes, supplemented where possible with ellipse fits of isophotes that served as a check on the cuts. We generally avoided ellipse fitting in favor of cuts because the isophotes are far from elliptical over a large range of radii, and ellipse fits tend to fail in the presence of significant midplane dust absorption. For each data source, we investigated a range of cut widths over different radius ranges in order to construct light profiles of the highest possible signal-to- noise ratio (S/N) at large radii while preserving resolution at small radii. Consequently, the cut boxes effectively had stairstep shapes tapering to progressively narrower widths at smaller radii; the effective dimensions and orientations of these cut boxes are illustrated in Figure 6.1, in which they are superimposed over an optical image of the galaxy. The sky level in each image was determined by sampling regions at large radii as free from contamination by foreground and background objects as possible. 1D profiles were extracted by block-averaging pixels along the short dimension of a cut box in IRAF. In order to mitigate the effect of midplane dust absorption where it interferes with the minor-axis light profile, we excised points by hand from the profile that were obviously impacted adversely by the dust. For the major-axis profile, we defined the cut box parameters to carefully avoid the dust lane (see Figure 6.1 for placement).

All photometric data were given an absolute calibration by tying them to the 2MASS K_s points in order to place them on a common photometric system. To assemble a composite light profile from a number of data sources,

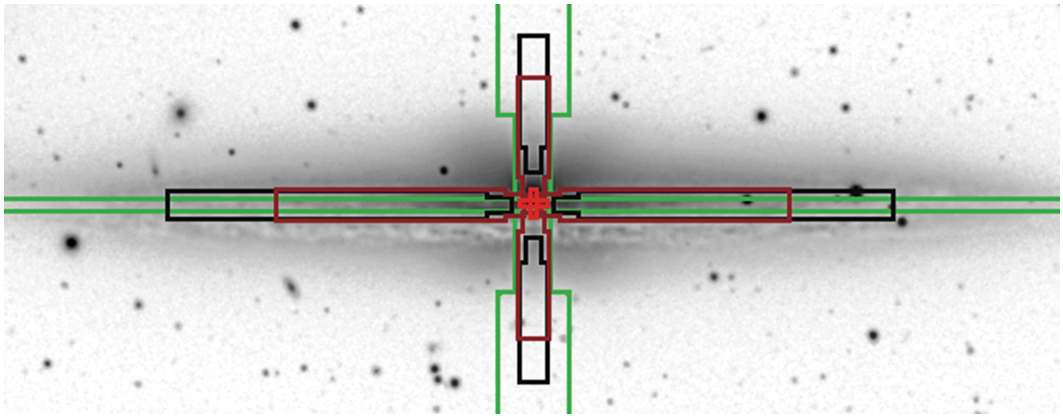

Figure 6.1 An 8100 s R-band image of NGC 5746, rendered with an inverted colormap, onto which has been superimposed a set of colored overlays representing the effective sizes and shapes of the cut boxes used in performing surface photometry. The image has been rotated such that the major axis is aligned with the image rows. The colors of the boxes indicate the data sources: SDSS (green), HST NICMOS F160W (red), 2MASS K_s (brown), and Spitzer IRAC 3.6 μm (black), and match the colors of the data points in the minor- and major- axis light profiles presented in Figures 6.3 and 6.4. The radial extent of the boxes reflects the radial range of points plotted in the light profiles.

arbitrary constants were added to light profiles generated for each source individually to bring data points into coincidence with those of the 2MASS profile over the radius regime in which they overlap. Profiles tend to plateau at small radii for data sources with poor spatial resolution; these points were trimmed from the final profile of each object. Additionally, points were trimmed at large radii at which the instrumental sensitivity rapidly diminishes, otherwise leading to an underestimate of the surface brightness. We present the final versions of the light profiles for each object with symbol colors corresponding relatively to the wavelengths of the data sources to help guide the eye.

6.2.4 1D Radial Profile Decompositon

After extracting the profiles, we decomposed them into three components: a Sérsic function for the central pseudobulge, another Sérsic function for the boxy bulge, and an outer exponential representing the disk. The choice of an exponential is consistent with the van der Kruit & Searle (1981) model of the disk as a locally isothermal sheet. All components were fitted with a χ^2-minimization algorithm employing the simplex optimization method. Our fitting code allows for the simultaneous decomposition of a given profile into a single Sérsic and single exponential function with five free parameters: the radius and surface brightness of the bulge (R_n, μ_n), the radius and surface brightness of the disk (R_d, μ_d), and the Sérsic index, n.

We considered the possibility that our observations might reach a limiting magnitude sufficient to reveal the presence of an extended halo around NGC 5746, thereby informing the choice of the functional form of the fit to the largest radii in our profiles. We searched for evidence of an extended halo in a deep (8100 s) R-band image of NGC 5746 obtained with the WIYN 0.9m telescope and S2KB CCD camera at Kitt Peak National Observatory over two observing seasons in 2011-12. Brightness contours of the image are shown in Figure 6.2. Despite contamination of the faintest isophotes from the bright nearby star HD 129827, we do not find any convincing detection of a halo to a limiting surface brightness of $\sim$23 mag arcsec^{-2} in K_s. Thus we do not include an explicit halo component in the light profile fits at large radii. Specific details of the fit, including its functional form, are not critical to the analysis

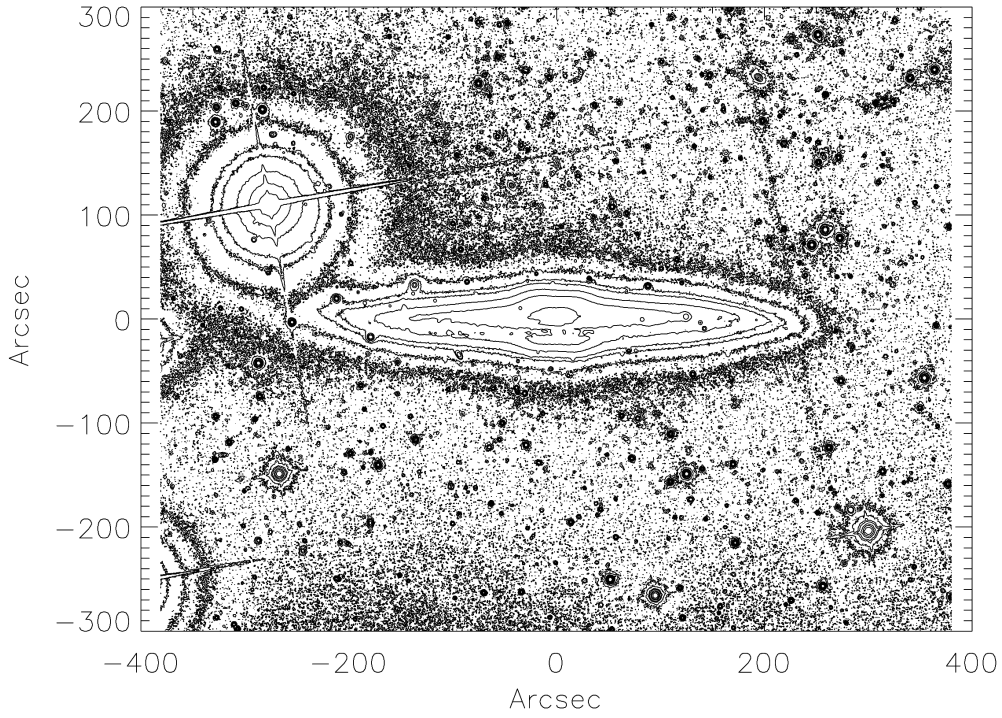

Figure 6.2 A brightness contour plot of NGC 5746 made from the 8100 s R-band image of NGC 5746 in Figure 6.1. The contours are at -9, 10, 30, 75, 125, 325, 800, and 4000 ADU above the mean sky background as measured $\sim 10'$ from the center of the galaxy along its minor axis. The isophotes nearest the sky level do not show any obvious indication of an extended halo. The bright star at upper left is HD 129827.

presented here. We also did not include a component representing a central Seyfert nucleus or a nuclear star cluster in the fit at the smallest radii. A bright central point was seen in our NGC 4565 data but we did not attempt to fit it, whereas we do not see a corresponding point in the NGC 5746 images.

We subtracted the disk exponential and box Sérsic fits from a given profile, leaving the profile of the pseudobulge itself. Once the pseudobulge light profiles were obtained for both axes, the total luminosity of the pseudobulge was obtained by integrating the light in each direction and adding the results. A proper comparison of light profiles of the minor and major axes of an edge-on galaxy with a boxy pseudobulge should take into account the fact that the box typically has an axial ratio other than 1. As a result, a feature seen at radius r along the minor axis will be seen at radius $(b/a)r$ along the major axis, where a and b are the sides of the box. Our major-axis light profiles are shifted in radius by a factor of 1.4, the axial ratio of the box measured from the SDSS *gri* composite image, placing the profiles on a common spatial scale.

6.3 Results

The minor- and major-axis light profiles we obtain for NGC 5746 are shown in Figures 6.3 and 6.4, respectively. A simultaneous decomposition of the box and exponential disk yielded Sérsic indices of $n = 1.16 \pm 0.18$ along the minor axis and 1.78 ± 0.25 along the major axis. Fitting the box along the major axis is complicated by the presence of a bright ring, described below, seen in the infrared imagery. Interior to this ring, at radii 1.8 arcsec$^{1/4} \lesssim r^{1/4}$

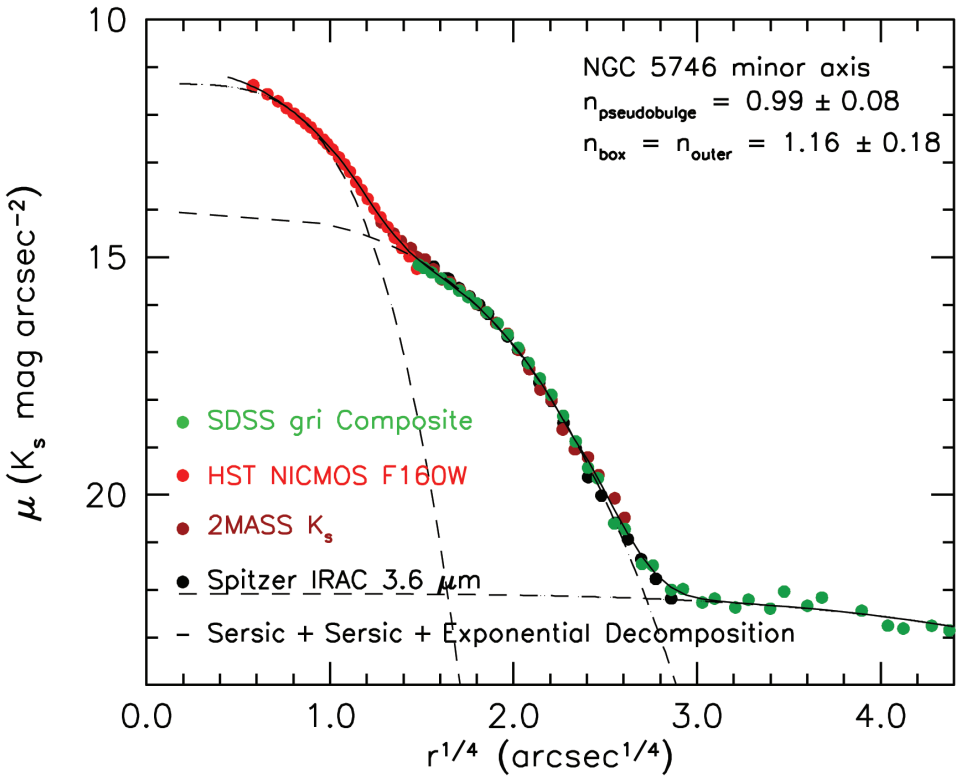

Figure 6.3 Minor-axis light profile of NGC 5746 from the following data sources: combined SDSS *gri* (green points), HST NICMOS F160W (red points), 2MASS K_s (brown points), and Spitzer IRAC 3.6 μm (black points). A Sérsic-Sérsic-exponential decomposition is overplotted as dashed lines, representing the inner pseudobulge, boxy bar, and outer halo, respectively. The solid line represents the sum of these three components.

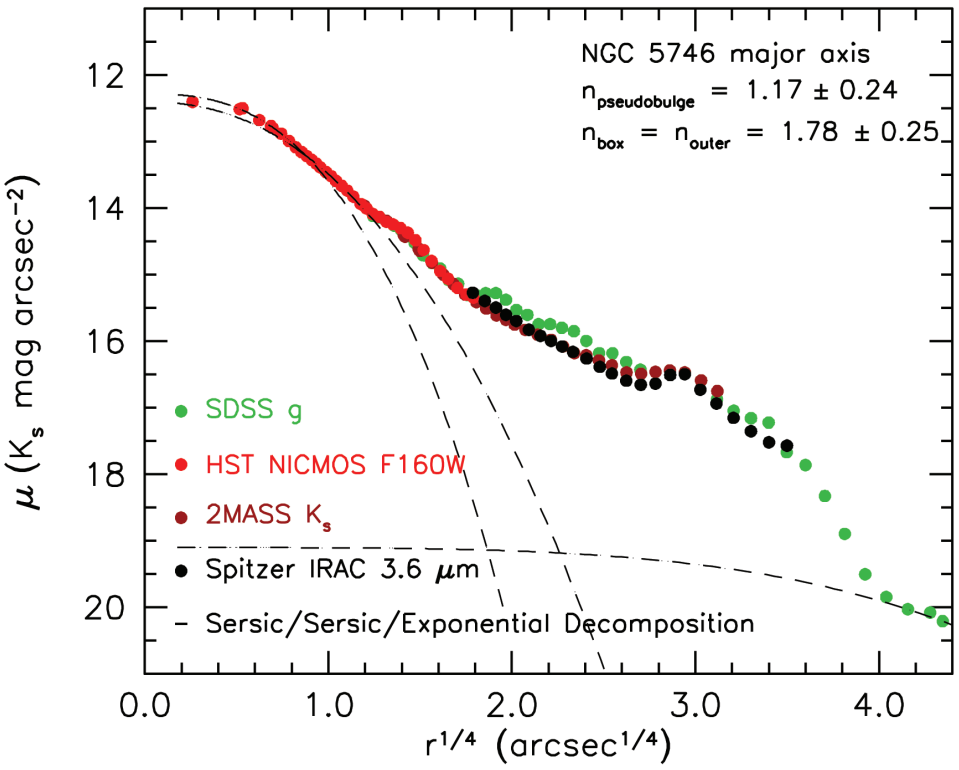

Figure 6.4 Major-axis light profile of NGC 5746. The data sources are the same as in Figure 6.3. A Sérsic-Sérsic-exponential decomposition is overplotted as dashed lines.

$\lesssim$ 2.7 arcsec$^{1/4}$, the infrared flux is low relative to the optical flux.

The central pseudobulge was fitted with a single Sérsic component over only the inner $\sim 2''$, corresponding roughly to the angular extent of the NICMOS data. The Sérsic indices of the central pseudobulge are 0.99 ± 0.08 along the minor axis and $n = 1.17 \pm 0.24$ along the major axis. Prior evidence of a bar in NGC 5746 (Bureau & Freeman 1999) is bolstered by our finding of $n < 2$ for the box. Therefore, the true bulge in NGC 5746 is a pseudobulge, con-

sistent with both our results for NGC 4565 and the observational definition in Fisher & Drory (2008) that bulges with $n \lesssim 2$ are pseudobulges, not classical bulges. It is also evident that, as in NGC 4565, the apparent "boxy bulge" of NGC 5746 is in fact a bar seen nearly end-on. The emerging picture of NGC 5746 is that viewed face on, it would have a bar and an inner ring much like those inferred in NGC 4565.

The fits give additional information about the nature of the central pseudobulge. The best Sérsic fits yield a scale height of $0\farcs74 \pm 0\farcs10$ along the minor axis and a scale length of $0\farcs64 \pm 0\farcs20$ along the major axis. At our adopted distance to NGC 5746, these correspond to 100 ± 13 pc and 86 ± 27 pc, respectively. From the fit to the boxy bar plus the disk, we compute a scale height of 755 ± 145 pc. We measured the thick disk scale height as a function of radial distance along the major axis from the IRAC 3.6 μm data; the cuts we used are shown superimposed on the IRAC image in Figure 6.5. Again, the cut box widths vary to preserve resolution at small radii along the major axis and S/N at larger radii. The mean of eight measurements of the thick disk scale height at $r > 38''$ (51 kpc) is $8\farcs6 \pm 0\farcs7$ (1.2 ± 0.1 kpc). For comparison, we found for NGC 4565 a pseudobulge scale height of 90 pc, a boxy bar plus disk scale height of 740 pc, and a thick disk scale height of 1.03 kpc.

We integrate the fits to the various components of the light profiles and find a mean value and 1σ scatter of 0.136 ± 0.019 for the pseudobulge-to-total ratio (PB/T) of NGC 5746. In Table 6.2, we show the Sérsic n values measured

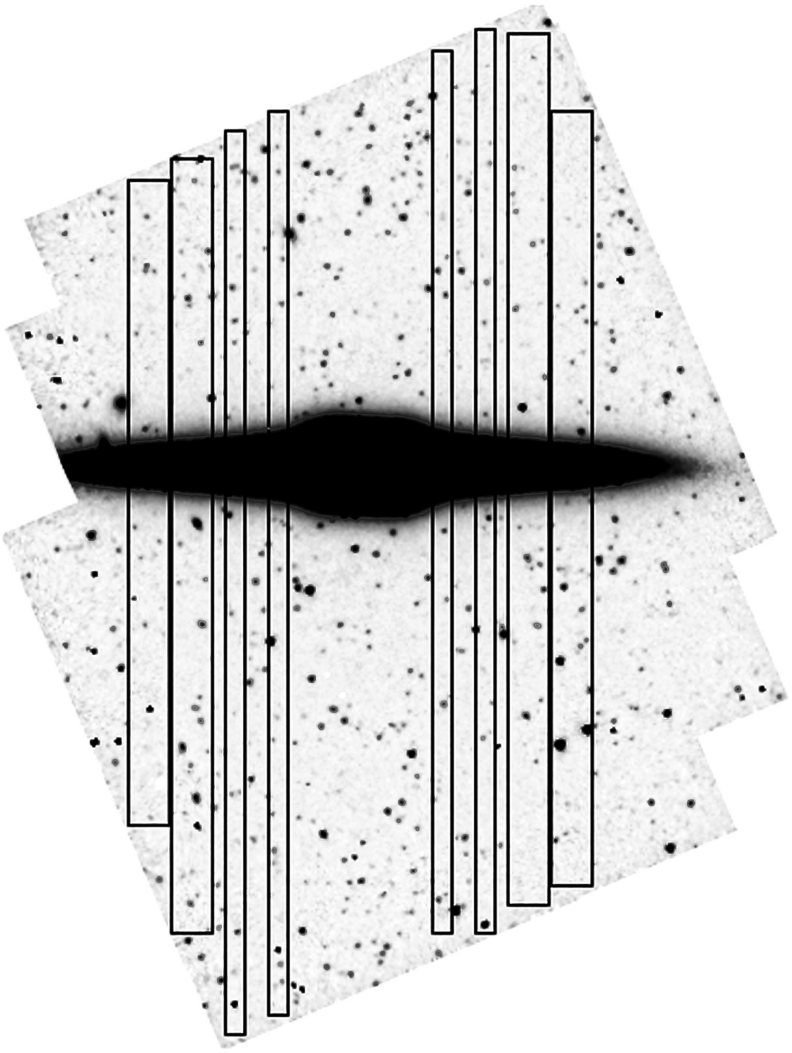

Figure 6.5 The IRAC 3.6 μm image of NGC 5746, rendered with an inverted colormap, showing the dimensions and extent of the cut boxes used to extract minor axis light profiles for determination of the thick disk scale height as a function of radial distance along the major axis. The image has been rotated such that the major axis is aligned with the image rows.

Table 6.2. Sérsic Indices and Pseudobulge-To-Total (PB/T) Ratios For NGC 4565 and NGC 5746

Designation	v_c[a](km s^{-1})	Box Sérsic n		Pseudobulge Sérsic n		PB/T
		Minor	Major	Minor	Major	
NGC 4565	255±10[b]	1	–	1.33±0.12	1.55±0.07	0.061±0.010
NGC 5746	318.5±9.8[c]	1.16±0.18	1.78±0.25	0.99±0.08	1.17±0.24	0.136±0.019

[a]Maximum circular velocity, corrected for the inclination angle.

[b]Rupen (1991)

[c]Kuijken & Merrifield (1995b)

along both minor and major axes and the resulting PB/T ratio for this galaxy along with those reported for NGC 4565 in Kormendy & Barentine (2010) for purposes of comparison. Measurements of the index of the boxy component of the apparent bulge and the true (pseudo)bulge are given along with the consequent pseudobulge-to-total (PB/T) ratios. The pseudobulge in NGC 5746 contributes relatively little light to the galaxy. Balcells et al. (2007), following a similar procedure, quote a Sérsic index of $n = 1.55 \pm 0.14$ and a B/D ratio of 0.1 for this galaxy. While we recognize the care with which their measurements were made, we note that in neither case was allowance made for a nuclear component which could introduce uncertainty into values of the Sérsic n. However, the differences are not enough to affect our fundamental conclusion, one which the measurements of Balcells et al. support – the bulge in NGC 5746 is a pseudobulge.

Figure 6.6 shows the 3.6 μm and 8 μm IRAC images along with the

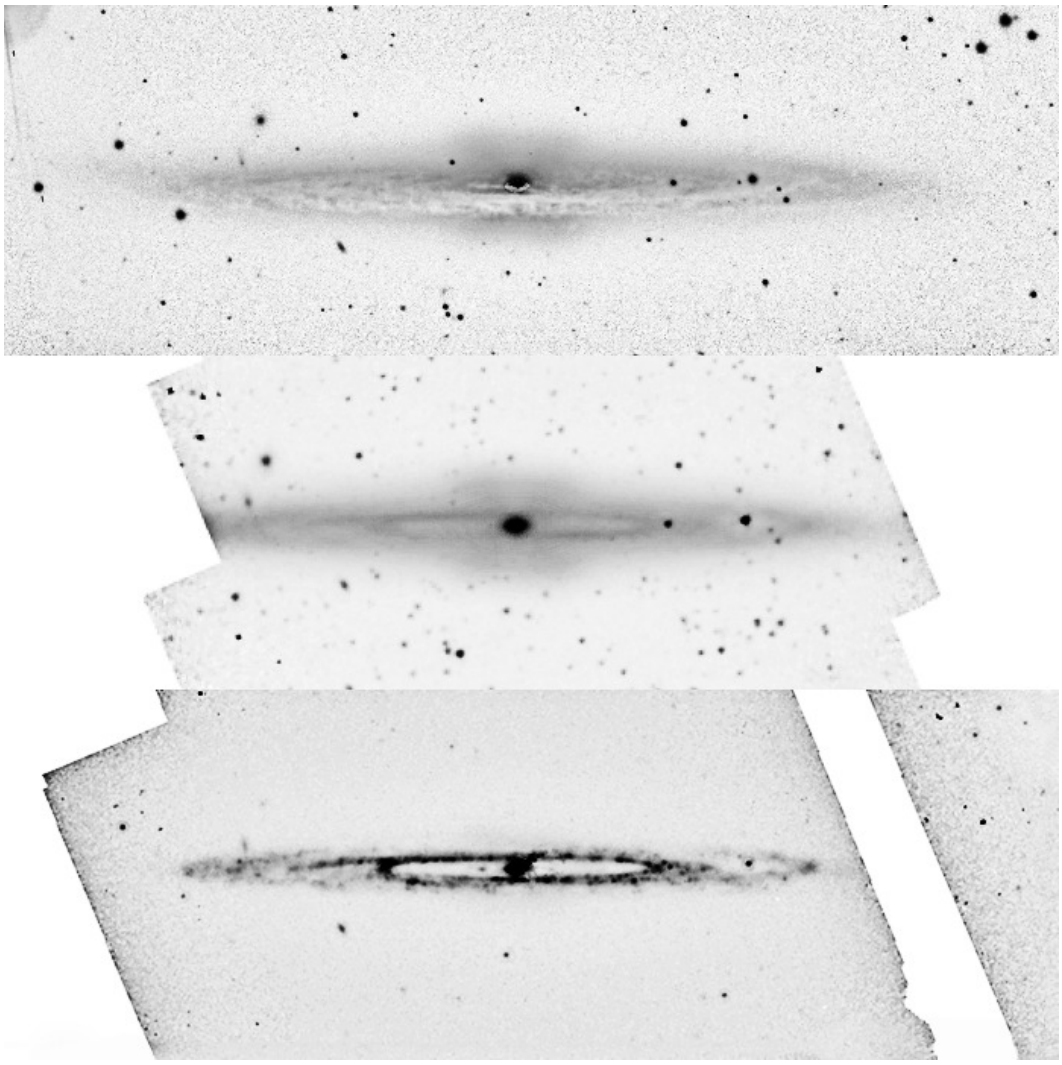

Figure 6.6 Three views of NGC 5746 from the optical to the mid-infrared: the sum of SDSS *gri* (top), *Spitzer* IRAC 3.6 μm (middle), and IRAC 8 μm (bottom). The images have been rotated such that the major axis is aligned with the image rows. Irregularities in the IRAC images are caused by boundaries of the mosaicked regions used to make the composite image in each case.

SDSS *gri* composite for optical context, each individually stretched to emphasize the inner ring. Inspection of the 3.6 μm image clearly indicates a bright

ring with an inner radius of $\sim$57″ (9.1 kpc) and an average radial width of 10″ (1.6 kpc) as measured at the tangent points. The ring is clearly present in Figure 6.4 as a shallow rise in the major-axis light profile between 2.7 arcsec$^{1/4}$ $\leq r^{1/4} \leq$ 3.2 arcsec$^{1/4}$ and is slightly brighter at its outer edge than inner edge, particularly at optical wavelengths. In the IRAC 8 μm band, associated with emission by polycyclic aromatic hydrocarbons (PAHs; Léger & Puget 1984, Allamandola et al. 1985, 1989, Puget & Léger 1989, Tielens et al. 1999, 2000), the ring is considerably brighter, indicating a high rate of star formation (Verstraete et al. 2001, Peeters et al. 2004, Wu et al. 2005, Calzetti et al. 2007, Bendo et al. 2008).

Another slight rise in the major-axis profile exists at much smaller radii, from 1.2 arcsec$^{1/4}$ $\leq r^{1/4} \leq$ 1.6 arcsec$^{1/4}$ (280 pc $\leq r \leq$ 880 pc). This feature appears to be real as three of the four data sources trace it; the 2MASS data are not useful at small radii and therefore do not cover the radius range of this shallower feature. Brightness contours of the inner 12.″9 $\times$ 12.″9 (1.7 kpc $\times$ 1.7 kpc) of the NICMOS image are shown in Figure 6.7; the isophotes transition from elliptical to disky over the radius range indicated by the bump in the major-axis light profile. This may indicate the presence of a nuclear disk partially obscured by dust. In the region defined by elliptical isophotes, the profile is nearly linear in $r^{1/4}$ until it turns over at the limit of the NICMOS resolution. It is well fitted by a Sérsic function with an index very similar to that observed along the major axis of NGC 4565. We believe this is additional evidence indicating the presence of a central pseudobulge.

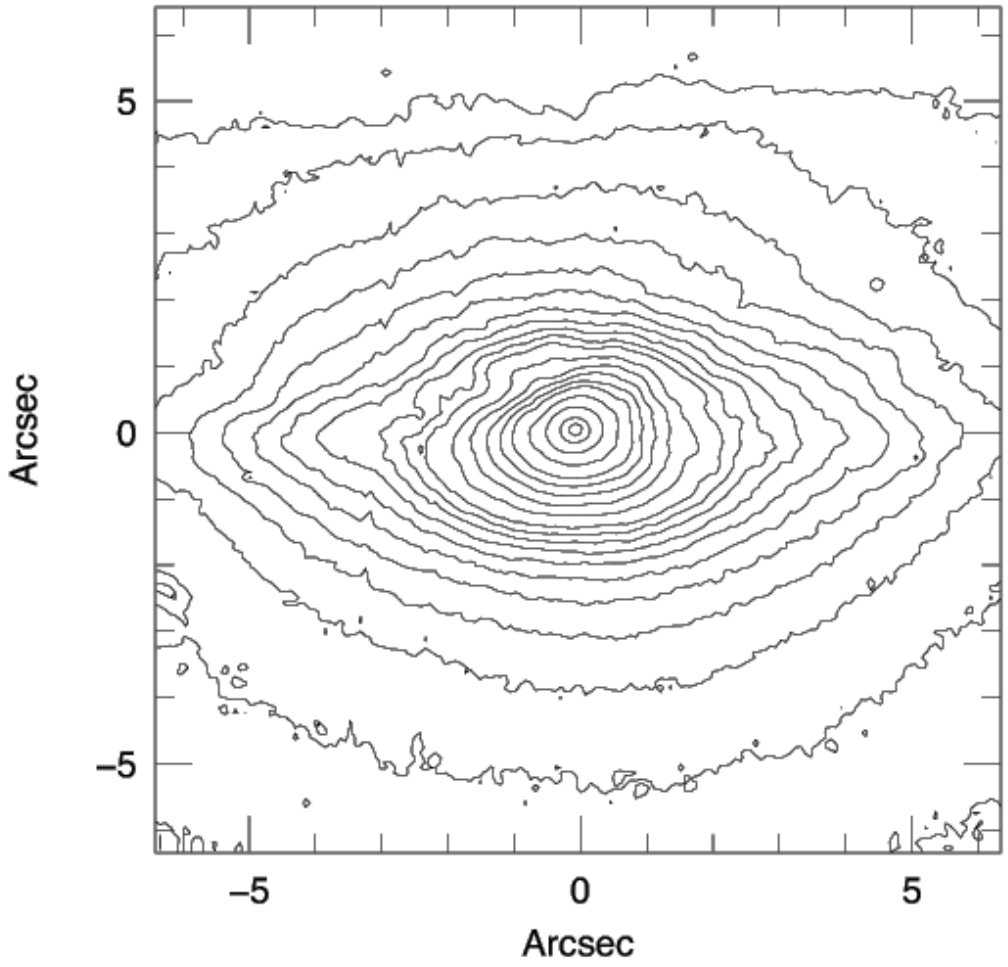

Figure 6.7 A brightness contour plot of the nuclear region of the NICMOS H-band image of NGC 5746. The image has been derotated such that the galaxy's major axis lies along the rows of the diagram and was cleaned of contaminants before the contours were generated. The contours are at pixel levels of 0.1, 0.5, 1, 1.5, 2, 2.5, 3, 3.5, 4, 4.5, 5, 6, 7, 8, 9, 10, 12, 15, 20, and 25 ADU after sky subtraction. The vertical and horizontal scales are arranged such that the coordinate origin corresponds to the highest pixel value in the frame. Deformation of the isophotes in the upper-left quadrant is due to absorption by the dust lane.

The major-axis light profile is consistently brighter in the SDSS optical colors between the inner bright feature and the ring over an approximate radius range of 1.8 arcsec$^{1/4} \leq r^{1/4} \leq$ 2.7 arcsec$^{1/4}$ (1.4 kpc $\lesssim r \lesssim$ 7.1 kpc). The bluer light again dominates from 3.2 arcsec$^{1/4} \leq r^{1/4} \leq$ 3.4 arcsec$^{1/4}$ (14.0 kpc $\lesssim r \lesssim$ 17.9 kpc). This is roughly the radius range between the outer edge of the ring and what in the 8 μm IRAC image appears to be the inner edge of a set of spiral arms. In both cases, interior to the ring and between the ring and spiral arms, the apparent blue color excess in the light profile results from starlight evenly distributed in the plane of the disk. PAH emission in the inner ring contributes as much flux in the near- and mid-IR as the starlight does, whereas in the case of the spiral arms, there are insufficient IR data at large radii to determine the relative contribution of stars and PAH emission. The last IRAC data point in Figure 6.4 suggests the profile is rising in the mid-IR as it crosses the spiral arms and would again dominate in this region if data existed. Seeing relatively unextincted starlight in the region between the inner ring and the bar is consistent with removal of gas and dust from this region, and should be observable in other inner-ring galaxies.

6.4 Summary

Using archival data from multiple ground-based surveys and space-craft missions, we carried out surface photometry on the almost-edge-on spiral galaxy NGC 5746 and extracted 1D light profiles along the galaxy's minor and major axes. The profiles were decomposed into multiple Sérsic and expo-

nential functions corresponding to the central pseudobulge, the boxy bar, and the disk. We computed Sérsic indices for the pseudobulge, finding $n = 0.99 \pm 0.08$ and 1.17 ± 0.24 for the minor and major axes, respectively, and an axial ratio of $\sim$0.85. The degree of flattening of this pseudobulge is consistent with the amount we found previously for the pseudobulge in NGC 4565. We further note that the central pseudobulge is the most compact component of the light profiles, with a scale height of only 100 ± 20 pc. Near- and mid-IR imagery reveals the presence of an inner ring of inner radius 9.1 kpc and width of 1.6 kpc, another structure whose presence is consistent with secular evolution. The ring and a set of outer spiral arms are clearly indicated in the major axis light profile as well. All this implies that NGC 5746 is a well developed, nearly-edge-on SB(r)bc galaxy.

Thus NGC 5746, like NGC 4565, is a giant galaxy whose structure shows no recognizable remnant of a recent major merger. Such galaxies are common in field environments. It remains difficult to understand how they form in a hierarchically clustering universe.

Chapter 7

Summary and Future Directions

In this chapter we recount the narrative of the role of gas in the evolution of galaxies and their contents, review the lessons learned as a result of the work described in this thesis, and speculate as to where future research on this subject may lead.

7.1 To understand galaxies, follow the gas

Gas is the ultimate source of fuel for galaxies' growth and evolution as the constituent material of stars. Once organized into stars, it is transformed from its most primitive state, hydrogen, to the heaviest naturally-occurring element, uranium, through a variety of nuclear reaction routes. The death of massive stars in core-collapse supernovae results in the transfer of heavy elements into the ISM in the debris from those explosions. As highly energetic events, supernovae also inject significant amounts of mechanical energy into the ISM, encouraging the collapse and fragmentation of giant molecular clouds that initiates the next cycle of star formation. As an isolated system, the average metal content of a galaxy is expected to steadily increase with time as its supply of hydrogen wanes, replaced by heavier elements synthesized in

successive generations of massive stars. For a galaxy with the mass of the Milky Way ($\sim 10^{12}$ $M_{\odot}$; Kalberla et al. 2007, Reid et al. 2009), given the observed rate of star formation in typical disk galaxies, we expect that all of the gas in its ISM would be turned into stars on a timescale of about a Gyr.

But this is not what we observe. The average metallicity of the ISM, as preserved in the "fossil record" of long-lived dwarf star atmospheres, has not changed significantly over the $\sim$ 10 Gyr history of the Milky Way, and star formation evidently continues to the present day. Clearly, galaxies are *not* "closed boxes", so we seek to understand the source(s) of low-metallicity hydrogen that dilute the metal content of the ISM and fuel the ongoing formation of massive stars. Galaxy collisions, in the form of major mergers, are obvious suspects, but the major merger rate began an ongoing decline at $z \sim 1$; the "Stelliferous Era" of the Universe is now slowly waning. To explain the continued formation of stars at roughly constant metallicity, we must invoke other, dynamically "cold" sources of neutral hydrogen. We believe these are found among infalling high- velocity clouds, which in turn may be connected to a reservoir of gas comprising the "Cosmic Web" seen in cosmological simulations. The HVCs are a viable explanation of late-time accretion that primarily drives the external evolution of galaxies in the field.

Fresh gas arriving via this process participates in a rich chemistry of its own before becoming incorporated into nascent stars and planets; some of these chemical processes are thought to result in the molecular inventory that may have led to the origin of life on Earth. That we see many of the same

compounds in the ISM and in the vicinity of newly-forming stars supports ideas that complex chemistry is common throughout the Galaxy, while the recent (and rapidly-growing) field of exoplanet detection and characterization leads us toward the discovery of worlds where prebiotic synthesis may occur. Life on Earth arose quickly after the formation of the planet itself, so we have reasons to believe that a continual process of star formation through the Milky Way's history increases the probability that life arose and persists elsewhere in the Galaxy.

As a constituent of both stars and the ISM, gas plays an important role in the unfolding internal, "secular" evolution of galaxies like the Milky Way. Among galaxies in (relative) isolation, we find a variety of processes driven by resonant gravitational interactions in disks that yield diverse structures such as bars, rings, and spiral structure. These structures arise and persist over a few rotations before being destroyed by additional interactions, the stars (as luminous tracers of those structures) phase-mixing together until new resonant structures arise. As the era of major merger activity recedes into the Universe's past, these internal evolutionary processes are replacing mergers as the primary driver of galactic structure and evolution outside cluster environments.

7.2 What we have learned in the present work

For my Ph.D. work, I have completed three projects investigating the details of the role of gas in various incarnations as it relates to the growth and evolution of the Milky Way. The results are generalizable to similar galaxies

and contribute to our overall understanding of galaxies as individual organisms in the cosmological ecosystem.

7.2.1 HVCs are closer than we once thought, and their gas content represents both fuel for and waste from star formation

In the first part of my work with Dr. Bart Wakker, I helped collect and reduce spectroscopic and photometric data in support of an effort to place reliable, meaningful brackets on the distances to a number of HVCs and IVCs. At the time I began this work in 2003, the distances to the Clouds was still very much an open question; I became interested in the problem given that (1) the relation of these large, massive H I structures to the Milky Way was still unknown, as speculation placed them everywhere from hovering just above the Disk to truly cosmological distances, and (2) the advent of sensitive, high-resolution spectroscopy on 10 m-class telescopes enabled an answer to this question for the first time. While our results cannot absolutely preclude the existence of HVCs floating freely within the Local Group, we found the major, known HVC groups (excluding the Magellanic Stream) at several-kpc scales from the Disk, making them a distinctly local phenomenon, a conclusion made more robust by the observation of similar clouds of anomalous-velocity H I clouds situated near the disks of nearby external galaxies. IVCs are found to be generally closer than HVCs, supporting their origin in a Galactic Fountain that circulates gas between the Disk and Halo. Further evidence of the Clouds' origins could be found in their gas-phase metallicities; until recently, very few such measurements were reported in the literature, and those that were suffered

somewhat from inconsistent approaches in their determinations.

In 2011, we set out to survey as many lines of sight through the Clouds as possible based on a combination of available archival data and new *HST* observations specifically for this purpose, making the best metallicity determinations for them we could. By the end of my thesis work, I completed measurements for fifteen sightlines containing thirty-nine individual absorption components, many of them previously unpublished. Observations of sightlines whose components have been previously studied served as a check on the reliability of our measurement method. We found support for each of the major ideas proposed to explain HVCs and IVCs: (1) infall of low-metallicity ($Z \sim 0.1\ Z_{\odot}$) gas from the Halo or beyond, (2) tidal stripping of gas from dwarf galaxies orbiting the Milky Way, and (3) Galactic Fountain material at generally supersolar abundances. In the process, we roughly doubled the number of known metallicities of HVCs and IVCs in ions most resistant to ionization effects and depletion onto dust, making the results less model-dependent than many previous measurement attempts. Additional sightlines, beyond the scope of the thesis but for which we have data in hand, remain to be completed.

7.2.2 Massive star formation is like a scaled-up version of low-mass star formation (and we may be significantly underestimating molecular abundances in protostellar envelopes)

In earlier work with Dr. John Lacy, I developed my abundance analysis skills in spectroscopic observations of molecular gas in the environment of the high-mass protostellar object NGC 7538 IRS 9 obtained with his Texas

Echelon Cross (X) Echelle Spectrometer. I compared the results with previous work on NGC 7538 IRS 1, another object in the same OB association, and against chemical models of the envelopes of forming high-mass stars. I found differences between the objects attributable to variations in their radiation and thermal environments, leading us to conclude that the two objects represent evolutionary snapshots in time of high-mass protostars that began as molecular cloud cores with similar masses and chemical compositions. Taken in concert with the work of other authors on additional infrared sources in NGC 7538, we conclude that a wave of triggered star formation is sweeping across this molecular cloud complex, causing the sequential collapse of cores in a rough temporal sequence as it moves from northwest to southeast across the region. Our observations of IRS 9 also allowed us to construct a toy model of IRS 9 that validate many of the ideas about the structure of accreting, high-mass protostars and their environments, including an opaque inner region $\leq$ 2000 AU in size where a "hot-core" chemistry is taking place; a considerably larger, cool envelope; and a rarified, bipolar outflow cavity in which shocked gas is seen, suggesting a turbulent flow.

An unexpected outcome of this project was the observation of an apparent radiative transfer effect involving NH_3. The strengths of detected P-branch lines in the spectrum of IRS 9 do not follow the predictions of a simple model of radiative transfer assuming LTE. Rather, we found that the strength of lines on the P-branch is explained by the radiative "pumping" of lines on the R-branch by light emitted in the 9.7 μm silicate dust feature; as the ex-

cited ammonia molecules radiatively decay, branching ratios determine the observed intensities of P- and R-branch emission features. From this, we concluded that the dust in the inner envelope of IRS 9 must be physically close to the ammonia, if not actually mixed. If this pumping scheme similarly affects other molecules in dusty environments, we the literature abundances of certain species may be underestimated by as much as a factor of ten. Work continues to more fully articulate the problem, our proposed solution, and its impact on molecular spectroscopy of astrophysical sources.

7.2.3 Galaxies are more structurally-complicated beasts than we thought, and hierarchical assembly models are limited in their ability to explain the observed structures of individual field galaxies

In the third major project comprising my thesis, I worked with Dr. John Kormendy on the secular evolution of disk galaxies. We began with a the following premise: if the identification of kinematic structures by automated surface photometry on large samples of galaxies failed on simple examples, results of the large-scale application of automated decompositions of galaxy structures could be called into question. The success of large-area sky surveys such as 2MASS and SDSS in the past two decades is built on the extension of astrophysical study to very large samples, thus enabling rigorous statistical analyses for the first time. This work has clearly revolutionized astronomy, but the success of this approach relies heavily on the detailed, correct understanding of prototype cases before generalizations can be extended to samples

of thousands to millions of individual objects. The 2-D photometric decomposition of disk galaxies seeks to determine the mass fraction in the disks, bulges, and bars of objects seen at a variety of distances and inclinations to the line of sight and has proceeded apace as data from the large sky surveys began streaming in during the late 1990s. These decomposition surveys often rely on simple ratios of the relative contribution of individual structures to the total light of a galaxy such as the bulge-to-total (B/T) ratio. We suggested that the automated approach taken to apply decomposition methods to samples of thousands of distant galaxies may be more aggressive than can be justified given apparent shortcomings in the understanding of bright, nearby galaxies whose structures are more clearly delineated.

We identified two examples of large, massive, nearby disk galaxies seen edge-on, NGC 4565 and NGC 5746, in which historical efforts based on visible-wavelength observations fundamentally misclassified the objects as otherwise normal Sb galaxies. Their high inclinations allow detailed measurements of their vertical structure, made clearer by infrared observations that penetrate the thick dust in their midplanes. The misunderstanding of the structure and classification of these galaxies originated in the interpretation of what appears in visible light as a merger-built, "classical" bulge, but is seen in the infrared as a very small scale-height structure inconsistent with a merger origin. The visible- light "boxy" bulge of each galaxy is then interpreted as a bar seen nearly end-on, not a classical bulge. In a series of two papers based on observations spanning a range of wavelengths from ground- and space-based

facilities, we reported the discovery of a dynamically cold structure at the heart of each galaxy we identified as a "pseudobulge" grown in a slow manner from the disk, rather than a "hot" classical bulge showing signs of past merger violence. This remains something of a problem in the context of hierarchical assembly models in the ΛCDM cosmology paradigm, which implies a bottom-up pathway of galaxy assembly and growth through the mergers of increasingly massive objects over cosmic time. We find in detailed, 1-D decompositions of the structures of these two galaxies that neither must have experienced a major merger at any recent time in its history, and certainly not since the ongoing decline major merger rate began roughly 5 Gyr ago. It is therefore difficult to understand how it is possible to grow galaxies to the masses implied by the large circular velocities of NGC 4565 (255 km s^{-1}) and NGC 5746 (319 km s^{-1}) without major mergers, whose dynamical violence would have left a lasting kinematic impression on their structures. ΛCDM has experienced great success in predicting the observed large-scale structure of the Universe, but it may not be the whole story on the level of individual galaxy formation and growth.

7.3 Directions for future work

The directions of study presented in this thesis have something of a natural crosstalk when considered in the context of an integrated view of galaxy formation. This leads to a series of questions.

- **How is infall/accretion tied to the IGM in the context of cosmo-**

logical models?

In the ΛCDM paradigm, baryons from the IGM enter galaxy halos in the form of gas streaming along filaments of a "cosmic web". Some fraction of that gas will never be shock-heated to the virial temperature of the halo, and will therefore be incorporated into the galaxy through a mechanism called a "cold flow" (Kereš et al. 2005), although it is worth noting that in this context, "cold" still means temperatures $\lesssim 10^{5.5}$ K, but still somewhat below typical halo temperatures. This accretion mode dominated at high redshift ($z \gtrsim 2$) and still does for low-mass galaxies, but for galaxies with masses like the Milky Way in the present era, shock-heated "hot mode" accretion rules. In the latter picture, the gas does not connect directly with the disk, but cold flows are still important at low redshift as the cold gas is shielded from interaction with the hot halo medium by the hot-mode gas surrounding it (Joung et al. 2012). However, cold flows have never been confirmed observationally even though its covering fraction within massive halos at high redshift is expected to be as high as 25% (Dekel et al. 2009). Since we have strong theoretical reasons to believe they exist, efforts to directly detect cold filaments of accreting gas around external galaxies should continue. Observations of low-ionization metal line absorption in the UV, as described in Chapter 3 to obtain HVC metallicities, may be the key to solving this apparent problem (Kimm et al. 2011).

- **How does incoming atomic gas get converted to molecular gas for star formation?**

Previous studies have shown, and our results described here confirm, that the gas delivered from galaxy halos to disks via HVCs is almost entirely atomic, consisting mostly of H I with a low metal content. Krumholz et al. (2009) showed that the extragalactic star formation rate (SFR)-gas relation rises steeply at low gas surface densities, where the gas is mostly atomic, and transitions to a constant slope in a regime of normal spiral galaxies, and then grows superlinearly above a surface density of 85 $M_{\odot}$ pc^{-2}. Obviously, it is not sufficient to merely deposit a given quantity of H I onto a disk and expect star formation to take place immediately (and efficiently). We have still to develop a detailed understanding of how the incoming fuel is converted into molecular gas that can condense, cool, and form stars.

- **How "typical" is the Milky Way?**

Heiderman et al. (2010) found that a sample of Milky Way starforming regions lie well above the extragalactic SFR-gas relations such as the Kennicutt-Schmidt law (Schmidt 1959, Kennicutt 1998) by factors of up to 17. They are unable to explain away the difference entirely on the basis of resolution differences between Milky Way and extragalactic studies, suggesting our Galaxy's SFR at a given gas surface density is often considerably higher than expected even after correcting for resolution differences. A result of our HVC distance work, summarized in Chapter 2, is an estimate for the HVC mass accretion rate onto the Milky Way, but it falls short by about an order of magnitude relative to the recent Galactic SFR. Furthermore, simulations

suggest that cold do not survive passage through the warm/hot Halo medium. Observations of low-redshift, starforming spiral galaxies show relatively little H I gas in their halos, further suggesting that galaxy halos may not be most important source of gas to fuel star formation (Sancisi et al. 2008, Heald et al. 2011). This problem, then, is even more acute in the case of the Milky Way. The solution in both cases may be ionized extraplanar gas (Bauermeister et al. 2010, Lehner & Howk 2011, Putman et al. 2012a). Clearly, a self- consistent dynamical model is required to reconcile the proposed star formation fueling mechanism in the Milky Way with observational constraints, and further, to explain why the resulting Galactic SFR apparently exceeds that of most "normal" spirals at low redshift.

Future advances in these subjects will be driven strongly by the relentless march of technology. Having learned important lessons from 2MASS and SDSS, future efforts such as the Panoramic Survey Telescope and Rapid Response System (Pan-STARRS; Kaiser et al. 2002, 2010), the Large Synoptic Survey Telescope (LSST; Tyson 2002, Sweeney 2006), and the *Gaia* high-precision astrometry mission (Lindegren et al. 1994, 1995) will map the locations millions of stars with unprecedented precision. This work will further elucidate the detailed structure of the Milky Way and likely involve the discovery of additional stellar streams tracing the orbits of previously disrupted/accreted dwarf satellite galaxies.

Progress continues on enabling increasingly sensitive, very high resolution mid-infrared spectroscopy with airborne facilities. The Stratospheric

Observatory for Infrared Astronomy (SOFIA; Wiltsee & Brooks 1989, Davidson & Erickson 1989, Becklin & Gehrz 2009) recently saw first light with its first-generation facility instruments including the Echelon-Cross-Echelle Spectrograph (EXES; Richter et al. 2006a, DeWitt et al. 2012). A direct descendant of the TEXES instrument used as part of this thesis, it will provide spectroscopic capabilities between 4.5-28.3 μm at $R \sim 50000 - 1000000$ with a wavelength coverage of 0.5-1.5%. Fitted to a 3 m telescope aboard a modified Boeing 747 jet aircraft, EXES will fly at altitudes above 12000 m and 99.8% of the water vapor in the Earth's atmosphere, obtaining subarcsecond angular resolution spectroscopy of sources down to a spectral flux density limit of $\sim$0.2 Jy at 10 μm. Its operating altitude will open to study in protostellar envelopes and outflows many molecules unobservable on the ground due to atmospheric absorption. We expect great advances in our understanding of the chemistry of star formation in coming years as a result of EXES observations.

Continuing work on HVC/IVC abundances, however, is rapidly reaching a bottleneck defined by dwindling resources in support of U.S. spacecraft platforms. UV spectroscopy remains the best available option for abundance studies, but remains the sole province of space-based observations and a few rocket-borne missions. Since the end of the *FUSE* mission in 2007, there is no dedicate UV spectrograph currently on- orbit. COS has improved the ultraviolet sensitivity of *HST* by a factor of about ten over previous instruments, and a factor of $\sim$ 70 when observing extremely faint objects, but it is only one of several instruments aboard *HST* that compete for beam time.

The design emphasis of space observatories favors surveys with large fields in which spectroscopic capabilities are treated as add-ons and are not integral to telescope designs (Gull 2009).

Proposals for next-generation space UV spectrographs have not been successful since the deployment of COS. In 1998-99, NASA authorized and funded a mission study of the proposed Space Ultraviolet/Visible Observatory (SUVO), a 4-8 m aperture Great Observatory facility to replace *HST* (Shull 2003). This mission was not funded. While the James Webb Space Telescope (JWST) is scheduled to fly around 2018, it is optimized specifically for near-infrared observations. The American astronomical community has proposed the Advanced Technology Large Aperture Space Telescope (ATLAST; Postman et al. 2010), an 8-16-m UV/optical/IR space observatory for launch in roughly 2025-2030. NASA has also funded a study of a 4 m-class telescope mission known as the Telescope for Habitable Earths and Interstellar/ Intergalactic Astronomy (THEIA; Spergel 2009, Spergel et al. 2009) for combined wide-eld UV imaging, UV spectroscopy, and extrasolar planet characterization. The June 2012 announcement by the National Reconnaissance Office offering NASA two space-qualified, wide-field, 2.4 m- aperture optics packages in the form of spare spy satellite packages was welcome news (Achenbach 2012 June 4), but NASA is eyeing its new acquisitions for a hypothetical Wide-Field Infrared Survey Telescope (WFIRST; Goullioud et al. 2012).

Recent political events in the U.S. threaten an era of austerity policy in which broad swaths of government face sharp budget cuts, jeopardizing

any long-term plans of a publicly-funded, space-based, UV-sensitive facility to continue these abundance studies once *HST* is decommissioned. Facing frequent cost overruns and budget shortfalls, NASA rarely operates on long-term budgets. In a white paper prepared as part of the last National Academies Astrophysics Decadal Survey, Shull (2010) put it, "One of the important tasks for us, and for NASA administrators, is to convince everyone − the public, our profession, and Congress − that space astrophysics is an exciting area in which to invest. The problems are compelling, they excite the public, they stimulate education and technology, and they deserve more than the $1B/year currently devoted to the Astrophysics Division of NASA. A rising tide will raise all ships (and many wavelength bands)." The technology transfer proposition of the NRO spy satellite gesture is one avenue along which we may regain on-orbit UV spectroscopy capabilities in the post-*HST* era. At this point in time, however, it is more likely that Europe or the developing world will fund and launch such a platform before the U.S. acts to retain its pre-eminence in this field.

Bibliography

Abadi, M. G., Navarro, J. F., Steinmetz, M., & Eke, V. R. 2003, ApJ, 591, 499

Achenbach, J. 2012 June 4, The Washington Post

Akabane, K., Matsuo, H., Kuno, N., & Sugitani, K. 2001, PASJ, 53, 821

Allamandola, L. J., Tielens, A. G. G. M., & Barker, J. R. 1985, ApJ, 290, L25

—. 1989, ApJS, 71, 733

Araya, E., Hofner, P., Goss, W. M., et al. 2007, ApJS, 170, 152

Arnal, E. M., Bajaja, E., Larrarte, J. J., Morras, R., & Pöppel, W. G. L. 2000, A&As, 142, 35

Arnett, D. 1996, Supernovae and Nucleosynthesis: An Investigation of the History of Matter from the Big Bang to the Present (Supernovae and Nucleosynthesis: An Investigation of the History of Matter, from the Big Bang to the Present, by D. Arnett. Princeton: Princeton University Press, 1996.)

Asplund, M., Grevesse, N., & Sauval, A. J. 2005, in Astronomical Society of the Pacific Conference Series, Vol. 336, Cosmic Abundances as Records of Stellar Evolution and Nucleosynthesis, ed. T. G. Barnes, III & F. N. Bash, 25

Athanassoula, E. 2005, MNRAS, 358, 1477

Athanassoula, E. & Misiriotis, A. 2002a, MNRAS, 330, 35

—. 2002b, MNRAS, 330, 35

Bahcall, J. N., Bergeron, J., Boksenberg, A., Hartig, G. F., Jannuzi, B. T., Kirhakos, S., Sargent, W. L. W., Savage, B. D., Schneider, D. P., Turnshek, D. A., Weymann, R. J., & Wolfe, A. M. 1993, ApJS, 87, 1

Bajaja, E., Cappa de Nicolau, C. E., Cersosimo, J. C., Martin, M. C., Loiseau, N., Morras, R., Olano, C. A., & Poeppel, W. G. L. 1985, ApJS, 58, 143

Balcells, M., Graham, A. W., & Peletier, R. F. 2007, ApJ, 665, 1084

Bally, J. & Zinnecker, H. 2005, AJ, 129, 2281

Balog, Z., Kenyon, S. J., Lada, E. A., et al. 2004, AJ, 128, 2942

Barger, K. A., Haffner, L. M., Wakker, B. P., Hill, A. S., Madsen, G. J., & Duncan, A. K. 2012, ApJ, 761, 145

Bauermeister, A., Blitz, L., & Ma, C.-P. 2010, ApJ, 717, 323

Becklin, E. E. & Gehrz, R. D. 2009, in Society of Photo-Optical Instrumentation Engineers (SPIE) Conference Series, Vol. 7453, Society of Photo-Optical Instrumentation Engineers (SPIE) Conference Series

Beichman, C. A., Neugebauer, G., Habing, H. J., Clegg, P. E., & Chester, T. J., eds. 1988, Infrared astronomical satellite (IRAS) catalogs and atlases. Volume 1: Explanatory supplement, Vol. 1

Belokurov, V., Evans, N. W., Irwin, M. J., Lynden-Bell, D., Yanny, B., Vidrih, S., Gilmore, G., Seabroke, G., Zucker, D. B., Wilkinson, M. I., Hewett, P. C., Bramich, D. M., Fellhauer, M., Newberg, H. J., Wyse, R. F. G., Beers, T. C., Bell, E. F., Barentine, J. C., Brinkmann, J., Cole, N., Pan, K., & York, D. G. 2007, ApJ, 658, 337

Belokurov, V., Zucker, D. B., Evans, N. W., et al. 2006, ApJ, 642, L137

Ben Bekhti, N., Brüns, C., Kerp, J., & Westmeier, T. 2006, A&A, 457, 917

Bender, R., Burstein, D., & Faber, S. M. 1992, ApJ, 399, 462

Bendo, G. J., Draine, B. T., Engelbracht, C. W., et al. 2008, MNRAS, 389, 629

Besla, G., Kallivayalil, N., Hernquist, L., Robertson, B., Cox, T. J., van der Marel, R. P., & Alcock, C. 2007, ApJ, 668, 949

Bettoni, D. & Galletta, G. 1994, A&A, 281, 1

Beuther, H., Linz, H., & Henning, T. 2012, A&A, 543, A88

Bevington, P. R. & Robinson, D. K. 2003, Data reduction and error analysis for the physical sciences (Data reduction and error analysis for the physical

sciences, 3rd ed., by Philip R. Bevington, and Keith D. Robinson. Boston, MA: McGraw-Hill, ISBN 0-07-247227-8, 2003.)

Binney, J. 2004, in IAU Symposium, Vol. 220, Dark Matter in Galaxies, ed. S. Ryder, D. Pisano, M. Walker, & K. Freeman, 3

Binney, J. J., Davies, R. L., & Illingworth, G. D. 1990, ApJ, 361, 78

Blaauw, A. 1964, ARA&A, 2, 213

Blaauw, A. 1991, in NATO ASIC Proc. 342: The Physics of Star Formation and Early Stellar Evolution, ed. C. J. Lada & N. D. Kylafis, 125

Black, J. H. 1978, ApJ, 222, 125

Blades, J. C. & Morton, D. C. 1983, MNRAS, 204, 317

Bland-Hawthorn, J. & Maloney, P. R. 1999, in Astronomical Society of the Pacific Conference Series, Vol. 166, Stromlo Workshop on High-Velocity Clouds, ed. B. K. Gibson & M. E. Putman, 212

Blitz, L., Spergel, D. N., Teuben, P. J., Hartmann, D., & Burton, W. B. 1999, ApJ, 514, 818

Bonnell, I. A. & Bate, M. R. 2005, MNRAS, 362, 915

Bonnell, I. A., Bate, M. R., Clarke, C. J., & Pringle, J. E. 2001, MNRAS, 323, 785

Bonnell, I. A., Bate, M. R., & Zinnecker, H. 1998, MNRAS, 298, 93

Bonnell, I. A., Vine, S. G., & Bate, M. R. 2004, MNRAS, 349, 735

Boogert, A. C. A., Blake, G. A., & Öberg, K. 2004, ApJ, 615, 344

Boogert, A. C. A., Blake, G. A., & Tielens, A. G. G. M. 2002, ApJ, 577, 271

Bowen, D. V. & Blades, J. C. 1993, ApJ, 403, L55

Bowen, D. V., Pettini, M., Penston, M. V., & Blades, C. 1991a, MNRAS, 249, 145

—. 1991b, MNRAS, 248, 153

Brandt, J. C., Heap, S. R., Beaver, E. A., Boggess, A., Carpenter, K. G., Ebbets, D. C., Hutchings, J. B., Jura, M., Leckrone, D. S., Linsky, J. L., Maran, S. P., Savage, B. D., Smith, A. M., Trafton, L. M., Walter, F. M., Weymann, R. J., Ake, T. B., Bruhweiler, F., Cardelli, J. A., Lindler, D. J., Malumuth, E., Randall, C. E., Robinson, R., Shore, S. N., & Wahlgren, G. 1994, PASP, 106, 890

Braun, R. & Burton, W. B. 1999, A&A, 341, 437

—. 2000, A&A, 354, 853

Braun, R. & Thilker, D. A. 2004, A&A, 417, 421

Brüns, C., Kerp, J., Kalberla, P. M. W., & Mebold, U. 2000, A&A, 357, 120

Brüns, C., Kerp, J., & Pagels, A. 2001, A&A, 370, L26

Brüns, C., Kerp, J., Staveley-Smith, L., Mebold, U., Putman, M. E., Haynes, R. F., Kalberla, P. M. W., Muller, E., & Filipovic, M. D. 2005, A&A, 432, 45

Brüns, C. & Mebold, U. 2004, in Astrophysics and Space Science Library, Vol. 312, High Velocity Clouds, ed. H. van Woerden, B. P. Wakker, U. J. Schwarz, & K. S. de Boer, 251

Brunt, C. M. 2003, ApJ, 584, 293

Bryan, R. K. & Skilling, J. 1980, MNRAS, 191, 69

Bureau, M. & Freeman, K. C. 1999, AJ, 118, 126

Burrows, D. N. & Mendenhall, J. A. 1991, Nature, 351, 629

Burton, W. B., Braun, R., & de Heij, V. 2004, in Astrophysics and Space Science Library, Vol. 312, High Velocity Clouds, ed. van Woerden, H. and Wakker, B. P. and Schwarz, U. J. and de Boer, K. S. (Dordrecht: Kluwer)

Bushouse, H. 1997, in The 1997 HST Calibration Workshop with a New Generation of Instruments, ed. S. Casertano, R. Jedrzejewski, T. Keyes, & M. Stevens, 223–+

Buta, R. J., Corwin, H. G., & Odewahn, S. C. 2007, The de Vaucouleurs Altlas of Galaxies (Cambridge University Press)

Calzetti, D., Kennicutt, R. C., Engelbracht, C. W., et al. 2007, ApJ, 666, 870

Campbell, B. & Thompson, R. I. 1984, ApJ, 279, 650

Casey, A. R., Da Costa, G., Keller, S. C., & Maunder, E. 2013, ApJ, 764, 39

Chiappini, C., Matteucci, F., & Gratton, R. 1997, ApJ, 477, 765

Chiappini, C., Matteucci, F., & Romano, D. 2001, ApJ, 554, 1044

Cohen, M., Wheaton, W. A., & Megeath, S. T. 2003, AJ, 126, 1090

Collings, M. P., Anderson, M. A., Chen, R., et al. 2004, MNRAS, 354, 1133

Collins, J. A., Shull, J. M., & Giroux, M. L. 2003, ApJ, 585, 336

—. 2004, ApJ, 605, 216

—. 2005, ApJ, 623, 196

—. 2007, ApJ, 657, 271

—. 2009, ApJ, 705, 962

Combes, F., Debbasch, F., Friedli, D., & Pfenniger, D. 1990, A&A, 233, 82

Combes, F. & Sanders, R. H. 1981, A&A, 96, 164

Comerón, F. & Torra, J. 1995, in The Formation of the Milky Way, ed. E. J. Alfaro & A. J. Delgado, 130–133

Connors, T. W., Kawata, D., & Gibson, B. K. 2006, MNRAS, 371, 108

Copin, Y., Cretton, N., & Emsellem, E. 2004, A&A, 415, 889

Danforth, C. W., Stocke, J. T., & Shull, J. M. 2010, ApJ, 710, 613

Danly, L., Albert, C. E., & Kuntz, K. D. 1993, ApJ, 416, L29

Dartois, E., Demyk, K., d'Hendecourt, L., & Ehrenfreund, P. 1999, A&A, 351, 1066

Davidson, J. A. & Erickson, E. F. 1989, in Society of Photo-Optical Instrumentation Engineers (SPIE) Conference Series, Vol. 973, Society of Photo-Optical Instrumentation Engineers (SPIE) Conference Series, ed. R. K. Melugin & W. G. Pierce, 159–170

de Boer, K. S., Rodriguez Pascual, P., Wamsteker, W., Sonneborn, G., Fransson, C., Bomans, D. J., & Kirshner, R. P. 1993, A&A, 280, L15

de Heij, V., Braun, R., & Burton, W. B. 2002, A&A, 391, 159

de Vaucouleurs, G., de Vaucouleurs, A., Corwin, J., et al. 1991, Third Reference Catalogue of Bright Galaxies. Volume I: Explanations and references. Volume II: Data for galaxies between 0^h and 12^h. Volume III: Data for galaxies between 12^h and 24^h. (Springer-Verlag)

de Zeeuw, P. T., Bureau, M., Emsellem, E., Bacon, R., Carollo, C. M., Copin, Y., Davies, R. L., Kuntschner, H., Miller, B. W., Monnet, G., Peletier, R. F., & Verolme, E. K. 2002, MNRAS, 329, 513

Dekel, A., Birnboim, Y., Engel, G., Freundlich, J., Goerdt, T., Mumcuoglu, M., Neistein, E., Pichon, C., Teyssier, R., & Zinger, E. 2009, Nature, 457, 451

DeWitt, C., Richter, M. J., McKelvey, M. E., Seifahrt, A., Case, M., Barthel, J., Zell, P., & Lynch, D. 2012, in Society of Photo-Optical Instrumentation Engineers (SPIE) Conference Series, Vol. 8446, Society of Photo-Optical Instrumentation Engineers (SPIE) Conference Series

Dickel, H. R., Dickel, J. R., & Wilson, W. J. 1981, ApJ, 250, L43

Dixon, W. V., Sahnow, D. J., Barrett, P. E., Civeit, T., Dupuis, J., Fullerton, A. W., Godard, B., Hsu, J.-C., Kaiser, M. E., Kruk, J. W., Lacour, S., Lindler, D. J., Massa, D., Robinson, R. D., Romelfanger, M. L., & Sonnentrucker, P. 2007, PASP, 119, 527

Djorgovski, S. & Davis, M. 1987, ApJ, 313, 59

D'Onofrio, M., Capaccioli, M., Merluzzi, P., Zaggia, S., & Boulesteix, J. 1999, A&As, 134, 437

Doty, S. D., Schöier, F. L., & van Dishoeck, E. F. 2004, A&A, 418, 1021

Doty, S. D., van Dishoeck, E. F., van der Tak, F. F. S., & Boonman, A. M. S. 2002, A&A, 389, 446

Dwek, E., Arendt, R. G., Hauser, M. G., Kelsall, T., Lisse, C. M., Moseley, S. H., Silverberg, R. F., Sodroski, T. J., & Weiland, J. L. 1995, ApJ, 445, 716

Edmunds, M. G. 1990, MNRAS, 246, 678

Ekström, S., Georgy, C., Eggenberger, P., et al. 2012, A&A, 537, A146

Elmegreen, B. G. & Lada, C. J. 1977, ApJ, 214, 725

Emsellem, E., Cappellari, M., Peletier, R. F., McDermid, R. M., Bacon, R., Bureau, M., Copin, Y., Davies, R. L., Krajnović, D., Kuntschner, H., Miller, B. W., & de Zeeuw, P. T. 2004, MNRAS, 352, 721

Evans, II, N. J., Lacy, J. H., & Carr, J. S. 1991, ApJ, 383, 674

Faber, S. M., ed. 1987, Nearly normal galaxies: From the Planck time to the present; Proceedings of the Eighth Santa Cruz Summer Workshop in Astronomy and Astrophysics, Santa Cruz, CA, July 21-Aug. 1, 1986

Falcón-Barroso, J., Peletier, R. F., Emsellem, E., Kuntschner, H., Fathi, K., Bureau, M., Bacon, R., Cappellari, M., Copin, Y., Davies, R. L., & de Zeeuw, T. 2004, MNRAS, 350, 35

Fazio, G. G., Hora, J. L., Allen, L. E., et al. 2004, ApJS, 154, 10

Ferland, G. J., Korista, K. T., Verner, D. A., et al. 1998, PASP, 110, 761

Ferrante, R. F., Moore, M. H., Spiliotis, M. M., & Hudson, R. L. 2008, ApJ, 684, 1210

Ferrara, A. & Field, G. B. 1994, ApJ, 423, 665

Field, G. B. & Steigman, G. 1971, ApJ, 166, 59

Fischer, J., Joyce, R. R., Righini-Cohen, G., Simon, M., & Simon, T. 1980, ApJ, 240, L95

Fisher, D., Illingworth, G., & Franx, M. 1994, AJ, 107, 160

Fisher, D. B. & Drory, N. 2008, AJ, 136, 773

—. 2011, ApJ, 733, L47

Foster, T. & Routledge, D. 2003, ApJ, 598, 1005

Fox, A. J., Savage, B. D., & Wakker, B. P. 2006, ApJS, 165, 229

Fox, A. J., Savage, B. D., Wakker, B. P., et al. 2004, ApJ, 602, 738

Fox, A. J., Wakker, B. P., Savage, B. D., Tripp, T. M., Sembach, K. R., & Bland-Hawthorn, J. 2005, ApJ, 630, 332

Fox, A. J., Wakker, B. P., Smoker, J. V., Richter, P., Savage, B. D., & Sembach, K. R. 2010, ApJ, 718, 1046

Franco-Hernández, R., Moran, J. M., Rodríguez, L. F., & Garay, G. 2009, ApJ, 701, 974

Fujita, Y. 2001, ApJ, 547, 162

Galván-Madrid, R., Zhang, Q., Keto, E., et al. 2010, ApJ, 725, 17

Ganguly, R., Sembach, K. R., Tripp, T. M., & Savage, B. D. 2005, ApJS, 157, 251

Garnett, D. R. 1990, ApJ, 363, 142

Ghavamian, P., Aloisi, A., Lennon, D., Hartig, G., Kriss, G. A., Oliveira, C., Massa, D., Keyes, T., Proffitt, C., Delker, T., & Osterman, S. 2009, Preliminary Characterization of the Post-Launch Line Spread Function of COS, Tech. rep., Space Telescope Science Institute

Gibb, E. L., Whittet, D. C. B., Boogert, A. C. A., & Tielens, A. G. G. M. 2004, ApJS, 151, 35

Gibson, B. K. 2002, in Astronomical Society of the Pacific Conference Series, Vol. 273, The Dynamics, Structure & History of Galaxies: A Workshop in Honour of Professor Ken Freeman, ed. G. S. Da Costa, E. M. Sadler, & H. Jerjen, 205

Gibson, B. K., Giroux, M. L., Penton, S. V., Putman, M. E., Stocke, J. T., & Shull, J. M. 2000, AJ, 120, 1830

Gibson, B. K., Giroux, M. L., Penton, S. V., et al. 2001, AJ, 122, 3280

Giovanelli, R. 1981, AJ, 86, 1468

Giovanelli, R., Verschuur, G. L., & Cram, T. R. 1973, A&As, 12, 209

Goerigk, W. & Mebold, U. 1986, A&A, 162, 279

Goerigk, W., Mebold, U., Reif, K., Kalberla, P. M. W., & Velden, L. 1983, A&A, 120, 63

Goullioud, R., Content, D. A., Kuan, G. M., Moore, J. D., Chang, Z., Sunada, E. T., Villalvazo, J., Hawk, J. P., Armani, N. V., Johnson, E. L., & Powell,

C. A. 2012, in Society of Photo-Optical Instrumentation Engineers (SPIE) Conference Series, Vol. 8442, Society of Photo-Optical Instrumentation Engineers (SPIE) Conference Series

Governato, F., Brook, C., Mayer, L., et al. 2010, Nature, 463, 203

Green, J. C., Wilkinson, E., & Morse, J. A. 2003, in Society of Photo-Optical Instrumentation Engineers (SPIE) Conference Series, Vol. 4854, Society of Photo-Optical Instrumentation Engineers (SPIE) Conference Series, ed. J. C. Blades & O. H. W. Siegmund, 72–80

Gull, T. R. 2009, in American Institute of Physics Conference Series, Vol. 1135, American Institute of Physics Conference Series, ed. M. E. van Steenberg, G. Sonneborn, H. W. Moos, & W. P. Blair, 332–334

Hackwell, J. A., Grasdalen, G. L., & Gehrz, R. D. 1982, ApJ, 252, 250

Haffner, L. M. & Madsen, G. J. 2011, in Bulletin of the American Astronomical Society, Vol. 43, American Astronomical Society Meeting Abstracts #217, #251.05

Hanner, M. S., Brooke, T. Y., & Tokunaga, A. T. 1998, ApJ, 502, 871

Hartmann, D. & Burton, W. B. 1997, Atlas of Galactic Neutral Hydrogen (Cambridge University Press)

Haynes, M. P., van Zee, L., Hogg, D. E., Roberts, M. S., & Maddalena, R. J. 1998, AJ, 115, 62

Heald, G., Józsa, G., Serra, P., Zschaechner, L., Rand, R., Fraternali, F., Oosterloo, T., Walterbos, R., Jütte, E., & Gentile, G. 2011, A&A, 526, A118

Heckman, T. M., Sembach, K. R., Meurer, G. R., Strickland, D. K., Martin, C. L., Calzetti, D., & Leitherer, C. 2001, ApJ, 554, 1021

Heiderman, A., Evans, II, N. J., Allen, L. E., Huard, T., & Heyer, M. 2010, ApJ, 723, 1019

Heller, P. & Rohlfs, K. 1994, A&A, 291, 743

Henkel, C., Wilson, T. L., & Johnston, K. J. 1984, ApJ, 282, L93

Herbstmeier, U., Heithausen, A., & Mebold, U. 1993, A&A, 272, 514

Hetem, Jr., A. 1995, Astrophys. and Space Sci., 233, 181

Heyer, M. H., Carpenter, J. M., & Snell, R. L. 2001, ApJ, 551, 852

Ho, L. C., Filippenko, A. V., & Sargent, W. L. W. 1997, ApJS, 112, 315

Ho, L. C. & Keto, E. 2007, ApJ, 658, 314

Hodge, P. E., Hulbert, S. J., Lindler, D., Busko, I., Hsu, J.-C., Baum, S., McGrath, M., Goudfrooij, P., Shaw, R., Katsanis, R., Keener, S., & Bohlin, R. 1998, in Astronomical Society of the Pacific Conference Series, Vol. 145, Astronomical Data Analysis Software and Systems VII, ed. R. Albrecht, R. N. Hook, & H. A. Bushouse, 316

Hoffman, I. M. & Seojin Kim, S. 2011, AJ, 142, 202

Hsu, W.-H., Putman, M. E., Heitsch, F., Stanimirović, S., Peek, J. E. G., & Clark, S. E. 2011, AJ, 141, 57

Hulsbosch, A. N. M. 1968, Bull. Astron. Inst. Neth., 20, 33

Hulsbosch, A. N. M. & Oort, J. H. 1973, A&A, 22, 153

Hulsbosch, A. N. M. & Wakker, B. P. 1988, A&As, 75, 191

Hutawarakorn, B. & Cohen, R. J. 2003, MNRAS, 345, 175

Ibata, R., Irwin, M., Lewis, G. F., & Stolte, A. 2001, ApJ, 547, L133

Illingworth, G. & Schechter, P. L. 1982, ApJ, 256, 481

Ivezic, Z. & Christodoulou, D. M. 1997, ApJ, 486, 818

Jacquinet-Husson, N., Scott, N. A., Chédin, A., et al. 2005, Journal of Quantitative Spectroscopy and Radiative Transfer, 95, 429

Jarrett, T. H., Chester, T., Cutri, R., Schneider, S. E., & Huchra, J. P. 2003, AJ, 125, 525

Jarvis, B. 1990, Dynamics and Interactions of Galaxies (Springer)

Jenkins, E. B. 1987, in Astrophysics and Space Science Library, Vol. 134, Interstellar Processes, ed. D. J. Hollenbach & H. A. Thronson, Jr., 533–559

Jensen, E. B. & Thuan, T. X. 1982, ApJS, 50, 421

Jiang, Z., Tamura, M., Hoare, M. G., et al. 2008, ApJ, 673, L175

Jin, S. 2010, MNRAS, 408, L85

Johnston, K. G., Keto, E., Robitaille, T. P., & Wood, K. 2011, MNRAS, 415, 2953

Jones, B. F., Klemola, A. R., & Lin, D. N. C. 1994, AJ, 107, 1333

Joung, M. R., Putman, M. E., Bryan, G. L., Fernández, X., & Peek, J. E. G. 2012, ApJ, 759, 137

Kaiser, M. E., Hodge, P. E., Keyes, C., Sahnow, D., Ake, T., Aloisi, A., Béland, S., Diaz, R., Friedman, S., Froning, C., Ghavamian, P., Green, J., McPhate, J., Oliveira, C., Osterman, S., Penton, S., Shaw, B., & Wilkinson, E. 2008, in Society of Photo-Optical Instrumentation Engineers (SPIE) Conference Series, Vol. 7014, Society of Photo-Optical Instrumentation Engineers (SPIE) Conference Series

Kaiser, N., Aussel, H., Burke, B. E., Boesgaard, H., Chambers, K., Chun, M. R., Heasley, J. N., Hodapp, K.-W., Hunt, B., Jedicke, R., Jewitt, D., Kudritzki, R., Luppino, G. A., Maberry, M., Magnier, E., Monet, D. G., Onaka, P. M., Pickles, A. J., Rhoads, P. H. H., Simon, T., Szalay, A., Szapudi, I., Tholen, D. J., Tonry, J. L., Waterson, M., & Wick, J. 2002, in Society of Photo-Optical Instrumentation Engineers (SPIE) Conference Series, Vol. 4836, Society of Photo-Optical Instrumentation Engineers (SPIE) Conference Series, ed. J. A. Tyson & S. Wolff, 154–164

Kaiser, N., Burgett, W., Chambers, K., Denneau, L., Heasley, J., Jedicke, R., Magnier, E., Morgan, J., Onaka, P., & Tonry, J. 2010, in Society of Photo-Optical Instrumentation Engineers (SPIE) Conference Series, Vol. 7733, Society of Photo-Optical Instrumentation Engineers (SPIE) Conference Series

Kalberla, P. M. W., Burton, W. B., Hartmann, D., Arnal, E. M., Bajaja, E., Morras, R., & Pöppel, W. G. L. 2005a, A&A, 440, 775

Kalberla, P. M. W., Burton, W. B., Hartmann, D., et al. 2005b, A&A, 440, 775

Kalberla, P. M. W., Dedes, L., Kerp, J., & Haud, U. 2007, A&A, 469, 511

Kalberla, P. M. W. & Haud, U. 2006, A&A, 455, 481

Kalberla, P. W. M., Herbstmeier, U., & Mebold, U. 1984, in NASA Conference Publication, Vol. 2345, NASA Conference Publication, ed. Y. Kondo, F. C. Bruhweiler, & B. D. Savage, 243–247

Kallivayalil, N., van der Marel, R. P., & Alcock, C. 2006a, ApJ, 652, 1213

Kallivayalil, N., van der Marel, R. P., Alcock, C., Axelrod, T., Cook, K. H., Drake, A. J., & Geha, M. 2006b, ApJ, 638, 772

Kameya, O. 2006, in Proceedings of the 8th European VLBI Network Symposium

Keenan, F. P., Shaw, C. R., Bates, B., Dufton, P. L., & Kemp, S. N. 1995, MNRAS, 272, 599

Keeney, B. A., Danforth, C. W., Stocke, J. T., Penton, S. V., Shull, J. M., & Sembach, K. R. 2006, ApJ, 646, 951

Kennicutt, Jr., R. C. 1998, ApJ, 498, 541

Kereš, D. & Hernquist, L. 2009, ApJ, 700, L1

Kereš, D., Katz, N., Weinberg, D. H., & Davé, R. 2005, MNRAS, 363, 2

Keto, E. & Zhang, Q. 2010, MNRAS, 406, 102

Kimble, R. A., Woodgate, B. E., Bowers, C. W., Kraemer, S. B., Kaiser, M. E., Gull, T. R., Heap, S. R., Danks, A. C., Boggess, A., Green, R. F., Hutchings, J. B., Jenkins, E. B., Joseph, C. L., Linsky, J. L., & Maran, S. P. 1998, in Society of Photo-Optical Instrumentation Engineers (SPIE) Conference Series, Vol. 3356, Society of Photo-Optical Instrumentation Engineers (SPIE) Conference Series, ed. P. Y. Bely & J. B. Breckinridge, 188–202

Kimm, T., Slyz, A., Devriendt, J., & Pichon, C. 2011, MNRAS, 413, L51

Knez, C., Lacy, J. H., Evans, N. J., van Dishoeck, E. F., & Richter, M. J. 2009, ApJ, 696, 471

Kormendy, J. 1993, in IAU Symposium, Vol. 153, Galactic Bulges, ed. H. Dejonghe & H. J. Habing, 209

Kormendy, J. & Barentine, J. C. 2010, ApJ, 715, L176

Kormendy, J. & Bender, R. 2012, ApJS, 198, 2

Kormendy, J., Drory, N., Bender, R., & Cornell, M. E. 2010, ApJ, 723, 54

Kormendy, J., Fisher, D. B., Cornell, M. E., & Bender, R. 2009, ApJS, 182, 216

Kormendy, J. & Illingworth, G. 1982, ApJ, 256, 460

Kormendy, J. & Kennicutt, Jr., R. C. 2004, ARA&A, 42, 603

Kriss, G. A. 2011, Improved Medium Resolution Line Spread Functions for COS FUV Spectra, Tech. rep., Space Telescope Science Institute

Krumholz, M. R., McKee, C. F., & Tumlinson, J. 2009, ApJ, 699, 850

Kuijken, K. & Merrifield, M. R. 1995a, ApJ, 443, L13

—. 1995b, ApJ, 443, L13

Kunth, D., Lequeux, J., Sargent, W. L. W., & Viallefond, F. 1994, A&A, 282, 709

Kuntz, K. D. & Danly, L. 1993, in Star Formation, Galaxies and the Interstellar Medium, ed. J. Franco, F. Ferrini, & G. Tenorio-Tagle, 99

Kuntz, K. D. & Danly, L. 1996, ApJ, 457, 703

Lacy, J. H., Carr, J. S., Evans, II, N. J., et al. 1991, ApJ, 376, 556

Lacy, J. H. & Jaffe, D. T. 2007, in American Astronomical Society Meeting Abstracts, Vol. 211, American Astronomical Society Meeting Abstracts, #76.03

Lacy, J. H., Richter, M. J., Greathouse, T. K., Jaffe, D. T., & Zhu, Q. 2002, PASP, 114, 153

Larson, R. B. 1972, Nature Physical Science, 236, 7

Léger, A. & Puget, J. L. 1984, A&A, 137, L5

Lehner, N. 2002, ApJ, 578, 126

Lehner, N. & Howk, J. C. 2011, Science, 334, 955

Lehner, N., Howk, J. C., Keenan, F. P., & Smoker, J. V. 2008, ApJ, 678, 219

Lehner, N., Howk, J. C., Thom, C., Fox, A. J., Tumlinson, J., Tripp, T. M., & Meiring, J. D. 2012, MNRAS, 424, 2896

Lehner, N., Wakker, B. P., & Savage, B. D. 2004, ApJ, 615, 767

Lilienthal, D., Wennmacher, A., Herbstmeier, U., & Mebold, U. 1991, A&A, 250, 150

Lindegren, L., Perryman, M. A., Bastian, U., Dainty, J. C., Hog, E., van Leeuwen, F., Kovalevsky, J., Labeyrie, A., Loiseau, S., Mignard, F., Noordam, J. E., Le Poole, R. S., Thejll, P., & Vakili, F. 1994, in Society of Photo-Optical Instrumentation Engineers (SPIE) Conference Series, Vol.

2200, Society of Photo-Optical Instrumentation Engineers (SPIE) Conference Series, ed. J. B. Breckinridge, 599–608

Lindegren, L., Perryman, M. A., & Loiseau, S. 1995, in Society of Photo-Optical Instrumentation Engineers (SPIE) Conference Series, Vol. 2477, Society of Photo-Optical Instrumentation Engineers (SPIE) Conference Series, ed. R. D. Reasenberg, 91–103

Lockman, F. J., Jahoda, K., & McCammon, D. 1986, ApJ, 302, 432

Lockman, F. J., Murphy, E. M., Petty-Powell, S., & Urick, V. J. 2002, ApJS, 140, 331

Lu, L., Sargent, W. L. W., & Barlow, T. A. 1998a, AJ, 115, 55

Lu, L., Sargent, W. L. W., Savage, B. D., et al. 1998b, AJ, 115, 162

Lu, L., Savage, B. D., & Sembach, K. R. 1994, ApJ, 437, L119

Lugo, J., Lizano, S., & Garay, G. 2004, ApJ, 614, 807

Lupton, R., Gunn, J. E., Ivezić, Z., Knapp, G. R., & Kent, S. 2001, in Astronomical Society of the Pacific Conference Series, Vol. 238, Astronomical Data Analysis Software and Systems X, ed. F. R. Harnden Jr., F. A. Primini, & H. E. Payne, 269–+

Lynds, B. T. 1965, ApJS, 12, 163

Madsen, G. J., Haffner, L. M., & Reynolds, R. J. 2006, Mem. della Soc. Astron. Ital., 77, 1163

Maller, A. H. & Bullock, J. S. 2004, MNRAS, 355, 694

Maloney, P. 1993, ApJ, 414, 41

Maloney, P. R. & Putman, M. E. 2003, ApJ, 589, 270

Mann, R. K. & Williams, J. P. 2009, ApJ, 694, L36

Marconi, G., Matteucci, F., & Tosi, M. 1994, MNRAS, 270, 35

Mastropietro, C., Moore, B., Mayer, L., Wadsley, J., & Stadel, J. 2005, MNRAS, 363, 509

Mathewson, D. S., Cleary, M. N., & Murray, J. D. 1974, ApJ, 190, 291

Matteucci, F. & François, P. 1989, in Nuclear Astrophysics, ed. W. Hillebrandt & E. Müller, 142

Matteucci, F. & Francois, P. 1989, MNRAS, 239, 885

Matthews, D., Staveley-Smith, L., Dyson, P., & Muller, E. 2009, ApJ, 691, L115

McClure-Griffiths, N. M., Madsen, G. J., Gaensler, B. M., McConnell, D., & Schnitzeler, D. H. F. M. 2010, ApJ, 725, 275

McKee, C. F. & Ostriker, E. C. 2007, ARA&A, 45, 565

Mebold, U., Cernicharo, J., Velden, L., Reif, K., Crezelius, C., & Goerigk, W. 1985, A&A, 151, 427

Mebold, U. & Kalberla, P. W. M. 1984, in NASA Conference Publication, Vol. 2345, NASA Conference Publication, ed. Y. Kondo, F. C. Bruhweiler, & B. D. Savage, 249–252

Merrifield, M. R. 1996, in Astronomical Society of the Pacific Conference Series, Vol. 91, IAU Colloq. 157: Barred Galaxies, ed. R. Buta, D. A. Crocker, & B. G. Elmegreen, 179

Merrifield, M. R. & Kuijken, K. 1999, A&A, 345, L47

Meurer, G. R., Freeman, K. C., Dopita, M. A., & Cacciari, C. 1992, AJ, 103, 60

Meyer, D. M. & Roth, K. C. 1991, ApJ, 383, L41

Michelson, A. A. 1898, ApJ, 8, 37

Miller, E. D. & Bregman, J. N. 2005, in Astronomical Society of the Pacific Conference Series, Vol. 331, Extra-Planar Gas, ed. R. Braun, 261

Mirabel, I. F. & Morras, R. 1984, ApJ, 279, 86

Mitchell, G. F. & Hasegawa, T. I. 1991, ApJ, 371, L33

Mitchell, G. F., Maillard, J.-P., Allen, M., Beer, R., & Belcourt, K. 1990, ApJ, 363, 554

Miville-Deschênes, M.-A., Boulanger, F., Reach, W. T., & Noriega-Crespo, A. 2005, ApJ, 631, L57

Moore, B. & Davis, M. 1994, MNRAS, 270, 209

Moritz, P., Wennmacher, A., Herbstmeier, U., Mebold, U., Egger, R., & Snowden, S. L. 1998, A&A, 336, 682

Morras, R., Bajaja, E., Arnal, E. M., & Pöppel, W. G. L. 2000, A&As, 142, 25

Morton, D. C. 1991, ApJS, 77, 119

—. 2003, ApJS, 149, 205

Moscadelli, L., Reid, M. J., Menten, K. M., et al. 2009, ApJ, 693, 406

Muller, C. A., Raimond, E., Schwarz, U. J., & Tolbert, C. R. 1963, Bull. Astron. Inst. Neth. Suppl., 1, 213

Muller, E., Staveley-Smith, L., & Zealey, W. J. 2003, MNRAS, 338, 609

Münch, G. & Zirin, H. 1961, ApJ, 133, 11

Murphy, E. M., Sembach, K. R., Gibson, B. K., Shull, J. M., Savage, B. D., Roth, K. C., Moos, H. W., Green, J. C., York, D. G., & Wakker, B. P. 2000, ApJ, 538, L35

Murray, S. D. & Lin, D. N. C. 2004, ApJ, 615, 586

Narayan, R. & Nityananda, R. 1986, ARA&A, 24, 127

Newberg, H. J., Willett, B. A., Yanny, B., & Xu, Y. 2010, ApJ, 711, 32

Nicastro, F., Zezas, A., Drake, J., Elvis, M., Fiore, F., Fruscione, A., Marengo, M., Mathur, S., & Bianchi, S. 2002, ApJ, 573, 157

Nicastro, F., Zezas, A., Elvis, M., Mathur, S., Fiore, F., Cecchi-Pestellini, C., Burke, D., Drake, J., & Casella, P. 2003, Nature, 421, 719

Nichols, M. & Bland-Hawthorn, J. 2009, ApJ, 707, 1642

Nidever, D. L. 2009, PhD thesis, University of Virginia

Nidever, D. L., Majewski, S. R., & Burton, W. B. 2008, ApJ, 679, 432

Ojalvo, I. & Wakker, B. 2005, in Bulletin of the American Astronomical Society, Vol. 37, American Astronomical Society Meeting Abstracts, 1256

Oort, J. H. 1966, Bull. Astron. Inst. Neth., 18, 421

—. 1970, A&A, 7, 381

Oosterloo, T., Fraternali, F., & Sancisi, R. 2007, AJ, 134, 1019

Osterbrock, D. E. & Ferland, G. J. 2006, Astrophysics of gaseous nebulae and active galactic nuclei (Astrophysics of gaseous nebulae and active galactic nuclei, 2nd. ed. by D.E. Osterbrock and G.J. Ferland. Sausalito, CA: University Science Books, 2006)

Pagel, B. E. J. 1989, in Evolutionary Phenomena in Galaxies, ed. J. E. Beckman & B. E. J. Pagel, 201–223

Pagel, B. E. J. 1997, Nucleosynthesis and Chemical Evolution of Galaxies (Cambridge University Press)

Pagel, B. E. J. & Patchett, B. E. 1975, MNRAS, 172, 13

Palumbo, M. E., Geballe, T. R., & Tielens, A. G. G. M. 1997, ApJ, 479, 839

Panagia, N. 1973, AJ, 78, 929

Parsons, S. B., Wilson, I. R., Crawford, J. R., Dempsey, R. C., Ewald, R. A., Gillam, S. D., Giovane, E. A., Kochte, M. C., Schultz, A. B., Scott, J. F., & Swade, D. A. 1993, in Bulletin of the American Astronomical Society, Vol. 25, American Astronomical Society Meeting Abstracts #182, 832

Patel, N. A., Curiel, S., Sridharan, T. K., et al. 2005, Nature, 437, 109

Peebles, P. J. E. & Nusser, A. 2010, Nature, 465, 565

Peek, J. E. G., Heiles, C., Putman, M. E., & Douglas, K. 2009, ApJ, 692, 827

Peeters, E., Spoon, H. W. W., & Tielens, A. G. G. M. 2004, ApJ, 613, 986

Pendleton, Y. J., Tielens, A. G. G. M., Tokunaga, A. T., & Bernstein, M. P. 1999, ApJ, 513, 294

Pestalozzi, M. R., Elitzur, M., Conway, J. E., & Booth, R. S. 2004, ApJ, 603, L113

Pestalozzi, M. R., Minier, V., Motte, F., & Conway, J. E. 2006, A&A, 448, L57

Pfenniger, D. & Friedli, D. 1991, A&A, 252, 75

Pfenniger, D. & Norman, C. 1990, ApJ, 363, 391

Pilyugin, L. S. 1993, A&A, 277, 42

Pisano, D. J., Barnes, D. G., Gibson, B. K., Staveley-Smith, L., Freeman, K. C., & Kilborn, V. A. 2007, ApJ, 662, 959

Planck Collaboration, Abergel, A., Ade, P. A. R., Aghanim, N., Arnaud, M., Ashdown, M., Aumont, J., Baccigalupi, C., Balbi, A., Banday, A. J., & et al. 2011, A&A, 536, A24

Postman, M., Brown, T., Sembach, K., Giavalisco, M., Traub, W., Stapelfeldt, K., Calzetti, D., Oegerle, W., Rich, R. M., Stahl, H. P., Tumlinson, J., Mountain, M., Soummer, R., & Hyde, T. 2010, in Society of Photo-Optical Instrumentation Engineers (SPIE) Conference Series, Vol. 7731, Society of Photo-Optical Instrumentation Engineers (SPIE) Conference Series

Puget, J. L. & Léger, A. 1989, ARA&A, 27, 161

Putman, M. E. 2000, Publ. Astron. Soc. of Australia, 17, 1

Putman, M. E., Bland-Hawthorn, J., Veilleux, S., Gibson, B. K., Freeman, K. C., & Maloney, P. R. 2003a, ApJ, 597, 948

Putman, M. E., de Heij, V., Staveley-Smith, L., Braun, R., Freeman, K. C., Gibson, B. K., Burton, W. B., Barnes, D. G., Banks, G. D., Bhathal, R., de Blok, W. J. G., Boyce, P. J., Disney, M. J., Drinkwater, M. J., Ekers, R. D.,

Henning, P. A., Jerjen, H., Kilborn, V. A., Knezek, P. M., Koribalski, B., Malin, D. F., Marquarding, M., Minchin, R. F., Mould, J. R., Oosterloo, T., Price, R. M., Ryder, S. D., Sadler, E. M., Stewart, I., Stootman, F., Webster, R. L., & Wright, A. E. 2002, AJ, 123, 873

Putman, M. E., Peek, J. E. G., & Heitsch, F. 2012a, in EAS Publications Series, Vol. 56, EAS Publications Series, ed. M. A. de Avillez, 267–274

Putman, M. E., Peek, J. E. G., & Joung, M. R. 2012b, ARA&A, 50, 491

Putman, M. E., Saul, D. R., & Mets, E. 2011, MNRAS, 418, 1575

Putman, M. E., Staveley-Smith, L., Freeman, K. C., Gibson, B. K., & Barnes, D. G. 2003b, ApJ, 586, 170

Qiu, K., Zhang, Q., & Menten, K. M. 2011, ApJ, 728, 6

Raha, N., Sellwood, J. A., James, R. A., & Kahn, F. D. 1991, Nature, 352, 411

Rand, R. J. & Benjamin, R. A. 2008, ApJ, 676, 991

Reid, M. A. & Wilson, C. D. 2005, ApJ, 625, 891

Reid, M. J., Menten, K. M., Zheng, X. W., Brunthaler, A., Moscadelli, L., Xu, Y., Zhang, B., Sato, M., Honma, M., Hirota, T., Hachisuka, K., Choi, Y. K., Moellenbrock, G. A., & Bartkiewicz, A. 2009, ApJ, 700, 137

Renzini, A. & Voli, M. 1981, A&A, 94, 175

Richter, M. J., Lacy, J. H., Jaffe, D. T., Mar, D. J., Goertz, J., Moller, W. M., Strong, S., & Greathouse, T. K. 2006a, in Society of Photo-Optical Instrumentation Engineers (SPIE) Conference Series, Vol. 6269, Society of Photo-Optical Instrumentation Engineers (SPIE) Conference Series

Richter, P., Savage, B. D., Sembach, K. R., & Tripp, T. M. 2006b, A&A, 445, 827

Richter, P., Savage, B. D., Tripp, T. M., & Sembach, K. R. 2004, ApJS, 153, 165

Richter, P., Savage, B. D., Wakker, B. P., Sembach, K. R., & Kalberla, P. M. W. 2001a, ApJ, 549, 281

Richter, P., Sembach, K. R., Wakker, B. P., & Savage, B. D. 2001b, ApJ, 562, L181

Richter, P., Sembach, K. R., Wakker, B. P., et al. 2001c, ApJ, 559, 318

Richter, P., Wakker, B. P., Savage, B. D., & Sembach, K. R. 2003, ApJ, 586, 230

Rodríguez, L. F., Zapata, L. A., & Ho, P. T. P. 2007, ApJ, 654, L143

Rose, J., Akella, R., Binegar, S., Choo, T. H., Heller-Boyer, C., Hester, T., Hyde, P., Perrine, R., Rose, M. A., & Steuerman, K. 1995, in Astronomical Society of the Pacific Conference Series, Vol. 77, Astronomical Data Analysis

Software and Systems IV, ed. R. A. Shaw, H. E. Payne, & J. J. E. Hayes, 429

Rupen, M. P. 1991, AJ, 102, 48

Russell, S. C. & Dopita, M. A. 1992, ApJ, 384, 508

Ryan, Jr., R. E., Cohen, S. H., Windhorst, R. A., & Silk, J. 2008, ApJ, 678, 751

Ryans, R. S. I., Keenan, F. P., Sembach, K. R., & Davies, R. D. 1997a, MNRAS, 289, 986

—. 1997b, MNRAS, 289, 83

Sahnow, D. J., Gummin, M. A., Gaines, G. A., Fullerton, A. W., Kaiser, M. E., & Siegmund, O. H. 2000, in Society of Photo-Optical Instrumentation Engineers (SPIE) Conference Series, Vol. 4139, Society of Photo-Optical Instrumentation Engineers (SPIE) Conference Series, ed. S. Fineschi, C. M. Korendyke, O. H. Siegmund, & B. E. Woodgate, 149–162

Sahu, M. S. 1998, AJ, 116, 1205

Sahu, M. S. & Blades, J. C. 1997, ApJ, 484, L125

Sales, L. V., Helmi, A., Starkenburg, E., Morrison, H. L., Engle, E., Harding, P., Mateo, M., Olszewski, E. W., & Sivarani, T. 2008, MNRAS, 389, 1391

Sancisi, R., Fraternali, F., Oosterloo, T., & van der Hulst, T. 2008, A&Ar, 15, 189

Sandage, A. 1961, The Hubble atlas of galaxies (Carnegie Institution)

Sandell, G., Goss, W. M., & Wright, M. 2005, ApJ, 621, 839

Sandell, G., Goss, W. M., Wright, M., & Corder, S. 2009, ApJ, 699, L31

Savage, B. D., Lu, L., Weymann, R. J., Morris, S. L., & Gilliland, R. L. 1993, ApJ, 404, 124

Savage, B. D. & Sembach, K. R. 1991, ApJ, 379, 245

—. 1996, ARA&A, 34, 279

Schlegel, D. J., Finkbeiner, D. P., & Davis, M. 1998, ApJ, 500, 525

Schmidt, M. 1959, ApJ, 129, 243

Schreyer, K., Semenov, D., Henning, T., & Forbrich, J. 2006, ApJ, 637, L129

Schulman, E., Bregman, J. N., Brinks, E., & Roberts, M. S. 1996, AJ, 112, 960

Schulman, E., Bregman, J. N., & Roberts, M. S. 1994, ApJ, 423, 180

Schulman, E., Brinks, E., Bregman, J. N., & Roberts, M. S. 1997a, AJ, 113, 1559

Schulman, E., Ockels, F., & Knezek, P. M. 1997b, in Bulletin of the American Astronomical Society, Vol. 29, American Astronomical Society Meeting Abstracts, 1332

Schwarz, U. J., Wakker, B. P., & van Woerden, H. 1995, A&A, 302, 364

Schweizer, F. 1990, Interactions in our time. (Springer), 60–71

Sembach, K. R., Gibson, B. K., Fenner, Y., & Putman, M. E. 2002, ApJ, 572, 178

Sembach, K. R., Howk, J. C., Savage, B. D., & Shull, J. M. 2001a, AJ, 121, 992

Sembach, K. R., Howk, J. C., Savage, B. D., Shull, J. M., & Oegerle, W. R. 2001b, ApJ, 561, 573

Sembach, K. R. & Savage, B. D. 1992, ApJS, 83, 147

Sembach, K. R., Savage, B. D., Lu, L., & Murphy, E. M. 1995, ApJ, 451, 616

—. 1999, ApJ, 515, 108

Sembach, K. R., Savage, B. D., Shull, J. M., Jenkins, E. B., Murphy, E. M., York, D. G., Ake, T., Blair, W. P., Davidsen, A. F., Friedman, S. D., Gibson, B. K., Kruk, J. W., Moos, H. W., Oegerle, W. R., Sahnow, D., & Sonneborn, G. 2000, ApJ, 538, L31

Sembach, K. R., Wakker, B. P., Savage, B. D., et al. 2003, ApJS, 146, 165

Sembach, K. R., Wakker, B. P., Tripp, T. M., et al. 2004, ApJS, 150, 387

Sérsic, J. L. 1968, Atlas de galaxias australes (Observatorio Astronomico, Cordoba, Argentina)

Shapiro, P. R. & Field, G. B. 1976, ApJ, 205, 762

Shaw, M., Wilkinson, A., & Carter, D. 1993, A&A, 268, 511

Shaw, M. A. & Gilmore, G. 1989, MNRAS, 237, 903

Shelton, R. L., Henley, D. B., & Dixon, W. V. 2010, ApJ, 722, 302

Shen, J., Rich, R. M., Kormendy, J., et al. 2010, ApJ, 720, L72

Shull, J. M. 2003, in Astronomical Society of the Pacific Conference Series, Vol. 291, Hubble's Science Legacy: Future Optical/Ultraviolet Astronomy from Space, ed. K. R. Sembach, J. C. Blades, G. D. Illingworth, & R. C. Kennicutt, Jr., 17

Shull, J. M. 2010, NASA Missions: The Future of Ultraviolet-Optical Astronomy in Space, Tech. Rep. 98.62.Ra, Association of Universities for Research In Astronomy, http://www.aura-astronomy.org/news/Astro2010PanelDocs/AURA-space.pdf

Shull, J. M. & Beckwith, S. 1982, ARA&A, 20, 163

Shull, J. M., Jones, J. R., Danforth, C. W., & Collins, J. A. 2009, ApJ, 699, 754

Shull, J. M., Stevans, M., Danforth, C., et al. 2011, ApJ, 739, 105

Shull, J. M., Tumlinson, J., Jenkins, E. B., Moos, H. W., Rachford, B. L., Savage, B. D., Sembach, K. R., Snow, T. P., Sonneborn, G., York, D. G.,

Blair, W. P., Green, J. C., Friedman, S. D., & Sahnow, D. J. 2000, ApJ, 538, L73

Simien, F. & de Vaucouleurs, G. 1986, ApJ, 302, 564

Simon, J. D., Blitz, L., Cole, A. A., Weinberg, M. D., & Cohen, M. 2006, ApJ, 640, 270

Skrutskie, M. F., Cutri, R. M., Stiening, R., et al. 2006, AJ, 131, 1163

Smith, R. L., Pontoppidan, K. M., Young, E. D., Morris, M. R., & van Dishoeck, E. F. 2009, ApJ, 701, 163

Smoker, J. V., Lynn, B. B., Rolleston, W. R. J., Kay, H. R. M., Bajaja, E., Poppel, W. G. L., Keenan, F. P., Kalberla, P. M. W., Mooney, C. J., Dufton, P. L., & Ryans, R. S. I. 2004, MNRAS, 352, 1279

Snowden, S. L., Mebold, U., Hirth, W., Herbstmeier, U., & Schmitt, J. H. M. 1991, Science, 252, 1529

Sofia, U. J. & Jenkins, E. B. 1998, ApJ, 499, 951

Songaila, A., York, D. G., Cowie, L. L., & Blades, J. C. 1985, ApJ, 293, L15

Spergel, D. N. 2009, in Bulletin of the American Astronomical Society, Vol. 41, American Astronomical Society Meeting Abstracts #213, #234.10

Spergel, D. N., Kasdin, J., Belikov, R., Atcheson, P., Beasley, M., Calzetti, D., Cameron, B., Copi, C., Desch, S., Dressler, A., Ebbets, D., Egerman,

R., Fullerton, A., Gallagher, J., Green, J., Guyon, O., Heap, S., Jansen, R., Jenkins, E., Kasting, J., Keski-Kuha, R., Kuchner, M., Lee, R., Lindler, D., Linfield, R., Lisman, D., Lyon, R., Malhotra, S., Mathews, G., McCaughrean, M., Mentzel, J., Mountain, M., NIkzad, S., O'Connell, R., Oey, S., Padgett, D., Parvin, B., Procashka, J., Reeve, W., Reid, I. N., Rhoads, J., Roberge, A., Saif, B., Scowen, P., Seager, S., Seigmund, O., Sembach, K., Shaklan, S., Shull, M., & Soummer, R. 2009, in Bulletin of the American Astronomical Society, Vol. 41, American Astronomical Society Meeting Abstracts #213, #458.04

Spitzer, Jr., L. 1956, ApJ, 124, 20

Springob, C. M., Masters, K. L., Haynes, M. P., Giovanelli, R., & Marinoni, C. 2009a, ApJS, 182, 474

—. 2009b, ApJS, 182, 474

Stanimirović, S., Hoffman, S., Heiles, C., Douglas, K. A., Putman, M., & Peek, J. E. G. 2008, ApJ, 680, 276

Sternberg, A., McKee, C. F., & Wolfire, M. G. 2002, ApJS, 143, 419

Surcis, G., Vlemmings, W. H. T., Torres, R. M., van Langevelde, H. J., & Hutawarakorn Kramer, B. 2011, A&A, 533, A47

Sweeney, D. W. 2006, in Society of Photo-Optical Instrumentation Engineers (SPIE) Conference Series, Vol. 6267, Society of Photo-Optical Instrumentation Engineers (SPIE) Conference Series

Thilker, D. A., Braun, R., Walterbos, R. A. M., et al. 2004, ApJ, 601, L39

Thom, C., Putman, M. E., Gibson, B. K., Christlieb, N., Flynn, C., Beers, T. C., Wilhelm, R., & Lee, Y. S. 2006, ApJ, 638, L97

Thompson, R. I. 1994, in Society of Photo-Optical Instrumentation Engineers (SPIE) Conference Series, Vol. 2209, Society of Photo-Optical Instrumentation Engineers (SPIE) Conference Series, ed. M. G. Cerutti-Maori & P. Roussel, 319–330

Tielens, A. G. G. M. 2005, The Physics and Chemistry of the Interstellar Medium (The Physics and Chemistry of the Interstellar Medium, by A. G. G. M. Tielens, pp. . ISBN 0521826349. Cambridge, UK: Cambridge University Press, 2005.)

Tielens, A. G. G. M., Hony, S., van Kerckhoven, C., & Peeters, E. 1999, in ESA Special Publication, Vol. 427, The Universe as Seen by ISO, ed. P. Cox & M. Kessler, 579

Tielens, A. G. G. M., van Kerckhoven, C., Peeters, E., & Hony, S. 2000, in IAU Symposium, Vol. 197, From Molecular Clouds to Planetary, ed. Y. C. Minh & E. F. van Dishoeck, 349

Toomre, A. 1977, in Evolution of Galaxies and Stellar Populations, ed. B. M. Tinsley & R. B. G. Larson, D. Campbell, 401

Tosi, M. 1988, A&A, 197, 47

Tripp, T. M., Sembach, K. R., Bowen, D. V., Savage, B. D., Jenkins, E. B., Lehner, N., & Richter, P. 2008, ApJS, 177, 39

Tripp, T. M., Wakker, B. P., Jenkins, E. B., et al. 2003, AJ, 125, 3122

Tufte, S. L., Reynolds, R. J., & Haffner, L. M. 1998, ApJ, 504, 773

Tully, R. B. 1988, Nearby galaxies catalog (Cambridge University Press)

Tully, R. B., Rizzi, L., Shaya, E. J., et al. 2009, AJ, 138, 323

Tully, R. B., Shaya, E. J., Karachentsev, I. D., et al. 2008, ApJ, 676, 184

Tyson, J. A. 2002, in Society of Photo-Optical Instrumentation Engineers (SPIE) Conference Series, Vol. 4836, Society of Photo-Optical Instrumentation Engineers (SPIE) Conference Series, ed. J. A. Tyson & S. Wolff, 10–20

Ulich, B. L. & Haas, R. W. 1976, ApJS, 30, 247

van Broekhuizen, F. A., Keane, J. V., & Schutte, W. A. 2004, A&A, 415, 425

van den Bergh, S. 1962, AJ, 67, 486

van der Kruit, P. C. & Searle, L. 1981, A&A, 95, 105

van der Tak, F. F. S. 2005, in IAU Symposium, Vol. 227, Massive Star Birth: A Crossroads of Astrophysics, ed. R. Cesaroni, M. Felli, E. Churchwell, & M. Walmsley, 70–79

van Woerden, H., Schwarz, U. J., Peletier, R. F., Wakker, B. P., & Kalberla, P. M. W. 1999, Nature, 400, 138

van Woerden, H. & Wakker, B. P. 2004, in Astrophysics and Space Science Library, Vol. 312, High Velocity Clouds, ed. H. van Woerden, B. P. Wakker, U. J. Schwarz, & K. S. de Boer, 195

Verolme, E. K., Cappellari, M., Copin, Y., van der Marel, R. P., Bacon, R., Bureau, M., Davies, R. L., Miller, B. M., & de Zeeuw, P. T. 2002, MNRAS, 335, 517

Verstraete, L., Pech, C., Moutou, C., et al. 2001, A&A, 372, 981

Vietri, M., Ferrara, A., & Miniati, F. 1997, ApJ, 483, 262

Vogelaar, M. G. R. & Wakker, B. P. 1994, A&A, 291, 557

Wakelam, V., Caselli, P., Ceccarelli, C., Herbst, E., & Castets, A. 2004, A&A, 422, 159

Wakelam, V., Hersant, F., & Herpin, F. 2011, A&A, 529, A112+

Wakker, B., Howk, C., Schwarz, U., van Woerden, H., Beers, T., Wilhelm, R., Kalberla, P., & Danly, L. 1996, ApJ, 473, 834

Wakker, B. P. 1990, PhD thesis, PhD thesis, Univ. Groningen, (1990)

—. 1991, A&A, 250, 499

—. 2001a, ApJS, 136, 463

—. 2001b, ApJS, 136, 463

Wakker, B. P. 2004, in IAU Symposium, Vol. 217, Recycling Intergalactic and Interstellar Matter, ed. P.-A. Duc, J. Braine, & E. Brinks, 2

—. 2006, ApJS, 163, 282

Wakker, B. P. 2012, in EAS Publications Series, Vol. 56, EAS Publications Series, ed. M. A. de Avillez, 257–265

Wakker, B. P., Howk, J. C., Savage, B. D., van Woerden, H., Tufte, S. L., Schwarz, U. J., Benjamin, R., Reynolds, R. J., Peletier, R. F., & Kalberla, P. M. W. 1999a, Nature, 402, 388

Wakker, B. P., Kalberla, P. M. W., van Woerden, H., de Boer, K. S., & Putman, M. E. 2001, ApJS, 136, 537

Wakker, B. P., Lockman, F. J., & Brown, J. M. 2011, ApJ, 728, 159

Wakker, B. P. & Mathis, J. S. 2000, ApJ, 544, L107

Wakker, B. P., Oosterloo, T. A., & Putman, M. E. 2002, AJ, 123, 1953

Wakker, B. P. & Savage, B. D. 2009, ApJS, 182, 378

Wakker, B. P., Savage, B. D., Fox, A. J., Benjamin, R. A., & Shapiro, P. R. 2012, ApJ, 749, 157

Wakker, B. P., Savage, B. D., Sembach, K. R., Richter, P., Meade, M., Jenkins, E. B., Shull, J. M., Ake, T. B., Blair, W. P., Dixon, W. V., Friedman, S. D., Green, J. C., Green, R. F., Kruk, J. W., Moos, H. W., Murphy, E. M.,

Oegerle, W. R., Sahnow, D. J., Sonneborn, G., Wilkinson, E., & York, D. G. 2003, ApJS, 146, 1

Wakker, B. P. & Schwarz, U. J. 1991, A&A, 250, 484

Wakker, B. P. & van Woerden, H. 1991, A&A, 250, 509

—. 1997a, ARA&A, 35, 217

—. 1997b, ARA&A, 35, 217

Wakker, B. P., van Woerden, H., & Gibson, B. K. 1999b, in Astronomical Society of the Pacific Conference Series, Vol. 166, Stromlo Workshop on High-Velocity Clouds, ed. B. K. Gibson & M. E. Putman, 311

Wakker, B. P., York, D. G., Howk, J. C., Barentine, J. C., Wilhelm, R., Peletier, R. F., van Woerden, H., Beers, T. C., Ivezić, Ž., Richter, P., & Schwarz, U. J. 2007, ApJ, 670, L113

Wakker, B. P., York, D. G., Wilhelm, R., Barentine, J. C., Richter, P., Beers, T. C., Ivezić, Ž., & Howk, J. C. 2008, ApJ, 672, 298

Wannier, P., Wrixon, G. T., & Wilson, R. W. 1972, A&A, 18, 224

Weiner, B. J. 2003, in Astrophysics and Space Science Library, Vol. 281, The IGM/Galaxy Connection. The Distribution of Baryons at z=0, ed. J. L. Rosenberg & M. E. Putman, 163

Welsh, B. Y., Sallmen, S., & Lallement, R. 2004, A&A, 414, 261

Welty, D. E., Frisch, P. C., Sonneborn, G., & York, D. G. 1999, ApJ, 512, 636

Welty, D. E., Lauroesch, J. T., Blades, J. C., Hobbs, L. M., & York, D. G. 1997, ApJ, 489, 672

Werner, M. W., Becklin, E. E., Gatley, I., et al. 1979, MNRAS, 188, 463

Wesselius, P. R. & Fejes, I. 1973, A&A, 24, 15

Westmeier, T., Braun, R., Brüns, C., Kerp, J., & Thilker, D. A. 2007, New Astron. Rev., 51, 108

Westmeier, T., Brüns, C., & Kerp, J. 2005, A&A, 432, 937

White, S. D. M. & Rees, M. J. 1978, MNRAS, 183, 341

Whittet, D. C. B., Schutte, W. A., Tielens, A. G. G. M., et al. 1996, A&A, 315, L357

Wilhelm, R., Beers, T. C., & Gray, R. O. 1999, AJ, 117, 2308

Willick, J. A., Courteau, S., Faber, S. M., et al. 1997, ApJS, 109, 333

Willner, S. P., Gillett, F. C., Herter, T. L., et al. 1982, ApJ, 253, 174

Wilson, T. L. 1999, Reports on Progress in Physics, 62, 143

Wiltsee, C. B. & Brooks, W. F. 1989, in Society of Photo-Optical Instrumentation Engineers (SPIE) Conference Series, Vol. 973, Society of Photo-Optical Instrumentation Engineers (SPIE) Conference Series, ed. R. K. Melugin & W. G. Pierce, 148–158

Winkel, B., Ben Bekhti, N., Darmstädter, V., Flöer, L., Kerp, J., & Richter, P. 2011, A&A, 533, A105

Winter, L. M., Danforth, C., Vasudevan, R., Brandt, W. N., Scott, J., Froning, C., Keeney, B., Shull, J. M., Penton, S., Mushotzky, R., Schneider, D. P., & Arav, N. 2011, ApJ, 728, 28

Wolfire, M. G., McKee, C. F., Hollenbach, D., & Tielens, A. G. G. M. 1995, ApJ, 453, 673

Wu, H., Burstein, D., Deng, Z., Zhou, X., Shang, Z., Zheng, Z., Chen, J., Su, H., Windhorst, R. A., Chen, W.-p., Zou, Z., Xia, X., Jiang, Z., Ma, J., Xue, S., Zhu, J., Cheng, F., Byun, Y.-I., Chen, R., Deng, L., Fan, X., Fang, L.-Z., Kong, X., Li, Y., Lin, W., Lu, P., Sun, W.-h., Tsay, W.-s., Xu, W., Yan, H., Zhao, B., & Zheng, Z. 2002, AJ, 123, 1364

Wu, H., Cao, C., Hao, C.-N., et al. 2005, ApJ, 632, L79

Yao, Y., Shull, J. M., & Danforth, C. W. 2011, ApJ, 728, L16+

York, D. G., Adelman, J., Anderson, Jr., J. E., et al. 2000, AJ, 120, 1579

York, D. G., Caulet, A., Rybski, P., Gallagher, J., Blades, J. C., Morton, D. C., & Wamsteker, W. 1990, ApJ, 351, 412

Zech, W. F., Lehner, N., Howk, J. C., Dixon, W. V. D., & Brown, T. M. 2008, ApJ, 679, 460

Zinnecker, H. & Yorke, H. W. 2007, ARA&A, 45, 481

Zucker, D. B., Belokurov, V., Evans, N. W., Kleyna, J. T., Irwin, M. J., Wilkinson, M. I., Fellhauer, M., Bramich, D. M., Gilmore, G., Newberg, H. J., Yanny, B., Smith, J. A., Hewett, P. C., Bell, E. F., Rix, H.-W., Gnedin, O. Y., Vidrih, S., Wyse, R. F. G., Willman, B., Grebel, E. K., Schneider, D. P., Beers, T. C., Kniazev, A. Y., Barentine, J. C., Brewington, H., Brinkmann, J., Harvanek, M., Kleinman, S. J., Krzesinski, J., Long, D., Nitta, A., & Snedden, S. A. 2006, ApJ, 650, L41

Zuo, L. & Lu, L. 1993, ApJ, 418, 601